

<sup>1</sup> **Searches for Supersymmetric signatures in  
2 all hadronic final states with the  $\alpha_T$   
3 variable.**

<sup>4</sup> Darren Burton

<sup>5</sup> Imperial College London  
<sup>6</sup> Department of Physics

<sup>7</sup> A thesis submitted to Imperial College London  
<sup>8</sup> for the degree of Doctor of Philosophy

---

## Abstract

A search for supersymmetric particles in events with high  $p_T$  jets and a large missing energy signature, is conducted using data recorded by the Compact Muon Solenoid detector based at the Large Hadron Collider. The analysis is performed with  $11.7 \text{ fb}^{-1}$  of data, collected with a center-of-mass collision energy of 8 TeV during the 2012 run period. The dimensionless kinematic variable  $\alpha_T$  is used as a tool to select events with genuine missing energy signatures, whilst Standard Model backgrounds in the signal region are estimated using data driven control samples, which have similar kinematics to the signal region. No excess of over Standard Model expectations is found. Exclusion limits are set at the 95% confidence level in the parameter space of a range of supersymmetric simplified model topologies, with special emphasis on those with compressed spectra (small mass splittings) and natural SUSY scenarios (large number of final state b flavoured jets). A complementary method to search for natural SUSY signatures, through the use of a simple template fit is also presented. The event selections of the  $\alpha_T$  search are used as a vehicle to validate the technique in both data and simulation. Estimated Standard Model backgrounds from the template fits are compared with those determined from the data driven background estimation method of the  $\alpha_T$  search within the signal search region, where good agreement between the individual predictions and that of data are observed. Additionally the efficiency of the hadronic Level-1 single jet triggers are measured throughout the 2012 run period, where a change to the jet seed algorithm was implemented during the data taking period. This change was introduced to negate an increase in rate which can be attributed to pile-up jets, whilst maintaining similar performance in the triggering of physics events.

38

## Declaration

39

I, the author of this thesis, declare that the work presented within this  
40 document to be my own. The work presented in Chapters 4, 5, 6 and Section  
41 3.4, is a result of the author's own work, or that of which I have been a major  
42 contributor unless explicitly stated otherwise, and is carried out within the  
43 context of the Imperial College London and CERN SUSY groups, itself a  
44 subsection of the greater CMS collaboration. All figures and studies taken  
45 from external sources are referenced appropriately throughout this document.

46

Darren Burton

47

## Acknowledgements

48 I would like to thank the many people whom I have had the pleasure of working with  
49 during the course of the last three and a half years. The opportunity to work as part  
50 of the largest scientific collaboration during one of the most exciting times in particle  
51 physics for decades, has been a real privilege to be a part of. I could not have achieved  
52 the results presented in this thesis without the help of my colleagues who were part of the  
53 RA1 team, Edward Laird, Chris Lucas, Henning Flaecher, Yossof Eshaq, Bryn Mathais,  
54 Sam Rogerson, Zhaoxia Meng and Georgia Karapostoli whom I worked with on L1 jets. I  
55 also thank my supervisor Oliver Buchmuller for his guidance in getting me to this point.

56 I also feel it important to single out thanks to the postdocs that I have worked with during  
57 my PhD. Jad Marrouche from whom I have learnt a great deal and Robert Bainbridge  
58 who has been like a second supervisor to me, helping me during my time at Imperial and  
59 CERN, especially during those most stressful of times approaching conference deadlines!

60 My fellow PhD students who I live with and have seen on an almost daily basis for the  
61 last few years, Andrew Gilbert, Patrick Owen, Indrek Sepp, Matthew Kenzie and my  
62 girlfriend Hannah. Thanks for putting up with the whinging, complaining and clopping.

63 Finally my largest thanks go to my Mum and Dad whose patience, encouragement and  
64 considerable financial support have allowed me to take the many steps that lead me here  
65 today.

# **Contents**

66	<b>List of Figures</b>	viii
68	<b>List of Tables</b>	xiii
69	<b>1. Introduction</b>	2
70	<b>2. A Theoretical Overview</b>	5
71	2.1. The Standard Model . . . . .	5
72	2.1.1. Gauge Symmetries of the SM . . . . .	7
73	2.1.2. The Electroweak Sector and Electroweak Symmetry Breaking . . . . .	9
74	2.2. Motivation for Physics Beyond the Standard Model . . . . .	13
75	2.3. Supersymmetry Overview . . . . .	14
76	2.3.1. R-Parity . . . . .	16
77	2.4. Experimental Signatures of SUSY at the LHC . . . . .	16
78	2.4.1. Simplified models . . . . .	18
79	<b>3. The LHC And The CMS Detector</b>	20
80	3.1. The LHC . . . . .	20
81	3.2. The CMS Detector . . . . .	23
82	3.2.1. Detector subsystems . . . . .	23
83	3.2.2. Tracker . . . . .	24
84	3.2.3. Electromagnetic calorimeter . . . . .	25
85	3.2.4. Hadronic calorimeter . . . . .	26
86	3.2.5. Muon systems . . . . .	28
87	3.3. Event Reconstruction and Object Definition . . . . .	28
88	3.3.1. Jets . . . . .	28
89	3.3.2. B-tagging . . . . .	30
90	3.4. Triggering System . . . . .	33
91	3.4.1. The Level-1 trigger . . . . .	34

92	3.4.2. The L1 trigger jet algorithm . . . . .	35
93	3.4.3. Measuring L1 jet trigger efficiencies . . . . .	37
94	3.4.4. Effects of the L1 jet seed . . . . .	38
95	3.4.5. Robustness of L1 jet performance against pile-up . . . . .	40
96	3.4.6. Summary . . . . .	43
97	<b>4. SUSY Searches In Hadronic Final States</b>	<b>45</b>
98	4.1. An Introduction to the $\alpha_T$ Search . . . . .	46
99	4.1.1. The $\alpha_T$ variable . . . . .	48
100	4.2. Search Strategy . . . . .	50
101	4.2.1. Physics objects . . . . .	53
102	4.2.2. Event selection . . . . .	57
103	4.2.3. Control sample definition and background estimation . . . . .	60
104	4.2.4. Estimating the QCD multi-jet background . . . . .	67
105	4.3. Trigger Strategy . . . . .	69
106	4.4. Measuring MC Normalisation Factors via $H_T$ Sidebands . . . . .	70
107	4.5. Determining MC Simulation Yields with Higher Statistical Precision . . . . .	71
108	4.5.1. The formula method . . . . .	72
109	4.5.2. Establishing proof of principle . . . . .	73
110	4.5.3. Correcting measured efficiencies in simulation to data . . . . .	74
111	4.6. Systematic Uncertainties on Transfer Factors . . . . .	77
112	4.6.1. Determining systematic uncertainties from closure tests . . . . .	80
113	4.7. Simplified Models, Efficiencies and Systematic Uncertainties . . . . .	83
114	4.7.1. Signal efficiency . . . . .	83
115	4.7.2. Applying b-tag scale factor corrections in signal samples . . . . .	84
116	4.7.3. Experimental uncertainties . . . . .	86
117	4.8. Statistical Interpretation . . . . .	89
118	4.8.1. Hadronic sample . . . . .	89
119	4.8.2. $H_T$ evolution model . . . . .	90
120	4.8.3. Electroweak Sector (EWK) control samples . . . . .	90
121	4.8.4. Contributions from signal . . . . .	93
122	4.8.5. Total likelihood . . . . .	94
123	<b>5. Results And Interpretation</b>	<b>96</b>
124	5.1. Compatibility with the Standard Model Hypothesis . . . . .	96
125	5.2. SUSY . . . . .	105
126	5.2.1. The $CL_s$ method . . . . .	105

127	5.2.2. Interpretation in simplified signal models . . . . .	106
128	<b>6. Searching For Natural SUSY With B-tag Templates.</b>	110
129	6.1. Concept . . . . .	110
130	6.2. Application to the $\alpha_T$ Search . . . . .	113
131	6.2.1. Proof of principle in simulation . . . . .	114
132	6.2.2. Results in a data control sample . . . . .	116
133	6.2.3. Application to the $\alpha_T$ hadronic search region . . . . .	118
134	6.3. Summary . . . . .	120
135	<b>7. Conclusions</b>	122
136	<b>A. Miscellaneous</b>	124
137	A.1. Jet Identification Criteria . . . . .	124
138	A.2. Primary Vertices . . . . .	125
139	<b>B. L1 Jets</b>	126
140	B.1. Jet matching efficiencies . . . . .	126
141	B.2. Leading Jet Energy Resolution . . . . .	127
142	B.3. Resolution for Energy Sum Quantities . . . . .	130
143	<b>C. Additional material on background estimation methods</b>	132
144	C.1. Determination of $k_{QCD}$ . . . . .	132
145	C.2. Effect of varying background cross sections on closure tests . . . . .	133
146	<b>D. Additional Material For B-tag Template Method</b>	135
147	D.1. Templates Fits in Simulation . . . . .	135
148	D.2. Pull Distributions for Template Fits . . . . .	138
149	D.3. Templates Fits in Data Control Sample . . . . .	139
150	D.4. Templates Fits in Data Signal Region . . . . .	141
151	<b>Bibliography</b>	144

# <sup>152</sup> List of Figures

<sup>153</sup> 2.1.	One loop quantum corrections to the Higgs squared mass parameter $m_h^2$ due to a fermion. . . . .	<sup>14</sup>
<sup>155</sup> 2.2.	Two example simplified model decay chains. . . . .	<sup>19</sup>
<sup>156</sup> 3.1.	A top down layout of the LHC, with the position of the four main detectors labelled. . . . .	<sup>21</sup>
<sup>158</sup> 3.2.	The total integrated luminosity delivered to and collected by Compact Muon Solenoid (CMS) during the 2012 8 TeV $pp$ runs . . . . .	<sup>22</sup>
<sup>160</sup> 3.3.	A pictorial depiction of the CMS detector. . . . .	<sup>24</sup>
<sup>161</sup> 3.4.	Illustration of the CMS Electromagnetic CALorimeter (ECAL). . . . .	<sup>26</sup>
<sup>162</sup> 3.5.	Schematic of the CMS Hadronic CALorimeter (HCAL). . . . .	<sup>27</sup>
<sup>163</sup> 3.6.	Combined Secondary Vertex (CSV) algorithm discriminator values in enriched ttbar and inclusive multi jet samples . . . . .	<sup>31</sup>
<sup>165</sup> 3.7.	Data/MC b-tag scale factors derived using the Combined Secondary Vertex Medium Working Point (CSVM) tagger. . . . .	<sup>32</sup>
<sup>167</sup> 3.8.	Data/MC mis-tag scale factors derived using the CSVM tagger. . . . .	<sup>33</sup>
<sup>168</sup> 3.9.	The CMS Level 1 Trigger (L1) Trigger system. . . . .	<sup>34</sup>
<sup>169</sup> 3.10.	Illustration of the Level-1 jet finding algorithm. . . . .	<sup>36</sup>
<sup>170</sup> 3.11.	L1 jet efficiency turn-on curves as a function of the offline CaloJet and PFJet $E_T$ . . . . .	<sup>38</sup>
<sup>172</sup> 3.12.	L1 jet efficiency turn-on curves as a function of the offline CaloJet $E_T$ for the 2012 run period B and C. . . . .	<sup>39</sup>

---

174	3.13. Trigger cross section for the L1HTT150 trigger path. . . . .	40
175	3.14. L1 $H_T$ efficiency turn-on curves as a function of the offline CaloJet $H_T$ . . . . .	41
176	3.15. L1 jet efficiency turn-on curves as a function of the leading offline $E_T$ Calo	
177	(left) and PF (right) jet, for low, medium and high pile-up conditions. . . . .	42
178	3.16. Fit values from an Exponentially Modified Gaussian (EMG) function fitted	
179	to the resolution plots of leading Calo jet $E_T$ measured as a function of	
180	$\frac{(L1\ E_T - \text{Offline}\ E_T)}{\text{Offline}\ E_T}$ for low, medium and high pile-up conditions. . . . .	43
181	3.17. Fit values from an EMG function fitted to the resolution plots of leading	
182	PF jet $E_T$ measured as a function of $\frac{(L1\ E_T - \text{Offline}\ E_T)}{\text{Offline}\ E_T}$ for low, medium and	
183	high pile-up conditions. . . . .	44
184	4.1. Reconstructed offline $H_T$ distribution in the hadronic signal selection, from	
185	$11.7\text{fb}^{-1}$ of data, in which no $\alpha_T$ requirement is made. . . . .	48
186	4.2. The event topologies of background QCD dijet events (right) and a generic	
187	SUSY signature with genuine $Z_T$ (left). . . . .	48
188	4.3. The $\alpha_T$ distributions for the low 2-3 (left) and high $\geq 4$ (right) jet	
189	multiplicities after a full analysis selection and shown for $H_T > 375$ . . . . .	50
190	4.4. Pictorial depiction of the analysis strategy employed by the $\alpha_T$ search to	
191	increase sensitivity to a wide spectra of SUSY models. . . . .	53
192	4.5. Data/MC comparisons of key variables for the hadronic signal region. . . . .	60
193	4.6. Data/MC comparisons of key variables for the $\mu +$ jets selection. . . . .	63
194	4.7. Data/MC comparisons of key variables for the $\mu\mu +$ jets selection. . . . .	64
195	4.8. Data/MC comparisons of key variables for the $\gamma +$ jets selection. . . . .	66
196	4.9. QCD sideband regions, used for determination of $k_{\text{QCD}}$ . . . . .	68
197	4.10. Tagging efficiencies of (a) b-jets, (b) c-jets, and (c) light-jets determined	
198	from all jets within each individual analysis $H_T$ bin. . . . .	75
199	4.11. Sets of closure tests overlaid on top of the systematic uncertainty used for	
200	each of the five $H_T$ regions. . . . .	82

---

201	4.12. Signal efficiencies fo the Simplified Model Spectra (SMS) models (a) T1 202 and (b) T2. . . . .	84
203	5.1. Comparison of the observed yields and Standard Model (SM) expectations 204 given by the simultaneous fit in bins of $H_T$ for the (a) hadronic, (b) $\mu +$ 205 jets, (c) $\mu\mu +$ jets and (d) $\gamma +$ jets samples when requiring $n_b^{reco} = 0$ and 206 $n_{jet} \leq 3$ . . . . .	98
207	5.2. Comparison of the observed yields and SM expectations given by the 208 simultaneous fit in bins of $H_T$ for the (a) hadronic, (b) $\mu +$ jets, (c) $\mu\mu +$ 209 jets and (d) $\gamma +$ jets samples when requiring $n_b^{reco} = 1$ and $n_{jet} \leq 3$ . . . . .	99
210	5.3. Comparison of the observed yields and SM expectations given by the 211 simultaneous fit in bins of $H_T$ for the (a) hadronic, (b) $\mu +$ jets, (c) $\mu\mu +$ 212 jets and (d) $\gamma +$ jets samples when requiring $n_b^{reco} = 2$ and $n_{jet} \leq 3$ . . . . .	100
213	5.4. Comparison of the observed yields and SM expectations given by the 214 simultaneous fit in bins of $H_T$ for the (a) hadronic, (b) $\mu +$ jets, (c) $\mu\mu +$ 215 jets and (d) $\gamma +$ jets samples when requiring $n_b^{reco} = 0$ and $n_{jet} \geq 4$ . . . . .	101
216	5.5. Comparison of the observed yields and SM expectations given by the 217 simultaneous fit in bins of $H_T$ for the (a) hadronic, (b) $\mu +$ jets, (c) $\mu\mu +$ 218 jets and (d) $\gamma +$ jets samples when requiring $n_b^{reco} = 1$ and $n_{jet} \geq 4$ . . . . .	102
219	5.6. Comparison of the observed yields and SM expectations given by the 220 simultaneous fit in bins of $H_T$ for the (a) hadronic, (b) $\mu +$ jets, (c) $\mu\mu +$ 221 jets and (d) $\gamma +$ jets samples when requiring $n_b^{reco} = 2$ and $n_{jet} \geq 4$ . . . . .	103
222	5.7. Comparison of the observed yields and SM expectations given by the 223 simultaneous fit in bins of $H_T$ for the (a) hadronic, (b) $\mu +$ jets, (c) $\mu\mu +$ 224 jets and (d) $\gamma +$ jets samples when requiring $n_b^{reco} = 3$ and $n_{jet} \geq 4$ . . . . .	103
225	5.8. Comparison of the observed yields and SM expectations given by the 226 simultaneous fit in bins of $H_T$ for the (a) hadronic, (b) $\mu +$ jets, (c) $\mu\mu +$ 227 jets and (d) $\gamma +$ jets samples when requiring $n_b^{reco} \geq 4$ and $n_{jet} \geq 4$ . . . . .	104
228	5.9. Production and decay modes for the various SMS models interpreted 229 within the analysis. . . . .	108
230	5.10. Upper limit of cross section at 95% CL as a function of $m_{\tilde{q}/\tilde{g}}$ and $m_{LSP}$ 231 for various SMS models. . . . .	109

---

232	6.1. The b-tagging (a), c-quark mis-tagging (b), and light-quark mis-tagging rate (c) as measured in simulation after the $\alpha_T$ analysis, $\mu + \text{jets}$ control sample selection in the region $H_T > 375$ . . . . .	112
235	6.2. The results of fitting the $Z = 0$ and $Z = 2$ templates to the $n_b^{reco} = 0, 1, 2$ bins taken directly from simulation in the region $H_T > 375$ GeV, for the $n_{jet} \geq 5$ category. . . . .	116
238	6.3. The results of fitting the $Z = 0$ and $Z = 2$ templates to the $n_b^{reco} = 0, 1, 2$ bins taken from data, for the $n_{jet} \geq 5$ category and medium CSV working point. . . . .	117
241	6.4. The results of fitting the $Z = 0$ and $Z = 2$ templates to the $n_b^{reco} = 0, 1, 2$ bins taken from data, in the $n_{jet} \geq 5$ and $H_T > 375$ category for all CSV working points. . . . .	119
244	B.1. Leading jet matching efficiency as a function of the offline CaloJet $E_T$ . . . . .	126
245	B.2. Resolution plots of the leading offline Calo $E_T$ measured as a function of $\frac{(L1 E_T - \text{Offline } E_T)}{\text{Offline } E_T}$ for low (a), medium (b) and high (c) pile-up conditions. . . . .	128
247	B.3. Resolution plots of the leading off-line PF $E_T$ measured as a function of $\frac{(L1 E_T - \text{Offline } E_T)}{\text{Offline } E_T}$ for low (a), medium (b) and high (c) pile-up conditions. . . . .	130
249	B.4. $H_T$ resolution parameters in bins of Calo $H_T$ measured in the defined low, medium and high pile up conditions. . . . .	130
251	B.5. $H_T$ resolution parameters in bins of PF $H_T$ measured in the defined low, medium and high pile up conditions. . . . .	131
253	B.6. $\mathcal{H}_T$ resolution parameters in bins of $\mathcal{H}_T$ measured in the defined low, medium and high pile up conditions. . . . .	131
255	B.7. $\mathcal{H}_T$ resolution parameters in bins of PF $\mathcal{H}_T$ measured in the defined low, medium and high pile up conditions. . . . .	131
257	C.1. $R_{\alpha_T}(H_T)$ and exponential fits for each of the data sideband regions. Fit is conducted between the $H_T$ region $275 < H_T < 575$ . . . . .	132
259	C.2. Sets of closure tests overlaid on top of the systematic uncertainty used for each of the five $H_T$ regions. . . . .	133

---

261	C.3. Sets of closure tests overlaid on top of the systematic uncertainty used for each of the five $H_T$ regions. . . . .	133
262		
263	D.1. The results of fitting the $Z = 0$ and $Z = 2$ templates to the $n_b^{reco} = 0, 1, 2$ bins taken directly from simulation in the region $H_T > 375$ GeV, for the $n_{jet} = 3$ category. . . . .	136
264		
265		
266	D.2. The results of fitting the $Z = 0$ and $Z = 2$ templates to the $n_b^{reco} = 0, 1, 2$ bins taken directly from simulation in the region $H_T > 375$ GeV, for the $n_{jet} = 4$ category. . . . .	137
267		
268		
269	D.3. Pull distributions of $\frac{(\theta - \hat{\theta})}{\sigma}$ for $10^4$ pseudo-experiments generated from a gaussian distribution centred on the $n_b^{reco}$ template values from simulation with width $\sigma$ . . . . .	138
270		
271		
272	D.4. The results of fitting the $Z = 0$ and $Z = 2$ templates to the $n_b^{reco} = 0, 1, 2$ bins taken directly from data, for the $n_{jet} = 3$ category and medium CSV working point. . . . .	139
273		
274		
275	D.5. The results of fitting the $Z = 0$ and $Z = 2$ templates to the $n_b^{reco} = 0, 1, 2$ bins taken directly from data, for the $n_{jet} = 4$ category and medium CSV working point. . . . .	140
276		
277		
278	D.6. The results of fitting the $Z = 0$ and $Z = 2$ templates to the $n_b^{reco} = 0, 1, 2$ bins taken from data, in the $n_{jet} = 3$ and $H_T > 375$ category for all CSV working points. . . . .	141
279		
280		
281	D.7. The results of fitting the $Z = 0$ and $Z = 2$ templates to the $n_b^{reco} = 0, 1, 2$ bins taken from data, in the $n_{jet} = 4$ and $H_T > 375$ category for all CSV working points. . . . .	142
282		
283		

# <sup>284</sup> List of Tables

285	2.1. The fundamental particles of the SM, with spin, charge and mass displayed.	6
286	3.1. Results of a cumulative EMG function fit to the turn-on curves for L1	
287	single jet triggers in 2012 Run Period C. . . . .	38
288	3.2. Results of a cumulative EMG function fit to the turn-on curves for L1	
289	single jet triggers in the 2012 run period B and C. . . . .	40
290	3.3. Results of a cumulative EMG function fit to the turn-on curves for $H_T$ in	
291	2012 run period B and C. . . . .	41
292	3.4. Results of a cumulative EMG function fit to the efficiency turn-on curves	
293	for L1 single jet triggers in the 2012 run period C, for low,medium and	
294	high pile-up conditions. . . . .	41
295	3.5. Results of a cumulative EMG function fit to the efficiency turn-on curves	
296	for Level-1 single jet triggers in the 2012 run period C, for low,medium	
297	and high pile-up conditions. . . . .	42
298	4.1. A summary of the SMS models interpreted in this analysis, involving both	
299	direct (D) and gluino-induced (G) production of squarks and their decays.	46
300	4.2. Muon Identification criteria used within the analysis for selection/veto	
301	purposes in the muon control/signal selections. . . . .	54
302	4.3. Photon Identification criteria used within the analysis for selection/veto	
303	purposes in the $\gamma +$ jets control/signal selections. . . . .	55
304	4.4. Electron Identification criteria used within the analysis for veto purposes.	56
305	4.5. Noise filters that are applied to remove spurious and non-physical $\cancel{E}_T$	
306	signatures within the CMS detector. . . . .	57

307	4.6. Jet thresholds used in the three $H_T$ regions of the analysis. . . . .	58
308	4.7. Best fit values for the parameters $k_{\text{QCD}}$ obtained from sideband regions	
309	B,C <sub>1</sub> ,C <sub>2</sub> ,C <sub>3</sub> . . . . .	69
310	4.8. Measured efficiencies of the $H_T$ and $\alpha_T$ legs of the HT and HT_alphaT	
311	triggers in independent analysis bins. . . . .	70
312	4.9. k-factors calculated for different EWK processes. . . . .	71
313	4.10. Comparing yields in simulation within the $\mu + \text{jets}$ selection determined	
314	from the formula method described in Equation (4.11), and that taken	
315	directly from simulation . . . . .	74
316	4.11. The absolute change in the Transfer Factor (TF)'s used to predict the	
317	entire signal region SM background, using the $\mu + \text{jets}$ control sample	
318	when the systematic uncertainties of the data to simulation scale factors	
319	are varied by $\pm 1\sigma$ . . . . .	76
320	4.12. A summary of the results obtained from zeroeth order polynomial (i.e.	
321	a constant) and linear fits to five sets of closure tests performed in the	
322	$2 \geq n_{\text{jet}} \geq 3$ category. . . . .	79
323	4.13. A summary of the results obtained from zeroeth order polynomial (i.e.	
324	a constant) and linear fits to five sets of closure tests performed in the	
325	$n_{\text{jet}} \geq 4$ category. . . . .	79
326	4.14. A summary of the results obtained from zeroeth order polynomial (i.e. a	
327	constant) and linear fits to three sets of closure tests performed between	
328	the $2 \leq n_{\text{jet}} \leq 3$ and $n_{\text{jet}} \geq 4$ categories. . . . .	80
329	4.15. Calculated systematic uncertainties for the five $H_T$ regions, determined	
330	from the closure tests. . . . .	81
331	4.16. Estimates of systematic uncertainties on the signal efficiency (%) for	
332	various SMS models when considering points in the region near to the	
333	diagonal . . . . .	88
334	4.17. Estimates of systematic uncertainties on the signal efficiency (%) for	
335	various SMS models when considering points in the region near to the	
336	diagonal . . . . .	88

---

337	4.18. The systematic parameters used in $H_T$ bins. . . . .	92
338	4.19. Nuisance parameters used within the different hadronic signal bins of the	
339	analysis . . . . .	94
340	5.1. Summary of control samples used by each fit results, and the Figures in	
341	which they are displayed. . . . .	97
342	5.2. Comparison of the measured yields in each $H_T$ , $n_{jet}$ and $n_b^{reco}$ jet multiplicity bins for the hadronic sample with the SM expectations and combined	
343	statistical and systematic uncertainties given by the simultaneous fit. . .	97
344		
345	5.3. A table representing the SMS models interpreted within the analysis. . .	107
346	6.1. Typical underlying b-quark content of different SM processes which are	
347	common to many SUSY searches. . . . .	111
348	6.2. Summary of the fit predictions in the $n_b^{reco}$ signal region for $n_{jet} = 3, =$	
349	$4, \geq 5$ . The fit region is $n_b^{reco} = 0, 1, 2$ and simulation yields are normalised	
350	to an integrated luminosity of $10 \text{ fb}^{-1}$ . . . . .	115
351	6.3. Summary of the fit predictions in the $n_b^{reco}$ signal region of the $\mu + \text{jets}$	
352	control sample, for $n_{jet} = 3, = 4, \geq 5$ . The fit region is $n_b^{reco} = 0, 1, 2$	
353	using $11.5 \text{ fb}^{-1}$ of data at $\sqrt{s} = 8\text{TeV}$ . . . . .	118
354	6.4. Summary of the fit predictions in the $n_b^{reco}$ signal region of the $\mu + \text{jets}$	
355	control sample, for $n_{jet} = 3, = 4, \geq 5$ . The fit region is $n_b^{reco} = 0, 1, 2$	
356	using $11.5 \text{ fb}^{-1}$ of data at $\sqrt{s} = 8\text{TeV}$ . . . . .	120
357	A.1. Criteria for a reconstructed jet to pass the loose calorimeter jet id. . . . .	124
358	A.2. Criteria for a reconstructed jet to pass the loose PF jet id. . . . .	125
359	A.3. Criteria for a vertex in an event to be classified as a 'good' reconstructed	
360	primary vertex. . . . .	125
361	B.1. Results of a cumulative EMG function fit to the turn-on curves for the	
362	matching efficiency of the leading jet in an event to a Level-1 jet in run	
363	2012C and 2012B data. . . . .	127

---

364	C.1. Translation factors constructed from the $\mu +$ jets control sample and signal selection MC, to predict yields for the $W +$ jets and $t\bar{t}$ back-grounds in the signal region. . . . .	134
365		
366		

*“The Universe is about 1,000,000 years old.”*

— Matthew Kenzie, 1987-present : Discoverer of the Higgs Boson.

# Chapter 1.

## <sup>369</sup> Introduction

<sup>370</sup> During the 20th century, great advances have been made in the human understanding  
<sup>371</sup> of the universe, its origins, its future and its composition. The Standard Model (**SM**)  
<sup>372</sup> first formulated in the 1960s is one of the crowning achievements in science's quest to  
<sup>373</sup> explain the most fundamental processes and interactions that make up our universe. It  
<sup>374</sup> has provided a highly successful explanation of a wide range of phenomena in Particle  
<sup>375</sup> Physics and has stood up to extensive experimental scrutiny [1].

<sup>376</sup> Despite its success it is not a complete theory, with significant questions remaining  
<sup>377</sup> unanswered. It describes only three of the four known forces with gravity not incorporated  
<sup>378</sup> within the framework of the **SM**. Cosmological experiments infer that just  $\sim 4\%$  of the  
<sup>379</sup> observable universe exists as matter, with elusive "Dark Matter" accounting for a further  
<sup>380</sup>  $\sim 23\%$  [2]. However no particle predicted by the **SM** is able to account for it. At higher  
<sup>381</sup> energy scales and small distances, the (non-)unification of the fundamental forces point  
<sup>382</sup> to problems with the **SM** at least at higher energies not yet probed experimentally.

<sup>383</sup> Many theories exist as extensions to the **SM**, predicting a range of observables that can  
<sup>384</sup> be detected at the Large Hadron Collider (**LHC**) of which SUperSYmmetry (**SUSY**) is  
<sup>385</sup> one such example. It predicts a new symmetry of nature in which all current particles  
<sup>386</sup> in the **SM** would have a corresponding supersymmetric partner. Common to most  
<sup>387</sup> Supersymmetric theories is a stable, weakly interacting Lightest Supersymmetric Partner  
<sup>388</sup> (**LSP**), which has the properties of a possible dark matter candidate. The **SM** and the  
<sup>389</sup> main principles of Supersymmetric theories are outlined in Chapter 2, with emphasis  
<sup>390</sup> placed on how experimental signatures of **SUSY** may reveal themselves in proton collisions  
<sup>391</sup> at the **LHC**.

392 The experimental goal of the LHC is to further test the framework of the SM, exploring the  
393 TeV mass scale for the first time, and to seek a connection between the particles produced  
394 in proton collisions and dark matter. The first new discovery by this extraordinary  
395 machine was announced on the 4th of July 2012. The long-awaited discovery was the  
396 culmination of decades of experimental endeavours in the search for the Higgs boson,  
397 providing an answer to the mechanism of electroweak symmetry breaking within the SM  
398 [3][4].

399 This discovery was made possible through data taken by the two multi purpose detectors  
400 (Compact Muon Solenoid (CMS) and A Toroidal LHC ApparatuS (ATLAS)) located  
401 on the LHC ring. An experimental description of the CMS detector and the LHC is  
402 described in Chapter 3, including some of the object reconstruction used by CMS in  
403 searches for SUSY signatures.

404 The performance of the CMS Level-1 single jet trigger, measured over the course of  
405 the year is also included within this chapter. The Level-1 triggers are of paramount  
406 importance to the recording of physics events at CMS, and to which a change in the jet  
407 seed algorithm was introduced approximately half way through the data taking period.  
408 The aim of this change, was to facilitate a reduction in the rate at which data from  
409 events not of interest to physics analyses were recorded, whilst avoiding impact on those  
410 which were.

411 Chapter 4, contains a description of the search for evidence of the production of Su-  
412 persymmetric particles at the LHC. The main basis of the search centres around the  
413 kinematic dimensionless  $\alpha_T$  variable, which provides strong rejection of backgrounds with  
414 fake missing energy signatures whilst maintaining good sensitivity to a variety of SUSY  
415 topologies. The author's work (as an integral part of the analysis group) is documented  
416 in detail, and which has culminated in numerous publications over the past two years,  
417 the latest results having been published in the European Physical Journal C (EPJC) [5].  
418 The results and interpretations within the framework of a variety of Simplified Model  
419 Spectra (SMS), which describe an array of possible SUSY event topologies is documented  
420 in Chapter 5.

421 The author in particular has played a major role in the extension of the  $\alpha_T$  analysis into  
422 the additional b-tagged and jet multiplicity dimensions increasing the sensitivity of the  
423 analysis to a range of SUSY topologies. Additionally the author has worked extensively  
424 in both increasing the statistical precision of electroweak predictions measured from  
425 simulation through analytical techniques, and the derivation of a data driven systematic

- 426 uncertainty through the establishment of closure tests within the control samples of the  
427 analysis.
- 428 Finally a method to search for **SUSY** signatures rich in top and bottom flavoured jet final  
429 states, is introduced in Chapter 6. These particular **SUSY** topologies are increasingly of  
430 interest to physicists in light of the discovery of the Higgs boson, and is discussed within  
431 the chapter. A parametrisation of the b-tagging distribution for different Electroweak  
432 processes is used to establish template shapes, which are then fitted at low b-tagged jet  
433 multiplicity (0-2), to estimate the expected number of 3 and 4 b-tagged jet events from  
434 **SM** processes. The  $\alpha_T$  event selections are used to test the functionality of this template  
435 method in both data and simulation, with background predictions from the signal region  
436 selection compared to those presented in Chapter 5.
- 437 Natural units are used throughout this thesis in which  $\hbar = c = 1$ .

# Chapter 2.

## <sup>438</sup> A Theoretical Overview

<sup>439</sup> Within this chapter, a brief introduction and background to the **SM** is given. Its success  
<sup>440</sup> as a rigorously tested and widely accepted theory is discussed as are its deficiencies,  
<sup>441</sup> leading to the argument that this theory is not a complete description of our universe.  
<sup>442</sup> The motivations for new physics at the TeV scale and in particular Supersymmetric  
<sup>443</sup> theories are outlined within Section (2.3), with the chapter concluding with how an  
<sup>444</sup> experimental signature of such theories can be produced and observed at the **LHC**,  
<sup>445</sup> Section (2.4).

### <sup>446</sup> 2.1. The Standard Model

<sup>447</sup> The **SM** is the name given to the relativistic Quantum Field Theory (**QFT**), where  
<sup>448</sup> particles are represented as excitations of fields, which describe the interactions and  
<sup>449</sup> properties of all the known elementary particles [6][7][8][9]. It is a renormalisable field  
<sup>450</sup> theory which contains three symmetries:  $SU(3)$  for colour charge,  $SU(2)$  for weak isospin  
<sup>451</sup> and  $U(1)$  relating to weak hyper charge, which require its Lagrangian  $\mathcal{L}_{SM}$  to be invariant  
<sup>452</sup> under local gauge transformation.

<sup>453</sup> Within the **SM** theory, matter is composed of spin  $\frac{1}{2}$  fermions, which interact with each  
<sup>454</sup> other via the exchange of spin-1 gauge bosons. A summary of the known fundamental  
<sup>455</sup> fermions and bosons is given in Table 2.1.

<sup>456</sup> Fermions are separated into quarks and leptons of which only quarks interact with the  
<sup>457</sup> strong nuclear force. Quarks unlike leptons are not seen as free particles in nature, but  
<sup>458</sup> rather exist only within baryons, composed of three quarks with an overall integer charge,  
<sup>459</sup> and quark-anti-quark pairs called mesons. Both leptons and quarks are grouped into

Particle	Symbol	Spin	Charge	Mass (GeV)
<b>First Generation Fermions</b>				
Electron Neutrino	$\nu_e$	$\frac{1}{2}$	0	$< 2.2 \times 10^{-6}$
Electron	e	$\frac{1}{2}$	-1	$0.51 \times 10^{-3}$
Up Quark	u	$\frac{1}{2}$	$\frac{2}{3}$	$2.3^{+0.7}_{-0.5} \times 10^{-3}$
Down Quark	d	$\frac{1}{2}$	$-\frac{1}{3}$	$4.8^{+0.7}_{-0.3} \times 10^{-3}$
<b>Second Generation Fermions</b>				
Muon Neutrino	$\nu_\mu$	$\frac{1}{2}$	0	-
Muon	$\mu$	$\frac{1}{2}$	-1	$1.05 \times 10^{-3}$
Charm Quark	c	$\frac{1}{2}$	$\frac{2}{3}$	$1.275 \pm 0.025$
Strange Quark	s	$\frac{1}{2}$	$-\frac{1}{3}$	$95 \pm 5 \times 10^{-3}$
<b>Third Generation Fermions</b>				
Tau Neutrino	$\nu_\tau$	$\frac{1}{2}$	0	-
Tau	$\tau$	$\frac{1}{2}$	-1	1.77
Top Quark	t	$\frac{1}{2}$	$\frac{2}{3}$	$173.5 \pm 0.8$
Bottom Quark	b	$\frac{1}{2}$	$-\frac{1}{3}$	$4.65 \pm 0.03$
<b>Gauge Bosons</b>				
Photon	$\gamma$	1	0	0
W Boson	$W^\pm$	1	$\pm 1$	$80.385 \pm 0.015$
Z Boson	Z	1	0	$91.187 \pm 0.002$
Gluons	g	1	0	0
Higgs Boson	H	0	0	$125.3 \pm 0.5$ [4]

**Table 2.1.:** The fundamental particles of the SM, with spin, charge and mass displayed. Latest mass measurements taken from [1].

460 three generations which have the same properties, but with ascending mass in each  
461 subsequent generation.

462 The gauge bosons mediate the interactions between fermions. The field theories of  
463 Quantum Electro-Dynamics (QED) and Quantum Chromo-Dynamics (QCD), yield  
464 massless mediator bosons, the photon and eight coloured gluons which are consequences  
465 of the gauge invariance of those theories, detailed in Section (2.1.1).

466 The unification of the electromagnetic and weak-nuclear forces into the current Elec-  
467 troweak theory yield the weak gauge bosons,  $W^\pm$  and Z through the mixing of the  
468 associated gauge fields. The force carriers of this theory were experimentally detected by  
469 the observation of weak neutral current, discovered in 1973 in the Gargamelle bubble  
470 chamber located at European Organization for Nuclear Research (CERN) [10], with the  
471 masses of the weak gauge bosons measured by the UA1 and U2 experiments at the Super  
472 Proton Synchrotron (SPS) collider in 1983 [11][12].

### <sup>473</sup> 2.1.1. Gauge Symmetries of the SM

- <sup>474</sup> Symmetries are of fundamental importance in the description of physical phenomena.  
<sup>475</sup> Noether's theorem states that for a dynamical system, the consequence of any symmetry  
<sup>476</sup> is an associated conserved quantity [13]. Invariance under translations, rotations, and  
<sup>477</sup> Lorentz transformations in physical systems lead to conservation of momentum, energy  
<sup>478</sup> and angular momentum.
- <sup>479</sup> In the **SM**, a quantum theory described by Lagrangian formalism, the weak, strong and  
<sup>480</sup> electromagnetic interactions are described in terms of “gauge theories”. A gauge theory  
<sup>481</sup> possesses invariance under a set of “local transformations”, which are transformations  
<sup>482</sup> whose parameters are space-time dependent. The requirement of gauge invariance within  
<sup>483</sup> the **SM** necessitates the introduction of force-mediating gauge bosons and interactions  
<sup>484</sup> between fermions and the bosons themselves. Given the nature of the topics covered by  
<sup>485</sup> this thesis, the formulation of **EWK** within the **SM** Lagrangian is reviewed within this  
<sup>486</sup> section.
- <sup>487</sup> The simplest example of the application of the principle of local gauge invariance within  
<sup>488</sup> the **SM** is in Quantum Electro-Dynamics (**QED**), the consequences of which require a  
<sup>489</sup> massless photon field [14][15].
- <sup>490</sup> Starting from the free Dirac Lagrangian written as

$$\mathcal{L} = \bar{\psi}(i\gamma^\mu \partial_\mu - m)\psi, \quad (2.1)$$

- <sup>491</sup> where  $\psi$  represents a free non interacting fermionic field, with the matrices  $\gamma^\mu$ ,  $\mu \in 0, 1, 2, 3$   
<sup>492</sup> defined by the anti commutator relationship  $\gamma^\mu \gamma^\nu + \gamma^\nu \gamma^\mu = 2\eta^{\mu\nu} I_4$ , with  $\eta^{\mu\nu}$  being the  
<sup>493</sup> flat space-time metric  $(+, -, -, -)$ , and  $I_4$  the  $4 \times 4$  identity matrix.
- <sup>494</sup> Under a local U(1) abelian gauge transformation in which  $\psi$  transforms as:

$$\psi(x) \rightarrow \psi'(x) = e^{i\theta(x)}\psi(x) \quad \bar{\psi}(x) \rightarrow \bar{\psi}'(x) = e^{i\theta(x)}\bar{\psi}(x) \quad (2.2)$$

- <sup>495</sup> the kinetic term of the Lagrangian will not remain invariant, due to the partial derivative  
<sup>496</sup> interposed between the  $\bar{\psi}$  and  $\psi$  yielding,

$$\partial_\mu \psi \rightarrow e^{i\theta(x)} \partial_\mu \psi + ie^{i\theta(x)} \psi \partial_\mu \theta. \quad (2.3)$$

497 To ensure that  $\mathcal{L}$  remains invariant, a modified derivative,  $D_\mu$ , that transforms covari-  
498 antly under phase transformations is introduced. In doing this a vector field  $A_\mu$  with  
499 transformation properties that cancel out the unwanted term in (2.3) must also be  
500 included,

$$D_\mu \equiv \partial_\mu - ieA_\mu, \quad A_\mu \rightarrow A_\mu + \frac{1}{e} \partial_\mu \theta. \quad (2.4)$$

501 Invariance of the Lagrangian is then achieved by replacing  $\partial_\mu$  by  $D_\mu$ :

$$\begin{aligned} \mathcal{L} &= i\bar{\psi}\gamma^\mu D_\mu \psi - m\bar{\psi}\psi \\ &= \bar{\psi}(i\gamma^\mu \partial_\mu - m)\psi + e\bar{\psi}\gamma^\mu \psi A_\mu \end{aligned} \quad (2.5)$$

502 An additional interaction term is now present in the Lagrangian, coupling the Dirac  
503 particle to this vector field, which is interpreted as the photon in QED. To regard this  
504 new field as the physical photon field, a term corresponding to its kinetic energy must be  
505 added to the Lagrangian from Equation (2.5). Since this term must also be invariant  
506 under the conditions of Equation (2.4), it is defined in the form  $F_{\mu\nu} = \partial^\mu A^\nu - \partial^\nu A^\mu$ .

507 This then leads to the Lagrangian of QED:

$$\mathcal{L}_{QED} = \underbrace{i\bar{\psi}\gamma^\mu \partial_\mu \psi - \frac{1}{4}F_{\mu\nu}F^{\mu\nu}}_{\text{kinetic term}} + \underbrace{m\bar{\psi}\psi}_{\text{mass term}} + \underbrace{e\bar{\psi}\gamma^\mu \psi A_\mu}_{\text{interaction term}} \quad (2.6)$$

508 Within the Lagrangian there remains no mass term of the form  $m^2 A_\mu A^\mu$ , which is  
509 prohibited by gauge invariance. This implies that the gauge particle, the photon, must  
510 be massless.

### 2.1.2. The Electroweak Sector and Electroweak Symmetry Breaking

- The same application of gauge symmetry and the requirement of local gauge invariance can be used to unify QED and the Weak force in the Electroweak Sector (EWK). The nature of EWK interactions is encompassed within a Lagrangian invariant under transformations of the group  $SU(2)_L \times U(1)_Y$ .
- The weak interactions from experimental observation [16], are known to violate parity and are therefore not symmetric under interchange of left and right helicity fermions. Thus within the SM the left and right handed parts of these fermion fields are treated separately. A fermion field is then split into two left and right handed chiral components,  $\psi = \psi_L + \psi_R$ , where  $\psi_{L/R} = (1 \pm \gamma^5)\psi$ .
- The  $SU(2)_L$  group is the special unitary group of  $2 \times 2$  matrices  $U$  satisfying  $UU^\dagger = I$  and  $\det(U) = 1$ . It may be written in the form  $U = e^{-i\omega_i T_i}$ , with the generators of the group  $T_i = \frac{1}{2}\tau_i$  where  $\tau_i$ ,  $i \in 1,2,3$  being the  $2 \times 2$  Pauli matrices

$$\tau_1 = \begin{pmatrix} 0 & 1 \\ 1 & 0 \end{pmatrix} \quad \tau_2 = \begin{pmatrix} 0 & -i \\ i & 0 \end{pmatrix} \quad \tau_3 = \begin{pmatrix} 1 & 0 \\ 0 & -1 \end{pmatrix}, \quad (2.7)$$

- which form a non Abelian group obeying the commutation relation  $[T^a, T^b] \equiv if^{abc}T^c \neq 0$ . The gauge fields that accompany this group are represented by  $\hat{W}_\mu = (\hat{W}_\mu^1, \hat{W}_\mu^2, \hat{W}_\mu^3)$  and act only on the left handed component of the fermion field  $\psi_L$ .
- One additional generator  $Y$  which represents the hypercharge of the particle under consideration is introduced through the  $U(1)_Y$  group acting on both components of the fermion field, with an associated vector boson field  $\hat{B}_\mu$ .
- The  $SU(2)_L \times U(1)_Y$  transformations of the left and right handed components of  $\psi$  are summarised by,

$$\begin{aligned} \chi_L &\rightarrow \chi'_L = e^{i\theta(x) \cdot T + i\theta(x)Y} \chi_L, \\ \psi_R &\rightarrow \psi'_R = e^{i\theta(x)Y} \psi_R, \end{aligned} \quad (2.8)$$

<sup>533</sup> where the left handed fermions form isospin doubles  $\chi_L$  and the right handed fermions  
<sup>534</sup> are isosinglets  $\psi_R$ . For the first generation of leptons and quarks this represents

$$\chi_L = \begin{pmatrix} \nu_e \\ e \end{pmatrix}_L, \quad \begin{pmatrix} u \\ d \end{pmatrix}_L, \\ \psi_R = e_R, \quad u_R, d_R. \quad (2.9)$$

<sup>535</sup> Imposing local gauge invariance within  $\mathcal{L}_{EWK}$  is once again achieved by modifying the  
<sup>536</sup> covariant derivative

$$D_\mu = \partial_\mu - \frac{ig}{2}\tau^i W_\mu^i - \frac{ig'}{2}YB_\mu, \quad (2.10)$$

<sup>537</sup> where  $g$  and  $g'$  are the coupling constant of the  $SU(2)_L$  and  $U(1)_Y$  groups respectively.  
<sup>538</sup> Taking the example of the first generation of fermions defined in Equation.(2.9), with input  
<sup>539</sup> hypercharge values of -1 and -2 for  $\chi_L$  and  $e_R$  respectively, would lead to a Lagrangian  
<sup>540</sup>  $\mathcal{L}_1$  of the form,

$$\mathcal{L}_1 = \bar{\chi}_L \gamma^\mu [i\partial_\mu - g \frac{1}{2} \tau \cdot W_\mu - g' (-\frac{1}{2}) B_\mu] \chi_L \\ + \bar{e}_R \gamma^\mu [i\partial_\mu - g' (-1) B_\mu] e_R - \frac{1}{4} W_{\mu\nu} \cdot W^{\mu\nu} - \frac{1}{4} B_{\mu\nu} B^{\mu\nu}. \quad (2.11)$$

<sup>541</sup> As in QED, these additional gauge fields introduce field strength tensors  $B_{\mu\nu}$  and  $W_{\mu\nu}$ ,

$$\hat{B}_{\mu\nu} = \partial_\mu \hat{B}_\nu - \partial_\nu \hat{B}_\mu \quad (2.12)$$

$$\hat{W}_{\mu\nu} = \partial_\mu \hat{W}_\nu - \partial_\nu \hat{W}_\mu - g \hat{W}_\mu \times \hat{W}_\mu \quad (2.13)$$

<sup>542</sup> corresponding to the kinetic energy and self coupling of the  $W_\mu$  fields and the kinetic  
<sup>543</sup> energy term of the  $B_\mu$  field.

- 544 None of these gauge bosons are physical particles, and instead linear combinations of  
545 these gauge bosons make up  $\gamma$  and the W and Z bosons, defined as

$$W^\pm = \frac{1}{\sqrt{2}} (W_\mu^1 \mp iW_\mu^2), \quad \begin{pmatrix} Z_\mu \\ A_\mu \end{pmatrix} = \begin{pmatrix} \cos\theta_W & -\sin\theta_W \\ \sin\theta_W & \cos\theta_W \end{pmatrix} \begin{pmatrix} W_\mu^3 \\ B_\mu \end{pmatrix}, \quad (2.14)$$

- 546 where the mixing angle,  $\theta_w = \tan^{-1} \frac{g'}{g}$ , relates the coupling of the neutral weak and  
547 electromagnetic interactions.

548 As in the case of the formulation of the QED Lagrangian there remains no mass term for  
549 the photon. However this is also the case for the W, Z and fermions in the Lagrangian,  
550 contrary to experimental measurement. Any explicit introduction of mass terms would  
551 break the symmetry of the Lagrangian and instead mass terms can be introduced through  
552 spontaneous breaking of the EWK symmetry via the Higgs mechanism.

553 The Higgs mechanism induces spontaneous symmetry breaking through the introduction  
554 of a complex scalar SU(2) doublet field  $\phi$  which attains a non-zero Vacuum Expectation  
555 Value (VEV) [17][18][19][20].

$$\phi = \begin{pmatrix} \phi^+ \\ \phi^0 \end{pmatrix} \quad \text{with} \quad \begin{aligned} \phi^+ &\equiv (\phi_1 + i\phi_2)/\sqrt{2} \\ \phi^0 &\equiv (\phi_3 + i\phi_4)/\sqrt{2} \end{aligned} \quad (2.15)$$

- 556 The Lagrangian defined in Equation (2.11) attains an additional term  $\mathcal{L}_{Higgs}$  of the form

$$\mathcal{L}_{Higgs} = \overbrace{(D_\mu \phi)^\dagger (D^\mu \phi)}^{\text{kinetic}} - \overbrace{\mu^2 \phi^\dagger \phi - \lambda (\phi^\dagger \phi)^2}^{\text{potential } V(\phi)} \quad (\mu^2, \lambda) > 0 \in \mathbb{R},$$

$$\mathcal{L}_{SM} = \mathcal{L}_{EWK} + \mathcal{L}_{Higgs}, \quad (2.16)$$

- 557 where the covariant derivative  $D_\mu$  is that defined in Equation (2.10). The last two terms  
558 of  $\mathcal{L}_{Higgs}$  correspond to the Higgs potential, in which real positive values of  $\mu^2$  and  $\lambda$  are  
559 required to ensure the generation of masses for the bosons and leptons. The minimum of

560 this potential is found at  $\phi^\dagger \phi = \frac{1}{2}(\phi_1^2 + \phi_2^2 + \phi_3^2 + \phi_4^2) = \mu^2/\lambda = v^2$ , where  $v$  represents  
561 the **VEV**.

562 Defining the ground state of the  $\phi$  field to be consistent with the  $V(\phi)$  minimum, and  
563 then expanding around a ground state chosen to maintain an unbroken electromagnetic  
564 symmetry thus preserving a zero photon mass [21] leads to

$$\phi_0 = \sqrt{\frac{1}{2}} \begin{pmatrix} 0 \\ v \end{pmatrix}, \quad \phi(x) = e^{i\tau \cdot \theta(x)/v} \sqrt{\frac{1}{2}} \begin{pmatrix} 0 \\ v + h(x) \end{pmatrix}, \quad (2.17)$$

565 where the fluctuations from the vacuum  $\phi_0$  are parametrized in terms of four real fields,  
566  $\theta_1, \theta_2, \theta_3$  and  $h(x)$ .

567 Choosing to gauge away the three massless Goldstone boson fields by setting  $\theta(x)$  to  
568 zero and substituting  $\phi(x)$  back into kinetic term of  $\mathcal{L}_{Higgs}$  from Equation (2.16) leads  
569 to mass terms for the  $W^\pm$  and Z bosons

$$(D_\mu \phi)^\dagger (D^\mu \phi) = \frac{1}{2} (\partial_\mu h)^2 + \frac{g^2 v^2}{2} W_\mu^+ W^{-\mu} + \frac{v^2 g^2}{8 \cos^2 \theta_w} Z_\mu Z^\mu + 0 A_\mu A^\mu, \quad (2.18)$$

570 where the relations between the physical and electroweak gauge fields from Equation  
571 (2.14) are used. The  $W^\pm$  and Z boson masses can then be determined to be

$$M_W = \frac{1}{2} g v \quad M_Z = \frac{1}{2} \frac{g v}{\cos \theta_w}. \quad (2.19)$$

572 This mechanism is also used to generate fermion masses by introducing a Yukawa coupling  
573 between the fermions and the  $\phi$  field [22], with the coupling strength of a particle to  
574 the  $\phi$  field governing its mass. Additionally a scalar boson  $h$  with mass  $m_h = v \sqrt{\frac{\lambda}{2}}$ , is  
575 also predicted as a result of this spontaneous symmetry breaking and became known as  
576 the Higgs boson. Its discovery by the CMS and ATLAS experiments in 2012 is the first  
577 direct evidence to support this method of mass generation within the **SM**.

## 578    2.2. Motivation for Physics Beyond the Standard 579    Model

580    As has been described, the **SM** has proven to be a very successful theory, predicting the  
581    existence of the  $W^\pm$  and  $Z$  bosons and the top quark long before they were experimentally  
582    observed. However the theory does not accurately describe all observed phenomena and  
583    has some fundamental theoretical flaws that hint at the need for additional extensions to  
584    the current theory.

585    On a theoretical level, the **SM** is unable to incorporate the gravitational interactions of  
586    fundamental particles within the theory. Whilst at the electroweak energy scales the  
587    relative strength of gravity is negligible compared to the other three fundamental forces,  
588    at much higher energy scales,  $M_{\text{planck}} \sim 10^{18} \text{GeV}$ , quantum gravitational effects become  
589    increasingly dominant. The failure to reconcile gravity within the **SM**, demonstrates that  
590    the **SM** must become invalid at some higher energy scale.

591    Other deficiencies with the **SM** include the fact that the predicted rate of Charge-Parity  
592    violation does not account for the matter dominated universe which we inhabit, and  
593    that the **SM** prediction of a massless neutrino conflicts with the observation of neutrino  
594    flavour mixing, attributed to mixing between neutrino mass eigenstates [23][24].

595    Perhaps one of the most glaring gaps in the predictive power of the **SM** is that there  
596    exists no candidate to explain the cosmic dark matter observed in galactic structures  
597    through indirect techniques including gravitational lensing and measurement of the  
598    orbital velocity of stars at galactic edges. Any such candidate must be very weakly  
599    interacting but must also be stable, owing to the lack of direct detection of the decay  
600    products of such a process. Therefore a stable dark matter candidate, is one of the  
601    main obstacles to address for any Beyond Standard Model (**BSM**) physics model.

602    The recent discovery of the Higgs boson whilst a significant victory for the predictive  
603    power of the **SM**, brings with it still unresolved questions. This issue is commonly  
604    described as the “hierarchy problem”.

605    In the absence of new physics between the TeV and Planck scale, calculating beyond  
606    tree-level contributions to the Higgs mass term given by its self interaction, result in  
607    divergent terms that push the Higgs mass up to the planck mass  $M_{\text{planck}}$ .

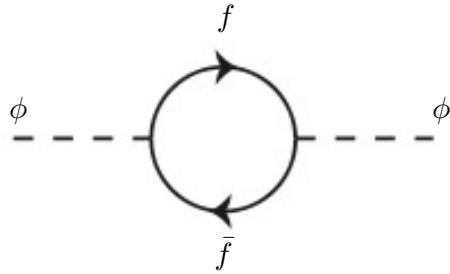


**Figure 2.1.:** One loop quantum corrections to the Higgs squared mass parameter  $m_h^2$  due to a fermion.

608 This can be demonstrated by considering the one loop quantum correction to the Higgs  
 609 mass with a fermion  $f$ , shown in Figure 2.1 with mass  $m_f$ . The Higgs field couples to  $f$   
 610 with a term in the Lagrangian  $-\lambda_f h \bar{f} f$ , yielding a correction of the form [25],

$$\delta m_h^2 = -\frac{|\lambda_f|^2}{8\pi^2} \Lambda^2 + \dots, \quad (2.20)$$

611 where  $\lambda_f$  represents the coupling strength for each type of fermion  $\propto m_f$ , and  $\Lambda$  the  
 612 cutoff energy scale at which the **SM** ceases to be a valid theory.

613 To recover the mass of the now discovered Higgs boson would require a fine-tuning of  
 614 the parameters to cancel out these mass corrections of the Higgs mass to the scale of  
 615 30 orders of magnitude. This appears as an unnatural solution to physicists and it is  
 616 this hierarchy problem that provides one of the strongest motivations for the theory of  
 617 SUperSYmmetry (**SUSY**).

### 618 2.3. Supersymmetry Overview

619 Supersymmetry provides potential solutions to many of the issues raised in the previous  
 620 section. It provides a dark matter candidate, can explain baryogenesis in the early  
 621 universe and also provides an elegant solution to the hierarchy problem [26][27][28][29].  
 622 At its heart it represents a new space-time symmetry that relates fermions and bosons.  
 623 This symmetry converts bosonic states into fermionic states, and vice versa, see Equation  
 624 (2.21) ,

$$Q|\text{Boson}\rangle = |\text{Fermion}\rangle \quad Q|\text{Fermion}\rangle = |\text{Boson}\rangle, \quad (2.21)$$

625 where the operator  $Q$  is the generator of these transformations. Quantum field theories  
 626 which are invariant under such transformations are called supersymmetric.

627 This symmetry operator therefore acts upon a particles spin altering it by a half integer  
 628 value. The consequences of the application of this additional space-time symmetry  
 629 introduce a new rich phenomenology. For example in supersymmetric theories, both  
 630 the left handed  $SU(2)$  doublet and right handed singlet of fermions will have a spin-0  
 631 superpartner, containing the same electric charge, weak isospin, and colour as its **SM**  
 632 partner. In the case of leptons  $(\nu_l, l)_L$ , they will have two superpartners, a sneutrino  $\tilde{\nu}_l{}_L$   
 633 and a slepton  $\tilde{l}_L$ , whilst the singlet  $l_R$  also has a superpartner slepton  $\tilde{l}_R$ .

634 Each particle in a supersymmetric theory is paired together with their superpartners as  
 635 a result of these supersymmetric transformations in a so called supermultiplet. These  
 636 superpartners will then consequently also contribute to the corrections to the Higgs mass.  
 637 Bosonic and fermionic loops contributing to the correction appear with opposite signs,  
 638 and therefore cancellation of these divergent terms will stabilise the Higgs mass, solving  
 639 the hierarchy problem [30][31].

640 One of the simplest forms of **SUSY**, is to simply have a set of **SM** supersymmetric  
 641 partners with the same mass and interactions as their counterparts. However the current  
 642 lack of any experimental evidence for that predicted sparticle spectrum implies **SUSY**  
 643 must be a broken symmetry in which any sparticle masses must be greater than their  
 644 **SM** counterparts.

645 There exist many techniques which can induce supersymmetric breaking [32][33][34]. Of  
 646 particular interest to experimental physicists are those at which the breaking scale is  
 647 of an order that is experimentally accessible to the **LHC** i.e.  $\sim$  TeV scale. Whilst  
 648 there is no requirement for supersymmetric breaking to occur at this energy scale, for  
 649 supersymmetry to provide a solution to the hierarchy problem, it is necessary for this  
 650 scale to not differ too drastically from the **EWK** scale [35][36].

### 651 2.3.1. R-Parity

652 Some supersymmetric theories also present a solution to the dark matter problem. These  
 653 theories contain a Lightest Supersymmetric Partner (**LSP**), which matches the criteria  
 654 of a Weakly Interacting Massive Particle (**WIMP**) required by cosmological observation  
 655 when R-parity is conserved.

656 Baryon (B) and Lepton (L) number conservation is forbidden in the **SM** by renormal-  
 657 isability requirements. The violation of Baryon or Lepton number results in a proton  
 658 lifetime much shorter than those set by experimental limits [37]. Another symmetry  
 659 called R-parity is then often introduced to **SUSY** theories to maintain baryon and lepton  
 660 conservation.

661 R-parity is described by the equation

$$R_P = (-1)^{3(B-L)+2s}, \quad (2.22)$$

662 where s represents the spin of the particles.  $B = \pm \frac{1}{3}$  for quarks/antiquarks and  $B = 0$   
 663 for all others,  $L = \pm 1$  for leptons/antileptons,  $L = 0$  for all others.

664 R-parity ensures the stability of the proton in **SUSY** models, and also has other conse-  
 665 quences for the production and decay of supersymmetric particles. In particle colliders  
 666 supersymmetric particles can only be pair produced, and similarly the decay of any pro-  
 667 duced supersymmetric particle is restricted to a **SM** particle and a lighter supersymmetric  
 668 particle as allowed by conservation laws. A further implication of R-parity is that once a  
 669 supersymmetric particle has decayed to the **LSP** it remains stable, unable to decay into  
 670 a **SM** particle.

671 A **LSP** will not interact in a detector at a particle collider, leaving behind a missing  
 672 energy  $\cancel{E}_T$  signature. The assumption of R-parity and its consequences are used to  
 673 determine the physical motivation and search strategies for **SUSY** models at the **LHC**.

## 674 2.4. Experimental Signatures of **SUSY** at the **LHC**

675 Should strongly interacting sparticles be within the experimental reach of the **LHC**, then  
 676 it is expected that they can be produced in a variety of ways :

- 677     • squark/anti-squark and gluino pairs can be produced via both gluon fusion and
- 678        quark/anti-quark scattering,
- 679     • a gluino and squark produced together via quark-gluon scattering,
- 680     • squark pairs produced via quark-quark scattering.

681 Whilst most **SUSY** searches invoke the requirement of R-parity to explore parameter  
682 phase space, there still exist a whole plethora of possible **SUSY** model topologies which  
683 could be waiting to be discovered at the **LHC**.

684 During the 2011 run period at  $\sqrt{s} = 7$  TeV, particular models were used to benchmark  
685 performance and experimental reach of both **CMS** searches and previous experiments.  
686 The Compressed Minimal SuperSymmetric Model (**CMSSM**) was initially chosen for  
687 a number of reasons [38], one of the most compelling being the reduction of the up to  
688 105 new parameters that can be introduced by **SUSY** (in addition to the existing 19 of  
689 the **SM**), to just 5 free extra free parameters. It was this simplicity, combined with the  
690 theory not requiring any fine tuning of particle masses to produce experimentally verified  
691 **SM** observables that made it an attractive model to interpret physics results.

692 However recent results from the **LHC** now strongly disfavour large swathes of **CMSSM**  
693 parameter space [39][40][41]. In the face of such results a more pragmatic model indepen-  
694 dent search strategy is now applied across most **SUSY** searches at the **LHC**, see Section  
695 (2.4.1).

696 As previously stated, a stable **LSP** that exhibits the properties of a dark matter candidate  
697 would be weakly interacting and therefore will not be directly detected in a detector  
698 environment. Additionally the cascade decays of supersymmetric particles to this **LSP**  
699 state would also result in significant hadronic activity. These signatures will then be  
700 characterised through large amounts of hadronic jets (see Section (3.3.1)), leptons and  
701 a significant amount of missing energy dependent upon the size of the mass splitting  
702 between the **LSP** and the supersymmetric particle it has decayed from.

703 The **SM** contains processes which can exhibit a similar event topology to that described  
704 above, with the largest contribution coming from the general QCD environment of a  
705 hadron collider. A multitude of different analytical techniques are used by experimental  
706 physicists to reduce or estimate any reducible or irreducible backgrounds, allowing a  
707 possible **SUSY** signature to be extracted. The techniques employed within this thesis are  
708 described in great detail within Section (4.1).

<sup>709</sup> **2.4.1. Simplified models**

<sup>710</sup> With such a variety of different ways for a **SUSY** signal to manifest itself, it is necessary  
<sup>711</sup> to be able to interpret experimental reach through the masses of gluinos and squarks  
<sup>712</sup> which can be excluded by experimental searches rather than on a model specific basis.

<sup>713</sup> This is accomplished through **SMS** models, which are defined by a set of hypothetical  
<sup>714</sup> particles and a sequence of their production and decay modes [42][43]. In the **SMS** models  
<sup>715</sup> considered within this thesis, only the production process for the two primary particles  
<sup>716</sup> are considered. Each primary particle can undergo a direct or a cascade decay through  
<sup>717</sup> an intermediate new particle. At the end of each decay chain there remains a neutral,  
<sup>718</sup> undetected **LSP** particle, denoted  $\tilde{\chi}_{LSP}$  which can represent a neutralino or gravitino.  
<sup>719</sup> Essentially it is easier to consider each **SMS** with branching ratios set to 100%. The  
<sup>720</sup> masses of the primary particle and the **LSP** remain as free parameters, in which the  
<sup>721</sup> absolute value and relative difference between the primary and **LSP** particle alter the  
<sup>722</sup> kinematics of the event.

<sup>723</sup> Different **SMS** models are denoted with a T-prefix, with a summary of the types interpreted  
<sup>724</sup> within this thesis listed below [44].

- <sup>725</sup> • **T1,T1xxxx**, models represent a simplified version of gluino pair production with  
<sup>726</sup> each gluino (superpartner to the gluon) undergoing a three-body decay to a quark-  
<sup>727</sup> antiquark pair and the **LSP** (i.e.  $\tilde{g} \rightarrow q\bar{q}\tilde{\chi}_{LSP}$ ). The resultant final state from this  
<sup>728</sup> decay is typically 4 jets +  $\cancel{E}_T$  in the absence of initial/final state radiation and  
<sup>729</sup> detector effects. xxxx denotes models in which the quarks are of a specific flavour,  
<sup>730</sup> typically t or b quark-antiquarks.
- <sup>731</sup> • **T2,T2xx**, models represent a simplified version of squark anti-squark production  
<sup>732</sup> with each squark undergoing a two-body decay into a light-flavour quark and **LSP**  
<sup>733</sup> (i.e.  $\tilde{q} \rightarrow q\tilde{\chi}_{LSP}$ ). This results in final states with less jets than gluino mediated  
<sup>734</sup> production, typically 2 jets +  $\cancel{E}_T$  when again ignoring the effect of initial/final state  
<sup>735</sup> radiation and detector effects. xx models represent decays in which both the quark  
<sup>736</sup> and the squark within the decay is of a specific flavour, which in this thesis are  
<sup>737</sup> again  $\tilde{t}/t$  or  $\tilde{b}/b$ .

<sup>738</sup> Models rich in b and t quarks are interpreted within this thesis as they remain of  
<sup>739</sup> particular interest within “Natural **SUSY**” scenarios [45][46]. The largest contribution  
<sup>740</sup> to the quadratic divergence in the Higgs mass parameter comes from a loop of top  
<sup>741</sup> quarks via the Yukawa coupling. Cancellation of these divergences can be achieved in

<sup>742</sup> supersymmetric theories by requiring a light right handed top squark,  $\tilde{t}_R$ , and left-handed  
<sup>743</sup> double  $SU(2)_L$  doublet containing top and bottom squarks,  $(\tilde{t}, \tilde{b})_L$  [47].

<sup>744</sup> These theories therefore solve the hierarchy problem by predicting light  $\sim$  EWK scale  
<sup>745</sup> third generation sleptons, to be accessible at the LHC. Search strategies involving the  
<sup>746</sup> requirement of b-tagging (see Section (3.3.2)) are used to give sensitivity to these type of  
<sup>747</sup> SUSY scenarios and are discussed in greater detail within Chapter 4.

<sup>748</sup> Two example decay chains are shown in Figure 2.2; the pair production of gluinos (T1)  
<sup>749</sup> and the pair production of squarks (T2) decaying into SM particles and LSP's.

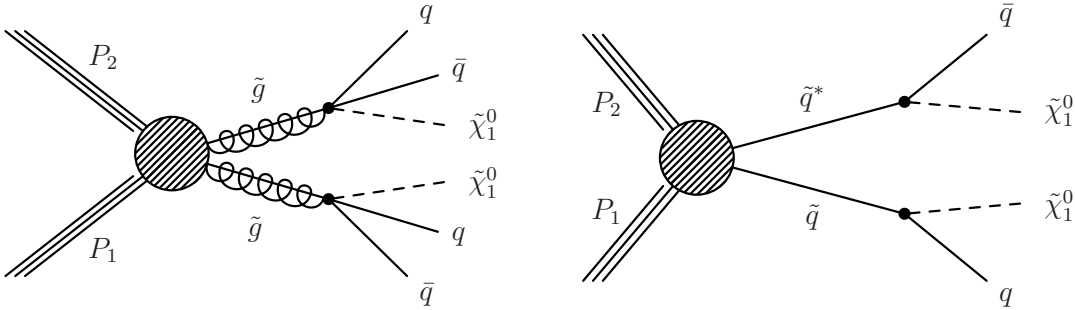


**Figure 2.2.:** Two example SMS model decays (T1 (left), T2 (right)), which are used in interpretations of physics reach by CMS.

# Chapter 3.

## <sup>750</sup> The LHC And The CMS Detector

<sup>751</sup> Probing the SM for signs of new physics would not be possible without the immensely  
<sup>752</sup> complex electronics and machinery that makes the TeV energy scale accessible to physi-  
<sup>753</sup> cists for the first time. This chapter will introduce both the LHC based at European  
<sup>754</sup> Organization for Nuclear Research (CERN) and the Compact Muon Solenoid (CMS)  
<sup>755</sup> detector (of which the author is a member). Section (3.2) serves to present an overview of  
<sup>756</sup> the different components of the CMS detector, with specific components relevant to the  
<sup>757</sup> search for supersymmetric particles described in greater detail. Section (3.3) will focus on  
<sup>758</sup> event and object reconstruction again with more emphasis on jet level quantities which  
<sup>759</sup> are most relevant to the author’s analysis research. Finally Section (3.4) will describe and  
<sup>760</sup> detail the service work for the CMS Collaboration performed by the author, in measuring  
<sup>761</sup> the performance of L1 single jet triggers in the Global Calorimeter Trigger (GCT) during  
<sup>762</sup> the 2012-2013 run period.

### <sup>763</sup> 3.1. The LHC

<sup>764</sup> The LHC is a storage ring, accelerator, and collider of circulating beams of protons or ions.  
<sup>765</sup> Housed in the tunnel dug for Large Electron-Positron Collidor (LEP), it is approximately  
<sup>766</sup> 27 km in circumference, 100 m underground, and straddles the border between France  
<sup>767</sup> and Switzerland outside of Geneva. It is currently the only collider in operation that  
<sup>768</sup> is able to study physics at the TeV scale. A double-ring circular synchrotron, it was  
<sup>769</sup> designed to collide both proton-proton (pp) and heavy ion (PbPb) with a centre of mass  
<sup>770</sup> energy  $\sqrt{s} = 14$  TeV at a final design luminosity of  $10^{34}\text{cm}^{-2}\text{s}^{-1}$ .

<sup>771</sup>

These counter-circulating beams of protons or Pb ions are merged in four sections around the ring to enable collisions of the beams, with each interaction point being home to one of the four major experiments; A Large Ion Collider Experiment (**ALICE**) [48] , A Toroidal LHC ApparatuS (**ATLAS**) [49], Compact Muon Solenoid (**CMS**) [50] and Large Hadron Collider Beauty (**LHCb**) [51] which record the resultant collisions. The layout of the **LHC** ring is shown in Figure 3.1. The remaining four sections contain acceleration, collimation and beam dump systems. In the eight arc sections, the beams are steered by magnetic fields of up to 8 T provided by super conduction dipole magnets, which are maintained at temperatures of 2 K using superfluid helium. Additional magnets for focusing and corrections are also present in straight sections within the arcs and near the interaction regions where the detectors are situated.

783

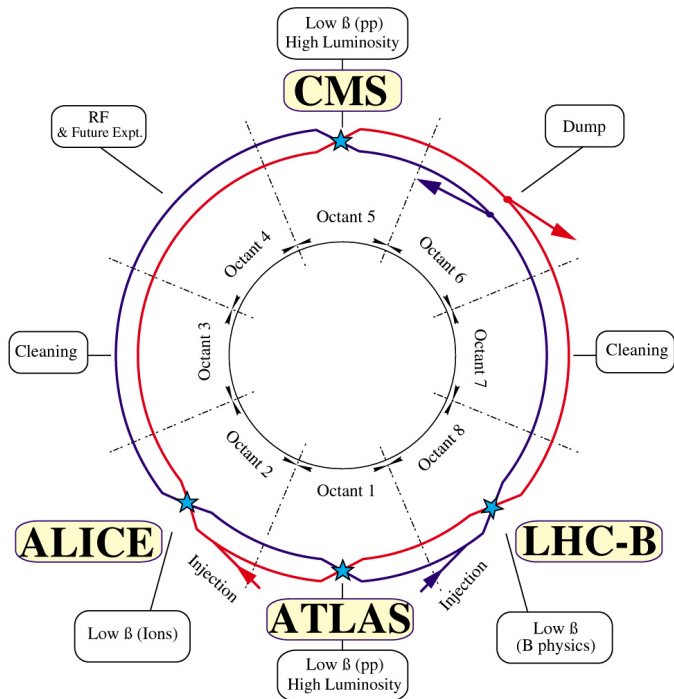


**Figure 3.1.:** A top down layout of the LHC. [52], with the position of the four main detectors labelled.

Proton beams are formed inside the Proton Synchrotron (**PS**) from bunches of protons 50 ns apart with an energy of 26 GeV. The protons are then accelerated in the Super Proton Synchrotron (**SPS**) to 450 GeV before being injected into the **LHC**. These **LHC** proton beams consists of many “bunches” (i.e. approximately  $1.1 \times 10^{11}$  protons localised into less than 1 ns in the direction of motion). Before collision, the beams are ramped to

789 4 TeV (2012) per beam in a process involving increasing the current passing through the  
 790 dipole magnets. Once the desired  $\sqrt{s}$  energy is reached then the beams are allowed to  
 791 collide at the interaction points. The luminosity falls regularly as the run progresses as  
 792 protons are lost in collisions, and eventually the beam is dumped before repeating the  
 793 process again.

794

795 Colliding the beams produced an instantaneous luminosity of approximately  $5 \times 10^{33}$   
 796  $\text{cm}^{-2}\text{s}^{-1}$  during the 2012 run. The high number of protons in each bunch increases  
 797 the likelihood of multiple interactions with each crossing of the counter-circulating  
 798 beams. This leads to isotropic energy depositions within the detectors positioned at these  
 799 interaction points, increasing the energy scale of the underlying event. This is known as  
 800 pile-up and the counteracting of it's effects are important to the many measurements  
 801 performed at the **LHC**.

802 In the early phase of prolonged operation after the initial shutdown the machine operated  
 803 in 2010-2011 at 3.5 TeV per beam,  $\sqrt{s} = 7$  TeV, delivering  $6.13 \text{ fb}^{-1}$  of data [53]. During  
 804 the 2012-2013 run period, data was collected at an increased  $\sqrt{s} = 8$  TeV improving the  
 805 sensitivity of searches for new physics. Over the whole run period  $23.3 \text{ fb}^{-1}$  of data was  
 806 delivered, of which  $21.8 \text{ fb}^{-1}$  was recorded by the **CMS** detector as shown in Figure 3.2  
 807 [53]. A total of  $12 \text{ fb}^{-1}$  of 8 TeV certified data was collected by October 2012, and it is  
 808 this data which forms the basis of the results presented within this thesis.

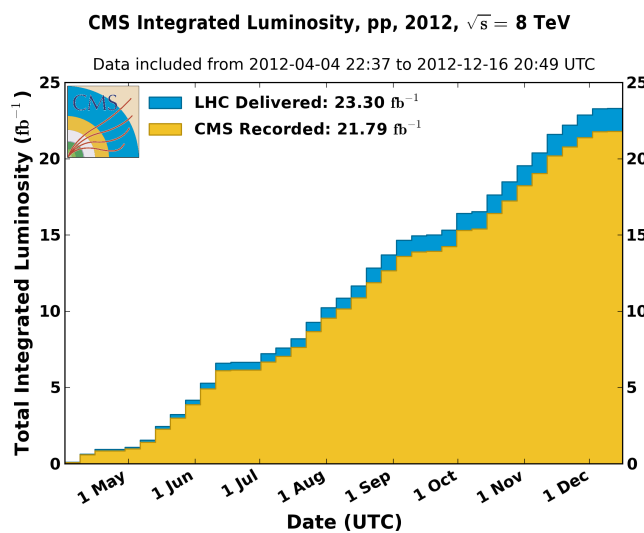


**Figure 3.2.:** The total integrated luminosity delivered to and collected by **CMS** during the 2012 8 TeV  $pp$  runs.

---

## 809 3.2. The CMS Detector

810 The Compact Muon Solenoid (**CMS**) detector is one of two general purpose detectors  
 811 at the **LHC** designed to search for new physics. The detector is designed to provide  
 812 efficient identification and measurement of many physics objects including photons,  
 813 electrons, muons, taus, and hadronic showers over wide ranges of transverse momentum  
 814 and direction. It's nearly  $4\pi$  coverage in solid angle allows for accurate measurement of  
 815 global transverse momentum imbalance. These design factors give **CMS** the ability to  
 816 search for direct production of **SUSY** particles at the TeV scale, making the search for  
 817 Supersymmetric particles one of the highest priorities among the wide range of physics  
 818 programmes at **CMS**.

819

820 **CMS** uses a right-handed Cartesian coordinate system with the origin at the interaction  
 821 point and the z-axis pointing along the beam axis, the x-axis points radially inwards to  
 822 the centre of the collider ring, with the y-axis points vertically upward. The azimuthal  
 823 angle,  $\phi$  ranging between  $[-\pi, \pi]$  is defined in the x-y plane starting from the x-axis. The  
 824 polar angle  $\theta$  is measured from the z axis. The common convention in particle physics is  
 825 to express an out going particle in terms of  $\phi$  and its pseudorapidity defined as

$$\eta = -\log \tan\left(\frac{\theta}{2}\right). \quad (3.1)$$

826 The variable  $\Delta R = \sqrt{\Delta\phi^2 + \Delta\eta^2}$  is commonly used to define angular distance between  
 827 objects within the detector and additionally energy and momentum is typically measured  
 828 in the transverse plane perpendicular to the beam line. These values are calculated  
 829 from the x and y components of the object and are denoted as  $E_T = E \sin \theta$  and  
 830  $p_T = \sqrt{p_x^2 + p_y^2}$ .

### 831 3.2.1. Detector subsystems

832 As the range of particles produced from  $pp$  collisions interact in different ways with  
 833 matter, **CMS** is divided into sub-detector systems, which perform complementary roles  
 834 to identify the identity, mass, and momentum of the different physics objects present in  
 835 each event. These detector sub-systems contained within **CMS** are wrapped in layers

836 around a central 13 m long 4 T super conducting solenoid as shown in Figure 3.3. With  
 837 the endcaps closed, CMS is a cylinder of length 22 m, diameter 15 m, and mass 12.5  
 838 kilotons. A more detailed complete description of the detector can be found elsewhere [50].  
 839

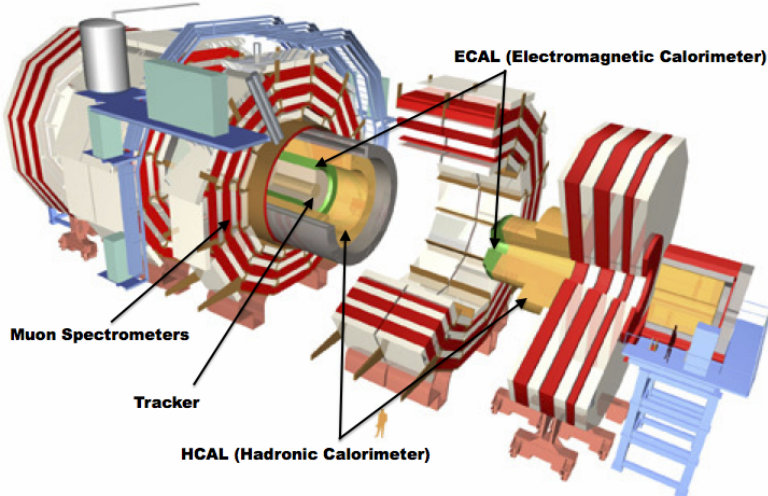


**Figure 3.3.:** A pictorial depiction of the CMS detector with the main detector subsystems labelled. [54]

### 840 3.2.2. Tracker

841 The inner-most sub-detector of the barrel is the multi-layer silicon tracker, formed of a  
 842 pixel detector component encased by layers of silicon strip detectors. The pixel detector  
 843 consists of three layers of silicon pixel sensors providing measurements of the momentum,  
 844 position coordinates of the charged particles as they pass, and the location of primary  
 845 and secondary vertices between 4 cm and 10 cm transverse to the beam. Outside the  
 846 pixel detector, ten cylindrical layers of silicon strip detectors extend the tracking system  
 847 out to a radius of 1.20 m from the beam line. The tracking system provides efficient  
 848 and precise determination of the charges, momenta, and impact parameters of charged  
 849 particles with the geometry of the tracker extending to cover a rapidity range up to  $|\eta| <$   
 850 2.5.

851

852 The tracking system also plays a crucial part in the identification of jets that originate  
 853 from b-quarks through the measurement of displaced secondary vertices. The methods  
 854 in which these b-flavoured jets are identified are discussed within Section (3.3.2). The

identification of b-jets is important in many searches for natural SUSY models and forms an important part of the inclusive search strategy described within Section (4.2).

### 3.2.3. Electromagnetic calorimeter

Immediately outside of the tracker, but still within the magnet core, sits the Electromagnetic CALorimeter (**ECAL**). Covering a pseudorapidity up to  $|\eta| < 3$  and comprising of over  $75 \times 10^3$  PbWO<sub>4</sub> (lead tungstate) crystals that scintillate as particles deposit energy, the **ECAL** provides high resolution measurements of the electromagnetic showers from photons and electrons in the detector.

863

Lead tungstate is used because of its short radiation length ( $X_0 \sim 0.9$  cm) and small Molieré radius ( $\sim 2.1$  cm) leading to high granularity and resolution. It's fast scintillation time ( $\sim 25$  ns) reduces the effects of pile-up, which occurs when energy from previous collisions are still being read out, and its radiation hardness gives it longevity. The crystals are arranged in modules which surround the beam line in a non-projective geometry, angled at  $3^\circ$  with respect to the interaction point to minimise the risk of particles escaping down the cracks between the crystals.

871

The **ECAL** is primarily composed of two sections, the Electromagnetic CALorimeter Barrel (**EB**) which extends in pseudo-rapidity to  $|\eta| < 1.479$  with a crystal front cross section of  $22 \times 22$  mm and a length of 230 mm corresponding to 25.8 radiation lengths, and the Electromagnetic CALorimeter Endcap (**EE**) covering a rapidity range of  $1.479 < |\eta| < 3.0$ , which consists of two identical detectors on either side of the **EB**. A lead-silicon sampling ‘pre-shower’ detector Electromagnetic CALorimeter pre-Shower (**ES**) is placed before the endcaps to aid in the identification of neutral pions. Their arrangement is shown in Figure 3.4.

880

Scintillation photons from the lead tungstate crystals are instrumented with Avalanche Photo-Diodes (**APD**) and Vacuum Photo-Triodes (**VPT**) located in the **EB** and **EE** respectively, converting the scintillating light into an electric signal which is consequently used to determine the amount of energy deposited within the crystal . These instruments are chosen for their resistance under operation to the strong magnetic field of **CMS**. The scintillation of the **ECAL** crystals as well as the response of the **APDs** varies as a function

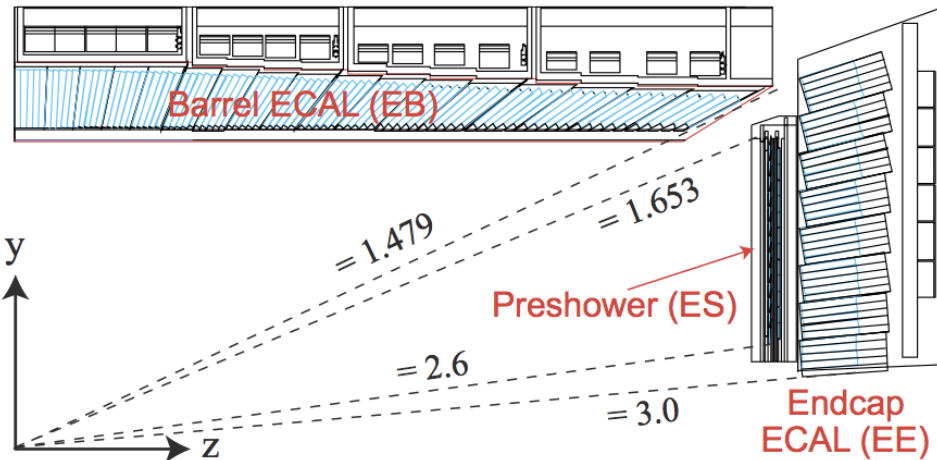


**Figure 3.4.:** Illustration of the **ECAL** showing the arrangement of the lead tungstate crystals in the **EB** and **EE**. The **ES** is also shown and is located in front of the **EE** [55].

887 of temperature and so cooling systems continually maintain an overall constant **ECAL**  
 888 temperature  $\pm 0.05^\circ\text{C}$ .

### 889 3.2.4. Hadronic calorimeter

890 Beyond the **ECAL** lies the Hadronic CALorimeter (**HCAL**) which is responsible for  
 891 the accurate measurement of hadronic showers, crucial for analyses involving jets or  
 892 missing energy signatures. The **HCAL** is a sampling calorimeter which consists of al-  
 893 ternating layers of brass absorber and plastic scintillator, except in the hadron forward  
 894 ( $3.0 < |\eta| < 5.0$ ) region in which steel absorbers and quartz fibre scintillators are used  
 895 because of their increased radiation tolerance. Hadron showers are initiated in the  
 896 absorber layers inducing scintillation in the plastic scintillator tiles. These scintillation  
 897 photons are converted by wavelength shifting fibres for read-out by hybrid photodiodes.  
 898

899 The **HCAL**'s size is constrained to a compact size by the presence of the solenoid, re-  
 900 quiring the placement of an additional outer calorimeter on the outside of the solenoid  
 901 to increase the sampling depth of the **HCAL**. A schematic of the **HCAL** can be seen in  
 902 Figure 3.5.

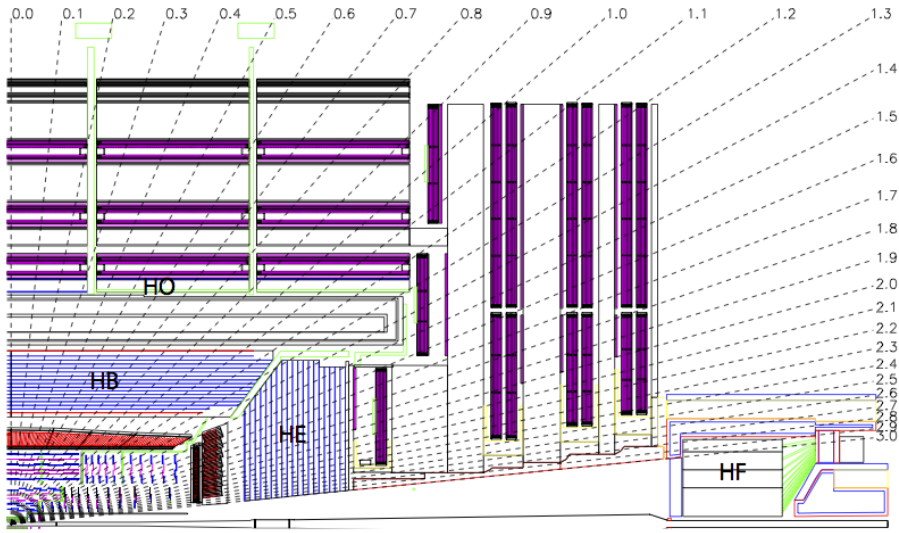


**Figure 3.5.:** Schematic of the hadron calorimeters in the r-z plane, showing the locations of the **HCAL** components and the **HF**. [50].

904 The **HCAL** covers the range  $|\eta| < 5$  and consists of four sub-detectors: the Hadron  
 905 Barrel (**HB**)  $|\eta| < 1.3$ , the Hadron Outer (**HO**), the Hadron Endcaps (**HE**)  $1.3 < |\eta| < 3.0$   
 906 and the Hadron Forward (**HF**). The **HB**, contained between the outer edge of the **ECAL**  
 907 and the inner edge of the solenoid is formed of 36 azimuthal wedges which are split  
 908 between two half-barrel segments. Each wedge is segmented into four azimuthal angle  
 909 ( $\phi$ ) sectors, and each half-barrel is further segmented into 16  $\eta$  towers. The electronic  
 910 readout chain, channels the light from the active scintillator layers from one  $\phi$ -segment  
 911 and all  $\eta$ -towers of a half-barrel to a Hybrid Photo Diode (**HPD**).

912 The relatively short number of interaction lengths ( $\lambda_l$ , the distance a hadron will travel  
 913 through the absorber material before it has lost  $\frac{1}{e}$  of its energy) within the **HB**, the lowest  
 914 being  $\lambda_l = 5.82$  at  $|\eta| = 0$ , facilitates the need for the ‘tail catching’ **HO** to increase the  
 915 sampling depth in the central barrel rapidity region  $|\eta| < 1.3$  to 11 interaction lengths .  
 916 Significant fractions of the hadrons energy will be deposited in the **ECAL** as it passed  
 917 through the detector. Therefore measurements of hadron energies in the central regions  
 918  $|\eta| < 3.0$  use both the **ECAL** and **HCAL** to reconstruct the true energy from showering  
 919 hadrons.

920 **3.2.5. Muon systems**

921 Muons being too massive to radiate away energy via Bremsstrahlung, interact little in  
922 the calorimeters and mostly pass through the detector until they reach the system of  
923 muon detectors which forms the outer most part of the CMS detector.

924 Outside of the superconducting solenoid are four muon detection layers interleaved with  
925 the iron return yokes which measure the muons energy via ionisation of gas within  
926 detector elements. Three types of gaseous chamber are used. The Drift Tube (DT),  
927 Cathode Stripe Chamber (CSC), and Resistive Plate Chamber (RPC) systems provide  
928 efficient detection of muons with pseudo-rapidity  $|\eta| < 2.4$ . The best reconstruction  
929 performance is obtained when the muon chamber is combined with the inner tracking  
930 information to determine muon trajectories and their momenta [56].

931

932 **3.3. Event Reconstruction and Object Definition**

933 The goal of event reconstruction is to take the raw information recorded by the detector  
934 and to compute from it higher-level quantities which can be used at an analysis level.  
935 These typically correspond to an individual particle’s energy and momenta, or groups of  
936 particles which shower in a narrow cone and the overall global energy and momentum  
937 balance of the event. The reconstruction of these objects are described in great detail in  
938 [57], however covered below are brief descriptions of those which are most relevant to the  
939 analysis detailed in Chapter 4.

940 **3.3.1. Jets**

941 Quarks and gluons are produced copiously at the LHC in the hard scattering of partons.  
942 As these quarks and gluons fragment, they hadronize and decay into a group of strongly  
943 interactive particles and their decay products. These streams of particles travel in the  
944 same direction, as they have been “boosted” by the momentum of the primary hadron.  
945 These collections of decay products are reconstructed and identified together as a “jet”.

946 At CMS jets are reconstructed from energy deposits in the detector using the anti-kt  
947 algorithm [58] with size parameter  $\Delta R = 0.5$ . The anti-kt jet algorithm clusters jets by  
948 defining a distance between hard (high  $p_T$ ) and soft (low  $p_T$ ) particles such that soft

949 particles are preferentially clustered with hard particles before being clustered between  
950 themselves. This produces jets which are robust to soft particle radiation from the pile-up  
951 conditions produced by the **LHC**.

952

953 There are two main type of jet reconstruction used at **CMS**, Calorimeter (Calo) and  
954 Particle Flow (PF) jets [59]. Calorimeter jets are reconstructed using both the **ECAL**  
955 and **HCAL** cells, combined into calorimeter towers . These calorimeter towers consist of  
956 geometrically matched **HCAL** cells and **ECAL** crystals. Electronics noise is suppressed by  
957 applying a threshold to the calorimeter cells, with pile-up effects reduced by a requirement  
958 placed on the tower energy [60]. Calorimeter jets are the jets used within the analysis  
959 presented in this thesis.

960 PF jets are formed from combining information from all of the **CMS** sub-detectors systems  
961 to determine which final state particles are present in the event. Generally, any particle  
962 is expected to produce some combination of a track in the silicon tracker, a deposit in  
963 the calorimeters, or a track in the muon system. The PF jet momentum and spatial  
964 resolutions are greatly improved with respect to calorimeter jets, as the use of the tracking  
965 detectors and of the high granularity of **ECAL** allows resolution and measurement of  
966 charged hadrons and photons inside a jet, which together constitute  $\sim 85\%$  of the jet  
967 energy [61].

968 The jets reconstructed by the clustering algorithm in **CMS** typically have an energy  
969 that differs to the ‘true’ energy measured by a perfect detector. This stems from the  
970 non-linear and nonuniform response of the calorimeters as well as other residual effects  
971 including pile-up and underlying events, and therefore additional corrections are applied  
972 to recover a uniform relative response as a function of pseudo-rapidity. These are applied  
973 as separate sub corrections [62].

- 974     • A pile-up correction is first applied to the jet. It subtracts the average extra energy  
975         deposited in the jet that comes from other vertices present in the event and is  
976         therefore not part of the hard jet itself.
- 977     •  $p_T$  and  $\eta$  dependant corrections derived from Monte Carlo simulations are used to  
978         account for the non-uniform response of the detector.
- 979     •  $p_T$  and  $\eta$  residual corrections are applied to data only to correct for difference  
980         between data and Monte Carlo. The residual is derived from QCD di-jet samples  
981         and the  $p_T$  residual from  $\gamma+$  jet and  $Z+$  jets samples in data.

---

### 982 3.3.2. B-tagging

983 The decays of b quarks are suppressed by small CKM matrix elements. As a result, the  
 984 lifetimes of b-flavoured hadrons, produced in the fragmentation of b quarks, are relatively  
 985 long;  $\mathcal{O}$  1ps. The identification of jets originating from b quarks is very important for  
 986 searches for new physics and for measurements of SM processes.

987

988 Many different algorithms developed by CMS select b-quark jets based on variables such  
 989 as the impact parameters of the charged-particle tracks, the properties of reconstructed  
 990 decay vertices, and the presence or absence of a lepton, or combinations thereof [63].  
 991 One of the most efficient of which is the Combined Secondary Vertex (CSV) which  
 992 operates based on secondary vertex and track-based lifetime information, benchmarked  
 993 in ‘Loose’, ‘Medium’ and ‘Tight’ working points, of which the medium point is the tagger  
 994 used within the  $\alpha_T$  search presented in Section (4.1). All figures within this sub-section,  
 995 demonstrating the performance of this b-tagging algorithm are taken from [64].

996 Using the CSV tagger, a likelihood-based discriminator distinguishes between jets from  
 997 b-quarks, and those from charm or light quarks and gluons, which is shown in Figure 3.6.  
 998 The minimum thresholds on the discriminator for each working point correspond to the  
 999 mis-identification probability for light-parton jets of 10%, 1%, and 0.1%, respectively, in  
 1000 jets with an average  $p_T$  of about 80 GeV.

1001 The b-tagging performance is evaluated to measure the b-jet tagging efficiency  $\epsilon_b$ , and the  
 1002 misidentification probability of charm  $\epsilon_c$  and light-parton jets  $\epsilon_s$ . The tagging efficiencies  
 1003 for each of these three jet flavours are compared between data and MC simulation, from  
 1004 which a series of  $p_T$  and  $|\eta|$  binned jet corrections are determined,

$$SF_{b,c,s} = \frac{\epsilon_{b,c,s}^{data}}{\epsilon_{b,c,s}^{MC}}. \quad (3.2)$$

1005 These are collectively named ‘Btag Scale Factors’ and allow MC simulation to accu-  
 1006 rately reflect the running conditions and performance of the tagging algorithm in data.  
 1007 Understanding of the b-tagging efficiency is essential in order to minimise systematic  
 1008 uncertainties in physics analyses that employ b-tagging.

1009

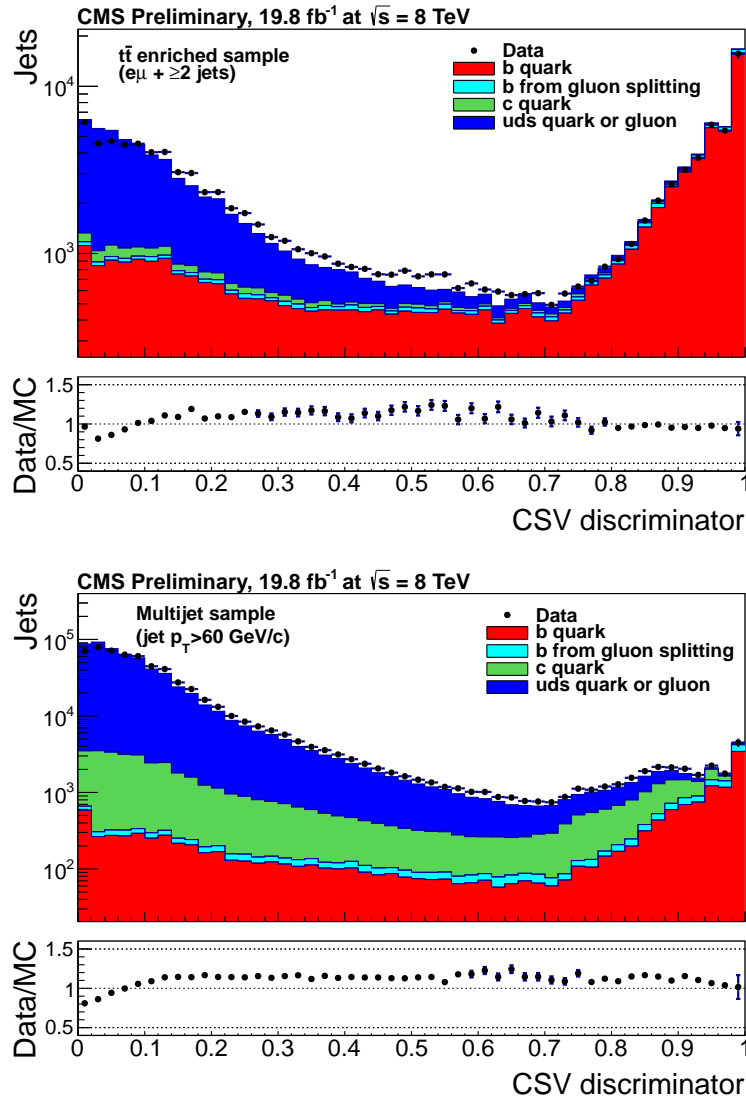


**Figure 3.6.:** CSV algorithm discriminator values in enriched ttbar (top) and inclusive multi jet samples (bottom) for b,c and light flavoured jets. The discriminator value used for each working points are determined from the misidentification probability for light-parton jets to be tagged as a b-jet, which are given as 0.244 (10%), 0.679 (1%) and 0.898 (0.1%) for the L, M and T working points respectively.

1010 The b-tagging efficiency is measured in data using several methods applied to multi  
 1011 jet events, primarily based on a sample of jets enriched in heavy flavour content. One  
 1012 method requires the collection of events with a soft muon within a cone  $\Delta R < 0.4$  around  
 1013 the jet axis. Because the semi-leptonic branching fraction of b hadrons is significantly  
 1014 larger than that for other hadrons, these jets are more likely to arise from b quarks than  
 1015 from another flavour, with the resultant momentum component of the muon transverse  
 1016 to the jet axis larger for muons from b-hadron decays than from light or charm jets.

1017 Additionally the performance of the tagger can also be benchmarked in  $t\bar{t}$  events where  
 1018 in the SM, the top quark is expected to decay to a W boson and a b quark about 99.8%  
 1019 of the time [1]. Further selection criteria is applied to these events to further enrich the  
 1020 b quark content of these events. The methods to identify b-jets in data are discussed  
 1021 in great detail at [65]. The jet flavours are determined in simulation using truth level  
 1022 information and are compared to data to determine the correction scale factors ( $SF_b$ ),  
 1023 which are displayed for the CSVM tagger in Figure 3.7.

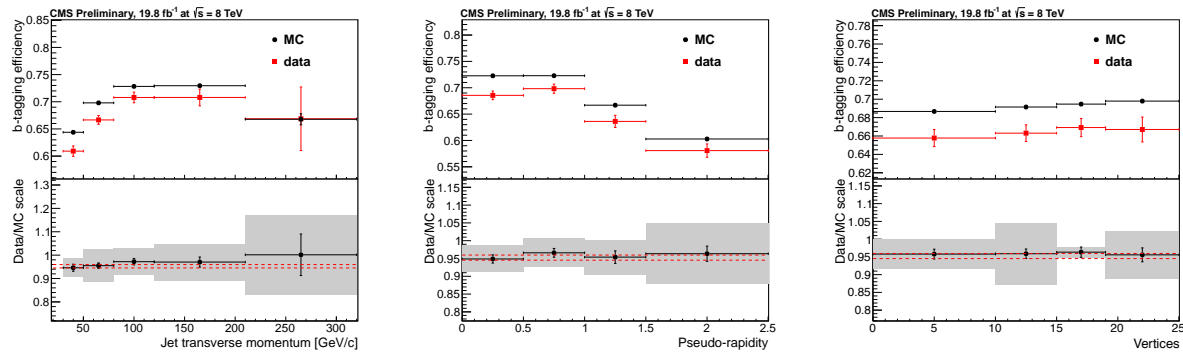


**Figure 3.7.:** Measured in  $t\bar{t} \rightarrow$  di-lepton events using the CSVM tagger: (upper panels) b-tagging efficiencies and (lower panels) data/MC scale factor  $SF_b$  as a function of (left) jet  $p_T$ , (middle) jet  $|\eta|$  and (right) number of primary vertices. In the lower panels, the grey filled areas represent the total statistical and systematic uncertainties, whereas the dotted lines are the average  $SF_b$  values within statistical uncertainties.

1024 The measurement of the misidentification probability for light-parton jets relies on the  
 1025 inversion of tagging algorithms, selecting non-b jets using the same variables and tech-  
 1026 niques used in benchmarking the b-tagging efficiency. The scale factors ( $SF_s$ ) to be  
 1027 applied to MC are shown in Figure 3.8 for the CSVM tagger.

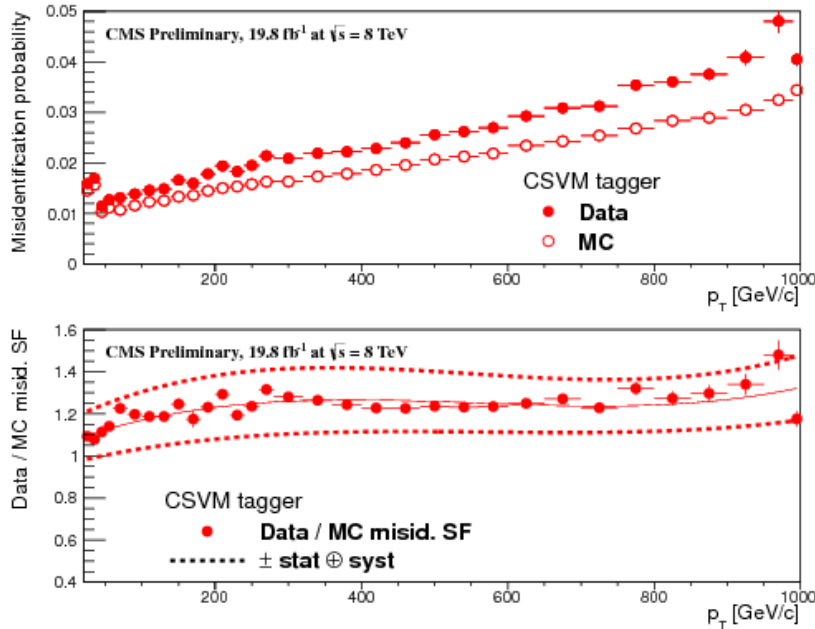


**Figure 3.8.:** For the **CSVM** tagging criterion: (top) misidentification probability in data (filled circles) and simulation (open circles); (bottom) scale factor for the misidentification probability. The last  $p_T$  bin in each plot includes all jets with  $p_T > 1000$  GeV. The solid curve is the result of a polynomial fit to the data points. The dashed curves represent the overall statistical and systematic uncertainties on the measurements.

## 1028 3.4. Triggering System

1029 With bunch crossings separated by just 25 ns, the rate at which data from all collisions  
1030 would have to be written out and processed would be unfeasible. A two-tiered triggering  
1031 system is applied at **CMS** in order to cope with the high collision rate of protons. The  
1032 **CMS** trigger is designed to use limited information from each event to determine whether  
1033 to record the event, reducing the rate of data taking to manageable levels whilst ensuring  
1034 a high efficiency of interesting physics object events are selected.

1035 The **L1** is a pipelined, dead-timeless system based on custom-built electronics [66], and is  
1036 a combination of several sub systems which is shown pictorially in Figure 3.9. The L1  
1037 system is covered in more detail within the following section along with a description  
1038 of the service work undertaken by the author to benchmark the performance of the L1  
1039 calorimeter trigger during the 2012 8 TeV run period.

1040 The Higher Level Trigger (**HLT**) is a large farm of commercial computers [67]. The **HLT**  
1041 processes events with software reconstruction algorithms that are more detailed, giving  
1042 performance more similar to the reconstruction used offline. The **HLT** reduces the event

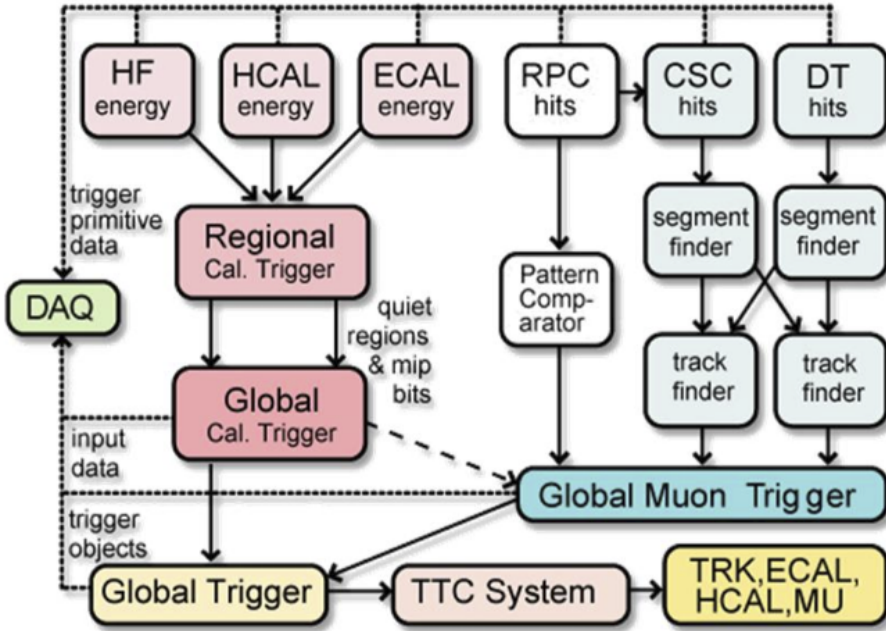


**Figure 3.9.:** The CMS L1 Trigger system.

1043 rate written to disk by a factor of  $\sim 500$  ( $\sim 200\text{Hz}$ ). The recorded events are transferred  
 1044 from CMS to the CERN computing centre, where event reconstruction is performed, and  
 1045 then distributed to CMS computing sites around the globe for storage and analysis.

### 1046 3.4.1. The Level-1 trigger

1047 The L1 trigger reduces the rate of events collected from 40 MHz to  $\sim 100\text{ kHz}$  using  
 1048 information from the calorimeters and muon chambers, but not the tracker. A tree  
 1049 system of triggers is used to decide whether to pass on an event to the HLT for further  
 1050 reconstruction. Firstly the calorimeter and muon event information is kept separate, with  
 1051 local reconstruction of objects ( $\mu$ ,  $e$ ,  $\gamma$ , and jets) performed by the Regional Calorimeter  
 1052 Trigger (RCT) and Regional Muon Trigger (RMT) respectively. The RCT generates up to  
 1053 72 isolated and non-isolated electromagnetic objects. These are sorted by rank, which is  
 1054 equivalent to transverse energy  $E_T$ , with the four highest ranked electromagnetic objects  
 1055 being passed via the Global Calorimeter Trigger (GCT) and Global MuonTrigger (GMT)  
 1056 to the Global Trigger (GT).

1057 In the L1 **GCT**, coarse measurements of the energy deposited in the electromagnetic and  
1058 hadronic calorimeters are combined, and by using sophisticated algorithms the following  
1059 physics objects are formed:

- 1060 • isolated and non-isolated electromagnetic objects ( $e$  and  $\gamma$ );
- 1061 • hadronic jets in the central and forward sections of the hadronic calorimeters;
- 1062 • hadronically decaying tau leptons;
- 1063 • total transverse energy ( $E_T$ ), the scalar sum of the energy measured at L1, and  
1064 missing transverse energy ( $\cancel{E}_T$ ), defined as the vector sum of the energy of L1  
1065 objects;
- 1066 • total transverse jet energy ( $H_T$ ), the scalar sum of the energy of all L1 jet objects,  
1067 and missing transverse jet energy ( $\cancel{H}_T$ ), defined as the vector sum of the energy of  
1068 L1 jets, are calculated from uncorrected L1 jets.

1069 In addition quantities suitable for triggering minimum bias events, forward physics and  
1070 beam background events are calculated. Additionally relevant muon isolation information  
1071 is also passed on to the **GMT** for decisions involving the muon triggers where it is  
1072 combined with information from across the three muon sub-systems. The resultant final  
1073 accept/reject decision at **L1** is then performed by the **GT** based on the objects received  
1074 from the **GCT** and **GMT** ( $e/\gamma$ ,  $\mu$ , jets,  $E_T$ ,  $\cancel{E}_T$ ,  $H_T$ ).

1075 The L1 trigger is therefore of upmost importance to the functioning of the detector.  
1076 Without a high-performing trigger and a good understanding of its performance, there  
1077 would be no data to analyse. Observations of how the L1 trigger performance is affected  
1078 by changing **LHC** running conditions over the 2012 run period and also the introduction  
1079 of a jet seed threshold to the L1 jet trigger algorithm is presented in the following Sections  
1080 (3.4.2 - 3.4.6).

### 1081 3.4.2. The L1 trigger jet algorithm

1082 The L1 jet trigger uses the transverse energy sums computed in the calorimeter (both  
1083 hadronic and electromagnetic) trigger regions. Each region consists of  $4 \times 4$  trigger tower  
1084 windows, spanning a region of  $\Delta\eta \times \Delta\phi = 0.087 \times 0.087$  in pseudorapidity-azimuth. The  
1085 jet trigger uses a  $3 \times 3$  calorimeter region (112 trigger towers) sliding window technique  
1086 which spans the full  $(\eta, \phi)$  coverage of the **CMS** calorimeter as shown in Figure 3.10.

1087 In forming a L1 jet is it required that the central region to be higher than the eight  
 1088 neighbouring regions  $E_T$  central >  $E_T$  surround. Additionally a minimum threshold of 5 GeV  
 1089 on  $E_T$  central was introduced during the 2012 run period to suppress noise from pile-up.  
 1090 A comparison between these two configurations is shown in Section (3.4.4).  
 1091 The L1 jets are characterised by the  $E_T$ , summed over the  $3 \times 3$  calorimeter regions,  
 1092 which corresponds to  $12 \times 12$  trigger towers in barrel and endcap or  $3 \times 3$  larger **HF**  
 1093 towers in the **HF**. The  $\phi$  size of the jet window is the same everywhere, whilst the  $\eta$   
 1094 binning gets somewhat larger at high  $\eta$  due to calorimeter and trigger tower segmentation.  
 1095 The jets are labelled by the  $(\eta, \phi)$  indices of the central calorimeter region.  
 1096 Jets with  $|\eta| > 3.0$  are classified as forward jets, whereas those with  $|\eta| < 3.0$  are classified  
 1097 as central. The four highest energy central, forward and  $\tau$  jets in the calorimeter are  
 1098 passed through Look Up Table (**LUT**)'s, which apply a programmable  $\eta$ -dependent jet  
 1099 energy scale correction. These are then used to make L1 trigger decisions.

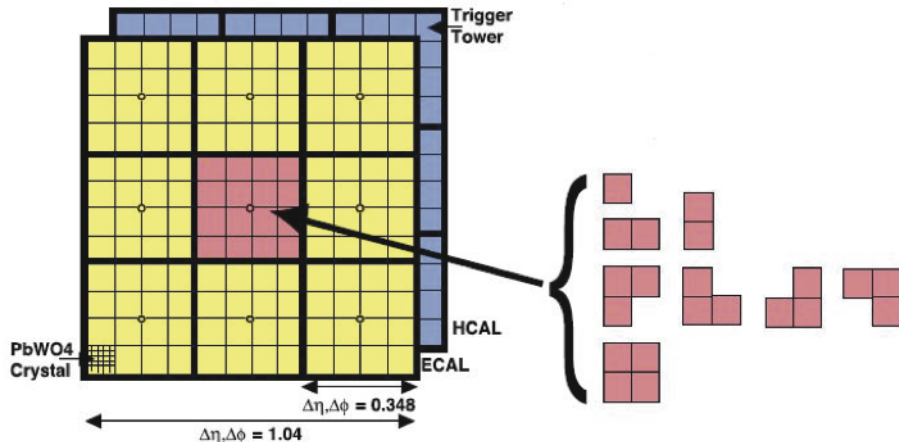


Figure 3.10.: Illustration of the Level-1 jet finding algorithm.

1100 The performance of the L1 jets is evaluated with respect to offline jets, which are taken  
 1101 from the standard Calo jet and the PF jet reconstruction algorithms of **CMS**. Jets are  
 1102 corrected for pile-up and detector effects as described in 3.3.1. A moderate level of noise  
 1103 rejection is applied to the offline jets by selecting jets passing the “loose” identification  
 1104 criteria for both Calo and PF. These jet criteria are listed in Appendix (A.1).

<sub>1105</sub> **3.4.3. Measuring L1 jet trigger efficiencies**

<sub>1106</sub> The L1 jet efficiency is defined as the fraction of leading offline jets which were matched  
<sub>1107</sub> with a L1 tau or central jet above a certain trigger threshold, divided by all the leading  
<sub>1108</sub> offline jets in the event. This quantity is then plotted as a function of the offline jet  $E_T$ ,  
<sub>1109</sub>  $\eta$  and  $\phi$ .

<sub>1110</sub> The efficiency is determined by matching the L1 and reconstructed offline jets spatially  
<sub>1111</sub> in  $\eta - \phi$  space. This is done by calculating the minimum separation in  $\Delta R$  between the  
<sub>1112</sub> highest offline reconstructed jet in  $E_T$  ( $E_T > 10$  GeV,  $|\eta| < 3$ ) and any L1 jet. A jet will  
<sub>1113</sub> be matched if this value is found to be  $< 0.5$ . Should more than one jet satisfy this, the  
<sub>1114</sub> jet closest in  $\Delta R$  is taken as the matched jet. The matching efficiency is close to 100%,  
<sub>1115</sub> above 30(45) GeV for run 2012B(C) data (see Appendix B.1).

<sub>1116</sub> Each efficiency curve is fitted with a function which is the cumulative distribution function  
<sub>1117</sub> of an Exponentially Modified Gaussian (EMG) distribution:

$$\text{f}(x; \mu, \sigma, \lambda) = \frac{\lambda}{2} \cdot e^{\frac{\lambda}{2}(2\mu + \lambda\sigma^2 - 2x)} \cdot \text{erfc}\left(\frac{\mu + \lambda\sigma^2 - x}{\sqrt{2}\sigma}\right) \quad (3.3)$$

where erfc is the complementary error function defined as:

$$\text{erfc}(x) = 1 - \text{erf}(x) = \frac{2}{\sqrt{\pi}} \int_x^\infty e^{-t^2} dt.$$

<sub>1119</sub> In this functional form, the parameter  $\mu$  determines the point of 50% of the plateau  
<sub>1120</sub> efficiency and the  $\sigma$  gives the resolution. This parametrisation is used to benchmark  
<sub>1121</sub> the efficiency at the plateau, the turn-on points and resolution for each L1 Jet trigger.  
<sub>1122</sub> The choice of function is purely empirical. Previous studies used the error function  
<sub>1123</sub> alone, which described the data well at high threshold values but could not describe the  
<sub>1124</sub> efficiencies well at lower thresholds [68].

<sub>1125</sub> The efficiency turn-on curves for various L1 jet thresholds are evaluated as a function of  
<sub>1126</sub> the offline reconstructed jet  $E_T$  for central jets with  $|\eta| < 3$ . These are measured using  
<sub>1127</sub> single isolated  $\mu$  triggers which have high statistics, and are orthogonal and therefore  
<sub>1128</sub> unbiased to the hadronic triggers under study. The efficiency is calculated with respect to  
<sub>1129</sub> offline Calo and PF Jets in Figure 3.11. Table 3.1 shows the values of these parameters,  
<sub>1130</sub> calculated for three example L1 single jet triggers taken from 2012 8 TeV data.

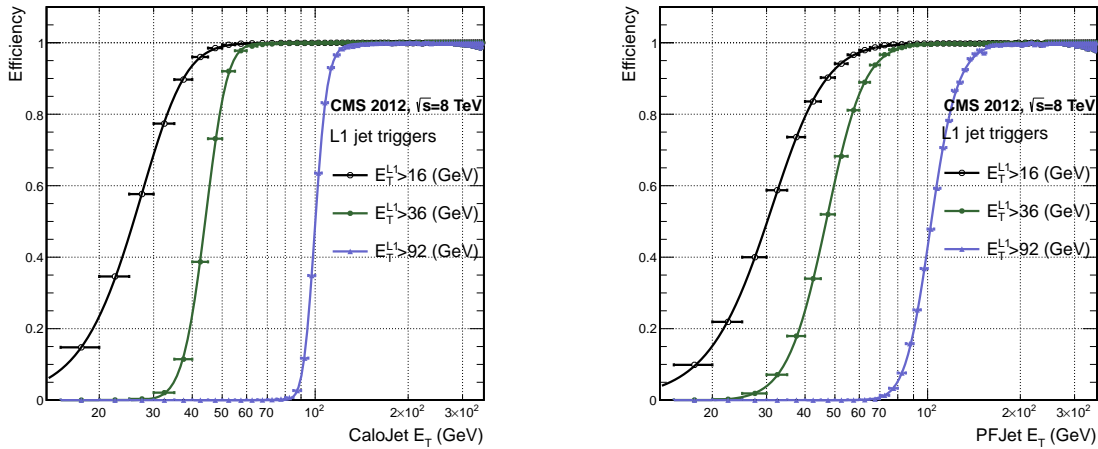


**Figure 3.11.:** L1 jet efficiency turn-on curves as a function of the offline CaloJet  $E_T$  (left) and PFJet  $E_T$  (right), measured in 2012 Run Period C data and collected with an isolated single  $\mu$  data sample.

Trigger	Calo		PF	
	$\mu$	$\sigma$	$\mu$	$\sigma$
L1_SingleJet16	$21.09 \pm 0.03$	$7.01 \pm 0.02$	$22.17 \pm 0.04$	$7.83 \pm 0.03$
L1_SingleJet36	$41.15 \pm 0.05$	$5.11 \pm 0.02$	$39.16 \pm 0.06$	$8.04 \pm 0.03$
L1_SingleJet92	$95.36 \pm 0.13$	$5.62 \pm 0.03$	$90.85 \pm 0.19$	$11.30 \pm 0.10$

**Table 3.1.:** Results of a cumulative EMG function fit to the turn-on curves for L1 single jet triggers in run 2012 Run Period C, measured in an isolated  $\mu$  data sample. The turn-on point,  $\mu$ , and resolution,  $\sigma$ , of the L1 jet triggers are measured with respect to offline Calo Jets (left) and PF Jets (right).

The results from the L1 single jet triggers shows good performance for both Calo and PF jets. A better resolution for Calo jets with respect to L1 jets quantities is observed. This effect is due to Calo jet reconstruction using the same detector systems as in L1 jets, whereas with PF jet construction using tracker and muon information, a more smeared resolution when compared to L1 is expected.

#### 3.4.4. Effects of the L1 jet seed

Between run period B and C of the 2012 data taking period, a jet seed threshold was introduced into the L1 trigger jet algorithm. There was previously no direct requirement made on the energy deposited in the central region. The introduction of a jet seed threshold required that the central region have  $E_T \geq 5\text{GeV}$ , and was introduced to

counteract the effects of high pile up running conditions which create a large number of soft non-collimated jets, that are then added to the jets from the primary interaction or other soft jets from other secondary interactions [69]. This in turn causes a large increase in trigger rate due to the increase in the likelihood that the event causes the L1 trigger to fire. This was implemented to maintain trigger thresholds by cutting the rate of events recorded without significant reduction in the efficiency of physics events of interest.

The effect of the introduction of this jet seed threshold between these two run periods is benchmarked through a comparison of the efficiency of the L1 jet triggers with respect to offline Calo jets shown in Figure 3.12, and the L1  $H_T$  trigger efficiency in Figure 3.14 which is compared to offline  $H_T$  constructed from Calo jets with  $E_T \geq 40\text{GeV}$ .

To negate any effects from different pile-up conditions in the run periods, the efficiencies are measured in events which contain between 15 and 20 primary vertices as defined in Appendix (A.2).

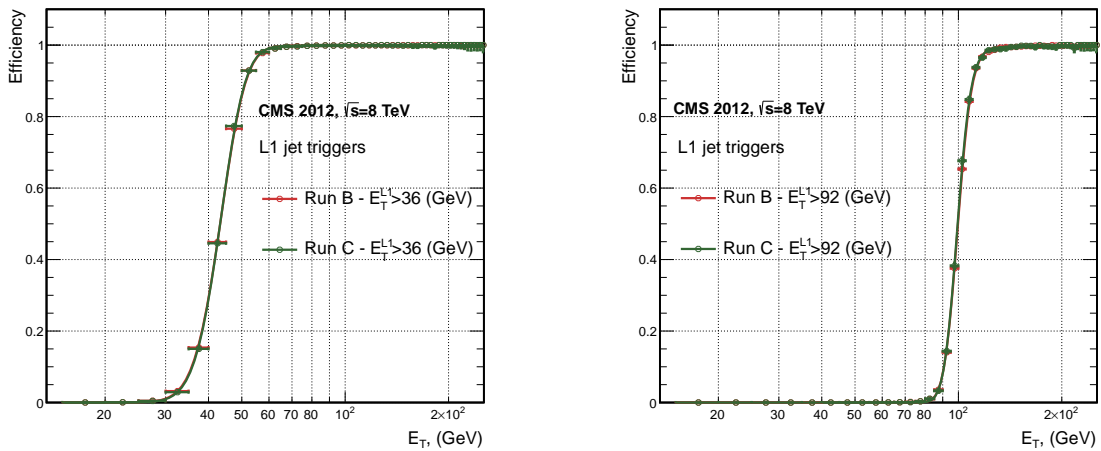


**Figure 3.12.:** L1 jet efficiency turn-on curves as a function of the offline CaloJet  $E_T$ , measured for the L1 SingleJet 36 and 92 trigger in 2012 run period B and C collected with an isolated single  $\mu'$  sample.

It can be seen that the performance of the  $E_T > 36, 92$  single jet are almost identical, with the jet seed having no measurable effect on these triggers as shown in Table 3.2 .

For the  $H_T$  triggers, a large increase in rate during high pile-up conditions is expected. This is due to the low energy threshold required for a jet to be added to the L1  $H_T$  sum, which is compiled from all uncorrected L1 jets formed in the RCT. The introduction of the jet seed threshold removes the creation of many of these soft low  $E_T$  jets, thus

Trigger	2012B		2012C	
	$\mu$	$\sigma$	$\mu$	$\sigma$
L1_SingleJet36	$40.29 \pm 0.04$	$5.34 \pm 0.02$	$40.29 \pm 0.11$	$5.21 \pm 0.05$
L1_SingleJet92	$94.99 \pm 0.09$	$5.93 \pm 0.06$	$94.82 \pm 0.29$	$5.74 \pm 0.18$

**Table 3.2.:** Results of a cumulative EMG function fit to the turn-on curves for L1 single jet triggers in the 2012 run period B and C, preselected on an isolated muon trigger. The turn-on point  $\mu$  and resolution  $\sigma$  of the L1 jet triggers are measured with respect to offline Calo Jets in run B (left) and run C (right).

lowering the  $H_T$  calculation at L1. The effect on the trigger cross section for L1  $H_T$  150 trigger can be seen in Figure 3.13.

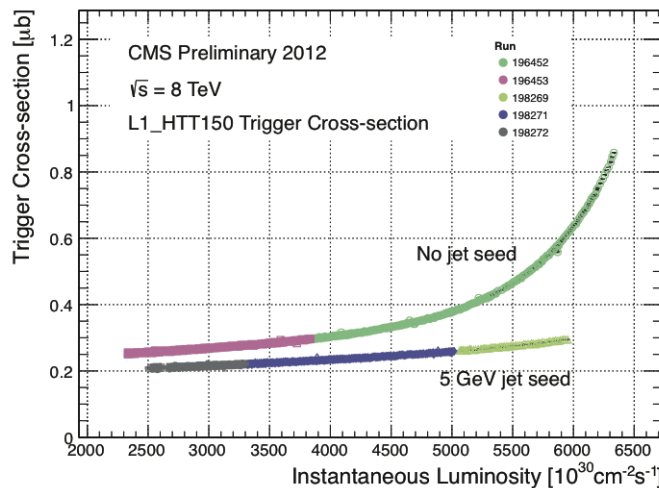


**Figure 3.13.:** Trigger cross section for the L1HTT150 trigger path. Showing that a 5 GeV jet seed threshold dramatically reduces the dependance of cross section on the instantaneous luminosity for L1  $H_T$  triggers [70].

Different behaviours for the trigger turn ons between these run periods are therefore expected. The turn on point is observed to shift to higher  $H_T$  values after the introduction of the jet seed threshold, whilst having a sharper resolution due to less pile-up jets being included in the  $H_T$  sum. This effect is demonstrated within Table 3.3.

### 3.4.5. Robustness of L1 jet performance against pile-up

The performance of the L1 single jet triggers is evaluated in different pile-up conditions to benchmark any dependence on pile-up. Three different pile-up bins of 0-10, 10-20 and  $>20$  vertices are defined, reflecting the low, medium and high pile-up running conditions

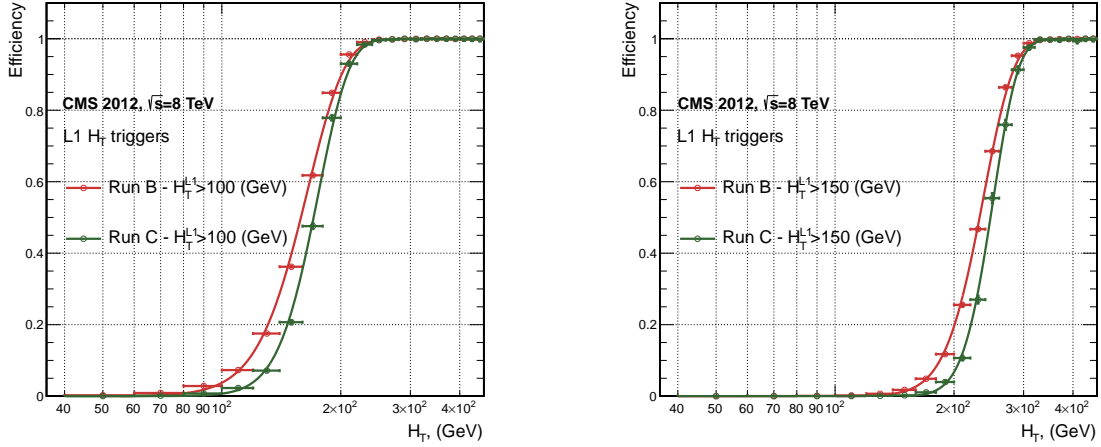


**Figure 3.14.:** L1  $H_T$  efficiency turn-on curves as a function of the offline CaloJet  $H_T$ , measured for the L1  $H_T$  100 and 150 trigger during the run 2012 B and C collected using an isolated single  $\mu$  triggered sample.

2012B			2012C		
Trigger	$\mu$	$\sigma$	$\mu$	$\sigma$	
L1 HT-100	$157.5 \pm 0.08$	$32.9 \pm 0.08$	$169.8 \pm 0.08$	$28.7 \pm 0.03$	
L1 H1-150	$230.9 \pm 0.02$	$37.3 \pm 0.01$	$246.4 \pm 0.16$	$31.8 \pm 0.05$	

**Table 3.3.:** Results of a cumulative EMG function fit to the turn-on curves for  $H_T$  in run 2012 B and C, preselected on an isolated single  $\mu$  trigger. The turn-on point  $\mu$ , resolution  $\sigma$  of the L1  $H_T$  triggers are measured with respect to offline  $H_T$  formed from CaloJets with a  $E_T \geq 40$  in run period B (left) and C (right).

at CMS in 2012. This is benchmarked relative to Calo and PF jets for the run 2012 C period where the jet seed threshold is applied, with L1 single jet thresholds of 16, 36 and 92 GeV, shown in Figure 3.15. The results of fits to these efficiency turn-on curves are given in Table 3.4 and Table 3.5 for Calo and PF jets respectively.

Vertices	0-10		11-20		> 20	
	$\mu$	$\sigma$	$\mu$	$\sigma$	$\mu$	$\sigma$
L1_SingleJet16	$19.9 \pm 0.1$	$6.1 \pm 0.3$	$20.8 \pm 0.1$	$6.5 \pm 0.1$	$22.3 \pm 0.2$	$7.5 \pm 0.1$
L1_SingleJet36	$41.8 \pm 0.1$	$4.6 \pm 0.1$	$40.9 \pm 0.1$	$5.1 \pm 0.1$	$40.6 \pm 0.6$	$5.9 \pm 0.2$
L1_SingleJet92	$95.9 \pm 0.2$	$5.4 \pm 0.1$	$95.2 \pm 0.2$	$5.6 \pm 0.1$	$94.5 \pm 0.6$	$6.2 \pm 0.3$

**Table 3.4.:** Results of a cumulative EMG function fit to the efficiency turn-on curves for L1 single jet triggers in the 2012 run period C, measured from isolated  $\mu$  triggered data. The turn-on point,  $\mu$ , and resolution,  $\sigma$ , of the L1 jet triggers are measured with respect to offline Calo jets in low (left), medium (middle) and high (right) pile-up conditions.

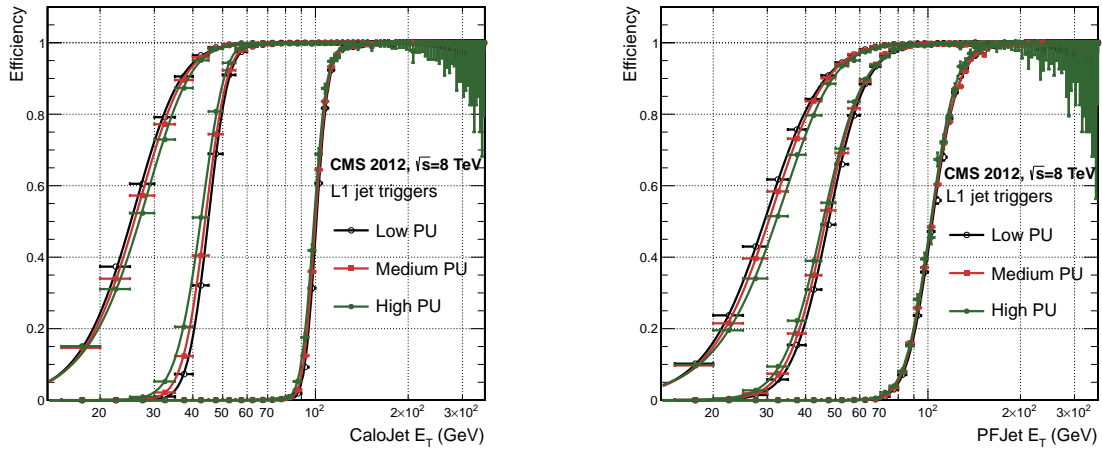


**Figure 3.15.:** L1 jet efficiency turn-on curves as a function of the leading offline  $E_T$ Calo (left) and PF (right) jet, for low, medium and high pile-up conditions.

Vertices	0-10		11-20		> 20	
	$\mu$	$\sigma$	$\mu$	$\sigma$	$\mu$	$\sigma$
L1_SingleJet16	21.1 $\pm$ 0.1	7.16 $\pm$ 0.05	22.34 $\pm$ 0.1	7.9 $\pm$ 0.1	24.6 $\pm$ 0.2	9.5 $\pm$ 0.1
L1_SingleJet36	39.6 $\pm$ 0.1	7.4 $\pm$ 0.1	38.4 $\pm$ 0.1	7.4 $\pm$ 0.1	37.1 $\pm$ 0.2	7.5 $\pm$ 0.1
L1_SingleJet92	91.6 $\pm$ 0.3	11.3 $\pm$ 0.2	90.4 $\pm$ 0.3	11.2 $\pm$ 0.1	92.0 $\pm$ 0.9	12.1 $\pm$ 0.4

**Table 3.5.:** Results of a cumulative EMG function fit to the efficiency turn-on curves for Level-1 single jet triggers in the 2012 run period C, measured from isolated  $\mu$  triggered data. The turn-on point,  $\mu$ , and resolution,  $\sigma$ , of the L1 jet triggers are measured with respect to offline PF jets in low (left), medium (middle) and high (right) pile-up conditions.

1174 No significant drop in efficiency is observed in the presence of a high number of primary  
 1175 vertices. The increase in hadronic activity in higher pile-up conditions, combined with  
 1176 the absence of pile-up subtraction for L1 jets, results in the expected observation of  
 1177 a decrease in the  $\mu$  value of the efficiency turn-ons as a function of pile-up, while the  
 1178 resolution,  $\sigma$  of the turn-ons are found to gradually worsen as expected with increasing  
 1179 pile-up.

1180 These features are further emphasised when shown as a function of

$$\frac{(L1 E_T - \text{Offline } E_T)}{\text{Offline } E_T} \quad (3.4)$$

1181 in bins of matched leading offline jet  $E_T$ , of which the individual fits can be found in  
1182 Appendix (B.2). Each of these distributions are fitted with an EMG function as defined  
1183 in Equation (3.3).

1184 The  $\mu$ ,  $\sigma$  and  $\lambda$  values extracted for the low, medium and high pile-up conditions are  
1185 shown for Calo and PF jets in Figure 3.16 and Figure 3.17 respectively. The central value  
1186 of  $\frac{(L1 E_T - \text{Offline } E_T)}{\text{Offline } E_T}$  is observed to increases as a function of jet  $E_T$ , whilst the resolution  
1187 is also observed to improve at higher offline jet  $E_T$ .

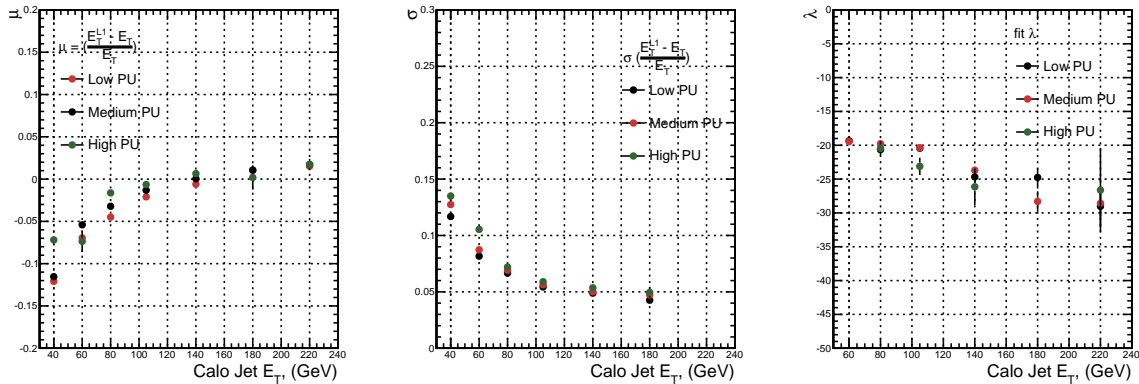


**Figure 3.16.:** Fit values from an EMG function fitted to the resolution plots of leading Calo jet  $E_T$  measured as a function of  $\frac{(L1 E_T - \text{Offline } E_T)}{\text{Offline } E_T}$  for low, medium and high pile-up conditions. The plots show the mean  $\mu$  (left), resolution  $\sigma$  (middle) of the Gaussian as well as the decay term  $\lambda$  (right) of the exponential.

1188 The resolution of other L1 jet based energy sum quantities,  $H_T$  and  $H_T$  parameterised  
1189 as in Equation (3.4), can be found in Appendix (B.3). The same behaviour observed for  
1190 the single jet triggers is also found for these quantities, where in the presence of higher  
1191 pile-up the  $\mu$  values are shifted to higher values, with a worsening resolution,  $\sigma$  again  
1192 due to the increase in soft pile-up jets and the absence of pile-up subtraction at L1.

### 1193 3.4.6. Summary

1194 The performance of the CMS Level-1 Trigger has been studied and evaluated for jets and  
1195 energy sum quantities using data collected during the 2012 LHC 8 TeV run. These studies  
1196 include the effect of introduction of a 5 GeV jet seed threshold into the jet algorithm  
1197 configuration, the purpose of which is to mitigate the effects of pile-up on the rate of  
1198 L1 triggers whilst not adversely affecting the efficiency of these triggers. No significant

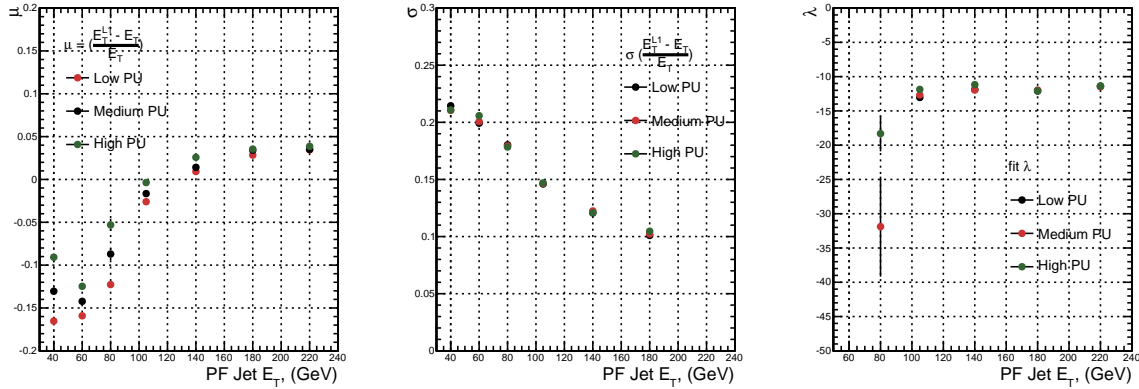


**Figure 3.17.:** Fit values from an **EMG** function fitted to the resolution plots of leading PF jet  $E_T$  measured as a function of  $\frac{(L1\ E_T - \text{Offline}\ E_T)}{\text{Offline}\ E_T}$  for low and medium pile-up conditions. The plots show the mean  $\mu$  (left), resolution  $\sigma$  (middle) of the Gaussian as well as the decay term  $\lambda$  (right) of the exponential.

1199 change in performance is observed with this change and good performance is observed  
 1200 for a range of L1 quantities.

# Chapter 4.

## 1201 SUSY Searches In Hadronic Final 1202 States

1203 In this chapter a model independent search for **SUSY** in hadronic final states with  
1204  $\cancel{E}_T$  using the  $\alpha_T$  variable at different b-quark and jet multiplicities is introduced and  
1205 described in detail. The results presented are based on a data sample of pp collisions  
1206 collected in 2012 at  $\sqrt{s} = 8$  TeV, corresponding to an integrated luminosity of  $11.7 \pm 0.5$   
1207  $\text{fb}^{-1}$  [5].

1208 The kinematic variable  $\alpha_T$  is motivated as a variable to provide strong rejection of the  
1209 overwhelming QCD background, prevalent to jets + $\cancel{E}_T$  final states at the **LHC**. This  
1210 is achieved whilst maintaining sensitivity to a possible **SUSY** signal and described in  
1211 Section (4.1). The search and trigger strategy in addition to the event reconstruction  
1212 and selection are outlined within Sections (4.2 - 4.3).

1213 The method in which the **SM** background is estimated using an analytical technique to  
1214 improve statistical precision at higher b-tag multiplicities is detailed within Section (4.5).  
1215 Included in this section is a discussion on the impact of b-tagging and mis-tagging scale  
1216 factors between data and simulation on any background predictions. Improved precision  
1217 in estimating background yields at large number of b-tagged jets, is important in the  
1218 context of interpreting natural **SUSY** models, first outlined in Section (2.4.1).

1219 A description of the formulation of appropriate systematic uncertainties applied to the  
1220 background predictions to account for theoretical uncertainties and limitations in the  
1221 simulation modelling of event kinematics and instrumental effects is covered in Section  
1222 (4.6). Similarly the systematic determination for the **SMS** signal samples used to interpret  
1223 the physics reach of the analysis are examined in Section (4.7).

1224 Finally the statistical likelihood model to interpret the observations in the signal and  
1225 control samples is described in Section (4.8). The experimental reach of the analysis  
1226 discussed within this thesis is interpreted in two classes of **SMS** models, both first  
1227 introduced in Section (2.4.1). The **SMS** models considered in this analysis are summarised  
1228 in Table 4.1. For each model, the **LSP** is assumed to be the lightest neutralino.

1229 Within the table are also defined reference points, parameterised in terms of parent  
1230 gluino/squark and **LSP** sparticle masses,  $m_{\text{parent}}$  and  $m_{\text{LSP}}$ , respectively, which are used  
1231 within the following two chapters to demonstrate potential yields within the signal region  
1232 of the search.

1233 The masses are chosen to reflect parameter space which is within the expected sensitivity  
1234 reach of the search, and also in the case of T1tttt and T1bbbb, reflect examples of  
1235 potential natural **SUSY** topologies.

Model	Production/decay mode	Reference model	
		$m_{\text{parent}}$	$m_{\text{LSP}}$
G1 (T1)	$pp \rightarrow \tilde{g}\tilde{g}^* \rightarrow q\bar{q}\tilde{\chi}_1^0 q\bar{q}\tilde{\chi}_1^0$	700	300
G2 (T1bbbb)	$pp \rightarrow \tilde{g}\tilde{g}^* \rightarrow b\bar{b}\tilde{\chi}_1^0 b\bar{b}\tilde{\chi}_1^0$	900	500
G3 (T1tttt)	$pp \rightarrow \tilde{g}\tilde{g}^* \rightarrow t\bar{t}\tilde{\chi}_1^0 t\bar{t}\tilde{\chi}_1^0$	850	250
D1 (T2)	$pp \rightarrow \tilde{q}\tilde{q}^* \rightarrow q\tilde{\chi}_1^0 q\tilde{\chi}_1^0$	600	250
D2 (T2bb)	$pp \rightarrow \tilde{b}\tilde{b}^* \rightarrow b\tilde{\chi}_1^0 b\tilde{\chi}_1^0$	500	150
D3 (T2tt)	$pp \rightarrow \tilde{t}\tilde{t}^* \rightarrow t\tilde{\chi}_1^0 t\tilde{\chi}_1^0$	400	0

**Table 4.1.:** A summary of the **SMS** models interpreted in this analysis, involving both direct (D) and gluino-induced (G) production of squarks and their decays. Reference models are also defined in terms of parent and **LSP** sparticle mass

## 1236 4.1. An Introduction to the $\alpha_T$ Search

1237 A proton-proton collision resulting in the production and decay of supersymmetric  
1238 particles, would manifest as a final state containing energetic jets and  $\cancel{E}_T$  in the hadronic  
1239 channel. The search focuses on topologies where new heavy supersymmetric, R-parity  
1240 conserving particles are pair-produced in pp collisions. These particles decaying to a  
1241 **LSP** escape the detector undetected, leading to significant missing energy and missing  
1242 hadronic transverse energy,

$$\mathcal{H}_T = \left| \sum_{i=1}^n \vec{p_T}^{jet_i} \right|, \quad (4.1)$$

1243 defined as the vector sum of the transverse energies of jets selected in an event. Energetic  
1244 jets produced in the decay of these supersymmetric particles also can produce significant  
1245 visible transverse energy,

$$H_T = \sum_{i=1}^n E_T^{jet_i}, \quad (4.2)$$

1246 defined as the scalar sum of the transverse energies of jets selected in an event.

1247 A search within this channel is greatly complicated in a hadron collider environment,  
1248 where the overwhelming background comes from inherently balanced multi-jet (“QCD”)  
1249 events which are produced with an extremely large cross section as demonstrated within  
1250 Figure 4.1.  $\cancel{E}_T$  can appear in such events with a substantial mis-measurement or  
1251 stochastic fluctuations of jet energy or missed objects due to detector mis-calibration or  
1252 noise effects.

1253 Additional SM background from EWK processes with genuine  $\cancel{E}_T$  from escaping neutrinos  
1254 comprise the irreducible background within this search and come mainly from:

- 1255 •  $Z \rightarrow \nu\bar{\nu}$  + jets,
- 1256 •  $W \rightarrow l\nu$  + jets in which a lepton falls outside of detector acceptance, is not  
1257 reconstructed, is mis-identified, or the lepton decays hadronically  $\tau \rightarrow$  had ,
- 1258 •  $t\bar{t}$  with at least one leptonically decaying W, which is missed in the detector as  
1259 detailed above,
- 1260 • small background contributions from DY, single top and Diboson (WW,ZZ,WZ)  
1261 processes.

1262 The search is designed to have a strong separation between events with genuine and  
1263 “fake”  $\cancel{E}_T$  which is achieved primarily through the dimensionless kinematic variable,  $\alpha_T$   
1264 [71][72].

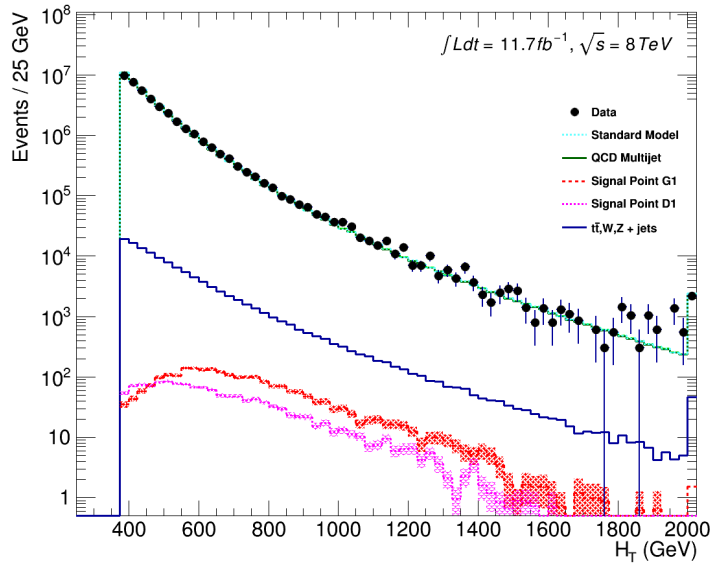


**Figure 4.1.:** Reconstructed offline  $H_T$  distribution in the hadronic signal selection, from  $11.7\text{fb}^{-1}$  of data, in which no  $\alpha_T$  requirement is made. Sample is collected from prescaled  $H_T$  triggers. Overlaid are expectations from MC simulation of EWK processes as well as two reference signal models (labelled G1 and D1 from Table 4.1).

### 1265 4.1.1. The $\alpha_T$ variable

1266 For a perfectly measured di-jet QCD event, conservation laws dictate that both jets must  
 1267 be of equal magnitude and produced in opposite directions. However in the case of di-jet  
 1268 events with genuine  $\cancel{E}_T$  (as detailed above), no such requirement is made of the two jets,  
 as depicted in Figure 4.2.

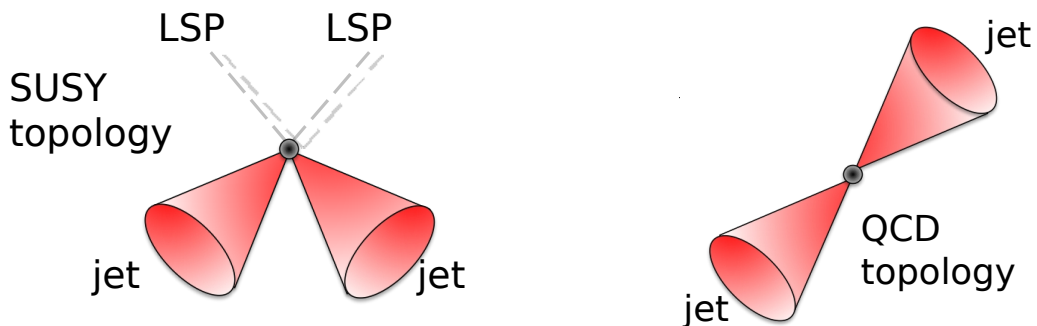


**Figure 4.2.:** The event topologies of background QCD dijet events (right) and a generic SUSY signature with genuine  $\cancel{E}_T$  (left).

1270 Exploiting this feature leads to the formulation of  $\alpha_T$  (first inspired by [73]) in di-jet  
1271 systems defined as,

$$\alpha_T = \frac{E_T^{j_2}}{M_T}, \quad (4.3)$$

1272 where  $E_T^{j_2}$  is the transverse energy of the least energetic of the two jets and  $M_T$  defined  
1273 as:

$$M_T = \sqrt{\left(\sum_{i=1}^2 E_T^{j_i}\right)^2 - \left(\sum_{i=1}^2 p_x^{j_i}\right)^2 - \left(\sum_{i=1}^2 p_y^{j_i}\right)^2} \equiv \sqrt{H_T^2 - \cancel{H}_T^2}. \quad (4.4)$$

1274 A perfectly balanced di-jet event i.e.  $E_T^{j_1} = E_T^{j_2}$  would yield an  $\alpha_T$  value of 0.5, where  
1275 as events with jets which are not back-to-back, for example in events in which a W or  
1276 Z recoils off a system of jets,  $\alpha_T$  can achieve values in excess of 0.5. Most importantly  
1277 balanced QCD events in which jets are mis-measured, will generally result in an  $\alpha_T$  of  
1278 less than 0.5, thus giving the  $\alpha_T$  variable discriminating power between these processes.

1279  $\alpha_T$  can be extended to apply to any arbitrary number of jets, undertaken by modelling  
1280 a system of  $n$  jets as a di-jet system, through the formation of two pseudo-jets [74].  
1281 The two pseudo-jets are built by merging the jets present in the event such that the  
1282 2 pseudo-jets are chosen to be as balanced as possible, i.e the  $\Delta H_T \equiv |E_T^{pj_1} - E_T^{pj_2}|$  is  
1283 minimised between the two pseudo jets. Using Equation (4.4),  $\alpha_T$  can be rewritten as,

$$\alpha_T = \frac{1}{2} \frac{H_T - \Delta H_T}{\sqrt{H_T^2 - \cancel{H}_T^2}} = \frac{1}{2} \frac{1 - \Delta H_T/H_T}{\sqrt{1 - (\cancel{H}_T/H_T)^2}}. \quad (4.5)$$

1284 The distribution of  $\alpha_T$  for the two jet categories used within this analysis,  $2 \leq n_{jet} \leq 3$   
1285 and  $n_{jet} \geq 4$  jets, is shown in the Figure 4.3. It can be seen that the distributions peak  
1286 at an  $\alpha_T$  of 0.5, before falling away sharply and being free of multi-jet background at  
1287 larger  $\alpha_T$  values. These distributions serve to demonstrate the ability of the  $\alpha_T$  variable  
1288 to discriminate between multi-jet events and EWK processes with genuine  $\cancel{E}_T$  in the  
1289 final state.

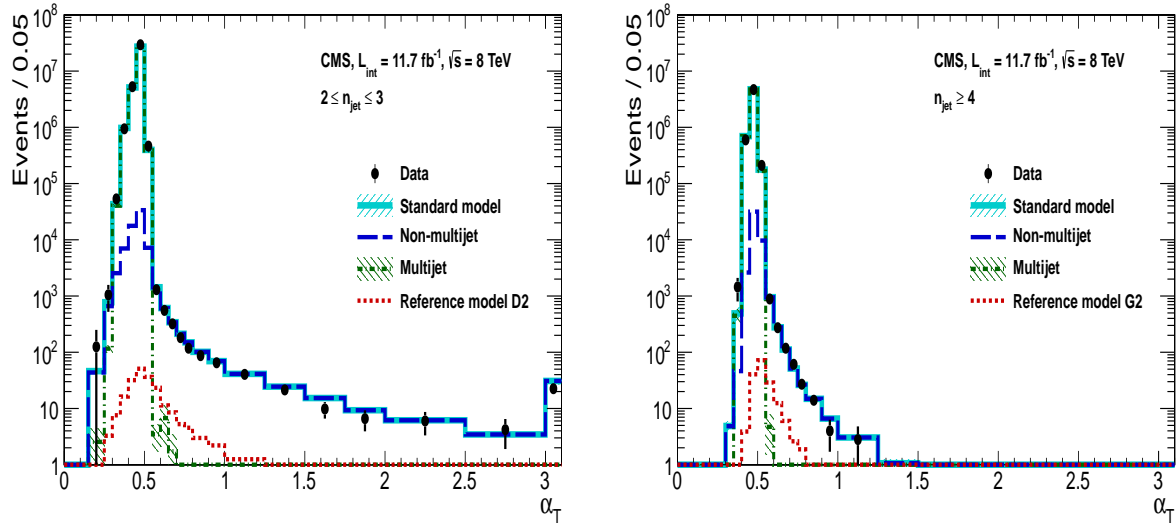


**Figure 4.3.:** The  $\alpha_T$  distributions for the low 2-3 (left) and high  $\geq 4$  (right) jet multiplicities after a full analysis selection and shown for  $H_T > 375$ . Data is collected using both prescaled  $H_T$  triggers and dedicated  $\alpha_T$  triggers for below and above  $\alpha_T = 0.55$  respectively. . Expected yields as given by simulation are also shown for multi-jet events (green dash-dotted line), EWK backgrounds with genuine  $E_T$  (blue long-dashed line), the sum of all SM processes (cyan solid line) and the reference signal model D2 (left, red dotted line) or G2 (right, red dotted line).

1290 The  $\alpha_T$  requirement used within the search is chosen to be  $\alpha_T > 0.55$  to ensure that  
 1291 the QCD multi-jet background is negligible even in the presence of moderate jet mis-  
 1292 measurement. There still remains other effects which can cause multi-jet events to  
 1293 artificially have a large  $\alpha_T$  value, which are discussed in detail in Section (4.2.2).

## 1294 4.2. Search Strategy

1295 The aim of the analysis presented in this thesis is to identify an excess of events in data  
 1296 over the SM background expectation in multi-jet final states and significant  $E_T$ . The  
 1297 essential suppression of the dominant QCD background for such a search is addressed by  
 1298 the  $\alpha_T$  variable described in the previous section. For estimation of the remaining EWK  
 1299 backgrounds, three independent data control samples are used to predict the different  
 1300 processes that compose the background :

- 1301 •  $\mu +$  jets control sample to determine  $W +$  jets,  $t\bar{t}$  and single top backgrounds,  
 1302 •  $\gamma +$  jets control sample to determine the irreducible  $Z \rightarrow \nu\bar{\nu} +$  jets background,

1303 •  $\mu\mu + \text{jets}$  control sample to also determine the irreducible  $Z \rightarrow \nu\bar{\nu} + \text{jets}$  background.

1304 These control samples are chosen to both be rich in specific **EWK** processes, be free of  
1305 QCD multi-jet events and to also be kinematically similar to the hadronic signal region  
1306 that they are estimating the backgrounds of, see Section (4.2.3). The redundancy of  
1307 using the  $\gamma + \text{jets}$  and  $\mu\mu + \text{jets}$  sample to predict the same background within the  
1308 signal region, brings an opportunity to reliably cross check and validate the background  
1309 estimation method and is utilised in both the determination of background estimation  
1310 systematics (Section(4.6)), and in the maximum likelihood fit (Section(4.8)).

1311 To remain inclusive to a large range of possible **SUSY** models, the signal region is split  
1312 into the following categories to allow for increased sensitivity in the interpretation of  
1313 results for different **SUSY** topologies:

1314 **Sensitivity to a range of SUSY mass splittings**

1315 The hadronic signal region is defined by  $H_T > 275$ , divided into eight bins in  $H_T$ .  
1316 – Two bins of width 50 GeV in the range  $275 < H_T < 375$  GeV,  
1317 – five bins of width 100 GeV in the range  $375 < H_T < 875$  GeV,  
1318 – and a final open bin,  $H_T > 875$  GeV.

1319 The choice of the lowest  $H_T$  bin in the analysis is driven primarily by trigger  
1320 constraints. The mass difference between the **LSP** and the particle that it decays  
1321 from is an important factor in the amount of hadronic activity in the event.

1322 A large mass splitting will lead to hard high  $p_T$  jets which contribute to the  $H_T$   
1323 sum. From Figure 4.1 it can be seen that the **SM** background falls sharply at high  
1324  $H_T$  values, therefore binning in  $H_T$  will lead to easier identification of such signals.  
1325 Conversely smaller mass splittings lead to softer jet  $p_T$ 's which will subsequently  
1326 fall into the lower  $H_T$  range.

1327 **Sensitivity to production method of SUSY particles**

1328 The production mechanism of any potential **SUSY** signal can lead to different event  
1329 topologies. One such way to discriminate between gluino ( $g\tilde{g}$  - “high multiplicity”),  
1330 and direct squark ( $q\tilde{q}$  - “low multiplicity”) induced production of **SUSY** particles is  
1331 realised through the number of reconstructed jets in the final state.

1332 The analysis is thus split into two jet categories : 2-3 jets ,  $\geq 4$  jets to give sensitivity  
1333 to both of these mechanisms.

1334 **Sensitivity to “Natural SUSY” via tagging jets from b-quarks**

1335 Jets originating from bottom quarks (b-jets) are identified through vertices that  
1336 are displaced with respect to the primary interaction. The algorithm used to tag  
1337 b-jets is the Combined Secondary Vertex Medium Working Point (**CSV**) tagger,  
1338 described within Section (3.3.2). A cut is placed on the discriminator variable of  
1339  $> 0.679$ , leading to a gluon/light-quark mis-tag rate of approximately 1% and a jet  
1340  $p_T$  dependant b-tagging efficiency of 60-70% [?].

1341 Natural **SUSY** models would be characterised through final-state signatures rich  
1342 in bottom quarks. A search relying on methods to identify jets originating from  
1343 bottom quarks through b-tagging, will significantly improve the sensitivity to this  
1344 class of signature. This gain in sensitivity stems from a vast reduction in the vector  
1345 boson + jet backgrounds (W,Z) at higher b-tag jet multiplicities, which typically  
1346 have no b-flavoured quarks in their decays.

1347 Therefore events are categorised according to the number of b-tagged jets recon-  
1348 structed in each event, in the following: 0,1,2,3, $\geq 4$  b-tag categories . In the highest  
1349  $\geq 4$  b-tag category due to a limited number of expected signal and background, just  
1350 three  $H_T$  bins are employed: 275-325 GeV, 325-375 GeV,  $\geq 375$  GeV.

1351 This characterisation is identically mirrored in all control samples, with the infor-  
1352 mation from all samples and b-tag categories used simultaneously in the likelihood  
1353 model, see Section (4.8).

1354 The combination of the  $H_T$ , jet multiplicity and b-tag categorisation of the signal region as  
1355 described above, resultantly leads to 67 different bins in which the analysis is interpreted  
1356 in, and is depicted in Figure 4.4.

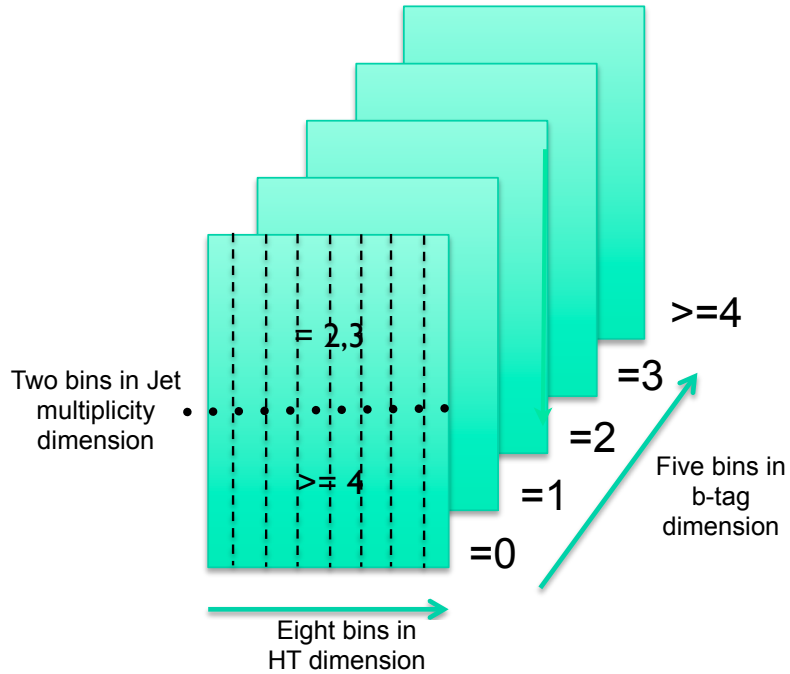


**Figure 4.4.:** Pictorial depiction of the analysis strategy employed by the  $\alpha_T$  search to increase sensitivity to a wide spectra of **SUSY** models.

### <sup>1357</sup> 4.2.1. Physics objects

<sup>1358</sup> The physics objects used in the analysis defined below, follow the recommendation of  
<sup>1359</sup> the various **CMS** Physics Object Groups (**POGs**).

#### <sup>1360</sup> • Jets

<sup>1361</sup> The jets used in this analysis are CaloJets, reconstructed as described in Section  
<sup>1362</sup> (3.3.1) using the anti- $k_T$  jet clustering algorithm.

<sup>1363</sup> To ensure the jet object falls within the calorimeter systems a pseudo-rapidity  
<sup>1364</sup> requirement of  $|\eta| < 3$  is applied. Each jet must pass a “loose” identification criteria  
<sup>1365</sup> to reject jets resulting from unphysical energy, the criteria of which are detailed in  
<sup>1366</sup> Table A.1 [75].

#### <sup>1367</sup> • Muons

<sup>1368</sup> Muons are selected in the  $\mu + \text{jets}$  and  $\mu\mu + \text{jets}$  control samples, and vetoed in  
<sup>1369</sup> the signal region. The same cut based identification criteria is applied to muons in  
<sup>1370</sup> both search regions and is summarised in Table 4.2 [76].

Variable	Definition
Is Global Muon	Muon contains both a hit in the muon chamber and a matched track in the inner tracking system .
$\chi^2 < 10$	$\chi^2$ of global muon track fit. Used to suppress hadronic punch-through and muons from decays in flight.
Muon chamber hits > 0	At least one muon chamber hit included in global muon track fit.
Muon station hits > 1	Muon segment hits in at least two muon stations, which suppresses hadronic punch-through and accidental track-to-segment matches.
$d_{xy} < 0.2\text{mm}$	The tracker track transverse impact parameter w.r.t the primary vertex. Suppresses cosmic muons and muons from decays in flight.
$d_z < 0.5\text{mm}$	The longitudinal distance of the tracker track w.r.t the primary vertex. Loose cut to further suppress cosmic muons, muons from decays in flight and tracks from pileup.
Pixel hits > 0	Suppresses muons from decays in flight by requiring at least one pixel hit in the tracker.
Track layer hits > 5	Number of tracker layers with hits, to guarantee a good $p_T$ measurement. Also suppresses muons from decays in flight.
PF Iso < 0.12	Isolation based upon the sum of the charged and neutral hadrons and photon objects within a $\Delta R$ 0.4 cone of the muon object, corrected for pile up effects on the isolation sum.

**Table 4.2.:** Muon Identification criteria used within the analysis for selection/veto purposes in the muon control/signal selections.

1371      Additionally muons are required to be within the acceptance of the muon tracking  
 1372      systems. For the muon control samples, trigger requirements necessitate a  $|\eta| <$   
 1373      2.1 for the selection of muons. In the signal region where muons are vetoed these  
 1374      conditions are relaxed to  $|\eta| < 2.5$  and a minimum threshold of  $p_T > 10 \text{ GeV}$  is  
 1375      required of muon objects.

1376      **• Photons**

1377      Photons are selected within the  $\gamma + \text{jets}$  control sample and vetoed in all other  
 1378      selections. Photons are identified in both cases according to the cut based criteria  
 1379      listed in Table 4.3 [77].

Variable	Definition
H/E < 0.05	The ratio of hadronic energy in the <b>HCAL</b> tower directly behind the <b>ECAL</b> super-cluster and the <b>ECAL</b> super-cluster itself.
$\sigma_{i\eta i\eta} < 0.011$	The log energy weighted width ( $\sigma$ ), of the extent of the shower in the $\eta$ dimension.
R9 < 1.0	The ratio of the energy of the $3 \times 3$ crystal core of the super-cluster compared to the total energy stored in the $5 \times 5$ super-cluster.
Combined Isolation < 6 GeV	The photons are required to be isolated with no electromagnetic or hadronic activity within a radius $\Delta R = 0.3$ of the photon object. A combination of the pileup subtracted [78], <b>ECAL</b> , <b>HCAL</b> and tracking isolation sums are used to determine the combined total isolation value.

**Table 4.3.:** Photon Identification criteria used within the analysis for selection/veto purposes in the  $\gamma +$  jets control/signal selections.

1380 Photon objects are also required to have a minimum momentum of  $p_T > 25$  GeV.

1381 **• Electrons**

1382 Electron identification is defined for veto purposes. They are selected according to  
1383 the following cut-based criteria listed in Table 4.4, utilising PF-based isolation.

1384 Electrons are required to be identified at  $|\eta| < 2.5$ , with a minimum  $p_T > 10$  GeV  
1385 threshold to ensure that the electrons fall within the tracking system of the detector.

Variable	Barrel	EndCap	Definition
$\Delta\eta_{In}$	<0.007	<0.009	$\Delta\eta$ between SuperCluster position and the coordinate of the associated track at the interaction vertex, assuming no radiation.
$\Delta\phi_{In}$	<0.15	<0.10	$\Delta\phi$ between SuperCluster position and track direction at interaction vertex extrapolated to ECAL assuming no radiation.
$\sigma_{in\eta\eta}$	<0.01	<0.03	Cluster shape covariance, measure the $\eta$ dispersion of the electrons electromagnetic shower over the ECAL supercluster.
H/E	<0.12	<0.10	The ratio of hadronic energy in the HCAL tower directly behind the ECAL super-cluster and the ECAL super-cluster itself.
d0 (vtx)	<0.02	<0.02	The tracker track transverse impact parameter w.r.t the primary vertex.
dZ (vtx)	<0.20	<0.20	The longitudinal distance of the tracker track w.r.t the primary vertex.
$ (\frac{1}{E_{ECAL}} - \frac{1}{p_{track}}) $	<0.05	<0.05	Comparison of energy at supercluster 1/ $E_{ECAL}$ and that of the track momentum at the vertex 1/ $p_{track}$ . Causes suppression of fake electrons at low $p_T$ .
PF Iso	<0.15	<0.15	Combined PF isolation of charged hadrons, photons, neutral hadrons within a $\Delta R < 0.3$ cone size. Isolation sum is corrected for pileup using effective area corrections for neutral particles.

**Table 4.4.:** Electron Identification criteria used within the analysis for veto purposes.

1386 **• Noise and  $\cancel{E}_T$  Filters**

1387 A series of Noise filters are applied to veto events which contain spurious non-physical  
 1388 jets that are not picked up by the jet id, and events which give large unphysical  $\cancel{E}_T$   
 1389 values. These filters are listed within Table 4.5.

Noise Filters	Variable	Definition
CSC tight beam halo filter		As proton beams circle the <b>LHC</b> , proton interactions with the residual gas particles or the beam collimators can occur, producing showers of secondary particles which can interact with the <b>CMS</b> detector.
HBHE noise filter with isolated noise rejection		Anomalous noise in the <b>HCAL</b> not due to electronics noise, but rather due to instrumentation issues associated with the <b>HPD</b> 's and Readout Boxes ( <b>RBXs</b> ).
HCAL laser filter		The <b>HCAL</b> uses laser pulses for monitoring the detector response. Some laser pulses have accidentally been fired in the physics orbit, and ended up polluting events recorded for physics analysis.
ECAL dead cell trigger primitive (TP) filter		<b>EB</b> and <b>EE</b> have single noisy crystals which are masked in reconstruction. Use the Trigger Primitive ( <b>TP</b> ) information to assess how much energy was lost in masked cells.
Bad EE Supercrystal filter		Two supercrystals in <b>EE</b> are found to occasionally produce high amplitude anomalous pulses in several channels at once, causing a large $E_T$ spike.
ECAL Laser correction filter		A laser calibration multiplicative factor is applied to correct for transparency loss in each crystal during irradiation. A small number of crystals receive unphysically large values of this correction and become very energetic, resulting in $E'_T$ .

**Table 4.5.:** Noise filters that are applied to remove spurious and non-physical  $\cancel{E}_T$  signatures within the **CMS** detector.

### <sup>1390</sup> 4.2.2. Event selection

<sup>1391</sup> The selection criteria for events within the analysis are detailed below. A set of common  
<sup>1392</sup> cuts are applied to both signal (maximise acceptance to a range of **SUSY** signatures), and  
<sup>1393</sup> control samples (retain similar jet kinematics for background predictions), with additional  
<sup>1394</sup> selection cuts applied to each control sample to enrich the sample in a particular **EWK**  
<sup>1395</sup> processes, see Section (4.2.3).

<sup>1396</sup> The jets considered in the analysis are required to have a transverse momentum  $p_T > 50$   
<sup>1397</sup> GeV, with a minimum of two jets required in the event. The highest  $E_T$  jet is required  
<sup>1398</sup> to lie within the central tracker acceptance  $|\eta| < 2.5$ , and the two leading  $p_T$  jets must  
<sup>1399</sup> each have  $p_T > 100$  GeV. Any event which has a jet with  $p_T > 50$  GeV that either fails  
<sup>1400</sup> the “loose” identification criteria described in Section(4.2.1) or has  $|\eta| > 3.0$ , is rejected.  
<sup>1401</sup> Similarly events in which an electron, muon or photon fails object identification but pass  
<sup>1402</sup>  $\eta$  and  $p_T$  restrictions, are identified as an “odd” lepton/photon and the event is vetoed.

<sup>1403</sup> At low  $H_T$ , the jet  $p_T$  threshold requirements required to be considered as part of the  
<sup>1404</sup> analysis and enter the  $H_T$  sum are scaled downwards. These are scaled down in order

1405 to extend phase space at low  $H_T$ , preserving similar jet multiplicities and background  
1406 admixture seen at higher  $H_T$ , as listed in Table 4.6.

$H_T$ bin	minimum jet $p_T$	second leading jet $p_T$
$275 < H_T < 325$	36.7	73.3
$325 < H_T < 375$	43.3	86.6
$375 < H_T$	50.0	100.0

**Table 4.6.:** Jet thresholds used in the three  $H_T$  regions of the analysis.

1407 Within the signal region, to suppress SM processes with genuine  $\cancel{E}_T$  from neutrinos,  
1408 events containing isolated electrons or muons are vetoed. Furthermore to ensure a pure  
1409 multi-jet topology, events are vetoed if an isolated photon is found with  $p_T > 25$  GeV.  
1410 An  $\alpha_T$  requirement of  $> 0.55$  is required to reduce the QCD multi-jet background  
1411 to a negligible amount. Finally additional cleaning cuts are applied to protect against  
1412 pathological deficiencies such as reconstruction failures or severe energy mis-measurements  
1413 due to detector inefficiencies:

- Significant  $\cancel{H}_T$  can arise in events with no real  $\cancel{E}_T$  due to multiple jets falling below the  $p_T$  threshold for selecting jets. This in turn leads to events which can then incorrectly pass the  $\alpha_T$  requirements of the analysis. This effect can be negated by requiring that the missing transverse momentum reconstructed from jets alone does not greatly exceed the missing transverse momentum reconstructed from all of the detector's calorimeter towers,

$$R_{miss} = \cancel{H}_T / \cancel{E}_T < 1.25.$$

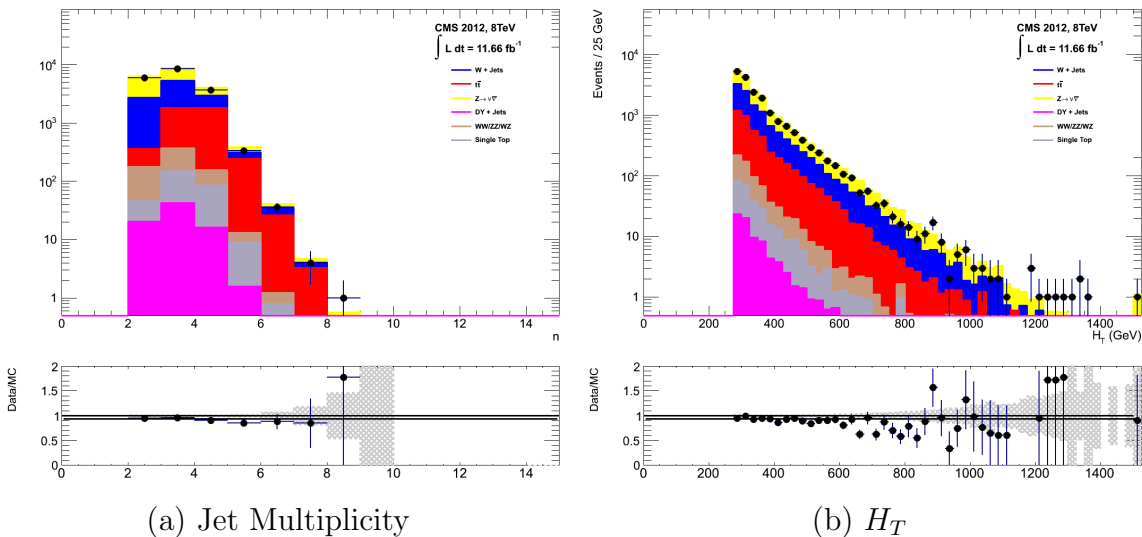
1414 • Fake  $\cancel{E}_T$  and  $\cancel{H}_T$  can arise due to significant jet mis-measurements caused by a small  
1415 number of non-functioning ECAL regions. These regions absorb electromagnetic  
1416 showers which are subsequently not added to the jet energy sum. To circumvent  
1417 this problem the following procedure is employed : For each jet in the event, the  
1418 angular separation

$$\Delta\phi_j^* \equiv \Delta\phi(\vec{p_j} - \sum_{i \neq j} \vec{p_i}), \quad (4.6)$$

is calculated where that jet is itself removed from the event. Here  $\Delta\phi^*$  is a measure of how aligned the  $H_T$  of an event is with a jet. A small value (i.e. the  $H_T$  vector lies along the jet axis) is indicative of an inherently balanced event in which a jet has been mis-measured. For every jet in a event with  $\Delta\phi^* < 0.5$ , if the  $\Delta R$  distance between the selected jet and the closest dead **ECAL** region is also  $< 0.3$ , then the event is rejected. Similarly events are rejected if the jet points within  $\Delta R < 0.3$  of the **ECAL** barrel-endcap gap at  $|\eta| = 1.5$ .

Some of the key distributions of the data used in this analysis compared to MC simulation are shown in Figure 4.5. The MC samples are normalised to a luminosity of  $11.7 \text{ fb}^{-1}$ , with no requirement placed upon the number of b-tagged jets or number of jets in the events. In the case of this inclusive selection the dominant backgrounds in the signal regions are,  $Z \rightarrow \nu\bar{\nu}$  and  $W + \text{jets}$  processes, with a smaller  $t\bar{t}$  background accompanied by other residual backgrounds.

The distributions shown are presented for purely illustrative purposes, with the MC simulation itself not used in absolute terms to estimate the yields from background processes, see Sections (4.2.3, 4.5). However it is nevertheless important to demonstrate that good agreement exists between simulation and observation in data.



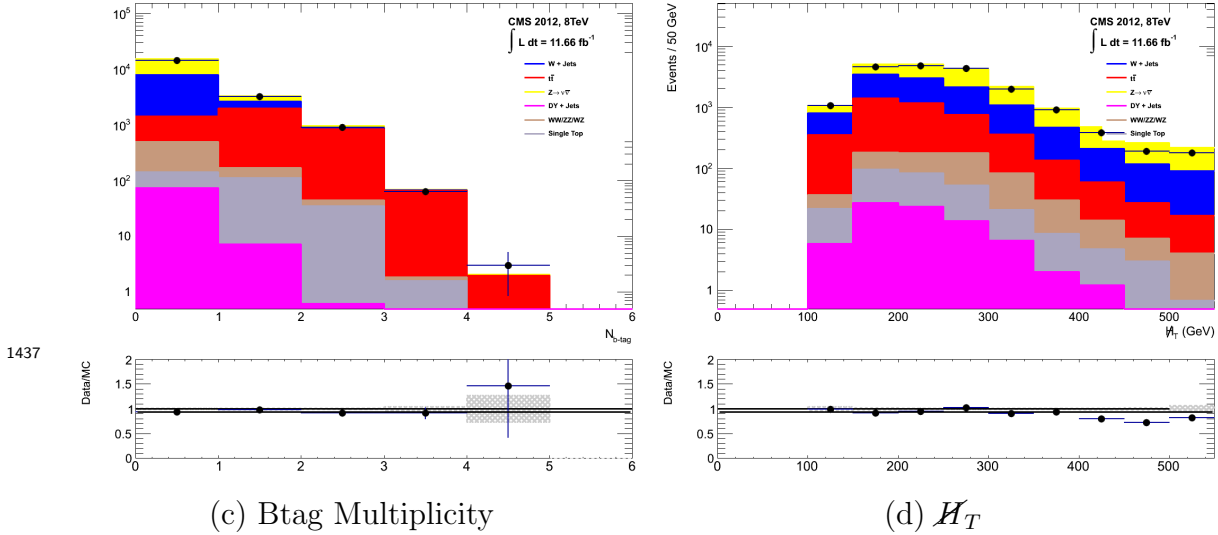


**Figure 4.5.:** Data/MC comparisons of key variables for the hadronic signal region, following the application of the hadronic selection criteria and the requirements of  $H_T > 275$  GeV and  $\alpha_T > 0.55$ . Bands represent the uncertainties due to the statistical size of the MC samples. No requirement is made upon the number of b-tagged jets or jet multiplicity in these distributions.

### 4.2.3. Control sample definition and background estimation

The method used to estimate the background contributions in the hadronic signal region relies on the use of a Transfer Factor (TF). This is determined from MC simulation in both the control,  $N_{MC}^{\text{control}}$ , and signal,  $N_{MC}^{\text{signal}}$ , region to transform the observed yield measured in data for a control sample,  $N_{\text{obs}}^{\text{control}}$ , into a background prediction,  $N_{\text{pred}}^{\text{signal}}$ , via Equation (4.7),

$$N_{\text{pred}}^{\text{signal}} = \frac{N_{MC}^{\text{signal}}}{N_{MC}^{\text{control}}} \times N_{\text{obs}}^{\text{control}}. \quad (4.7)$$

All MC samples are normalised to the luminosity of the data samples,  $11.7 \text{ fb}^{-1}$ . Through this method, “vanilla” predictions for the SM background in the signal region can be made by considering separately the sum of the prediction from either the  $\mu + \text{jets}$  and  $\gamma + \text{jets}$ , or  $\mu + \text{jets}$  and  $\mu\mu + \text{jets}$  samples. However the final background estimation from which results are interpreted, is calculated via a fitting procedure defined formally by the likelihood model described in Section (4.8).

1450 The sum of the expected yields from all MC processes, in each control sample enter the  
1451 denominator,  $N_{MC}^{\text{control}}$ , of the **TF** defined in Eq (4.7). However for the numerator,  $N_{MC}^{\text{signal}}$ ,  
1452 only the relevant processes that are being estimated, enter into the **TF**.

1453 For the  $\mu + \text{jets}$  sample the simulated MC processes which enter the numerator of the  
1454 **TF** are,

$$N_{MC}^{\text{signal}}(H_T, n_{\text{jet}}) = N_W + N_{t\bar{t}} + N_{DY} + N_t + N_{di-boson}, \quad (4.8)$$

1455 whilst for both the  $\mu\mu + \text{jets}$  and  $\gamma + \text{jets}$  samples the only MC process used in the  
1456 numerator is,

$$N_{MC}^{\text{signal}}(H_T, n_{\text{jet}}) = N_{Z \rightarrow \nu\bar{\nu}}. \quad (4.9)$$

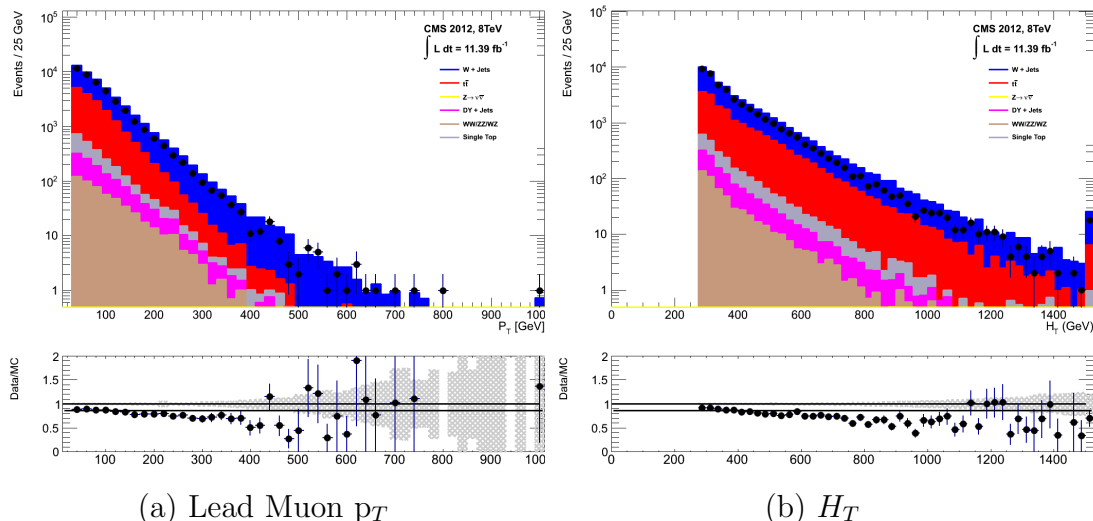
1457 The control samples and the **EWK** processes they are specifically tuned to select are  
1458 defined below, with distributions of key variables for each of the control samples shown  
1459 for illustrative purposes in Figures 4.6, 4.7 and 4.8. No requirement is placed upon  
1460 the number of b-tagged jets or jet multiplicity in the distributions shown. The MC  
1461 distributions highlight the background compositions of each control sample, where in  
1462 general, good agreement is observed between data and simulation, giving confidence  
1463 that the samples are well understood. The contribution from QCD multi-jet events is  
1464 expected to be negligible :

### 1465 The $\mu + \text{jets}$ control sample

1466 Events from  $W + \text{jets}$  and  $t\bar{t}$  processes enter into the hadronic signal sample due  
1467 to unidentified leptons from acceptance effects or reconstruction inefficiencies and  
1468 hadronic tau decays. These leptons originate from the decay of high  $p_T$   $W$  bosons.

1469 The control samples specifically identifies  $W \rightarrow \mu\bar{\nu}$  decays within a similar phase-  
1470 space of the signal region, where the muon is subsequently ignored in the calculation  
1471 of event level variables, i.e.  $H_T$ ,  $\cancel{H}_T$ ,  $\alpha_T$ . All kinematic jet-based cuts are identical  
1472 to those applied in the hadronic search region (with the exception of  $\alpha_T$ , discussed  
1473 below) detailed in Section (4.2.2), with the same  $H_T$ , jet multiplicity and b-jet  
1474 multiplicity binning described above.

- 1475 – Muons originating from W boson decays are selected by requiring one tightly  
 1476 isolated muon defined in Table 4.2, with a  $p_T > 30$  GeV and  $|\eta| < 2.1$ . Both of  
 1477 these threshold arise from trigger restrictions.
- 1478 – The transverse mass of the W candidate must satisfy  $M_T(\mu, \cancel{E}_T) > 30$  GeV ( to suppress QCD multi-jet events).
- 1479 – Events which contain a jet overlapping with a muon  $\Delta R(\mu, \text{jet}) < 0.5$  are vetoed to remove events from muons produced as part of a jet’s hadronisation process.
- 1480 – Events containing a second muon candidate which has failed id, but passing  
 1481  $p_T$  and  $|\eta|$  requirements, are checked to have an invariant mass that satisfies  
 1482  $|M_{\mu\mu} - m_Z| > 25$ , thus removing  $Z \rightarrow \mu\mu$  contamination.



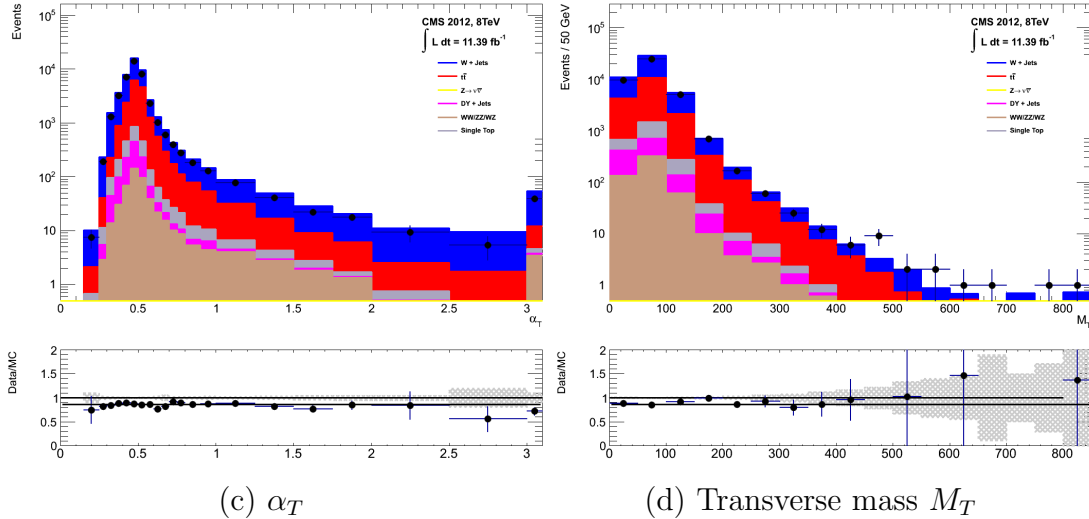


**Figure 4.6.:** Data/MC comparisons of key variables for the  $\mu + \text{jets}$  selection, following the application of selection criteria and the requirements that  $H_T > 275$  GeV. Bands represent the uncertainties due to the statistical size of the MC samples. No requirement is made upon the number of b-tagged jets or jet multiplicity in these distributions.

### The $\mu\mu + \text{jets}$ control sample

The  $Z \rightarrow \nu\bar{\nu} + \text{jets}$  background enters into the signal region from genuine  $\cancel{E}_T$  from the escaping neutrinos. This background is estimated using two control samples, the first of which is the  $Z \rightarrow \mu\bar{\mu} + \text{jets}$  process, which posses identical kinematic properties, but with different acceptance and branching ratio [1].

The same acceptance requirements as the  $\mu + \text{jets}$  selection for muons is applied, as defined in Table 4.2. Muons in the event are ignored for the purpose of the calculation of event level variables. Kinematic jet-based cuts and phase space binning identical to the hadronic search region are also applied.

- Muons originating from a  $Z$  boson decay are selected, requiring exactly two tightly isolated muons. Due to trigger requirements the leading muon is required to have  $p_T > 30$  GeV and  $|\eta| < 2.1$ . The requirement of the  $p_T$  on the second muon is relaxed to 10 GeV.
- Events are vetoed if containing a jet overlapping with a muon  $\Delta R(\mu, \text{jet}) < 0.5$ .
- In order to specifically select two muons both originating from a single  $Z$  boson decay, the invariant mass of the two muons must satisfy  $|M_{\mu\mu} - m_Z| < 25$ .

The  $\mu\mu + \text{jets}$  sample is able to make predictions in the signal region of the two lowest  $H_T$  bins, providing coverage where the  $\gamma + \text{jets}$  sample is unable to, due to trigger requirements. In higher  $H_T$  bins, the higher statistics of the  $\gamma + \text{jets}$  sample is also used in determining the  $Z \rightarrow \nu\bar{\nu}$  estimation.

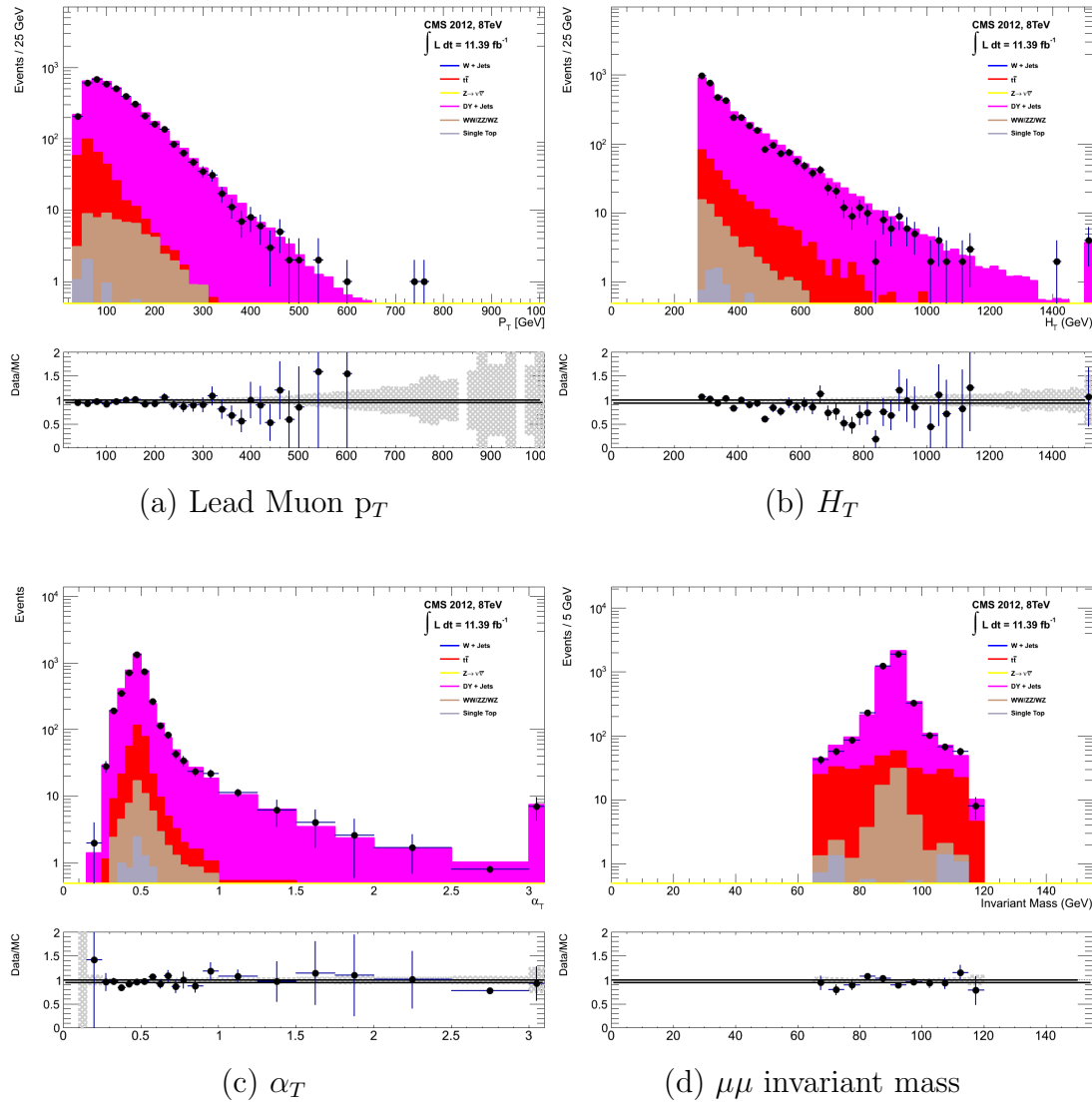


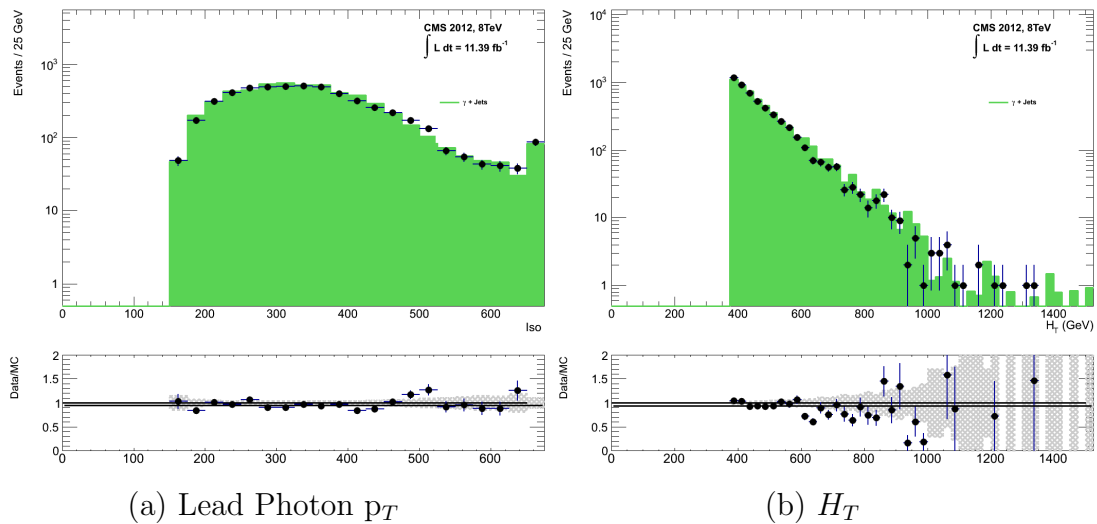
**Figure 4.7.:** Data/MC comparisons of key variables for the  $\mu\mu + \text{jets}$  selection, following the application of selection criteria and the requirements that  $H_T > 275$  GeV. Bands represent the uncertainties due to the statistical size of the MC samples. No requirement is made upon the number of b-tagged jets or jet multiplicity in these distributions.

### The $\gamma + \text{jets}$ control sample

The  $Z \rightarrow \nu\bar{\nu} + \text{jets}$  background is also estimated from a  $\gamma + \text{jets}$  control sample. When the  $E_T$  of the photon is greater than the mass of the  $Z$ , it possesses a larger

cross section and kinematic properties similar to those of  $Z \rightarrow \mu\bar{\mu}$  events where the photon is ignored [79]. The photon is ignored for the purpose of the calculation of event level variables, and identical selection cuts to the hadronic signal region are applied.

- Exactly one photon is selected, satisfying identification criteria as detailed in Table 4.3, with a minimum  $p_T > 165$  GeV to satisfy trigger thresholds and  $|\eta| < 1.45$  to ensure the photon remains in the barrel of the detector.
- A selection criteria of  $\Delta R(\gamma, jet) < 1.0$ , between the photon and all jets is applied to ensure the acceptance of only well isolated  $\gamma + jets$  events.
- Given that the photon is ignored, this control sample can only be applied in the  $H_T$  region  $> 375$  GeV, due to the trigger thresholds on the minimum  $p_T$  of the photon, and the  $H_T$  requirement of an  $\alpha_T > 0.55$  cut from Equation (4.5), which is maintained in this control sample due to contamination from QCD in the absence of an  $\alpha_T$  cut.



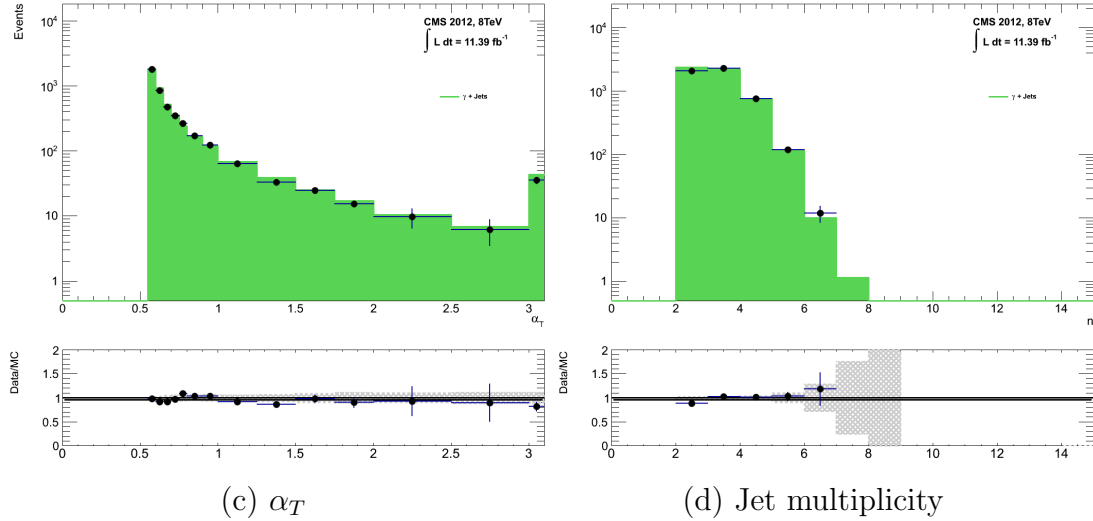


**Figure 4.8.:** Data/MC comparisons of key variables for the  $\gamma + \text{jets}$  selection, following the application of selection criteria and the requirements that  $H_T > 375 \text{ GeV}$  and  $\alpha_T > 0.55$ . Bands represent the uncertainties due to the statistical size of the MC samples. No requirement is made upon the number of b-tagged jets or jet multiplicity in these distributions.

1527 The selection criteria of the three control samples are defined to ensure background  
 1528 composition and event kinematics mirror closely the signal region. This is done in order  
 1529 to minimise the reliance on MC simulation to model correctly the backgrounds and event  
 1530 kinematics in the control and signal samples.

1531 However in the case of the  $\mu + \text{jets}$  and  $\mu\mu + \text{jets}$  samples, the  $\alpha_T$  requirement is relaxed  
 1532 in the selection criteria of these samples. This is made possible as contamination from  
 1533 QCD multi-jet events is suppressed to a negligible level by the other kinematic selection  
 1534 criteria within the two control samples, to select pure EWK processes. Thus in this way,  
 1535 the acceptance of the two muon control samples can be significantly increased, which  
 1536 simultaneously improves their predictive power and further reduces the effect of any  
 1537 potential signal contamination.

1538 The modelling of the  $\alpha_T$  variable is probed through a dedicated set of closure tests,  
 1539 described in Section (4.6), which demonstrate that the different  $\alpha_T$  acceptances for the  
 1540 control and signal samples have no significant systematic bias on the prediction.

---

#### <sup>1542</sup> 4.2.4. Estimating the QCD multi-jet background

<sup>1543</sup> A negligible background from QCD multi-jet events within the hadronic signal region  
<sup>1544</sup> is expected due to the selection requirement, and additional cleaning filters applied.  
<sup>1545</sup> However a conservative approach is still adopted and the likelihood model, see Section  
<sup>1546</sup> (4.8.2), is given the freedom to accommodate any potential QCD multi-jet contamination.

<sup>1547</sup> Any potential contamination can be identified through the variable  $R_{\alpha_T}$ , defined as the  
<sup>1548</sup> ratio of events above and below the  $\alpha_T$  threshold value used in the analysis. This is  
<sup>1549</sup> modelled by a  $H_T$  dependant falling exponential function which takes the form,

$$R_{\alpha_T}(H_T) = A_{\text{QCD}} \exp^{-k_{\text{QCD}} H_T}, \quad (4.10)$$

<sup>1550</sup> where the parameters  $A_{\text{QCD}}$  and  $k_{\text{QCD}}$  are the normalisation and exponential decay  
<sup>1551</sup> constants respectively.

<sup>1552</sup> For QCD event topologies, this exponential behaviour is expected as a function of  $H_T$   
<sup>1553</sup> for several reasons. The improvement of jet energy resolution at higher  $H_T$  due to higher  
<sup>1554</sup>  $p_T$  jets leads to a narrower peaked distribution, causing  $R_{\alpha_T}$  to fall. Similarly at higher  
<sup>1555</sup>  $H_T$  values  $> 375$  GeV, the jet multiplicity rises slowly with  $H_T$ . As shown in Figure 4.3,  
<sup>1556</sup> at higher jet multiplicities, the result of the combinatorics used in the determination of  
<sup>1557</sup>  $\alpha_T$ , then leads to a narrower distribution.

<sup>1558</sup> The value of the decay constant  $k_{\text{QCD}}$  is constrained via measurements within data  
<sup>1559</sup> sidebands to the signal region. This is also done to validate the falling exponential  
<sup>1560</sup> assumption for QCD multi-jet topologies. The sidebands are enriched in QCD multi-jet  
<sup>1561</sup> background and defined as regions where either  $\alpha_T$  is relaxed or that the  $R_{\text{miss}}$  cut is  
<sup>1562</sup> inverted. Figure 4.9 depicts the definition of these data sidebands used to constrain the  
<sup>1563</sup> value of  $k_{\text{QCD}}$ .

1564

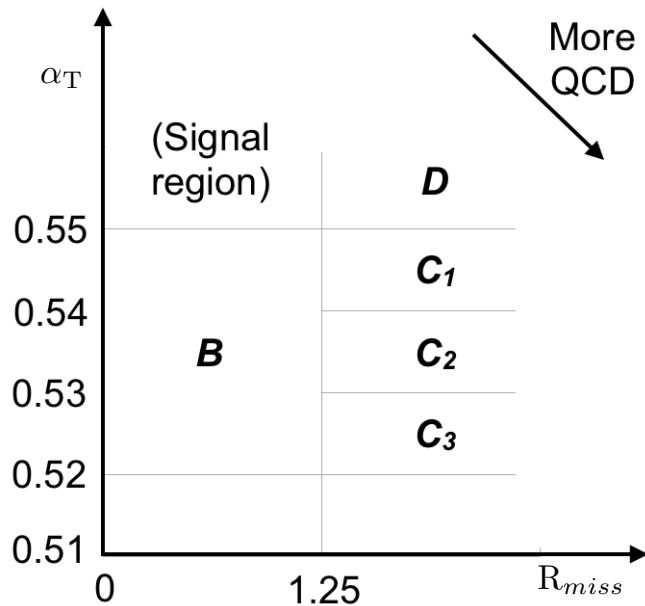


**Figure 4.9.:** QCD sideband regions, used for determination of  $k_{\text{QCD}}$ .

1565 The fits to determine the value of  $k_{\text{QCD}}$  are shown in Appendix (C.1), for which the best  
 1566 fit value obtained from sideband region B is determined to be  $k_{\text{QCD}} = 2.96 \pm 0.64 \times 10^{-2}$   
 1567  $\text{GeV}^{-1}$ .

1568 The best fit values of the remaining three C sideband regions are used to estimate  
 1569 the systematic uncertainty on the central value obtained from sideband region B. The  
 1570 variation of these measured values is used to determine the error on the determined  
 1571 central value, and is calculated to be  $1.31 \pm 0.26 \times 10^{-2} \text{ GeV}^{-1}$ . This relative error of  $\sim$   
 1572 20% gives an estimate of the systematic uncertainty of the measurement to be applied to  
 1573  $k_{\text{QCD}}$ .

1574 Finally the same procedure is performed for sideband region D as an independent cross  
 1575 check, to establish that the value of  $k_{\text{QCD}}$  extracted from a lower  $\alpha_T$  slice, can be applied  
 1576 to the signal region  $\alpha_T > 0.55$ . The likelihood fit is performed across all  $H_T$  bins within  
 1577 the QCD enriched region with no constraint applied to  $k_{\text{QCD}}$ . The resulting best fit  
 1578 value for  $k_{\text{QCD}}$  shows good agreement between that and the weighted mean determined  
 1579 from the three C sideband regions. This demonstrates that the assumption of using the  
 1580 central value determined from sideband region B, to provide an unbiased estimator for  
 1581  $k_{\text{QCD}}$  in the signal region ( $\alpha_T > 0.55$ ) is valid.

1582 Table 4.7, summarises the best fit  $k_{\text{QCD}}$  values determined for each of the sideband  
 1583 regions to the signal region.

Sideband region	$k_{\text{QCD}} (\times 10^{-2} \text{GeV}^{-1})$	$p$ -value
B	$2.96 \pm 0.64$	0.24
C <sub>1</sub>	$1.19 \pm 0.45$	0.93
C <sub>2</sub>	$1.47 \pm 0.37$	0.42
C <sub>3</sub>	$1.17 \pm 0.55$	0.98
C(weighted mean)	$1.31 \pm 0.26$	-
D(likelihood fit)	$1.31 \pm 0.09$	0.57

**Table 4.7.:** Best fit values for the parameters  $k_{\text{QCD}}$  obtained from sideband regions B,C<sub>1</sub>,C<sub>2</sub>,C<sub>3</sub>. The weighted mean is determined from the three measurements made within sideband region C. The maximum likelihood value of  $k_{\text{QCD}}$  given by the simultaneous fit using sideband region D. Quotes errors are statistical only.

### 4.3. Trigger Strategy

A cross trigger based on the  $H_T$  and  $\alpha_T$  values of an event, is used with varying thresholds across  $H_T$  bins to record the events used in the hadronic signal region. The  $\alpha_T$  legs of the HT\_alphaT triggers used in the analysis are chosen to suppress QCD multi-jet events and control trigger rate, whilst maintaining signal acceptance. To further maintain an acceptable rate for these analysis specific triggers, only calorimeter information is used in the reconstruction of the  $H_T$  sum, leading to the necessity for Calo jets to be used within the analysis.

A single object prescaled HT trigger is used to collect events for the hadronic control region described above in Section (4.2.4).

The performance of the  $\alpha_T$  and  $H_T$  triggers used to collect data for the signal and hadronic control region is measured with respect to a reference sample collected using the muon system. This allows measurement of both the Level 1 seed and higher level triggers simultaneously, as the reference sample is collected independent of any jet requirements.

The selection for the trigger efficiency measurement is identical to that described in Section (4.2.2), with the requirement of exactly one well identified muon with  $p_T > 30$  GeV which is subsequently ignored.

The efficiencies measured for the HT\_alphaT triggers in bins of the individual  $H_T$  and  $\alpha_T$  legs, is summarised in Table 4.8.

Data for the control samples of the analysis, detailed in Section (4.2.3), are collected using a single object photon trigger for the  $\gamma + \text{jets}$  sample, and a single object muon trigger for both the  $\mu + \text{jets}$  and  $\mu\mu + \text{jets}$  control samples.

$H_T$ range (GeV)	$\epsilon$ on $H_T$ leg (%)	$\epsilon$ on $\alpha_T$ leg (%)
275-325	$87.7^{+1.9}_{-1.9}$	$82.8^{+1.0}_{-1.1}$
325-375	$90.6^{+2.9}_{-2.9}$	$95.9^{+0.7}_{-0.9}$
375-475	$95.7^{+0.1}_{-0.1}$	$98.5^{+0.5}_{-0.9}$
475- $\infty$	$100.0^{+0.0}_{-0.0}$	$100.0^{+0.0}_{-4.8}$

**Table 4.8.:** Measured efficiencies of the  $H_T$  and  $\alpha_T$  legs of the HT and HT\_alphaT triggers in independent analysis bins. The product of the two legs gives the total efficiency of the trigger in a given offline  $H_T$  bin.

1606 The photon trigger is measured to be fully efficient for the threshold  $p_T^{\text{photon}} > 150$  GeV,  
 1607 whilst the single muon efficiency satisfying  $p_T^{\mu\text{on}} > 30$  GeV is measured to have an  
 1608 efficiency of  $(88 \pm 2)\%$  that is independent of  $H_T$ . In the case of the  $\mu\mu + \text{jets}$  control  
 1609 sample, the efficiency is measured to be  $(95 \pm 2)\%$  for the lowest  $H_T$  bin, rising (due to  
 1610 the average  $p_T$  of the second muon in the event increasing at larger  $H_T$ ) to  $(98 \pm 2)\%$  for  
 1611 the highest  $H_T$  bin.

## 1612 4.4. Measuring MC Normalisation Factors via $H_T$ 1613 Sidebands

1614 The theoretical cross sections of different SM processes at Next to Next Leading Order  
 1615 (NNLO) and the number of MC simulated events generated for that particular process,  
 1616 is typically used to determine the appropriate normalisation for a MC sample. However  
 1617 within the particular high- $H_T$  and high- $\cancel{E}_T$  corners of kinematic phase space probed  
 1618 within this search, the theoretical cross sections for various processes are far less well  
 1619 understood.

1620 To mitigate the problem of theoretical uncertainties and arbitrary choices of cross sections,  
 1621 the normalisation of the simulation samples used in the analysis are determined through  
 1622 the use of data sidebands. The sidebands are used to calculate sample specific correction  
 1623 factors (k-factors), that are appropriate for the  $H_T$ - $\cancel{E}_T$  phase space covered by this  
 1624 analysis.

1625 They are defined within the  $\mu + \text{jets}$  and  $\mu\mu + \text{jets}$  control sample, by the region  $200 <$   
 1626  $H_T < 275$ , using the same jet  $p_T$  thresholds as the adjacent first analysis bin. Individual  
 1627 EWK processes are isolated within each of these control samples via requirements on  
 1628 jet multiplicity and the requirement on b-tags, summarised in Table 4.9. The purity of

1629 the samples are typically  $> 90\%$  with any residual contamination corrected for. The  
1630 resultant k-factor for each process is determined by then taking ratio of the data yield  
1631 over the MC expectation in the sideband. Subsequently these k-factors are then applied  
1632 to the processes within the phase space of the analysis.

Process	Selection	Observation	MC expectation	k-factor
W + jets	$\mu + \text{jets}, n_b=0, n_{jet} = 2,3$	26950	$29993.2 \pm 650.1$	$0.90 \pm 0.02$
$Z \rightarrow \mu\mu + \text{jets}$	$\mu\mu + \text{jets}, n_b=0, n_{jet} = 2,3$	3141	$3402.0 \pm 43.9$	$0.92 \pm 0.02$
$t\bar{t}$	$\mu + \text{jets}, n_b=2, n_{jet} = \geq 4$	2190	$1967.8 \pm 25.1$	$1.11 \pm 0.02$

**Table 4.9.:** k-factors calculated for different **EWK** processes. All k-factors are derived relative to theoretical cross sections calculated in **NNLO**. The k-factors measured for the  $Z \rightarrow \mu\mu + \text{jets}$  processes, are also applied to the  $Z \rightarrow \nu\bar{\nu} + \text{jets}$  and  $\gamma + \text{jets}$  MC samples.

1633 It is worth pointing out that these correction factors have a negligible effect when  
1634 providing a background estimation for the signal region. The **TF**'s used in the analysis  
1635 are found to be unaffected by application of these k-factors due to the similarity in the  
1636 background composition of the control and signal regions. However when systematic  
1637 uncertainties are determined in Section (4.6), the closure tests performed are sensitive  
1638 to these corrections when extrapolations between different  $n_b^{\text{reco}}$  and  $n_{jet}$  categories are  
1639 performed.

## 1640 4.5. Determining MC Simulation Yields with 1641 Higher Statistical Precision

1642 Reconstructing events from **EWK** processes with many b-tagged jets ( $\geq 3$ ),  $n_b^{\text{reco}}$ , is largely  
1643 driven by the mis-tagging of light jets within the event. This is clear when considering  
1644 the main **EWK** backgrounds in the analysis, such as  $t\bar{t} + \text{jets}$  events, which typically  
1645 contain two b-flavoured jets from the decay of the top quarks, whilst W + jets and  
1646  $Z \rightarrow \mu\mu + \text{jets}$  events will typically contain no b-flavoured jets.

1647 When the expectation for the number of  $n_b^{\text{reco}}$  is taken directly from simulation, the  
1648 statistical uncertainty at large b-tag multiplicities becomes relatively large. In order to  
1649 reduce this uncertainty one approach is to use the information encoded throughout all  
1650 events in the simulation sample, to measure each of the four ingredients:

- 1651 1. the b-tagging efficiency in the event selection,

<sub>1652</sub> 2. the charm-tagging efficiency in the event selection  
<sub>1653</sub> 3. the mis-tagging rate in the event selection,  
<sub>1654</sub> 4. the underlying flavour distribution of the jets in the events,  
<sub>1655</sub> that determine the  $n_b^{\text{reco}}$  distribution of the process being measured. This method allows  
<sub>1656</sub> the determination of higher b-tag multiplicities to a higher degree of accuracy reducing  
<sub>1657</sub> the statistical uncertainties of the MC which enter into the TF's. For the discussion that  
<sub>1658</sub> follows, these predictions are determined on average (i.e not on an event-by-event basis),  
<sub>1659</sub> and is known as the formula method.

#### <sub>1660</sub> 4.5.1. The formula method

<sub>1661</sub> The assigning of jet flavours to reconstruction level jets in simulation is achieved via an  
<sub>1662</sub> algorithmic method defined as:

- <sub>1663</sub> • Try to find the parton that most likely determines the properties of the jet and  
<sub>1664</sub> assign that flavour as true flavour,
- <sub>1665</sub> • “final state” partons (after showering, radiation) are analysed (also within  $\Delta R <$   
<sub>1666</sub> 0.3 of reconstructed jet cone),
- <sub>1667</sub> • If there is a b/c flavoured parton within the jet cone: label as b/c flavoured jet,
- <sub>1668</sub> • Otherwise: assign flavour of the hardest parton.

<sub>1669</sub> This process is employed within each individual MC process and independently for each  
<sub>1670</sub>  $H_T$ -  $n_{\text{jet}}$  bin in the analysis. The  $n_b^{\text{reco}}$  distribution is then constructed in the following  
<sub>1671</sub> way:

<sub>1672</sub> Let  $N(n_b^{\text{gen}}, n_c^{\text{gen}}, n_q^{\text{gen}})$  represent the yield in simulation, of events with  $b$  underlying  
<sub>1673</sub> b-quarks,  $c$  underlying c-quarks and  $q$  underlying light quarks which are matched to  
<sub>1674</sub> reconstructed jets as detailed above. Light quarks defined as those which originate from  
<sub>1675</sub> a  $u$ ,  $d$ ,  $s$ ,  $g$  and  $\tau$  jets, which having similar mis-tagging rates are grouped together.  
<sub>1676</sub> Similarly  $\epsilon$ ,  $\beta$  and  $m$  represent the measured b-tagging, c-tagging and mis-tagging  
<sub>1677</sub> efficiency averaged over all the jets within that particular analysis bin.

<sub>1678</sub> Using this information the expected  $n_b^{\text{reco}}$  distribution can be analytically calculated  
<sub>1679</sub> using the formula :

$$N(n) = \sum_{n_b^{gen} + n_c^{gen} + n_q^{gen} = n_{jet}^{cat}} \sum_{n_b^{tag} + n_c^{tag} + n_q^{tag} = n} N(n_b^{gen}, n_c^{gen}, n_q^{gen}) \times P(n_b^{tag}, n_b^{gen}, \epsilon) \times \\ P(n_c^{tag}, n_c^{gen}, \beta) \times P(n_q^{tag}, n_q^{gen}, m), \quad (4.11)$$

1680 with  $N(n)$  representing the number of  $n$  b-tagged jets in a particular analysis bin as  
1681 determined by the formula method.

1682 The variables  $n_{b/c/q}^{tag}$  signify the number of times that a particular jet flavour results in a  
1683 b-tagged jet, of which the sum of the three terms must equal the number of  $n$  b-tagged  
1684 jets being estimated. Similarly  $n_{b/c/q}^{gen}$  represent the flavour admixture of the jets, which  
1685 having been identified using the above technique as b, c or light flavoured jets, are  
1686 required by definition that the sum of the three to fall within the  $n_{jet}$  category being  
1687 analysed.

1688 Finally  $P(n_b^{tag}, n_b^{gen}, \epsilon)$ ,  $P(n_c^{tag}, n_c^{gen}, \beta)$  and  $P(n_q^{tag}, n_q^{gen}, m)$  correspond to the binomial  
1689 probabilities for that particular jet flavour and tagging configuration to occur based  
1690 on the measured tagging efficiencies ( $\epsilon$ ,  $\beta$  and  $m$ ) for each jet flavour. This formula  
1691 is enacted over all five of the analysis b-tag categories to build up the resultant  $n_b^{reco}$   
1692 distribution for each process in turn.

1693 This approach ultimately results in a more precise  $n_b^{reco}$  distribution prediction, due to  
1694 the utilisation of the entire MC sample in extracting the estimated underlying  $n_b^{reco}$   
1695 distribution, particularly at higher  $n_b^{reco}$  multiplicities where a lack of events in simulation  
1696 can lead to relatively large statistical uncertainties.

### 1697 4.5.2. Establishing proof of principle

1698 In order to validate the procedure, the predictions determined from the formula method  
1699 summarised in Equation (4.11), are compared directly with those obtained directly from  
1700 simulation. Resultantly no simulation to data correction factors are applied when making  
1701 this comparison

1702 This sanity check for the  $\mu +$  jets control sample is presented in Table 4.10, for all  $n_b^{reco}$   
1703 and  $H_T$  bins with no requirement placed upon the jet multiplicity of the events.

$H_T$ Bin (GeV)	275–325	325–375	375–475	475–575
Formula $n_b = 0$	12632.66 $\pm$ 195.48	6696.08 $\pm$ 82.59	6368.96 $\pm$ 75.34	2906.27 $\pm$ 39.65
Vanilla $n_b = 0$	12612.95 $\pm$ 198.68	6687.97 $\pm$ 83.78	6359.27 $\pm$ 76.50	2898.27 $\pm$ 36.89
Formula $n_b = 1$	4068.09 $\pm$ 45.71	2272.76 $\pm$ 26.14	2181.32 $\pm$ 25.07	1089.14 $\pm$ 13.82
Vanilla $n_b = 1$	4067.73 $\pm$ 60.30	2268.02 $\pm$ 30.20	2180.69 $\pm$ 28.73	1094.37 $\pm$ 24.14
Formula $n_b = 2$	1963.71 $\pm$ 22.44	1087.55 $\pm$ 13.57	1055.57 $\pm$ 13.25	554.96 $\pm$ 7.95
Vanilla $n_b = 2$	1984.53 $\pm$ 26.19	1094.43 $\pm$ 16.67	1068.96 $\pm$ 16.36	558.14 $\pm$ 10.51
Formula $n_b = 3$	146.94 $\pm$ 2.07	79.97 $\pm$ 1.37	78.05 $\pm$ 1.35	49.84 $\pm$ 1.03
Vanilla $n_b = 3$	149.52 $\pm$ 4.84	85.98 $\pm$ 3.64	74.45 $\pm$ 3.29	49.54 $\pm$ 2.68
Formula $n_b \geq 4$	2.26 $\pm$ 0.12	1.29 $\pm$ 0.10	5.32 $\pm$ 0.20	-
Vanilla $n_b \geq 4$	1.84 $\pm$ 0.50	1.02 $\pm$ 0.39	4.86 $\pm$ 0.83	-
$H_T$ Bin (GeV)	575–675	675–775	775–875	>875
Formula $n_b = 0$	1315.68 $\pm$ 19.49	640.49 $\pm$ 11.90	327.81 $\pm$ 7.91	424.27 $\pm$ 9.27
Vanilla $n_b = 0$	1315.23 $\pm$ 20.20	641.96 $\pm$ 12.48	329.09 $\pm$ 8.36	424.02 $\pm$ 9.73
Formula $n_b = 1$	490.41 $\pm$ 7.45	226.95 $\pm$ 4.42	109.91 $\pm$ 2.84	129.97 $\pm$ 3.07
Vanilla $n_b = 1$	490.52 $\pm$ 9.92	222.22 $\pm$ 6.21	107.46 $\pm$ 4.15	129.64 $\pm$ 4.64
Formula $n_b = 2$	256.75 $\pm$ 4.58	113.45 $\pm$ 2.70	52.10 $\pm$ 1.69	59.29 $\pm$ 1.78
Vanilla $n_b = 2$	253.43 $\pm$ 6.52	117.17 $\pm$ 4.27	52.70 $\pm$ 2.80	59.45 $\pm$ 3.00
Formula $n_b = 3$	25.66 $\pm$ 0.69	12.48 $\pm$ 0.46	5.52 $\pm$ 0.31	6.83 $\pm$ 0.33
Vanilla $n_b = 3$	29.18 $\pm$ 2.06	11.77 $\pm$ 1.26	6.18 $\pm$ 0.95	7.53 $\pm$ 1.05

**Table 4.10.:** Comparing yields in simulation within the  $\mu +$  jets selection determined from the formula method described in Equation (4.11), and that taken directly from simulation . The numbers are normalised to  $11.4\text{fb}^{-1}$ . No simulation to data corrections are applied.

1704 It can be seen as expected, that there is good consistency between the results determined  
 1705 via the formula method and ‘raw’ simulation yields. Similarly the power of this approach  
 1706 can be seen in the reduction of this statistical error in the prediction across all  $H_T$  and  
 1707  $n_b^{reco}$  bins. In particular the statistical uncertainty is reduced by several factors in the  
 1708 highest  $n_b^{reco} \geq 4$  category.

#### 1709 4.5.3. Correcting measured efficiencies in simulation to data

1710 As detailed in Section (3.3.2), it is necessary for certain  $p_T$  and  $\eta$  dependant corrections,  
 1711 to be applied to both the b-tagging efficiency and mis-tagging rates in order correct the  
 1712 efficiencies from simulation to the distributions seen in data. These corrections factors

1713 are considered when determining the simulation yields for each selection, which are used  
1714 to construct the TF's of the analysis.

1715 Each of the corrections factors for the b, c and light flavoured jets come with an  
1716 associated systematic uncertainty. The uncertainties across different jet  $p_T$  and  $\eta$  bins,  
1717 are considered as fully correlated. When computing the magnitude of the effect of this  
1718 systematic uncertainty on the TF's of the analysis, the scale factors are therefore scaled  
1719 up/down simultaneously within each  $H_T$  bin of the analysis for all of the  $SF_{b,c,\text{light}}$  scale  
1720 factors. The magnitude of this correction is shown for each  $H_T$  bin within Figure 4.10.

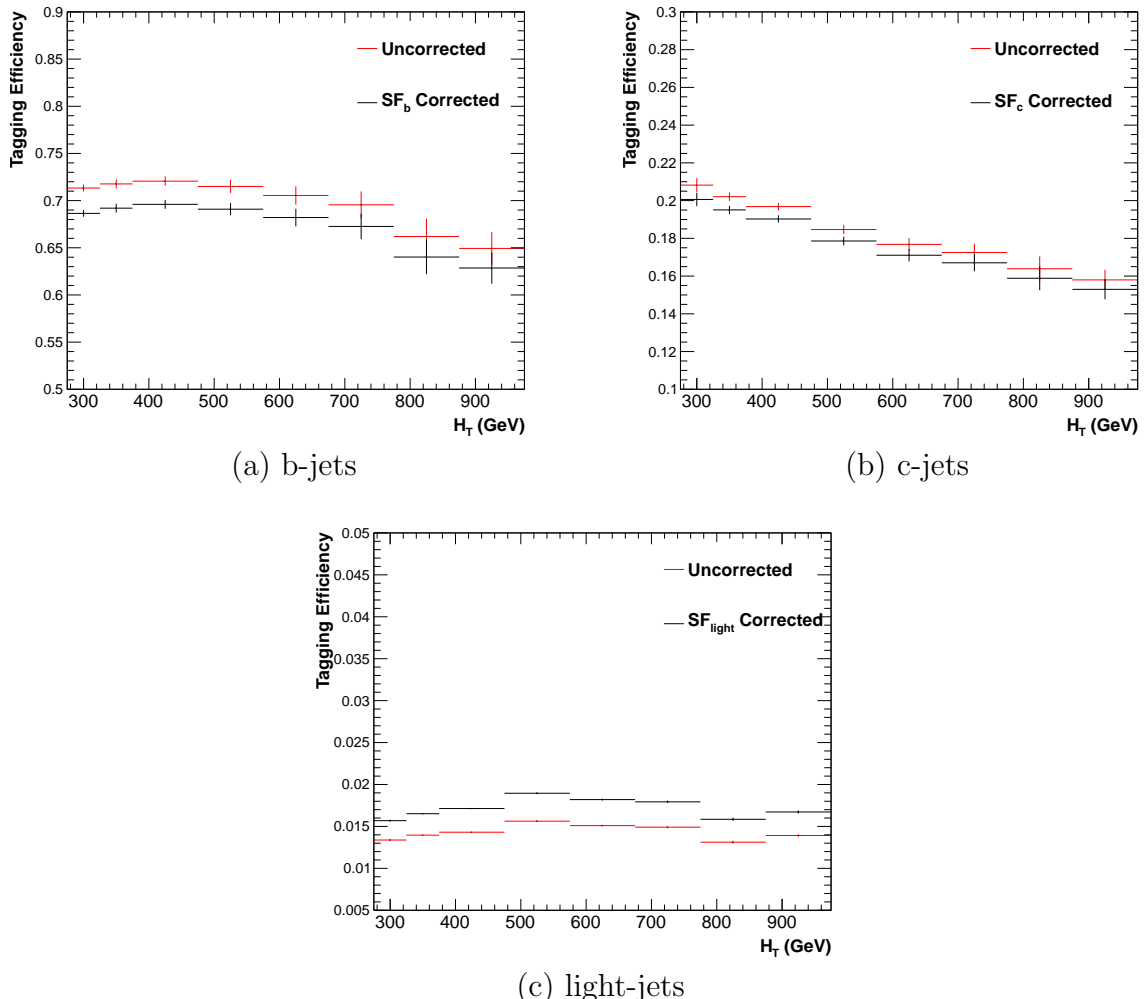


**Figure 4.10.:** Tagging efficiencies of (a) b-jets, (b) c-jets, and (c) light-jets as a function all jets within each individual analysis  $H_T$  bin. Efficiencies measured directly from simulation (black) and with data to simulation  $SF_{b,c,\text{light}}$  correction factors (red) are applied.

1721 Varying the scale factor corrections by their systematic uncertainty will change the  
1722 absolute yields within each  $n_b^{reco}$  bin of all selections. However, ultimately it is the change  
1723 in the **TF**'s which influences the final background prediction from each of the control  
1724 samples. The magnitude of the absolute change in each **TF**, constructed from when the  
1725  $\mu + \text{jets}$  control sample is used to predict the entire hadronic signal region background,  
1726 is shown in Table 4.11.,

$n_b^{reco}$	275–325	325–375	375–475	475–575
= 0	$0.557^{+0.001}_{-0.001} \pm 0.012$	$0.495^{+0.001}_{-0.001} \pm 0.009$	$0.383^{+0.001}_{-0.001} \pm 0.005$	$0.307^{+0.001}_{-0.002} \pm 0.006$
= 1	$0.374^{+0.006}_{-0.006} \pm 0.006$	$0.320^{+0.006}_{-0.005} \pm 0.005$	$0.251^{+0.005}_{-0.005} \pm 0.004$	$0.185^{+0.003}_{-0.003} \pm 0.004$
= 2	$0.226^{+0.002}_{-0.002} \pm 0.004$	$0.201^{+0.001}_{-0.002} \pm 0.004$	$0.159^{+0.001}_{-0.001} \pm 0.004$	$0.134^{+0.000}_{-0.001} \pm 0.004$
= 3	$0.221^{+0.002}_{-0.002} \pm 0.005$	$0.208^{+0.002}_{-0.001} \pm 0.007$	$0.164^{+0.001}_{-0.000} \pm 0.006$	$0.144^{+0.001}_{-0.001} \pm 0.007$
$\geq 4$	$0.222^{+0.004}_{-0.005} \pm 0.015$	$0.248^{+0.003}_{-0.003} \pm 0.035$	$0.123^{+0.002}_{-0.003} \pm 0.009$	-
	575–675	675–775	775–875	$\geq 875$
= 0	$0.263^{+0.001}_{-0.002} \pm 0.006$	$0.215^{+0.000}_{-0.001} \pm 0.007$	$0.171^{+0.000}_{-0.001} \pm 0.009$	$0.111^{+0.000}_{-0.001} \pm 0.006$
= 1	$0.154^{+0.003}_{-0.003} \pm 0.005$	$0.138^{+0.003}_{-0.004} \pm 0.006$	$0.121^{+0.005}_{-0.005} \pm 0.007$	$0.091^{+0.002}_{-0.002} \pm 0.006$
= 2	$0.104^{+0.000}_{-0.001} \pm 0.005$	$0.079^{+0.001}_{-0.001} \pm 0.006$	$0.063^{+0.001}_{-0.002} \pm 0.007$	$0.071^{+0.000}_{-0.000} \pm 0.008$
= 3	$0.116^{+0.001}_{-0.001} \pm 0.009$	$0.069^{+0.001}_{-0.001} \pm 0.007$	$0.079^{+0.001}_{-0.001} \pm 0.017$	$0.095^{+0.003}_{-0.002} \pm 0.020$

**Table 4.11.:** The absolute change in the **TF**'s used to predict the entire signal region **SM** background, using the  $\mu + \text{jets}$  control sample when the systematic uncertainties of the data to simulation scale factors are varied by  $\pm 1\sigma$ . The impact of the change is shown for each  $H_T$  and  $n_b^{reco}$  bin with no requirement made on the jet multiplicity of the events. (Also quoted are the statistical uncertainties)

1727 It can be seen that the **TF**'s are found to be relatively insensitive to the systematic  
1728 uncertainty of the b-tag scale factors (showing typically less than  $\sim 2\%$  change). This can  
1729 be accounted for by the similar composition of the signal and control sample backgrounds,  
1730 such that any change in the underlying  $n_b^{reco}$  distribution will be reflected in both signal  
1731 and control regions and cancel out in the **TF**.

1732 Any overall systematic effect on the overall background prediction of the analysis from  
1733 these b-tag scale factor uncertainties is incorporated within the data driven systematics  
1734 introduced in the following section.

## 1735 4.6. Systematic Uncertainties on Transfer Factors

- 1736 Since the TFs used to establish the background prediction are obtained from simulation,  
1737 an appropriate systematic uncertainty is assigned to each factor to account for theoretical  
1738 uncertainties [80] and limitations in the simulation modelling of event kinematics and  
1739 instrumental effects.
- 1740 The magnitudes of these systematic uncertainties are established through a set of data  
1741 driven method, in which the three independent control samples of the analysis ( $\mu + \text{jets}$ ,  
1742  $\mu\mu + \text{jets}$ ,  $\gamma + \text{jets}$ ) are used to in a series of closure tests. The yields from one of these  
1743 control samples, along with the corresponding TF obtained from simulation, are used to  
1744 predict the yields in another control sample, using the same method of establishing a  
1745 background prediction for the signal region as described in Section (4.2.3).
- 1746 The level of agreement between the predicted and observed yields is expressed as the  
1747 ratio

$$\frac{(N_{\text{obs}} - N_{\text{pred}})}{N_{\text{pred}}}, \quad (4.12)$$

1748 while considering only the statistical uncertainties on  $N_{\text{pred}}$ , the prediction, and  $N_{\text{obs}}$ , the  
1749 observation. No systematic uncertainty is assigned to the prediction, and resultantly the  
1750 level of closure is defined by the statistical significance of a deviation from the ratio from  
1751 zero.

1752 This ratio is measured for each  $H_T$  bin in the analysis, allowing these closure tests to be  
1753 sensitive to both the presence of any significant biases or any possible  $H_T$  dependence on  
1754 the level of closure.

1755 Eight sets of closure tests are defined between the three data control samples, conducted  
1756 independently between the two jet multiplicity ( $2 \leq n_{\text{jet}} \leq 3$ ,  $n_{\text{jet}} \geq 4$ ) bins. Each of  
1757 these tests are specifically chosen to probe each of the different key ingredients of the  
1758 simulation modelling that can affect the background prediction.

1759 Each of the different modelling components and the relevant closure tests are described  
1760 below :

1761  $\alpha_T$  modelling

1762 The modelling of the  $\alpha_T$  distribution in genuine  $E_T$  events is probed with the  $\mu$   
1763 + jets control sample. This test is important to verify the approach of removing  
1764 the  $\alpha_T > 0.55$  requirement from the  $\mu +$  jets and  $\mu\mu +$  jets samples to increase  
1765 the precision of the background prediction. The test uses the  $\mu +$  jets sample  
1766 without an  $\alpha_T$  cut to make a prediction into the  $\mu +$  jets sample defined with the  
1767 requirement  $\alpha_T > 0.55$ .

### 1768 **Background admixture**

1769 The sensitivity of the translation factors to the relative admixture of events from  
1770  $W +$  jets and  $t\bar{t}$  processes is probed by two closure tests. These tests represent  
1771 an extremely conservative approach as the admixture of the background remains  
1772 similar between the  $\mu +$  jets sample and the signal region, contrary to the defined  
1773 closure tests which make predictions between two very different admixtures of  $W +$   
1774 jets and  $t\bar{t}$  events.

1775 Within the  $\mu +$  jets sample, a  $W$  boson enriched sub-sample ( $n_b = 0$ ) is used  
1776 to predict yields in a  $t\bar{t}$  enriched sub-sample ( $n_b = 1$ ). Similarly the  $t\bar{t}$  enriched  
1777 sub-sample ( $n_b = 1$ ) is also used to predict yields for a further enriched  $t\bar{t}$  sub-sample  
1778 ( $n_b = 2$ ), further probing the modelling of the  $n_b^{\text{reco}}$  distribution.

1779 Similarly a further closure test probes the relative contribution of  $Z +$  jets to  $W +$  jets  
1780 and  $t\bar{t}$  events, through the use of the  $\mu +$  jets sample to predict yields for the  $\mu\mu +$   
1781 jets control sample. This closure test, also at some level probes the muon trigger  
1782 and reconstruction efficiencies, given that exactly one or two muons are required by  
1783 the different selections.

### 1784 **Consistency check between $Z \rightarrow \nu\bar{\nu}$ predictions**

1785 An important consistency check between the  $\mu\mu +$  jets and  $\gamma +$  jets, which are both  
1786 used in the prediction of the  $Z \rightarrow \nu\bar{\nu}$  in the signal region. This is conducted by  
1787 using the  $\gamma +$  jets sample to predict yields for the  $\mu\mu +$  jets control sample. Using  
1788  $\gamma +$  jets processes as a method to predict  $Z +$  jet processes is subject to theory  
1789 uncertainties [81], which can be probed by this data driven closure test within a  
1790  $Z \rightarrow \mu\mu$  control sample.

### 1791 **Modelling of jet multiplicity**

1792 The simulation modelling of the jet multiplicity within each control sample is  
1793 important due to the exclusive jet multiplicity binning within the analysis. This is

1794 probed via the use of each of the three control samples to independently predict from  
1795 the lower jet multiplicity category  $2 \leq n_{\text{jet}} \leq 3$ , to the high jet category  $n_{\text{jet}} \geq 4$ .

1796 For the case of the  $\mu + \text{jets}$  and  $\mu\mu + \text{jets}$  control samples, this test also serves as a  
1797 further probe of the admixture between  $W + \text{jets}/Z + \text{jets}$  and  $t\bar{t}$ .

1798 To test for the assumption that no  $H_T$  dependencies exist within the background predic-  
1799 tions of the analysis, the first five closure tests defined above are used, with zeroeth and  
1800 first order polynomial fits are applied to each test individually. This is summarised in  
1801 Table 4.12 and Table 4.13 which show the results for both the  $2 \leq n_{\text{jet}} \leq 3$  and  $\geq 4$  jet  
1802 multiplicity bins respectively.

Closure test	Symbol	Constant fit		Linear fit	
		Best fit value	p-value	Slope ( $10^{-4}$ )	p-value
$\alpha_T < 0.55 \rightarrow \alpha_T > 0.55 (\mu + \text{jets})$	Circle	$-0.06 \pm 0.02$	0.93	$-1.3 \pm 2.2$	0.91
$0 \text{ b-jets} \rightarrow 1 \text{ b-jet } (\mu + \text{jets})$	Square	$0.07 \pm 0.02$	0.98	$-1.6 \pm 1.6$	1.00
$1 \text{ b-jets} \rightarrow 2 \text{ b-jet } (\mu + \text{jets})$	Triangle	$-0.07 \pm 0.03$	0.76	$-2.7 \pm 3.0$	0.76
$\mu + \text{jets} \rightarrow \mu\mu + \text{jets}$	Cross	$0.10 \pm 0.03$	0.58	$-1.1 \pm 2.3$	0.49
$\mu\mu + \text{jets} \rightarrow \gamma + \text{jets}$	Star	$-0.06 \pm 0.04$	0.31	$4.2 \pm 4.3$	0.29

**Table 4.12.:** A summary of the results obtained from zeroeth order polynomial (i.e. a constant) and linear fits to five sets of closure tests performed in the  $2 \geq n_{\text{jet}} \geq 3$  category. The two columns show the best fit value for the slope obtained when performing a constant (left) and linear (right) fit and the p-value for that fit.

Closure test	Symbol	Constant fit		Linear fit	
		Best fit value	p-value	Slope ( $10^{-4}$ )	p-value
$\alpha_T < 0.55 \rightarrow \alpha_T > 0.55 (\mu + \text{jets})$	Circle	$-0.05 \pm 0.03$	0.21	$3.0 \pm 2.9$	0.21
$0 \text{ b-jets} \rightarrow 1 \text{ b-jet } (\mu + \text{jets})$	Square	$-0.03 \pm 0.03$	0.55	$-1.0 \pm 1.9$	0.47
$1 \text{ b-jets} \rightarrow 2 \text{ b-jet } (\mu + \text{jets})$	Triangle	$-0.02 \pm 0.03$	0.39	$1.1 \pm 2.2$	0.31
$\mu + \text{jets} \rightarrow \mu\mu + \text{jets}$	Cross	$0.08 \pm 0.07$	0.08	$4.8 \pm 4.3$	0.07
$\mu\mu + \text{jets} \rightarrow \gamma + \text{jets}$	Star	$-0.03 \pm 0.10$	0.72	$-4.0 \pm 7.0$	0.64

**Table 4.13.:** A summary of the results obtained from zeroeth order polynomial (i.e. a constant) and linear fits to five sets of closure tests performed in the  $n_{\text{jet}} \geq 4$  category. The two columns show the best fit value for the slope obtained when performing a constant (left) and linear (right) fit and the p-value for that fit.

1803 Table 4.14 shows the same fits applied to the three closure tests that probe the modelling  
1804 between the different  $n_{\text{jet}}$  bins. The best fit value and its uncertainty is listed for each  
1805 set of closure tests in all three tables, along with the p-value of the constant and linear  
1806 fits applied.

1807 The best fit value for the constant parameter is indicative of the level of closure, averaged  
1808 across the full range of  $H_T$  bins in the analysis, and the p-value an indicator of any

Closure test	Symbol	Constant fit		Linear fit	
		Best fit value	p-value	Slope ( $10^{-4}$ )	p-value
$\mu + \text{jets}$	Inverted triangle	$-0.03 \pm 0.02$	0.02	$0.0 \pm 1.0$	0.01
$\mu + \text{jets}$ (outlier removed)	Inverted triangle	$-0.04 \pm 0.01$	0.42	$-1.4 \pm 1.1$	0.49
$\gamma + \text{jets}$	Diamond	$0.12 \pm 0.05$	0.79	$6.0 \pm 4.7$	0.94
$\mu\mu + \text{jets}$	Asterisk	$-0.04 \pm 0.07$	0.20	$4.9 \pm 4.4$	0.20

**Table 4.14.:** A summary of the results obtained from zeroeth order polynomial (i.e. a constant) and linear fits to three sets of closure tests performed between the  $2 \leq n_{\text{jet}} \leq 3$  and  $n_{\text{jet}} \geq 4$  categories. The two columns show the best fit value for the slope obtained when performing a constant (left) and linear (right) fit and the p-value for that fit.

1809 significant dependence on  $H_T$  within the closure tests. The best fit values of all the tests  
 1810 are either statistically compatible with zero bias (i.e, less than  $2\sigma$  from zero) or at the  
 1811 level of 10% or less, with the exception of one closure test discussed below.

1812 Within Table 4.14, there exists one test that does not satisfy the above statement, which  
 1813 is the  $2 \leq n_{\text{jet}} \leq 3 \rightarrow n_{\text{jet}} \geq 4$  test using the  $\mu + \text{jets}$  control sample. The low p-value  
 1814 can be largely attributed to an outlier in the  $675 < H_T < 775$  GeV bin, rather than any  
 1815 significant trend in  $H_T$ . Removing this single outlier from the constant fit performed,  
 1816 gives a best fit value of  $-0.04 \pm 0.01$ ,  $\chi^2/\text{d.o.f} = 6.07/6$ . and a p-value of 0.42. These  
 1817 modified fit results are included within Table 4.14 .

1818 In addition the best fit values for the slope terms of the linear fits in all three tables are  
 1819 of the order  $10^{-4}$ , which corresponds to a percent level change per 100 GeV. However in  
 1820 all cases, the best fit values are fully compatible with zero (within  $1\sigma$ ) once again with  
 1821 the exception detailed above, indicating that the level of closure is  $H_T$  independent.

#### 1822 4.6.1. Determining systematic uncertainties from closure tests

1823 Once it has been established that no significant bias or trend exists within the closure  
 1824 tests, systematic uncertainties are determined. The statistical precision of the closure  
 1825 tests is considered a suitable benchmark for determining the systematic uncertainties  
 1826 that are assigned to the TFs, which are propagated through to the likelihood fit.

1827 The systematic uncertainty band is split into five separate regions of  $H_T$ . Within each  
 1828 region the square root of the sample variance,  $\sigma^2$ , is taken over the eight closure tests to  
 1829 determine the systematic uncertainties to be applied within that region.

1830 Using this procedure the systematic uncertainties for each region are calculated and are  
1831 shown in Table 4.15, with the systematic uncertainty to be used in the likelihood model  
1832 conservatively rounded up to the nearest decile and applied across all  $n_b^{\text{reco}}$  categories.

$H_T$ band (GeV)	$2 \leq n_{\text{jet}} \leq 3$	$n_{\text{jet}} \geq 4$
$275 < H_T < 325$	10%	10%
$325 < H_T < 375$	10%	10%
$375 < H_T < 575$	10%	10%
$575 < H_T < 775$	20%	20%
$H_T > 775$	20%	30%

**Table 4.15.:** Calculated systematic uncertainties for the five  $H_T$  regions, determined from the closure tests. Uncertainties shown for both jet multiplicity categories. Values used within the likelihood model are conservatively rounded up to the nearest decile.

1833 Figure 4.11 shows the sets of closure tests overlaid on top of grey bands that represent  
1834 the  $H_T$  dependent systematic uncertainties. These systematic uncertainties are assumed  
1835 to be fully uncorrelated between the different  $n_b$  multiplicity categories and across the  
1836 five  $H_T$  regions. This can be considered a more conservative approach given that some  
1837 correlations between adjacent  $H_T$  bins could be expected due to comparable kinematics.  
  
1838 These closure tests represent a conservative estimate of the systematic uncertainty in  
1839 making a background prediction for the signal region, which is due to significant differences  
1840 in the background composition and event kinematics between the two sub-samples used  
1841 in the closure tests. This is contrary to the signal region prediction where the two  
1842 sub-samples both have a comparable background admixture and similar kinematics owing  
1843 to the fact that the predictions are always made using the same ( $n_{\text{jet}}$ ,  $n_b^{\text{reco}}$ ,  $H_T$ ) bin.  
  
1844 This point is emphasised when we examine the sensitivity of the TFs to a change in the  
1845 admixture of  $W + \text{jets}$  and  $t\bar{t}$  with the control and signal samples. This is accomplished  
1846 by varying the cross sections of the  $W + \text{jets}$  and  $t\bar{t}$  by +20% and -20%, respectively.  
1847 Figures C.2 and C.3 within Appendix C, show the effect upon the closure tests for both  
1848 jet multiplicity categories. Given these variations in cross sections, the level of closure is  
1849 found to be significantly worse, with biases as large as  $\sim 30\%$ , most apparent in the  
1850 lowest  $H_T$  bins. However the TFs used to extrapolate from control to signal are seen to  
1851 change only at the percent level by this large change in cross section, shown in Table C.1.  
  
1852 Given the robust behaviour of the translation factors with respect to large (and opposite)  
1853 variations in the  $W + \text{jets}$  and  $t\bar{t}$  cross sections, one can assume with confidence that  
1854 any bias in the translation factors is adequately (and conservatively) covered by the  
1855 systematic uncertainties used in the analysis.

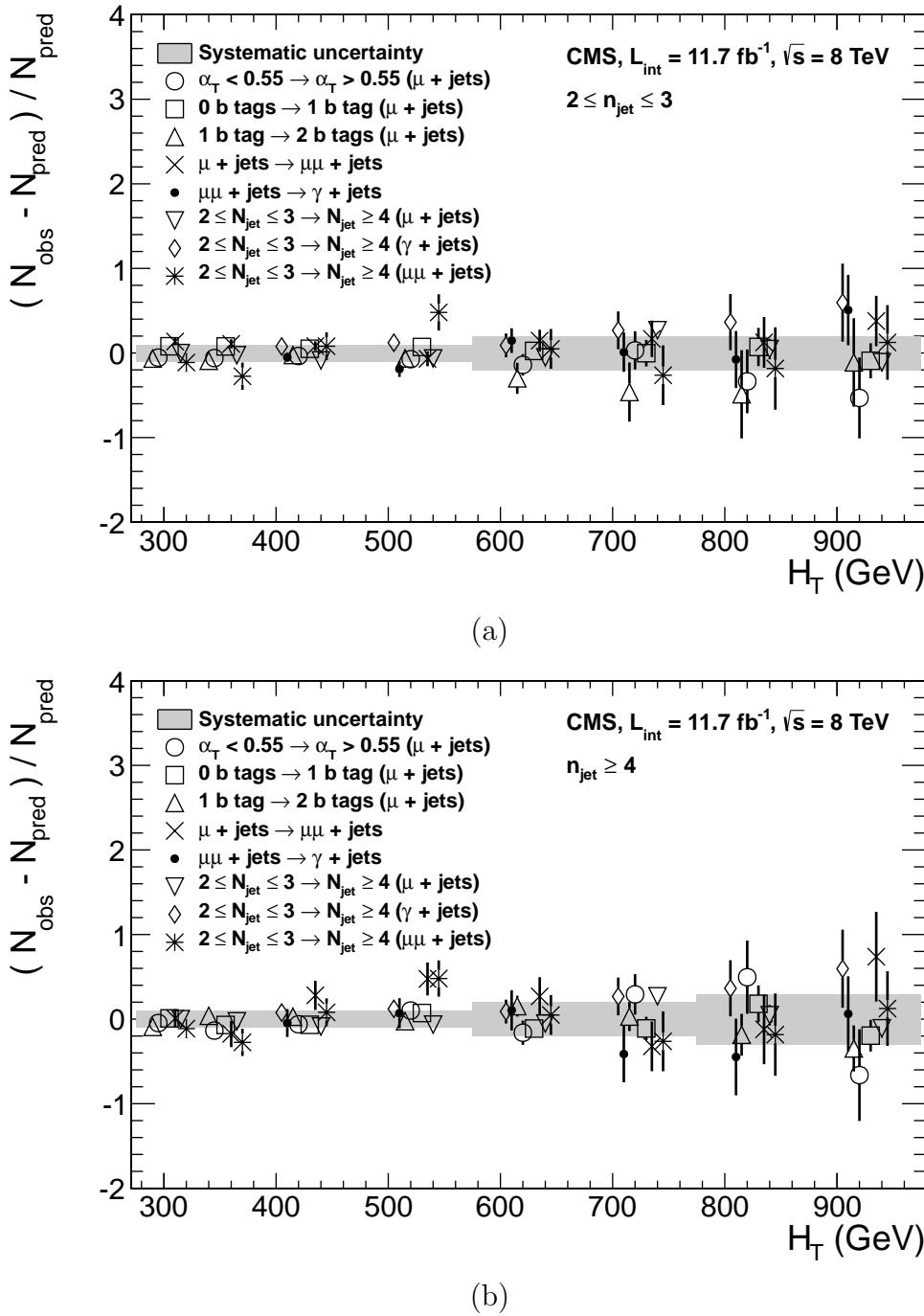


**Figure 4.11.:** Sets of closure tests (open symbols) overlaid on top of the systematic uncertainty used for each of the five  $H_T$  regions (shaded bands) and for the two different jet multiplicity categories: (a)  $2 \leq n_{\text{jet}} \leq 3$  and (b)  $n_{\text{jet}} \geq 4$ .

1856 **4.7. Simplified Models, Efficiencies and Systematic  
1857 Uncertainties**

1858 The results of the analysis are interpreted using various **SMS** signal models, which as  
1859 already introduced in Section (2.4.1) offer a natural starting point for quantifying and  
1860 characterising **SUSY** signals, and a means to identify the boundaries of search sensitivity  
1861 for different mass splittings, kinematic ranges, and final states.

1862 Each model is parameterised in a two dimensional parameter space, ( $m_{\tilde{q}/\tilde{g}}$ ,  $m_{\text{LSP}}$ ), from  
1863 which upper limits on the production cross sections of the various **SMS** models can be  
1864 set.

1865 Each signal sample is generated at Leading Order (**LO**) with Pythia [82], and cross  
1866 sections calculated for Next to Leading Order (**NLO**) and Next to Leading Logarithmic  
1867 Order (**NLL**) [83], with events simulated using the **Fastsim** framework. This framework  
1868 represents a simplified simulation of the **CMS** detector, but allows for faster production  
1869 of various signal topologies with different mass parameters. A series of correction factors  
1870 are applied to account for differences between **Fastsim** [84] and **Fullsim** [85] simulation,  
1871 which can affect the resultant  $n_b^{\text{reco}}$  distribution and which are detailed in Section (4.7.2).

1872 **4.7.1. Signal efficiency**

1873 The analysis selection efficiency,  $\epsilon$ , is measured for each mass point of the interpreted  
1874 model. This serves as a measure of the sensitivity of the signal selection for that particular  
1875 sparticle and **LSP** mass. The signal yield is then given by

$$Y(m_{\tilde{q}/\tilde{g}}, m_{\text{LSP}}) = \epsilon \times \sigma \times \mathcal{L}, \quad (4.13)$$

1876 where  $\sigma$  represents the model's cross section and  $\mathcal{L}$  the luminosity. An upper limit on  $\sigma$   
1877 taken from theory can then allow for the setting of limits in terms of the particle mass.

1878 Figure 4.12 shows the expected signal efficiency of the signal selection for the T1 and  
1879 T2 **SMS** models interpreted in this analysis. The efficiency maps are produced with the  
1880 requirement  $H_T > 275$  GeV (i.e., no binning in  $H_T$ ) and requirements on  $n_{\text{jet}}$  and  $n_b^{\text{reco}}$   
1881 that are appropriate for the model in question.

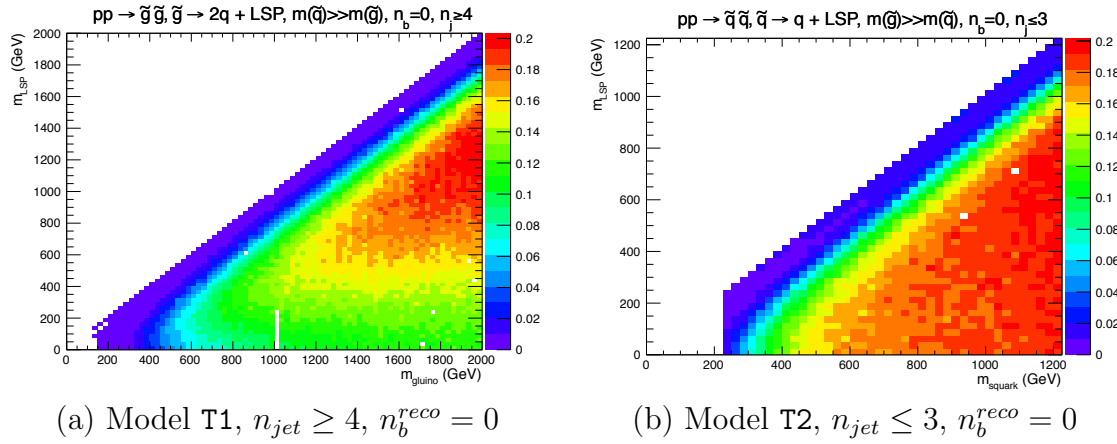


**Figure 4.12.:** Signal efficiencies for the **SMS** models (a) T1 ( $\tilde{g}\tilde{g}^* \rightarrow q\tilde{q}\chi_1^0 q\bar{q}\tilde{\chi}_1^0$ ) and (b) T2 ( $\tilde{q}\tilde{q}^* \rightarrow q\tilde{\chi}_1^0 \bar{q}\tilde{\chi}_1^0$ ) when requiring  $n_{jet} \geq 4$  and  $\leq 3$  respectively, and  $n_b^{reco} = 0$ .

1882 The same procedure is conducted in the analysis control samples. It is found in the  $\mu$   
 1883 + jets control samples, that the S/B ratios for the expected signal yields in each of the  
 1884 **SMS** models are many time smaller than in the hadronic signal region. The relative  
 1885 contamination for the  $\mu\mu$  + jets sample is smaller still due to the requirement of a second  
 1886 muon. The relative contamination for the  $\gamma$  + jets sample is expected to be zero for the  
 1887 models under consideration. These small, relative levels of contamination are accounted  
 1888 for in the fitting procedure, as described in Section (4.8.4).

### 1889 4.7.2. Applying b-tag scale factor corrections in signal samples

1890 High-statistic **FastSim** signal simulation samples are unavailable for each signal point,  
 1891 which means that a different procedure to the formula method described in Section  
 1892 (4.5) is employed. Furthermore, the use of the **FastSim** framework in the reconstruction  
 1893 introduces an extra set of scale-factor corrections, to be applied simultaneously with  
 1894 those correcting the full-simulation to the data.

1895 For these signal models, an event-by-event re-weighting procedure is applied. This applied  
 1896 weight depends on both the flavour content and the b-tagging status of the reconstruction  
 1897 level jets in the event.

1898 The re-weighting procedure can be described by first considering a single jet within a  
 1899 signal event. The flavour of the jet is determined using the method described in Section  
 1900 (4.5.1).

1901 Maps of tagging efficiencies determined from **FullSim** simulation samples for each of  
1902 the b, c and light jet flavours are produced, binned as a function of jet  $p_T$  and  $\eta$  after  
1903 the application of the hadronic signal selection. The binning of the maps are chosen  
1904 to reflect the set of  $p_T$  and  $\eta$  dependant corrections of simulation to data defined by  
1905 [86]. Taking the flavour,  $p_T$  and  $\eta$  values of each jet in the event, the expected tagging  
1906 efficiency,  $\epsilon_{MC}(p_T, \eta, f)$  is extracted from these maps.

1907 The actual tagging efficiency of the **FastSim** jet,  $\epsilon_{\text{FastSim}}(p_T, \eta, f)$ , differs from that  
1908 measured in **FullSim**,  $\epsilon_{MC}(p_T, \eta, f)$  and is related via an additional correction factor,

$$\epsilon_{\text{FastSim}}(p_T, \eta, f) = \frac{\epsilon_{MC}(p_T, \eta, f)}{SF_{\text{Fast} \rightarrow \text{Full}}(p_T, \eta, f)}, \quad (4.14)$$

1909 where  $SF_{\text{Fast} \rightarrow \text{Full}}(p_T, \eta, f)$  represents a set of  $p_T$  and  $\eta$  dependant corrections, that are  
1910 specific for each **SMS** model. These are calculated from the ratio of b-tagging rates  
1911 between a **FullSim**  $t\bar{t}$  sample, and a selection of mass points for that particular **FastSim**  
1912 **SMS** model, again measured individually for b, c and light-flavoured jets.

1913 Similarly the tagging efficiencies measured in data [?],  $\epsilon_{Data}(p_T, \eta, f)$ , are further related  
1914 to  $\epsilon_{\text{FastSim}}(p_T, \eta, f)$  by the equation,

$$\begin{aligned} \epsilon_{Data}(p_T, \eta, f) &= \epsilon_{MC}(p_T, \eta, f) \times SF_{MC \rightarrow Data}(p_T, \eta, f) \\ &= \epsilon_{\text{FastSim}}(p_T, \eta, f) \times \underbrace{SF_{\text{Fast} \rightarrow \text{Full}}(p_T, \eta, f) \times SF_{MC \rightarrow Data}(p_T, \eta, f)}_{SF_{\text{Fast} \rightarrow Data}}. \end{aligned} \quad (4.15)$$

1915 For each jet, the weight of the event is re-weighted according to whether the jet fires the  
1916 b-tagger. In the instance that the jet *is* b-tagged, the event weight will be modified by,

$$\text{weight} = SF_{\text{Fast} \rightarrow Data} \times \text{weight}, \quad (4.16)$$

1917 and in the case that the jet does *not* fire the b-tagger,

$$\text{weight} = \frac{1 - \epsilon_{\text{Data}}(p_T, \eta, f)}{1 - \epsilon_{\text{FastSim}}(p_T, \eta, f)} \times \text{weight}. \quad (4.17)$$

1918 All events that pass the selection criteria are reweighted in this way, and represent the  
1919 yields in each  $n_b^{reco}$  bin corrected from **Fastsim** to data.

### 1920 4.7.3. Experimental uncertainties

1921 The systematic uncertainty on the expected signal acceptance times analysis efficiency is  
1922 determined independently for the each **SMS** model considered. These systematics stem  
1923 from uncertainties on the parton distribution functions, the luminosity measurement, jet  
1924 energy scale, b-tag scale factor measurements and the efficiencies of various cuts used  
1925 in the signal selection, including the  $H_T / E_T$ , dead **ECAL** cleaning filter and lepton /  
1926 photon event vetoes.

1927 Rather than trying to estimate the level of systematic that is applicable point-by-point  
1928 in a model space, general behaviours are considered and instead constant systematics are  
1929 estimated in two regions of the **SMS** models parameter space.

1930 These two regions are defined as, near (small mass splittings) and far (large mass  
1931 splittings) from the mass degenerate diagonal, where the far region is bounded by the  
1932 condition

$$m_{\tilde{q}/\tilde{g}} - m_{LSP} > 350\text{GeV} \quad m_{\tilde{q}/\tilde{g}} > 475\text{GeV}.$$

1933 The total systematics in each region are evaluated in the following ways:

1934 **Jet energy scale** : The relative change in the signal efficiency is gauged by varying  
1935 the energy of all jets in an event up or down according to a  $p_T$  and  $\eta$  dependent jet  
1936 energy scale uncertainty. Within the two systematic regions, the resulting systematic  
1937 uncertainties for each **SMS** model are determined by taking the value of the 68<sup>th</sup>  
1938 percentile for the distributions of the relative change in the signal efficiency.

1939 **Luminosity measurement** : The measurement of luminosity taken propagates  
1940 through to an uncertainty on the signal event yield when considering any new  
1941 physics model, which is currently 4.4% [87].

1942 **Parton density function** : Each signal sample is produced using the CTEQ6L1  
1943 parton density function. The effect on the signal acceptance when re-weighting to  
1944 the central value of three different parton distribution functions, CT10, MSTW08  
1945 and NNPDF2.1 are examined [88]. It is found that the change of the signal efficiency  
1946 in different **SMS** models, due to the alternate PDF sets are typically a few percent,  
1947 and approaches 10% at higher squark/gluon and **LSP** masses.

1948  **$H_T/E_T$  cleaning cut** : The ratio of the efficiencies of the cleaning cut are compared  
1949 in simulation and data after application of the  $\mu +$  jets control sample selection.  
1950 No  $\alpha_T$  cut or further event cleaning filters are applied. The ratio of the efficiencies  
1951 observed in data and simulation for a cut value of  $H_T/E_T < 1.25$  and the two jet  
1952 multiplicity bins,  $2 \leq n_{\text{jet}} \leq 3$  and  $n_{\text{jet}} \geq 4$  are  $1.028 \pm 0.007$  and  $1.038 \pm 0.015$   
1953 respectively. These deviations are taken to represent the systematic uncertainty on  
1954 the simulation modelling of this variable.

1955 **Dead ECAL cleaning filter** : The ratio of the efficiencies observed in data and  
1956 simulation for this filter in the two jet multiplicity bins,  $2 \leq n_{\text{jet}} \leq 3$  and  $n_{\text{jet}} \geq 4$ ,  
1957 are  $0.961 \pm 0.008$  and  $0.961 \pm 0.009$ , respectively. These deviations from unity  
1958 are taken to represent the systematic uncertainties in the modelling in simulation of  
1959 this filter.

1960 **Lepton and photon vetoes** : The uncertainty on the efficiency of the lepton and  
1961 photon vetoes is determined by considering truth information. The efficiency of  
1962 the vetoes is measured after applying relevant object filters with identical logic,  
1963 but based on truth instead of reconstructed objects. Where the efficiency is found  
1964 to not be 100%, it is taken to represent the fraction of signal events that are  
1965 incorrectly vetoed. This deviation is taken directly as the systematic uncertainty on  
1966 the efficiency. The systematic uncertainty is only non-zero for models which contain  
1967 third-generation quarks in the final state, where the uncertainties are at the order  
1968 of 1% level.

1969 **B-tag scale factor uncertainties** : The relative change in the signal efficiency is  
1970 observed when relevant flavour,  $p_T$  and  $\eta$  dependant b-tag correction factors, are  
1971 varied up or down by their uncertainty. Within the two systematic regions, the  
1972 resulting systematic uncertainties for each **SMS** model are determined by taking

the value of the 68<sup>th</sup> percentile for the distributions of the relative change in the signal efficiency, over all mass points.

Tables 4.16 and 4.17 summarise all the aforementioned systematic uncertainties on the signal efficiencies for each individual SMS model interpreted in the analysis. In the case of the T1tttt model, in which pair produced gluinos decay to  $t\bar{t}$  pairs and the LSP, the near region of SMS space is not considered, and so no systematic uncertainties are included.

In both of the defined regions it is found that the systematic uncertainties are relatively flat justifying the approach taken. The systematic uncertainties used for the region near to the diagonal fall in the range 13-15%; similarly, for the region far from the diagonal, the uncertainties used fall in the range 12-23%. These uncertainties are all propagated through to the limit calculation.

Model	Luminosity	p.d.f	JES	$\mathcal{H}_T/\cancel{E}_T$	Dead ECAL	Lepton Vetoes	b-tagging	Total
T1	4.4	10.0	5.6	3.8	4.1	n/a	3.1	13.9
T2	4.4	10.0	4.1	2.8	4.1	n/a	2.4	12.9
T2tt	4.4	10.0	6.5	3.8	4.1	0.8	0.8	13.9
T2bb	4.4	10.0	4.8	2.8	4.1	0.3	2.2	13.1
T1tttt	n/a	n/a	n/a	n/a	n/a	n/a	n/a	n/a
T1bbbb	4.4	10.0	7.3	3.8	4.1	0.5	2.7	14.5

**Table 4.16.:** Estimates of systematic uncertainties on the signal efficiency (%) for various SMS models when considering points in the region near to the diagonal (i.e. small mass splitting and compressed spectra). The uncertainties are added in quadrature to obtain the total.

Model	Luminosity	p.d.f	JES	$\mathcal{H}_T/\cancel{E}_T$	Dead ECAL	Lepton Vetoes	b-tagging	Total
T1	4.4	10.0	0.8	3.8	4.1	n/a	6.6	14.0
T2	4.4	10.0	1.1	2.8	4.1	n/a	5.8	13.4
T2tt	4.4	10.0	3.5	3.8	4.1	0.6	1.6	12.9
T2bb	4.4	10.0	0.9	2.8	4.1	0.3	2.7	12.3
T1tttt	4.4	10.0	0.5	3.8	4.1	1.4	19.4	23.0
T1bbbb	4.4	10.0	1.5	3.8	4.1	0.4	10.1	16.0

**Table 4.17.:** Estimates of systematic uncertainties on the signal efficiency (%) for various SMS models when considering points in the region far from the diagonal (i.e. large mass splitting). The uncertainties are added in quadrature to obtain the total.

## 1985 4.8. Statistical Interpretation

1986 For a given category of events satisfying requirements on both  $n_{jet}$  and  $n_b^{reco}$ , a likelihood  
1987 model of the observations in multiple data samples is used to gauge agreement between  
1988 the observed yields in the hadronic signal region, and the predicted yields obtained from  
1989 the control samples. In addition to checking whether the predictions are compatible  
1990 with a **SM** only hypothesis, the likelihood model is also used to test for the presence  
1991 of a variety of signal models. The statistical framework outlined within this section is  
1992 presented in greater detail within [89].

### 1993 4.8.1. Hadronic sample

1994 Let  $N$  be the number of bins on  $H_T$ , with  $n^i$  the number of events observed satisfying  
1995 all selection requirements in each  $H_T$  bin i. The likelihood of the observations can then  
1996 be written :

$$L_{had} = \prod_i \text{Pois}(n^i | b^i + s^i), \quad (4.18)$$

1997 where  $b^i$  represents the expected **SM** background

$$b^i = EWK_i + QCD_i, \quad (4.19)$$

1998 and  $s^i$  the expected number of signal events from the different **SMS** models interpreted.  
1999 Pois refers to the Poisson distribution of these values and is defined as :

$$\text{Pois}(\chi|\lambda) = \frac{\lambda^\chi \exp^{-\lambda}}{k!}. \quad (4.20)$$

2000 **4.8.2.  $H_T$  evolution model**

- 2001 The hypothesis, that for a process the  $\alpha_T$  ratio falls exponentially (see Section (4.2.4))  
2002 in  $H_T$  is defined by Equation (4.10), where  $k_{QCD}$  is constrained by measurements in a  
2003 signal sideband region.
- 2004 The expected QCD background,  $QCD^i$ , within a bin  $i$  is then modelled as,

$$QCD^i = m^i A_{QCD} e^{-k_{QCD}\langle H_T \rangle}, \quad (4.21)$$

- 2005 where  $m_i$  represent the number of events observed with  $\alpha_T \leq 0.55$  in each  $H_T$  bin  $i$ , and  
2006  $\langle H_T \rangle$  represents the mean  $H_T$  of each bin. Expressed as functions of just the zeroth bin,  
2007  $QCD^0$ , and  $k_{QCD}$ , the QCD expectation is given by

$$QCD^i = QCD^0 \left( \frac{m^i}{m^0} \right) e^{-k_{QCD}(\langle H_T \rangle^i - \langle H_T \rangle^0)}. \quad (4.22)$$

2008 **4.8.3. EWK control samples**

- 2009 The **EWK** background estimation within each bin,  $i$ , is broken into two components, the  
2010 expected yield from  $Z \rightarrow \nu\bar{\nu}$  and  $t\bar{t}$ -W (plus other residual backgrounds) events. This is  
2011 written as,  $Z_{inv}^i$  and  $t\bar{t}W^i$ , and it follows that

$$EWK^i = Z_{inv}^i + t\bar{t}W^i. \quad (4.23)$$

- 2012 This can be further expressed as

$$Z_{inv}^i \equiv f_{Z_{inv}}^i \times EWK^i, \quad (4.24)$$

$$t\bar{t}W^i \equiv (1 - f_{Z_{inv}}^i) \times EWK^i, \quad (4.25)$$

2013 where  $f_{Zinv}^i$  represents the expected yield from  $Z \rightarrow \nu\bar{\nu}$  in bin  $i$  divided by the expected  
2014 **EWK** background  $EWK^i$ . This fraction is modelled as a linear component

$$f_{Zinv}^i = f_{Zinv}^0 + \frac{\langle H_T \rangle^i - \langle H_T \rangle^0}{\langle H_T \rangle^{N-1} - \langle H_T \rangle^0} (f_{Zinv}^{N-1} - f_{Zinv}^i), \quad (4.26)$$

2015 where  $N$  again represents the number of  $H_T$  bins, and  $f_{Zinv}^i$  and  $f_{Zinv}^{N-1}$  are float parameters  
2016 whose final values are limited between zero and one.

2017 Within each  $H_T$  bin there are three background measurements for the different control  
2018 samples,  $n_\gamma^i$ ,  $n_\mu^i$  and  $n_{\mu\mu}^i$ , representing the event yields from the  $\gamma +$  jets,  $\mu +$  jets and  
2019  $\mu\mu +$  jets control samples respectively. Each of these have a corresponding yield in  
2020 simulation,  $MC_\gamma^i$ ,  $MC_\mu^i$  and  $MC_{\mu\mu}^i$ . Within the hadronic signal region there are also  
2021 corresponding simulated yields for  $Z \rightarrow \nu\bar{\nu}$  ( $MC_{Zinv}^i$ ) and  $t\bar{t} + W$  ( $MC_{t\bar{t}+W}^i$ ), which are  
2022 used to define

$$r_\gamma^i = \frac{MC_\gamma^i}{MC_{Zinv}^i}; \quad r_{\mu\mu}^i = \frac{MC_{\mu\mu}^i}{MC_{Zinv}^i}; \quad r_\mu^i = \frac{MC_\mu^i}{MC_{t\bar{t}+W}^i}, \quad (4.27)$$

2023 where  $r_p^i$  represents the inverse of the **TFs** used to extrapolate the yield of each background  
2024 process.

2025 The likelihoods regarding the three measured yields  $n_\gamma^i$ ,  $n_{\mu\mu}^i$ ,  $n_\mu^i$  can then be fully expressed  
2026 as

$$L_\gamma = \prod_i \text{Pois}(n_\gamma^i | \rho_{\gamma Z}^j \cdot r_\gamma^i \cdot Z_{inv}^i), \quad (4.28)$$

$$L_{\mu\mu} = \prod_i \text{Pois}(n_{\mu\mu}^i | \rho_{\mu\mu Z}^j \cdot r_{\mu\mu}^i \cdot Z_{inv}^i), \quad (4.29)$$

$$L_\mu = \prod_i \text{Pois}(n_\mu^i | \rho_{\mu Y}^j \cdot r_\mu^i \cdot Y^i + s_\mu^i), \quad (4.30)$$

$$(4.31)$$

2027 which contain an additional term  $s_\mu^i$ , which represents the signal contamination in the  
2028  $\mu +$  jets sample. The parameters  $\rho_{\gamma Z}^j$ ,  $\rho_{\mu\mu}^j$  and  $\rho_\mu^j$  represent “correction factors” that

2029 accommodate the data driven systematic uncertainties derived from the control samples  
2030 in Section (4.12).

2031 Each of these equations are used to estimate the maximum likelihood value for relevant  
2032 background in the signal region given the observations  $n_p^i$  in each of the control samples  
2033 (see Section (4.2.3)).

2034 The measurements in each of the control samples and the hadronic signal region, along  
2035 with the ratios  $r_\gamma^i$ ,  $r_{\mu\mu}^i$ , and  $r_\mu^i$ , are all considered simultaneously through the relationships  
2036 defined by Equations (4.19),(4.24) and (4.25).

2037 In addition to the Poisson product, an additional log-normal term is introduced to  
2038 accommodate the systematic uncertainties given by,

$$L_{EWK \ syst} = \prod_j \text{Logn}(1.0 | \rho_{\mu W}^j, \sigma_{\mu W}^j) \times \text{Logn}(1.0 | \rho_{\mu\mu Z}^j, \sigma_{\mu\mu Z}^j) \times \text{Logn}(1.0 | \rho_{\gamma Z}^j, \sigma_{\gamma Z}^j), \quad (4.32)$$

2039 where  $\sigma_{\gamma Z}^j$ ,  $\sigma_{\mu\mu Z}^j$  and  $\sigma_{\mu W}^j$  represent the relative systematic uncertainties for the control  
2040 sample constraints and Logn is the log-normal distribution [90],

$$\text{Logn}(x | \mu, \sigma_{rel}) = \frac{1}{x\sqrt{2\pi}\ln k} \exp\left(\frac{\ln^2(\frac{x}{\mu})}{2\ln^2 k}\right); \quad k = 1 + \sigma_{rel}. \quad (4.33)$$

2041 Five parameters per control sample are used to span the eight  $H_T$  bins, with just one  
2042 used for the three  $H_T$  bins in the  $n_b^{reco} \geq 4$  category. These parameters span the same  
2043  $H_T$  ranges described in Section (4.6) and is shown in Table 4.18.

$H_T$ bin (i)	0	1	2	3	4	5	6	7
syst. parameter (j)	0	1	2	2	3	3	4	4

$H_T$ bin (i)	0	1	2
syst. parameter (j)	0	0	0

**Table 4.18.:** The systematic parameters used in  $H_T$  bins. Left: categories with eight bins;  
 right: category with three bins.

2044 Alternatively, in the higher  $n_b^{reco}$  categories ( $n_b^{reco} \geq 2$ ), only the single muon sample  
2045 is used to constrain the total EWK background. Therefore the likelihood function is  
2046 greatly simplified and is represented by

$$L'_\mu = \prod_i \text{Pois}(n_\mu^i | \rho_{\mu Y}^j \cdot r'_\mu \cdot EWK^i + s_\mu^i), \quad (4.34)$$

2047 where,

$$r'_\mu = \frac{MC_\mu^i}{MC_{tot}^i}. \quad (4.35)$$

2048 **4.8.4. Contributions from signal**

2049 The cross section for each model is represented by  $x$ , while  $l$  represents the total recorded  
2050 luminosity considered by the analysis in the signal region. Let  $\epsilon_{had}^i$  and  $\epsilon_\mu^i$  represent the  
2051 analysis selection efficiency for that particular signal model in  $H_T$  bin  $i$  of the hadronic  
2052 and  $\mu +$  jets control sample respectively. Letting  $\delta$  represent the relative uncertainty on  
2053 the signal yield, assumed to be fully correlated across all bins, and  $\rho_{sig}$  the “correction  
2054 factor” to the signal yield which accommodates this uncertainty.  $f$  represents an unknown  
2055 multiplicative factor on the signal cross section, for which an allowed interval is computed.

2056 The expected signal yield  $s^i$  is thus given by

$$s^i \equiv f \rho_{sig} x l \epsilon_{had}^i \quad (4.36)$$

2057 and signal contamination with the  $\mu +$  jets control sample by

$$s_\mu^i \equiv f \rho_{sig} x l \epsilon_\mu^i \quad (4.37)$$

2058 The systematic uncertainty on the signal is additionally included by the term

$$L_{sig} = \text{Logn}(1.0 | \rho_{sig}, \delta). \quad (4.38)$$

2059 A discussion of the **SMS** signal models through which the analysis is interpreted can be  
2060 found in the following Chapter.

2061 **4.8.5. Total likelihood**

2062 The total likelihood function for a given signal bin  $k(n_b^{reco}, n_{jet})$  is then given by the  
2063 product of the likelihood functions introduced within the previous sections:

$$L_{\text{Tot}}^k = L_{had}^k \times L_\mu^k \times L_\gamma^k \times L_{\mu\mu}^k \times L_{EWKsyst}^k \times L_{QCD}^k; \quad (0 \leq n_b^{\text{reco}} \leq 1)$$

$$L_{\text{Tot}}^k = L_{had}^k \times L_\mu'^k \times L_{\mu\text{syst}}^k \times L_{QCD}^k \quad (n_b^{\text{reco}} \geq 2). \quad (4.39)$$

2064 In categories containing eight  $H_T$  bins and utilising the three control samples ( $\mu + \text{jets}$ ,  $\mu\mu + \text{jets}$ ,  $\gamma + \text{jets}$ ), there are 25 nuisance parameters, whilst when just one control sample  
2065 is used to estimate the **EWK** background, there are 15 nuisance parameters. Where  
2066 three  $H_T$  bins are used (the highest  $n_b^{reco}$  category), there are 6 nuisance parameters.  
2067 This information is summarised within Table 4.19.

Nuisance parameter	Total
$(EWK^i)_{i:0-7(2)}$	8 (3)
$f_{Zinv}^0$	1*
$f_{Zinv}^7$	1*
$QCD^0$	1
$k_{QCD}$	1
$(\rho_{\gamma Z}^j)_{j:2-4}$	3 *
$(\rho_{\mu\mu Z}^j)_{j:0-4}$	5 *
$(\rho_{\mu W}^j)_{j:0-4(0)}$	5 (1)

**Table 4.19.:** Nuisance parameters used within the different hadronic signal bins of the analysis. Parameters denoted by a \* are not considered in the case of a single control sample being used to predict the **EWK** background. Numbers within brackets highlight the number of nuisance parameters in the case of three  $H_T$  bins being used.

2069 When considering **SUSY** signal models within the likelihood, the additional  $L_{\text{sig}}$  term  
2070 is included and therefore when multiple categories are fitted simultaneously the total  
2071 likelihood is then represented by

$$L_{\text{Tot}}^{\text{signal}} = L_{sig} \times \prod_k L_{\text{Tot}}^k. \quad (4.40)$$

# Chapter 5.

## <sup>2072</sup> Results And Interpretation

<sup>2073</sup> Using the statistical framework outlined in the previous chapter, results are compared to  
<sup>2074</sup> a SM-only hypothesis (Section (5.1)) and interpreted within various SMS models (Section  
<sup>2075</sup> (5.2)).

### <sup>2076</sup> 5.1. Compatibility with the Standard Model Hypothesis

<sup>2078</sup> The SM background only hypothesis is tested by removing any signal contributions  
<sup>2079</sup> within the signal and control samples, and the likelihood function is maximised over all  
<sup>2080</sup> parameters using Rootfit [91] and MINUIT [92]. The results of the search consist of the  
<sup>2081</sup> observed yields in the hadronic signal sample, and the  $\mu + \text{jets}$ ,  $\mu\mu + \text{jets}$  and  $\gamma + \text{jets}$   
<sup>2082</sup> control samples.

<sup>2083</sup> These observed yields along with the expectations and uncertainties given by the simulta-  
<sup>2084</sup> neous fit for the hadronic signal region are given in Table 5.2. The results obtained from  
<sup>2085</sup> the simultaneous fits, including that of the three control samples, are shown in Figure  
<sup>2086</sup> 5.1-5.8, as summarised in Table 5.1.

<sup>2087</sup> The figures show a comparison between the observed yields and the SM expectations  
<sup>2088</sup> across all  $H_T$  bins, and in all  $n_{jet}$  and  $n_b^{reco}$  multiplicity categories. In all categories the  
<sup>2089</sup> samples are well described by the SM only hypothesis. In particular no significant excess  
<sup>2090</sup> is observed above SM expectation within the hadronic signal region.

$n_{jet}$	$n_b^{reco}$	Control samples fitted	Figure
2-3	0	$\mu + \text{jets}, \mu\mu + \text{jets}, \gamma + \text{jets}$	5.1
2-3	1	$\mu + \text{jets}, \mu\mu + \text{jets}, \gamma + \text{jets}$	5.2
2-3	1	$\mu + \text{jets}$	5.3
$\geq 4$	0	$\mu + \text{jets}, \mu\mu + \text{jets}, \gamma + \text{jets}$	5.4
$\geq 4$	1	$\mu + \text{jets}, \mu\mu + \text{jets}, \gamma + \text{jets}$	5.5
$\geq 4$	2	$\mu + \text{jets}$	5.6
$\geq 4$	3	$\mu + \text{jets}$	5.7
$\geq 4$	4	$\mu + \text{jets}$	5.8

**Table 5.1.:** Summary of control samples used by each fit results, and the Figures in which they are displayed.

Cat	$n_b^{reco}$	$n_{jet}$	$H_T$ bin (GeV)							
			275-325	325-375	375-475	474-575	575-675	675-775	775-875	875- $\infty$
SM Data	0	$\leq 3$	$6235^{+100}_{-67}$ 6232	$2900^{+60}_{-54}$ 2904	$1955^{+34}_{-39}$ 1965	$558^{+14}_{-15}$ 552	$186^{+11}_{-10}$ 177	$51.3^{+3.4}_{-3.8}$ 58	$21.2^{+2.3}_{-2.2}$ 16	$16.1^{+1.7}_{-1.7}$ 25
		$\geq 4$	$1010^{+34}_{-24}$ 1009	$447^{+19}_{-16}$ 452	$390^{+19}_{-15}$ 375	$250^{+12}_{-11}$ 274	$111^{+9}_{-7}$ 113	$53.3^{+4.3}_{-4.3}$ 56	$18.5^{+2.4}_{-2.4}$ 16	$19.4^{+2.5}_{-2.7}$ 27
SM Data	1	$\leq 3$	$1162^{+37}_{-29}$ 1164	$481^{+18}_{-19}$ 473	$341^{+15}_{-16}$ 329	$86.7^{+4.2}_{-5.6}$ 95	$24.8^{+2.8}_{-2.7}$ 23	$7.2^{+1.1}_{-1.0}$ 8	$3.3^{+0.7}_{-0.7}$ 4	$2.1^{+0.5}_{-0.5}$ 1
		$\geq 4$	$521^{+25}_{-17}$ 515	$232^{+15}_{-12}$ 236	$188^{+12}_{-11}$ 204	$106^{+6}_{-6}$ 92	$42.1^{+4.1}_{-4.4}$ 51	$17.9^{+2.2}_{-2.0}$ 13	$9.8^{+1.5}_{-1.4}$ 13	$6.8^{+1.2}_{-1.1}$ 6
SM Data	2	$\leq 3$	$224^{+15}_{-14}$ 222	$98.2^{+8.4}_{-6.4}$ 107	$59.0^{+5.2}_{-6.0}$ 58	$12.8^{+1.6}_{-1.6}$ 12	$3.0^{+0.9}_{-0.7}$ 5	$0.5^{+0.2}_{-0.2}$ 1	$0.1^{+0.1}_{-0.1}$ 0	$0.1^{+0.1}_{-0.1}$ 0
		$\geq 4$	$208^{+17}_{-9}$ 204	$103^{+9}_{-7}$ 107	$85.9^{+7.2}_{-6.9}$ 84	$51.7^{+4.6}_{-4.7}$ 59	$19.9^{+3.4}_{-3.0}$ 24	$6.8^{+1.2}_{-1.3}$ 5	$1.7^{+0.7}_{-0.4}$ 1	$1.3^{+0.4}_{-0.3}$ 2
SM Data	3	$\geq 4$	$25.3^{+5.0}_{-4.2}$ 25	$11.7^{+1.7}_{-1.8}$ 13	$6.7^{+1.4}_{-1.2}$ 4	$3.9^{+0.8}_{-0.8}$ 2	$2.3^{+0.6}_{-0.6}$ 2	$1.2^{+0.3}_{-0.4}$ 3	$0.3^{+0.2}_{-0.1}$ 0	$0.1^{+0.1}_{-0.1}$ 0
		$\geq 4$	$0.9^{+0.4}_{-0.7}$ 1	$0.3^{+0.2}_{-0.2}$ 0				$0.6^{+0.3}_{-0.3}$ 2		

**Table 5.2.:** Comparison of the measured yields in each  $H_T$ ,  $n_{jet}$  and  $n_b^{reco}$  jet multiplicity bins for the hadronic sample with the **SM** expectations and combined statistical and systematic uncertainties given by the simultaneous fit.

<sup>2091</sup> Given the lack of an excess in data hinting at a possible supersymmetric signature within  
<sup>2092</sup> the data, interpretations are made on the production masses and cross section of a range  
<sup>2093</sup> of **SUSY** decay topologies within the following section.

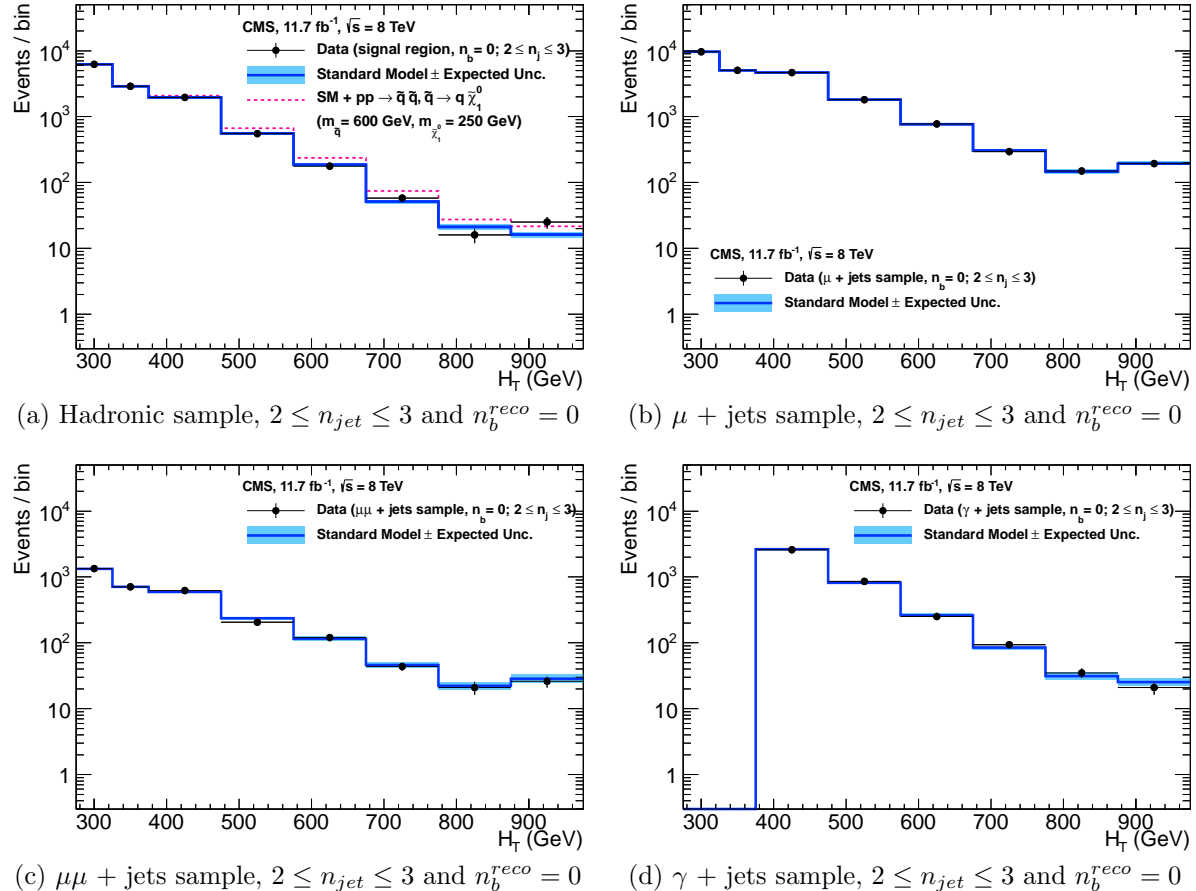


**Figure 5.1.:** Comparison of the observed yields and SM expectations given by the simultaneous fit in bins of  $H_T$  for the (a) hadronic, (b)  $\mu +$  jets, (c)  $\mu\mu +$  jets and (d)  $\gamma +$  jets samples when requiring  $n_b^{reco} = 0$  and  $n_{jet} \leq 3$ . The observed event yields in data (black dots) and the expectations and their uncertainties for all SM processes (blue line with light blue bands) are shown. An example signal expectation (red solid line) for the D1 SMS signal point from Table 4.1 is superimposed on the SM background expectation.

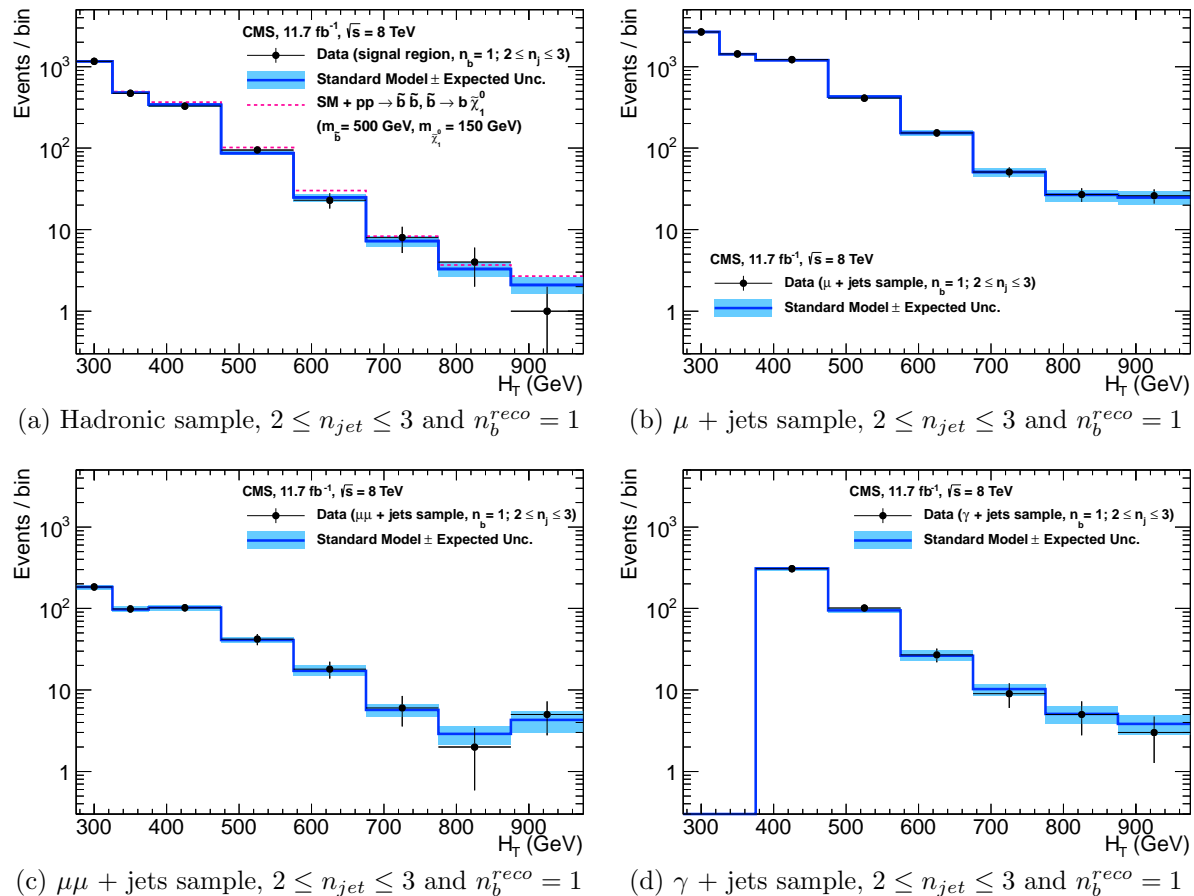


**Figure 5.2.:** Comparison of the observed yields and SM expectations given by the simultaneous fit in bins of  $H_T$  for the (a) hadronic, (b)  $\mu +$  jets, (c)  $\mu\mu +$  jets and (d)  $\gamma +$  jets samples when requiring  $n_b^{reco} = 1$  and  $n_{jet} \leq 3$ . The observed event yields in data (black dots) and the expectations and their uncertainties for all SM processes (blue line with light blue bands) are shown. An example signal expectation (red solid line) for the D2 SMS signal point from Table 4.1 is superimposed on the SM background expectation.

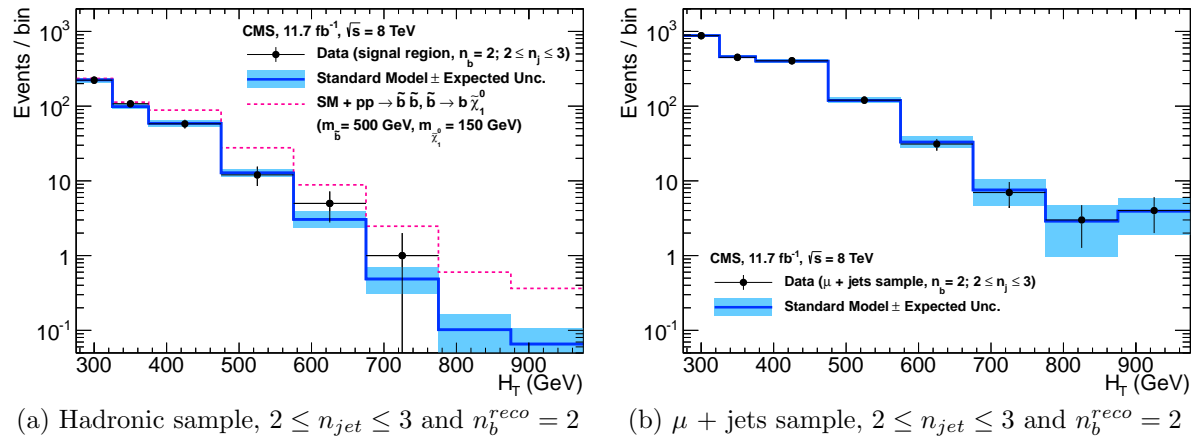


**Figure 5.3.:** Comparison of the observed yields and SM expectations given by the simultaneous fit in bins of  $H_T$  for the (a) hadronic, (b)  $\mu +$  jets, (c)  $\mu\mu +$  jets and (d)  $\gamma +$  jets samples when requiring  $n_b^{reco} = 2$  and  $n_{jet} \leq 3$ . The observed event yields in data (black dots) and the expectations and their uncertainties for all SM processes (blue line with light blue bands) are shown. An example signal expectation (red solid line) for the D2 SMS signal point from Table 4.1 is superimposed on the SM background expectation.

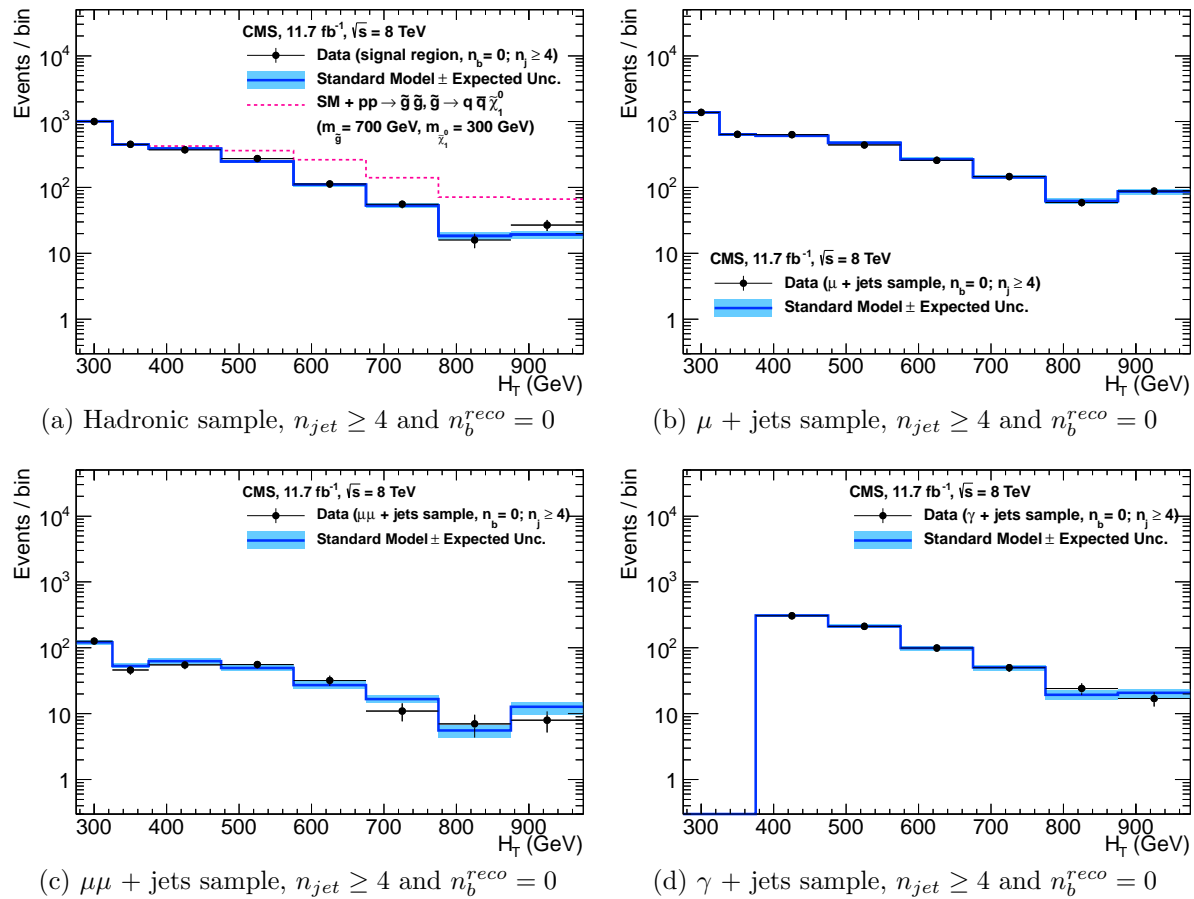


**Figure 5.4.:** Comparison of the observed yields and SM expectations given by the simultaneous fit in bins of  $H_T$  for the (a) hadronic, (b)  $\mu +$  jets, (c)  $\mu\mu +$  jets and (d)  $\gamma +$  jets samples when requiring  $n_b^{reco} = 0$  and  $n_{jet} \geq 4$ . The observed event yields in data (black dots) and the expectations and their uncertainties for all SM processes (blue line with light blue bands) are shown. An example signal expectation (red solid line) for the D2 SMS signal point from Table 4.1 is superimposed on the SM background expectation.

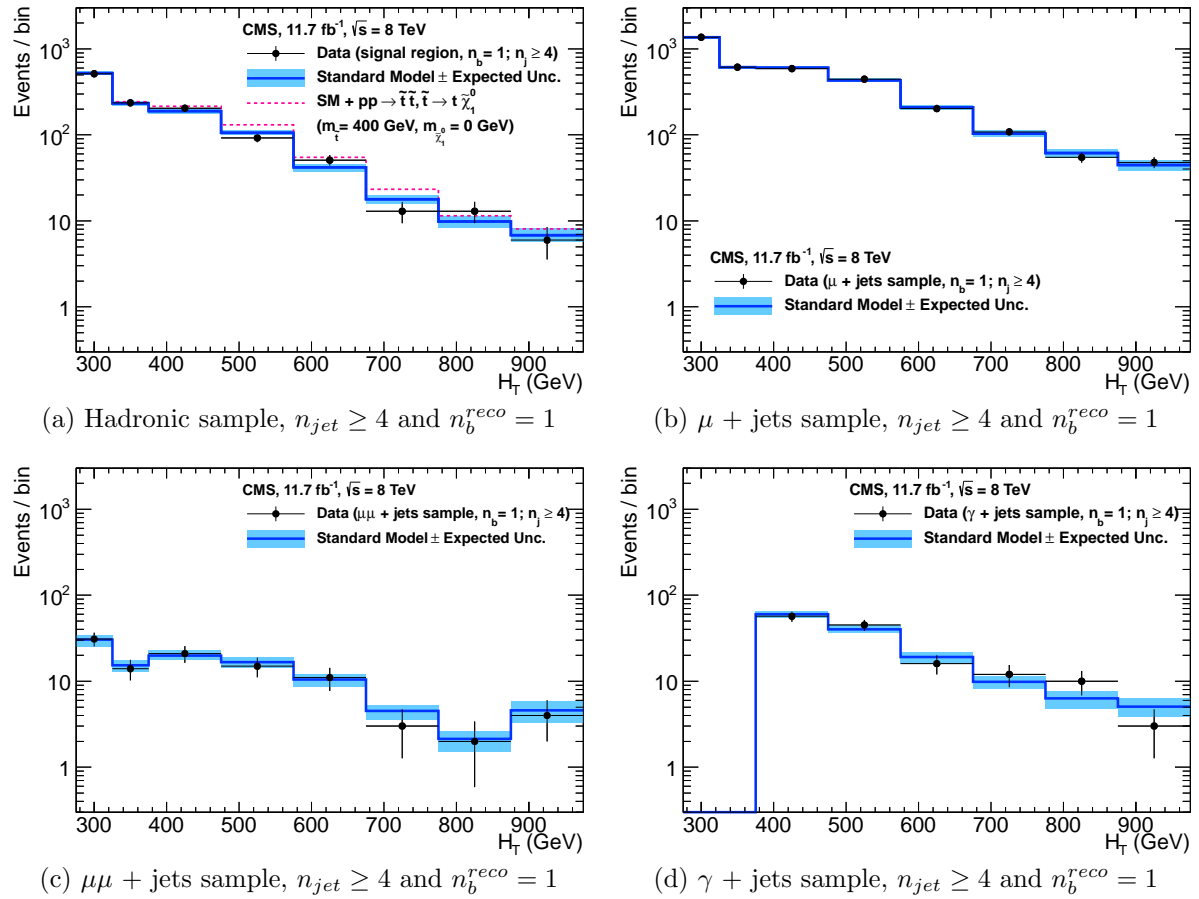


**Figure 5.5.:** Comparison of the observed yields and SM expectations given by the simultaneous fit in bins of  $H_T$  for the (a) hadronic, (b)  $\mu +$  jets, (c)  $\mu\mu +$  jets and (d)  $\gamma +$  jets samples when requiring  $n_b^{reco} = 1$  and  $n_{jet} \geq 4$ . The observed event yields in data (black dots) and the expectations and their uncertainties for all SM processes (blue line with light blue bands) are shown.

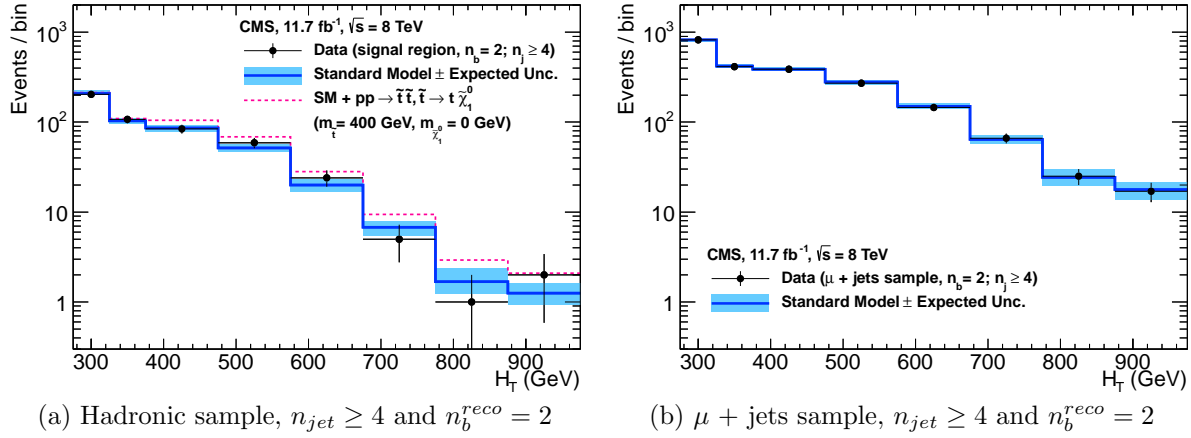


**Figure 5.6.:** Comparison of the observed yields and SM expectations given by the simultaneous fit in bins of  $H_T$  for the (a) hadronic, (b)  $\mu +$  jets, (c)  $\mu\mu +$  jets and (d)  $\gamma +$  jets samples when requiring  $n_b^{reco} = 2$  and  $n_{jet} \geq 4$ . The observed event yields in data (black dots) and the expectations and their uncertainties for all SM processes (blue line with light blue bands) are shown. An example signal expectation (red solid line) for the D3 SMS signal point from Table 4.1 is superimposed on the SM background expectation.

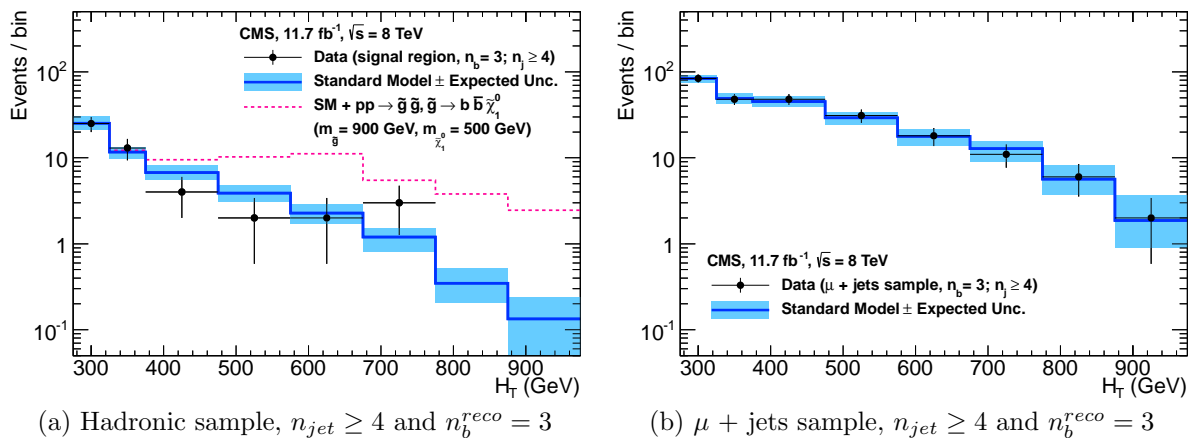


**Figure 5.7.:** Comparison of the observed yields and SM expectations given by the simultaneous fit in bins of  $H_T$  for the (a) hadronic, (b)  $\mu +$  jets, (c)  $\mu\mu +$  jets and (d)  $\gamma +$  jets samples when requiring  $n_b^{reco} = 3$  and  $n_{jet} \geq 4$ . The observed event yields in data (black dots) and the expectations and their uncertainties for all SM processes (blue line with light blue bands) are shown. An example signal expectation (red solid line) for the G2 SMS signal point from Table 4.1 is superimposed on the SM background expectation.

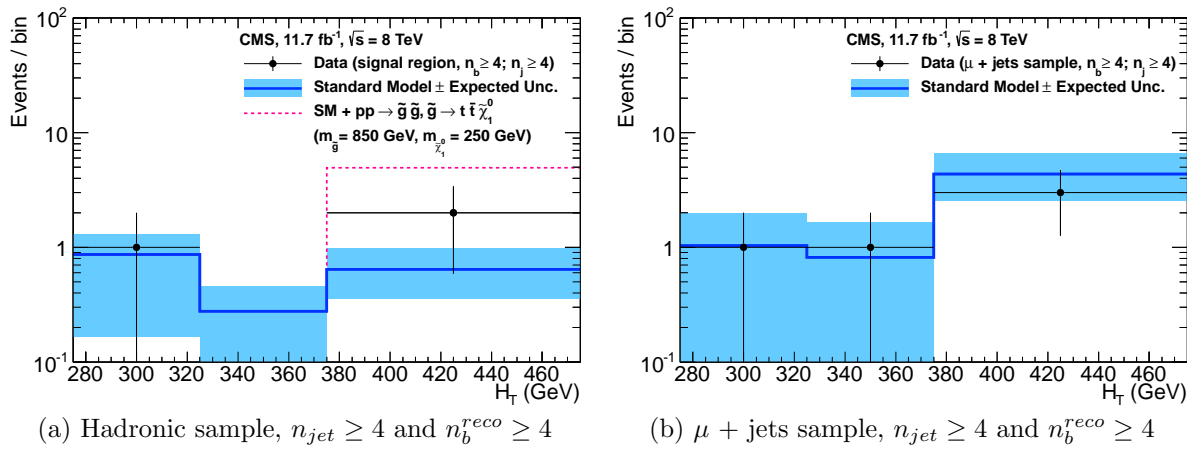


**Figure 5.8.: Comparison of the observed yields and SM expectations given by the simultaneous fit in bins of  $H_T$  for the (a) hadronic, (b)  $\mu +$  jets, (c)  $\mu\mu +$  jets and (d)  $\gamma +$  jets samples when requiring  $n_b^{reco} \geq 4$  and  $n_{jet} \geq 4$ . The observed event yields in data (black dots) and the expectations and their uncertainties for all SM processes (blue line with light blue bands) are shown. An example signal expectation (red solid line) for the G3 SMS signal point from Table 4.1 is superimposed on the SM background expectation.**

2094 **5.2. SUSY**

2095 Limits are set in the parameter space of a set of **SMS** models that characterise both  
2096 natural **SUSY** third generation squark production, and compressed spectra where the  
2097 mass splitting between the particle and **LSP** is small, leading to soft final state jets.  
2098 However as detailed in Section (2.4.1), the individual models are not representative of a  
2099 real physical **SUSY** model as only one decay process is considered. Instead these models  
2100 represent a way to test for signs of specific signatures indicating new physics.

2101 **5.2.1. The  $CL_s$  method**

2102 The  $CL_s$  method [93][94][95] is used to compute the limits for signal models, with the  
2103 one-sided profile likelihood ratio as the test statistic [96].

The test statistic is defined as

$$q(\mu) = \begin{cases} -2\log\lambda(\mu) & \text{when } \mu \geq \hat{\mu}, \\ 0 & \text{otherwise.} \end{cases} \quad (5.1)$$

2104 where

$$\lambda(\mu) = \frac{L(\mu, \theta_\mu)}{L(\hat{\mu}, \hat{\theta})} \quad (5.2)$$

2105 represents the profile likelihood ratio, in which  $\mu \equiv f$  from Section (4.8.4), is the  
2106 parameter characterising the signal strength.  $\hat{\mu}$  is defined as the maximum likelihood  
2107 value,  $\hat{\theta}$  the set of maximum likelihood values of the nuisance parameters and  $\theta_\mu$  the set  
2108 of maximum values of the nuisance parameters for a given value of  $\mu$ .

2109 When  $\mu \equiv f = 1$ , the signal model is considered at its nominal production cross section.  
2110 The distribution of  $q_\mu$  is built up via the generation of pseudo experiments in order to  
2111 obtain two distributions for the background (B) and signal plus background (S+B) cases.

2112 The compatibility of a signal model with observations in data is determined by the  
2113 parameter  $CL_s$ ,

$$\text{CL}_S = \frac{\text{CL}_{S+B}}{\text{CL}_B}, \quad (5.3)$$

2114 with  $\text{CL}_B$  and  $\text{CL}_{S+B}$  defined as one minus the quantiles of the observed value in the  
2115 data of the two distributions. A model is considered to be excluded at 95% confidence  
2116 level when  $\text{CL}_S \leq 0.05$  [97].

### 2117 5.2.2. Interpretation in simplified signal models

2118 Different  $n_{\text{jet}}$  and  $n_b^{\text{reco}}$  bins are used in the interpretation of different **SMS** models. The  
2119 choice of the categories used within each interpretation, are made to maximise the signal  
2120 to background ratio, increasing sensitivity to that particular type of final state signature.  
2121 The production and decay modes of the **SMS** models under consideration are summarised  
2122 in Table 5.3, with limit plots of the experimental reach in these models shown in Figure  
2123 5.10.

2124 The models T1 and T2 are used to characterise the pair production of gluinos and first or  
2125 second generation squarks, respectively, with parameters for the sparticle mass as well  
2126 as on the **LSP** mass. The low number of third generation quarks produced from this  
2127 decay topology makes choosing to interpret within the  $n_b^{\text{reco}} = 0$  category beneficial to  
2128 improving sensitivity to these models

2129 Conversely the T2bb, T1tttt, and T1bbbb **SMS** model describe various production and  
2130 decay mechanisms in the context of third-generation squarks. In this situation considering  
2131 only higher  $n_b^{\text{reco}}$  categories, bring significant improvements to the sensitivity to these  
2132 types of final state signature.

2133 Finally the choice of jet category is made dependant upon the production mechanism,  
2134 where gluino induced and direct squark production results in a large or small number of  
2135 final state jets respectively.

2136 Experimental uncertainties on the **SM** background predictions (10 – 30%, described in  
2137 Section (4.6.1)), the luminosity measurement (4.4%), and the total acceptance times  
2138 efficiency of the selection for the considered signal model (12 – 18%, from Section (4.7))  
2139 are included in the calculation of the limit.

Model	Production/decay	$n_{jet}$	$n_b^{reco}$	Process	Limit	$m_{\tilde{q}/\tilde{g}}^{\text{best}}$ (GeV)	$m_{\text{LSP}}^{\text{best}}$ (GeV)
T1	$pp \rightarrow \tilde{g}\tilde{g}^* \rightarrow q\bar{q}\tilde{\chi}_1^0 q\bar{q}\tilde{\chi}_1^0$	$\geq 4$	0	5.9(a)	5.10(a)	$\sim 950$	$\sim 450$
T2	$pp \rightarrow \tilde{q}\tilde{q}^* \rightarrow q\tilde{\chi}_1^0 q\tilde{\chi}_1^0$	$\leq 3$	0	5.9(b)	5.10(b)	$\sim 775$	$\sim 325$
T2bb	$pp \rightarrow \tilde{b}\tilde{b}^* \rightarrow b\tilde{\chi}_1^0 \bar{b}\tilde{\chi}_1^0$	$\leq 3$	1,2	5.9(c)	5.10(c)	$\sim 600$	$\sim 200$
T1tttt	$pp \rightarrow \tilde{g}\tilde{g}^* \rightarrow t\bar{t}\tilde{\chi}_1^0 t\bar{t}\tilde{\chi}_1^0$	$\geq 4$	2,3, $\geq 4$	5.9(d)	5.10(d)	$\sim 975$	$\sim 325$
T1bbbb	$pp \rightarrow \tilde{g}\tilde{g}^* \rightarrow b\bar{b}\tilde{\chi}_1^0 b\bar{b}\tilde{\chi}_1^0$	$\geq 4$	2,3, $\geq 4$	5.9(e)	5.10(e)	$\sim 1125$	$\sim 650$

**Table 5.3.:** A table representing the **SMS** models interpreted within the analysis. The model name and production and decay chain is specified in the first two columns. Each **SMS** model is interpreted in specific  $n_{jet}$  and  $n_b^{reco}$  categories which are detailed in the third and fourth columns. The last two columns indicate the search sensitivity for each model, representing the largest  $m_{\tilde{q}/\tilde{g}}$  mass beyond which no limit can be set for this particular decay topology. The quoted values are conservatively determined from the observed exclusion based on the theoretical production cross section minus  $1\sigma$  uncertainty.

- 2140 Signal efficiency in the kinematic region defined by  $0 < m_{\tilde{g}/\tilde{q}} < 175$  GeV or  $m_{\tilde{g}/\tilde{q}} < 300$  GeV is strongly affected by the presence of Initial State Radiation (**ISR**). This region in  
 2141 which direct (i.e., non-**ISR** induced) production is kinematically forbidden due to the  $H_T$   
 2142  $> 275$  GeV requirement, therefore a large percentage of signal acceptance is due to the  
 2143 effect of **ISR** jets. Given the large associated uncertainties, no interpretation is provided  
 2144 for this kinematic region.  
 2145
- 2146 The estimates on mass limits shown in Table 5.3, are determined conservatively from the  
 2147 observed exclusion based on the theoretical production cross section, minus  $1\sigma$  uncertainty.  
 2148 The most stringent mass limits on pair-produced sparticles are obtained at low **LSP**  
 2149 masses and larger squark and gluino masses due to the high  $p_T$  jets and consequently  
 2150 high  $H_T$  of such signal topologies. The limits are seen to weaken for compressed spectra  
 2151 points closer to the diagonal, where the signal is populates the lower  $H_T$  bins in which  
 2152 more background resides. For all of the considered models, there is an **LSP** mass beyond  
 2153 which no limit can be set, which can be observed from the figures referenced in the table.  
 2154
- 2155 Two small upwards fluctuations are observed within the data, and are seen at high  $H_T$   
 2156 within the  $n_b^{reco} = 0$  category and at mid- $H_T$  in the  $n_b^{reco} = 1, 2$  categories, see Table 5.2.  
 2157 As each of these fluctuations occur within at least one of the analysis categories that  
 2158 each **SMS** model interpretation is made, the observed exclusions within all **SMS** models  
 2159 are generally found to be weaker than the expected limits in the region of 1-2 standard  
 2160 deviations. In isolation these fluctuations are not significant and additional data would  
 be necessary to make any further conclusions.

Despite these fluctuations, the range of parameter space that can be excluded has been extended with respect to analysis based upon the  $\sqrt{s} = 7$  TeV dataset [98], by up to 225 and 150 GeV for  $m_{\tilde{q}(g)}^{\text{best}}$  and  $m_{LSP}^{\text{best}}$  respectively. The parameter space for light third generation squarks, the main tenet of natural SUSY models, is increasingly squeezed for larger mass splitting, with exclusions in the region of 1 TeV in these topologies.

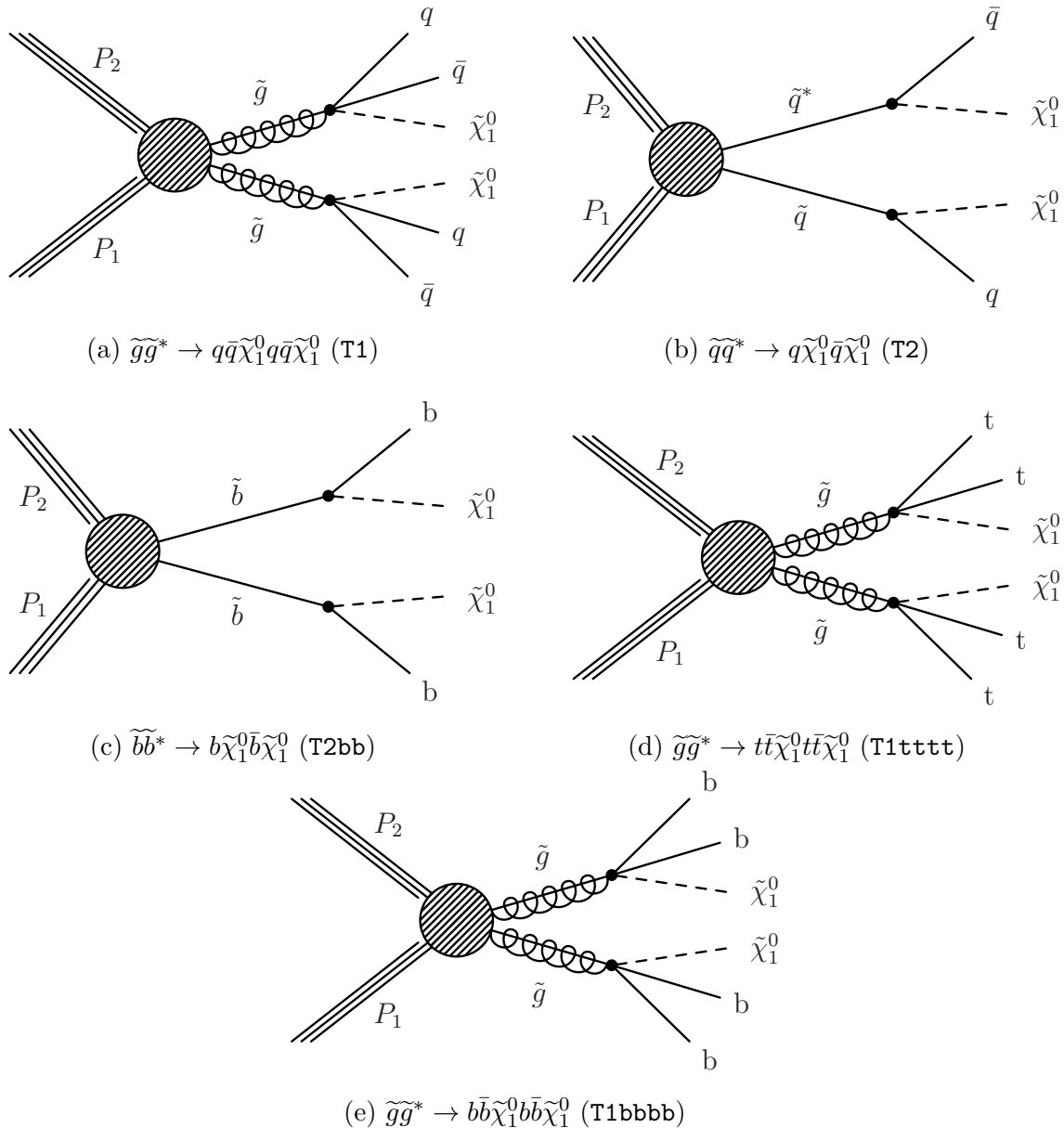


**Figure 5.9.:** Production and decay modes for the various SMS models interpreted within the analysis.

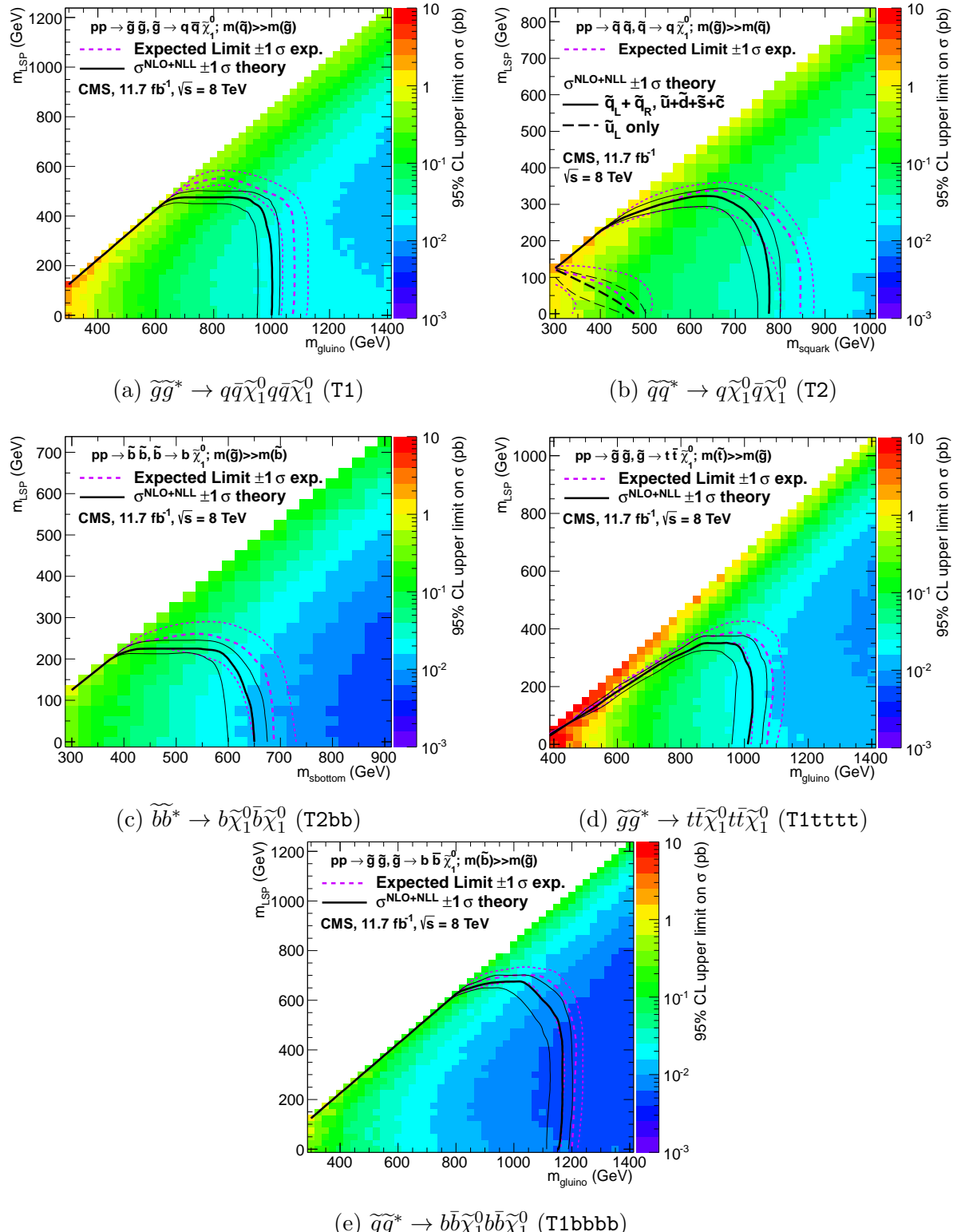


**Figure 5.10.:** Upper limit of cross section at 95% CL as a function of  $m_{\tilde{q}/\tilde{g}}$  and  $m_{LSP}$  for various SMS models. The solid thick black line indicates the observed exclusion region assuming NLO and NLL SUSY production cross section. The analysis selection efficiency is measured for each interpreted model, with the signal yield per point given by  $\epsilon \times \sigma$ . The thin black lines represent the observed excluded region when varying the cross section by its theoretical uncertainty. The dashed purple lines indicate the median (thick line)  $1\sigma$  (thin lines) expected exclusion regions.

# Chapter 6.

## <sup>2166</sup> Searching For Natural SUSY With <sup>2167</sup> B-tag Templates.

<sup>2168</sup> Within this chapter a complimentary technique is discussed as a means to predict the  
<sup>2169</sup> distribution of three and four reconstructed b-quark jets in an event. The recent discovery  
<sup>2170</sup> of the Higgs boson has made third-generation “Natural SUSY” models attractive, given  
<sup>2171</sup> that light top and bottom squarks are a candidate to stabilise divergent loop corrections  
<sup>2172</sup> to the Higgs boson mass.

<sup>2173</sup> Using the  $\alpha_T$  search as a base, a simple template fit is employed to estimate the SM  
<sup>2174</sup> background in higher b-tag multiplicities (3-4) from a fit conducted in a low number of  
<sup>2175</sup> reconstructed b-jets (0-2) control region. As a proof-of-concept, the procedure is applied  
<sup>2176</sup> to the SM enriched  $\mu + \text{jets}$  control sample of the  $\alpha_T$  all-hadronic search detailed in  
<sup>2177</sup> Chapter 4, in both data and simulation. To highlight the relative insensitivity of the  
<sup>2178</sup> choice of b-tagging algorithm working point in the effectiveness of the procedure, results  
<sup>2179</sup> are presented using the CSV tagger (introduced in Section (3.3.2)) for the “Loose”,  
<sup>2180</sup> “Medium” and “Tight” working points.

### <sup>2181</sup> 6.1. Concept

<sup>2182</sup> The dominant SM backgrounds of most SUSY searches are typically  $t\bar{t} + \text{jets}$ ,  $W +$   
<sup>2183</sup> jets,  $Z \rightarrow \nu\bar{\nu} + \text{jets}$  or other rare processes with neutrinos in the final state. These  
<sup>2184</sup> processes are characterised by typically having zero or two underlying b-quarks per event.  
<sup>2185</sup> Conversely a third generation squark production signal, such at the T1tttt and T1bbbb  
<sup>2186</sup> models described in the previous chapter, will typically have four underlying b-quarks in

its final state. As SM processes with similar topologies are rare, an excess of  $n_b^{\text{reco}} = 3, \geq 4$  events would be indicative of a potential natural SUSY signature. Therefore the compatibility of the  $n_b^{\text{reco}}$  distribution in data can be tested via the parameterisation of the SM backgrounds in terms of these two most common underlying b-quark topologies.

Typical underlying b-quark content	Process
= 0	$W \rightarrow l\nu + \text{jets}$ $Z \rightarrow \nu\bar{\nu} + \text{jets}$ $Z/\gamma^* \rightarrow \mu\mu + \text{jets}$
= 1	$t + \text{jets}$
= 2	$t\bar{t} + \text{jets}$

**Table 6.1.:** Typical underlying b-quark content of different SM processes which are common to many SUSY searches.

Thus two templates are defined, Z0 and Z2 (single top processes are a negligible background,  $\sim 1\%$  within the  $\alpha_T$  search, and are combined together with  $t\bar{t}$ ) which represent processes which have an underlying b-quark content of zero or two respectively.

Both these templates are generated through the application of the relevant event selection, and can then be taken from the underlying  $n_b^{\text{reco}}$  distribution directly from simulation. However as discussed within Section (4.5), there are large uncertainties for high  $n_b^{\text{reco}}$  multiplicities due to limited MC statistics. This is particularly prominent for the Z0 templates, where events with a large number of reconstructed b-tags jets are driven primarily by the mis-tagging of light-quarks. Within both the medium and tight working point of the CSV tagger, the expected mis-tagging rate is only around 1 and 0.1% respectively, leading to large uncertainties in the template shape in this region. Therefore to improve the statistical precision of the predictions within the signal region, the formula method introduced in Section (4.5.1) is used.

The generation of the template shapes, are dependant upon the jet-flavour content and b-tagging rate within the phase space of interest, with the tagging probabilities of a jet being a function of the jet  $p_T$ , the pseudo-rapidity  $|\eta|$ , and jet-flavour. This can be observed in Figure 6.1, where the b-tagging / c-quark mis-tagging / light mis-tagging efficiency for the three working points of the CSV tagger are shown as a function of jet  $p_T$ .

Before the template shapes are determined and applied to data, the relevant jet  $p_T$  and  $\eta$  corrections are applied to correct the measured b-tagging rate in simulation to that of

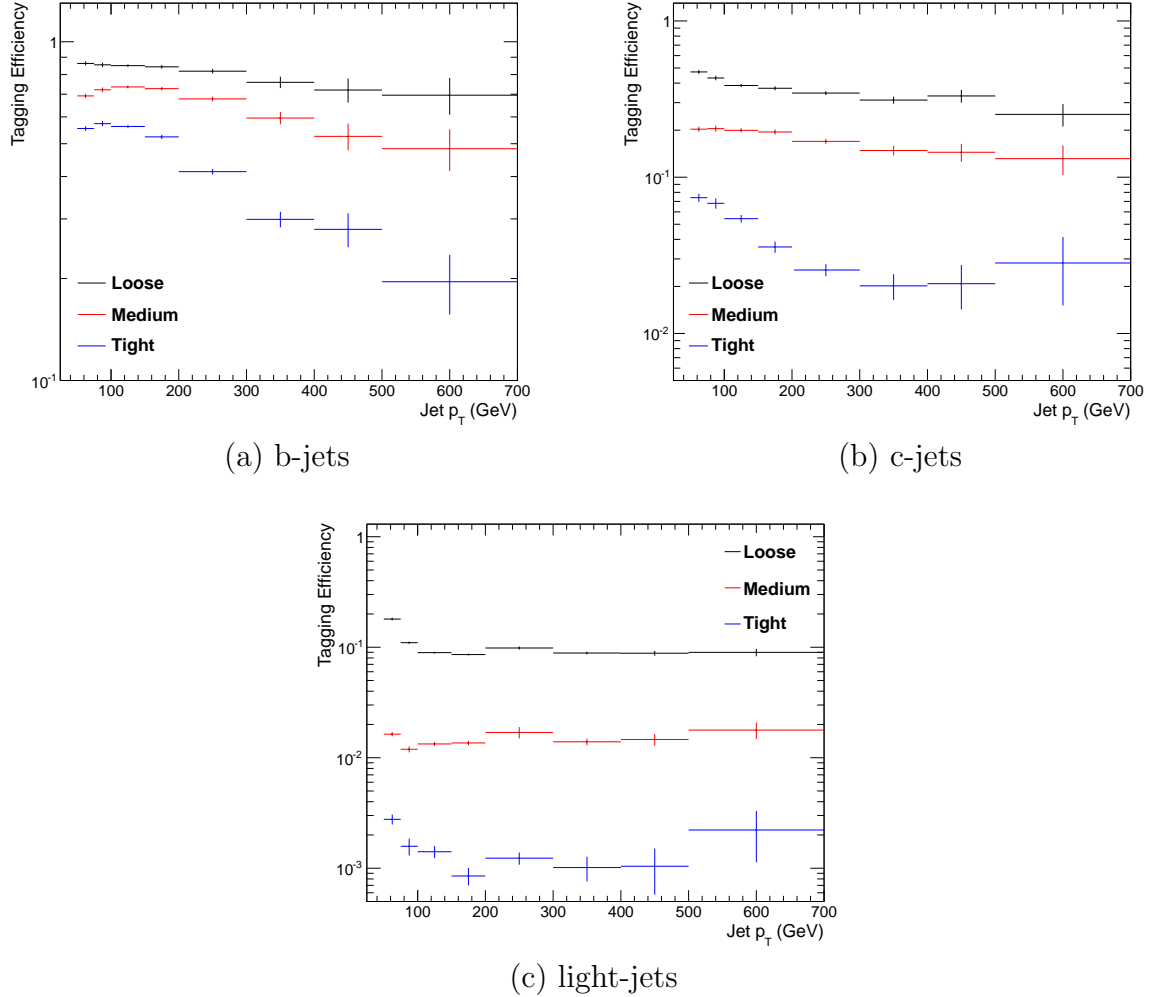


**Figure 6.1.:** The b-tagging (a), c-quark mis-tagging (b), and light-quark mis-tagging rate (c) as measured in simulation after the  $\alpha_T$  analysis,  $\mu + \text{jets}$  control sample selection in the region  $H_T > 375$ .

2212 data, as specified in Section (4.5.3), which propagate through to the average determined  
2213 b-tagging rates per analysis  $H_T$  bin, as in the  $\alpha_T$  analysis.

2214 These two template shapes once generated from simulation, can then be fitted to data in  
2215 a low  $n_b^{reco}$  control region (0-2), by allowing the normalisation constants  $\theta_{Z0}$  and  $\theta_{Z2}$  of  
2216 the two templates to float. The best fit values of  $\theta_{Z0}$  and  $\theta_{Z2}$  are used, along with the  
2217 knowledge of the template shapes, to extrapolate an estimate in the high  $n_b^{reco}$  signal  
2218 region (3,4), which is then compared to what is observed in data. Any large excess in  
2219 data compared to the template prediction would indicate that the  $n_b^{reco}$  distribution is  
2220 not adequately described by the SM backgrounds which compose the templates. This  
2221 method can, in principle, be applied to any analysis where the signal hypothesis has a

2222 larger underlying b-quark spectra than the **SM** backgrounds, as it solely relies on fitting  
2223 to the shape of the  $n_b^{\text{reco}}$  distribution.

2224 However in the scenario where a **SUSY** signal sits at a low number of underlying b-quarks,  
2225 the template would be unable to discriminate between this signal and background and  
2226 would be accommodated within the fit in the control region. This will be the case unless  
2227 the jet  $p_T$  distribution of the signal and background were drastically different, in which  
2228 case there would, anyway be many more sensitive ways to establish the presence of a  
2229 signal in the data than this method. Indeed the template method is only really applicable  
2230 to the hypothesis that any signal resides at high  $n_b^{\text{reco}}$  and that the control region  $0$   
2231  $\geq n_b^{\text{reco}} \leq 2$  is indeed signal free.

## 2232 6.2. Application to the $\alpha_T$ Search

2233 As detailed in the previous chapter, the  $\alpha_T$  analysis is a search for **SUSY** particles  
2234 in all-hadronic final states, utilising the kinematic variable  $\alpha_T$  to suppress QCD to a  
2235 negligible level. **SM** enriched control samples are used to estimate the background within  
2236 an all-hadronic signal region.

2237 The selection for the  $\mu +$  jets control samples defined in Section (4.2.3) is used to  
2238 demonstrate the template fitting procedure both conceptually in simulation, and also  
2239 when applied in data. This is chosen, as such a selection is dominated by events stemming  
2240 from the **SM** processes with little or no signal contamination from potential new physics.  
2241 Neither are contributions from rare **SM** processes with a higher underlying b-quark  
2242 content (e.g.  $t\bar{t}b\bar{b}$ ) expected. For these reasons, there is a degree of confidence that the  
2243 procedure should adequately describe the observations in data when extrapolated to the  
2244 signal region.

2245 The analysis presented here is binning in source jet multiplicity bins, of 3, 4 and  $\geq 5$   
2246 reconstructed jets per event (di-jet events are not included as there is no contribution  
2247 to the high  $n_b^{\text{reco}}$  region (3,4)) , in order to reduce the kinematic jet  $p_T$  dependence.  
2248 Furthermore the analysis is split into three  $H_T$  regions,

2249 • 275-325 GeV

2250 • 325-375 GeV

2251 •  $> 375$  GeV

2252 contrary to the eight used within the  $\alpha_T$  analysis. Templates for both underlying b-quark  
2253 content hypotheses are then generated for the nine defined analysis bins.

### 2254 6.2.1. Proof of principle in simulation

2255 In order to demonstrate that the template procedure produces accurate predictions  
2256 within simulation, the simulation samples in the analysis are firstly split into two to allow  
2257 for statistically independent fits to be performed.

2258 By combining the relevant ingredients necessary to employ the formula method,  $n_b^{\text{reco}}$   
2259 templates for  $Z = 0$  and  $Z= 2$  are generated individually for each  $n_{\text{jet}}$  and  $H_T$  bin using  
2260 one half of each simulation sample. A fit of these two templates is then performed in the  
2261 low  $n_b^{\text{reco}}$  (0-2) region, back to the sum of the other halves of each simulation sample in  
2262 order to check that the relevant information can be recovered in the  $n_b^{\text{reco}}$  signal region  
2263 (3-4).

2264 The fits are performed independently within each of the defined analysis bins to reduce the  
2265 dependence of the shapes of these distributions on simulation. The half of the simulation  
2266 sample for which the templates are fitted too, are taken directly from simulation, extending  
2267 this procedure to also be a validation of the formula method in accurately describing the  
2268  $n_b^{\text{reco}}$  distribution within the control region itself. Additionally as this test is performed  
2269 in simulation, the relevant corrections of the b-tagging rates between data and simulation  
2270 are *not* applied.

2271 Within Figure 6.2, the results of this fitting procedure are shown for each **CSV** working  
2272 point. Results are presented for the  $n_{\text{jet}} \geq 5$  category, using the  $\mu + \text{jets}$  control sample  
2273 selection in the inclusive  $H_T > 375$  GeV analysis bin. The grey bands represent the  
2274 statistical uncertainty on the template shapes. Additional fits are shown for other  $n_{\text{jet}}$   
2275 categories can be found within Appendix D.1.

2276 Furthermore the extrapolated fit predictions within the high  $n_b^{\text{reco}}$  signal region, are  
2277 summarised for all  $H_T$  bins and working points in Table 6.2.

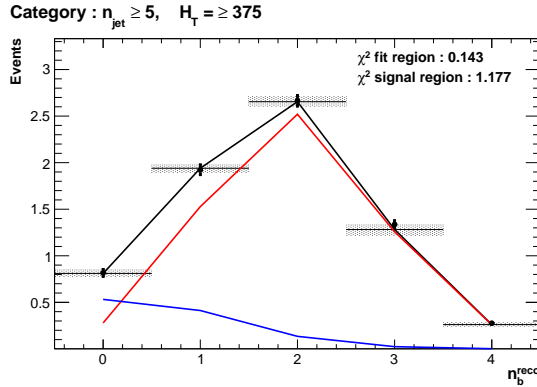
2278 The pull distributions for all the fits performed can be found in Appendix D.2, and are  
2279 compatible with a mean of zero and standard deviation of one, showing no obvious bias to  
2280 the fitting procedure. The good overall agreement summarised in the table validates both  
2281 the formula method used to generate the templates as well as the method of extrapolation  
2282 to the high  $n_b^{\text{reco}}$  signal region. The application of this method to the same selection in a

$H_T$	275-325	325-375	>375
Loose working point			
Simulation $n_b = 3$	$793.0 \pm 14.8$	$387.9 \pm 10.2$	$794.1 \pm 14.34$
Template $n_b = 3$	$820.4 \pm 26.7$	$376.3 \pm 11.9$	$780.1 \pm 15.1$
Simulation $n_b = 4$	$68.2 \pm 3.9$	$27.6 \pm 2.7$	$91.28 \pm 4.9$
Template $n_b = 4$	$72.5 \pm 4.7$	$28.25 \pm 2.34$	$84.4 \pm 3.8$
Medium working point			
Simulation $n_b = 3$	$133.7 \pm 5.7$	$74.5 \pm 4.5$	$164.2 \pm 6.4$
Template $n_b = 3$	$132.8 \pm 4.8$	$74.5 \pm 3.9$	$159.9 \pm 5.7$
Simulation $n_b = 4$	$1.6 \pm 0.6$	$0.6 \pm 0.4$	$3.4 \pm 0.9$
Template $n_b = 4$	$1.8 \pm 0.2$	$1.1 \pm 0.2$	$4.1 \pm 0.4$
Tight working point			
Simulation $n_b = 3$	$26.9 \pm 2.6$	$13.9 \pm 1.9$	$31.8 \pm 2.9$
Template $n_b = 3$	$24.7 \pm 1.5$	$13.8 \pm 1.2$	$28.1 \pm 1.5$
Simulation $n_b = 4$	$0.5 \pm 0.4$	-	-
Template $n_b = 4$	$0.1 \pm 0.1$	$0.1 \pm 0.1$	$0.2 \pm 0.1$

**Table 6.2.:** Summary of the fit predictions in the  $n_b^{reco}$  signal region for  $n_{jet} = 3, = 4, \geq 5$ . The fit region is  $n_b^{reco} = 0, 1, 2$  and simulation yields are normalised to an integrated luminosity of  $10 \text{ fb}^{-1}$ . The uncertainties quoted on the template yields are purely statistical.

2283 data control sample, is now used to demonstrate necessary control over the efficiency and  
 2284 mis-tagging rates when b-tagging scale factors are applied, and to test the assumption of  
 2285 no signal contamination with the  $\mu + \text{jets}$  control sample.

2286



(a) Loose working point :  $n_{jet} \geq 5$

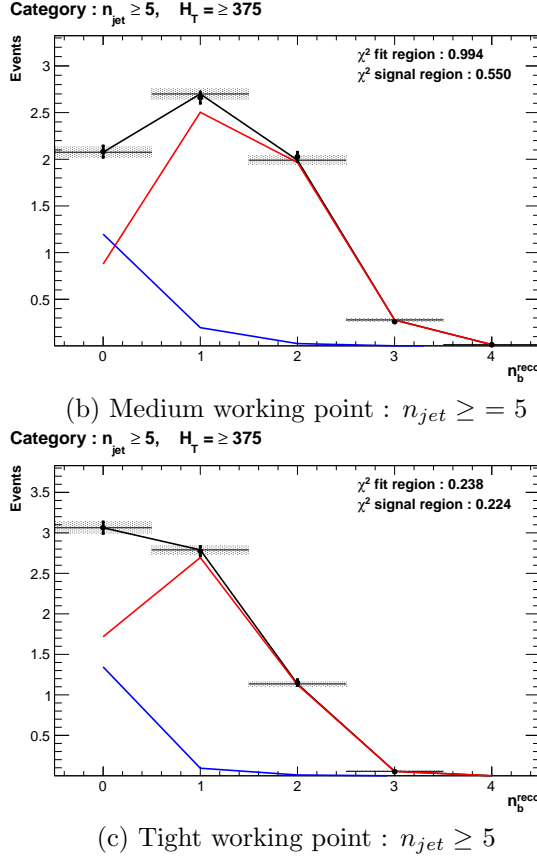


**Figure 6.2.:** The results of fitting the  $Z = 0$  and  $Z = 2$  templates to the  $n_b^{reco} = 0, 1, 2$  bins taken directly from simulation in the region  $H_T > 375$  GeV, for the  $n_{jet} \geq 5$  category. The blue template represents  $Z = 0$ , while the red template represents  $Z = 2$ . Grey bands represent the statistical uncertainty of the fit. The  $\chi^2$  parameter displayed represents the goodness of fit to the low  $n_b^{reco}$  (0-2) control region.

### 6.2.2. Results in a data control sample

The procedure is now applied to the 2012 8 TeV dataset in the  $\mu +$  jets control sample, to establish the validity of this method in data. The relevant data to simulation b-tagging scale factors are applied to produce corrected values of the efficiency and mis-tagging rates within each analysis bin [86].

Figure 6.3 shows the results of the templates derived from simulation to each of the three defined  $H_T$  bins, in the  $n_{jet} \geq 5$  category for the medium working point CSV tagger (the same working point used within the  $\alpha_T$  analysis). Grey bands represent the statistical uncertainty of the fit combined in quadrature with the systematic uncertainties of varying

the data to simulation scale factors up and down by their b-tag scale factor systematic uncertainties. Additional fit results for other jet multiplicities are found in Appendix D.3

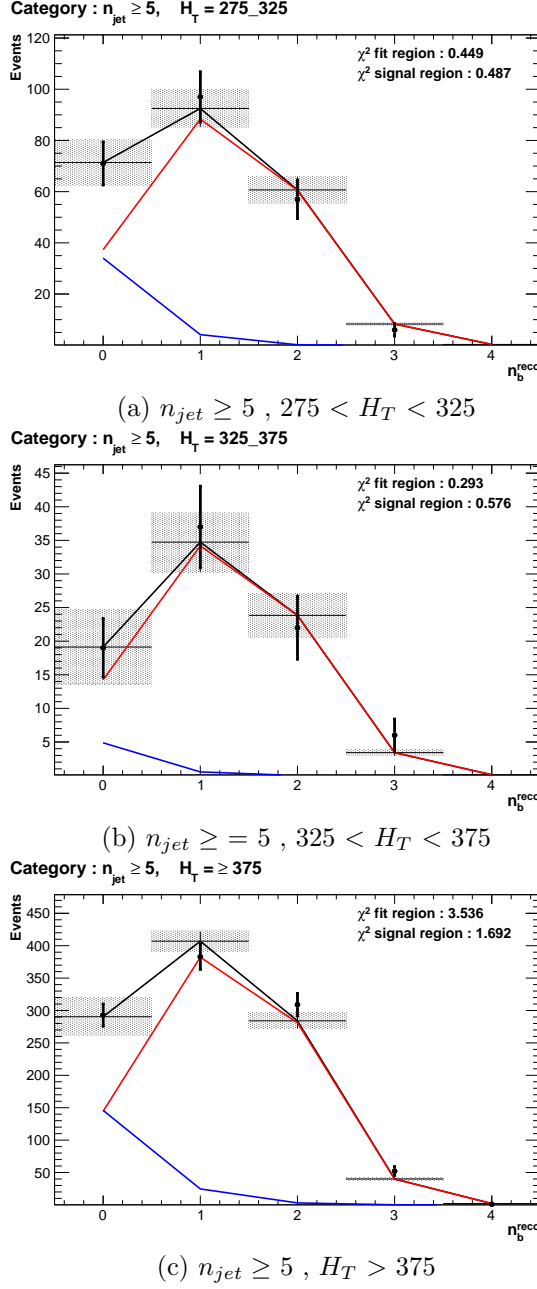


**Figure 6.3.:** The results of fitting the  $Z = 0$  and  $Z = 2$  templates to the  $n_b^{reco} = 0, 1, 2$  bins taken directly from data, for the  $n_{jet} \geq 5$  category and medium CSV working point. The blue template represents  $Z = 0$ , while the red template represents  $Z = 2$ . The  $\chi^2$  parameter displayed represents the goodness of fit to the low  $n_b^{reco}$  (0-2) control region.

2298 The numerical results and extrapolation to the  $n_b^{reco} = 3, 4$  bins for all  $H_T$  and working  
 2299 points is shown in Table 6.3.

$H_T$	275-325	325-375	>375
Loose working point			
Data $n_b = 3$	838	394	717
Template $n_b = 3$	$861.8 \pm 38.1$	$372.1 \pm 18.4$	$673.2 \pm 34.5$
Data $n_b = 4$	81	43	81
Template $n_b = 4$	$78.5 \pm 5.8$	$27.6 \pm 2.6$	$78.6 \pm 3.3$
Medium working point			
Data $n_b = 3$	137	79	152
Template $n_b = 3$	$131.2 \pm 4.3$	$66.1 \pm 2.9$	$137.8 \pm 5.7$
Data $n_b = 4$	1	1	3
Template $n_b = 4$	$1.8 \pm 0.1$	$0.9 \pm 0.1$	$3.1 \pm 0.2$
Tight working point			
Data $n_b = 3$	24	15	25
Template $n_b = 3$	$23.0 \pm 0.9$	$12.9 \pm 0.6$	$20.3 \pm 1.1$
Data $n_b = 4$	0	0	1
Template $n_b = 4$	$0.1 \pm 0.1$	$0.1 \pm 0.1$	$0.2 \pm 0.1$

**Table 6.3.:** Summary of the fit predictions in the  $n_b^{reco}$  signal region of the  $\mu +$  jets control sample, for  $n_{jet} = 3, = 4, \geq 5$ . The fit region is  $n_b^{reco} = 0, 1, 2$  using  $11.4 \text{ fb}^{-1}$  of data at  $\sqrt{s} = 8\text{TeV}$ . The uncertainties quoted on the template yields are purely statistical.

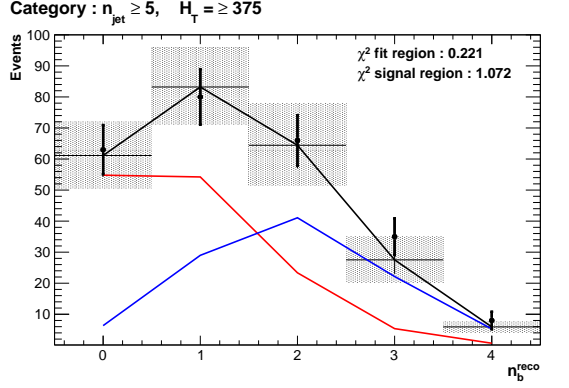
2300 When this method is applied to the  $\mu +$  jets control sample, it is expected that good  
 2301 agreement would be observed between prediction and observation (in the absence of signal  
 2302 contamination) if the procedure is valid. The good compatibility for all working points  
 2303 as shown in the table, demonstrate that this is the case. However no such assumptions  
 2304 can be made when applied to the signal region of the  $\alpha_T$  search.

### 2305 6.2.3. Application to the $\alpha_T$ hadronic search region

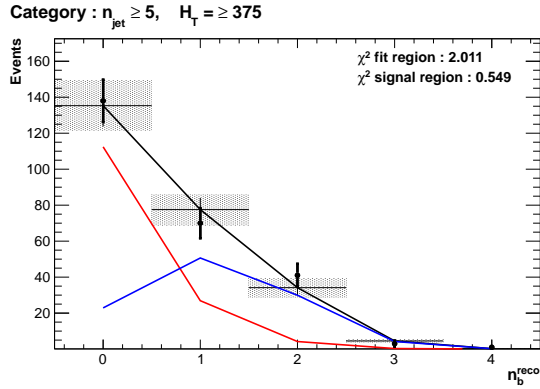
2306 As an accompaniment to the background estimation methods outlined in the  $\alpha_T$  search,  
 2307 the b-tag template method offers a complimentary way of testing the **SM** only background  
 2308 hypothesis within the hadronic signal region of the search. In the presence of a natural  
 2309 **SUSY** signature containing four underlying  $\tilde{b}$  or  $\tilde{t}$  squarks, which subsequently decay to t  
 2310 or b quarks, the number of reconstructed  $n_b^{reco} = 3, \geq 4$  events will be enhanced.

2311 Figure 6.4 show the the results of the templates derived from simulation to each of  
 2312 the three **CSV** working points, in the  $n_{jet} \geq 5, H_T > 375 \text{ GeV}$  category. Grey bands  
 2313 represent the statistical uncertainty of the fit combined in quadrature with the systematic  
 2314 uncertainties of varying the data to simulation scale factors up and down by their

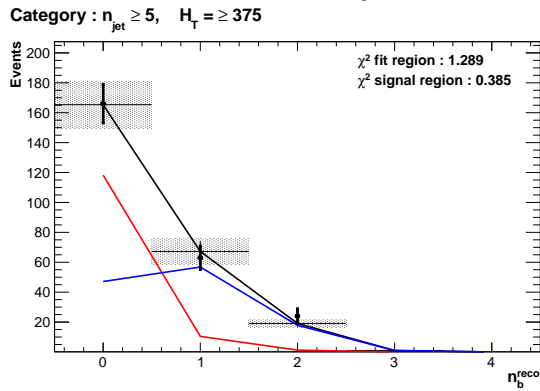
measured systematic uncertainties. Additional fit results for other jet multiplicities are found in Appendix D.4



(a) Loose working point :  $n_{jet} \geq 5, H_T > 375$



(b) Medium working point :  $n_{jet} \geq 5, H_T > 375$



(c) Tight working point :  $n_{jet} \geq 5, H_T > 375$

**Figure 6.4.:** The results of fitting the  $Z = 0$  and  $Z = 2$  templates to the  $n_b^{reco} = 0, 1, 2$  bins taken from data, in the  $n_{jet} \geq 5$  and  $H_T > 375$  category for all CSV working points. The blue template represents  $Z = 0$ , while the red template represents  $Z = 2$ . The  $\chi^2$  parameter displayed represents the goodness of fit to the low  $n_b^{reco}$  (0-2) control region.

2317 The numerical results and extrapolation to the  $n_b^{reco} = 3, 4$  bins for all  $H_T$  and working  
 2318 points are shown in Table 6.4. No excess of data is found and predictions from this  
 2319 method are found to be compatible with the  $\alpha_T$  maximum likelihood fit results from  
 2320 Table 5.2.

$H_T$	275-325	325-375	>375
Loose working point			
Data $n_b = 3$	198	85	126
Template $n_b = 3$	$207.1 \pm 33.3$	$103.4 \pm 10.9$	$124.98 \pm 16.2$
Data $n_b = 4$	15	9	16
Template $n_b = 4$	$15.9 \pm 3.7$	$8.05 \pm 1.2$	$13.1 \pm 2.2$
Medium working point			
Data $n_b = 3$	28	15	12
Template $n_b = 3$	$24.4 \pm 1.7$	$12.7 \pm 1.2$	$19.9 \pm 2.8$
Data $n_b = 4$	1	0	2
Template $n_b = 4$	$0.3 \pm 0.2$	$0.3 \pm 0.1$	$0.5 \pm 0.2$
Tight working point			
Data $n_b = 3$	5	2	0
Template $n_b = 3$	$4.03 \pm 0.3$	$2.4 \pm 0.3$	$3.1 \pm 0.3$
Data $n_b = 4$	1	0	0
Template $n_b = 4$	$0.1 \pm 0.1$	$0.1 \pm 0.1$	$0.0 \pm 0.1$

**Table 6.4.:** Summary of the fit predictions in the  $n_b^{reco}$  signal region of the  $\mu +$  jets control sample, for  $n_{jet} = 3, = 4, \geq 5$ . The fit region is  $n_b^{reco} = 0, 1, 2$  using  $11.7 \text{ fb}^{-1}$  of data at  $\sqrt{s} = 8\text{TeV}$ . The uncertainties quoted on the template yields are purely statistical.

### 2321 6.3. Summary

2322 A **SUSY** signature such as one from gluino-induced third-generation squark production,  
 2323 would result in a final state with an underlying b-quark content greater than two. In  
 2324 order to be able to discriminate such signatures from the **SM** background, templates are  
 2325 generated based on a parameterisation of the number of the **SM** processes, where the  
 2326 underlying b-quarks per event is typically zero or two. These templates are then fit to  
 2327 data in a low  $n_b^{reco}$  (0-2) control region in order to extrapolate a prediction in a high  
 2328  $n_b^{reco}$  (3-4) signal region. This approach is built upon the assumptions that the defined  
 2329 control region is almost entirely free of any possible signal contamination from either a  
 2330 third generation **SUSY** signal, or other possible event topologies with a small number of  
 2331 b quarks in the final state.

2332 The method was demonstrated both in simulation and also in data, using the **SM** enriched  
 2333  $\mu +$  jets selection from the  $\alpha_T$  search, to prove conceptually and experimentally that the

2334 method is valid and there is adequate control over the efficiency and mis-tagging rates  
2335 in data for all working points of the **CSV** tagger. Additionally this method was also  
2336 applied to the  $\alpha_T$  analysis signal region, where good agreement is observed between the  
2337 predictions from the template extrapolations, observations in data and the background  
2338 estimation method of the  $\alpha_T$  analysis.

# Chapter 7.

## <sup>2339</sup> Conclusions

- <sup>2340</sup> A search for supersymmetry is presented based on a data sample of pp collisions collected  
<sup>2341</sup> at  $\sqrt{s} = 8$  TeV, corresponding to an integrated luminosity of  $11.7 \pm 0.5$  fb<sup>-1</sup>. Final  
<sup>2342</sup> states with two or more jets and significant  $\cancel{E}_T$ , a typical final state topology of R-parity  
<sup>2343</sup> conserving SUSY models have been analysed and in which the  $\alpha_T$  variable is utilised  
<sup>2344</sup> as the main discriminator between balanced multi-jet backgrounds and those with real  
<sup>2345</sup> missing energy. An additional complementary approach using a template method to  
<sup>2346</sup> estimate the b-tag jet distribution of SM processes, to search for gluino induced third  
<sup>2347</sup> generation squark SUSY production is also introduced, in which the  $\alpha_T$  search selection  
<sup>2348</sup> is applied in both simulation and data to validate this technique.
- <sup>2349</sup> Additionally a measurement the performance of the Level-1 trigger for jets and energy  
<sup>2350</sup> sum quantities is also presented. These studies quantify any change in level-1 performance  
<sup>2351</sup> after the introduction of a 5 GeV jet seed threshold into the jet algorithm configuration.  
<sup>2352</sup> This change is introduced to facilitate a reduction in the rate at which jets are formed  
<sup>2353</sup> at level-1 from pile-up jets which are not of interest to physics analyses. This change  
<sup>2354</sup> is necessary to ensure that trigger thresholds can be maintained at lower values, in  
<sup>2355</sup> the presence of an increasing number of pile-up interactions per event over the 2012  
<sup>2356</sup> run period. No significant change in single jet trigger efficiencies is observed and good  
<sup>2357</sup> performance is observed for a range of level-1 quantities.
- <sup>2358</sup> Within the SUSY search presented in this analysis, the sum of standard model backgrounds  
<sup>2359</sup> binned in  $H_T$ ,  $n_b^{\text{reco}}$  and  $n_{\text{jet}}$  categories are estimated from a simultaneous binned likelihood  
<sup>2360</sup> fit to a hadronic signal selection and  $\mu + \text{jets}$ ,  $\mu\mu + \text{jets}$ , and  $\gamma + \text{jets}$  control samples.  
<sup>2361</sup> Systematic errors due to theory, detector effects and analysis choices are quantified  
<sup>2362</sup> through the use of data driven closure tests and accounted for in the final interpretation,  
<sup>2363</sup> where observations in data are found to be compatible with a SM only hypothesis.

- 2364 In the absence of a signal like excess the analysis is further interpreted in a set of **SMS**  
2365 models. In the considered models with gluino pair production and for small **LSP** masses,  
2366 exclusion limits of the gluino mass are in the range 950-1125 GeV. For **SMS** models  
2367 with direct squark pair production, first or second generation squarks are excluded up to  
2368 around 775 GeV and bottom squarks are excluded up to 600 GeV, again for small **LSP**  
2369 masses. In the context of ‘natural’ **SUSY** models, with many reconstructed b-jets in the  
2370 final state, limits are set in the range of 975-1125 GeV again for large mass splittings  
2371 between the parents squark and the **LSP**.
- 2372 The template method, whose purpose is to identify any excess in data arising from third  
2373 generation signatures, finds results that are compatible with the  $\alpha_T$  search and a **SM** only  
2374 hypothesis at a high number of reconstructed b-jets. As light third generation squarks  
2375 are an important feature of ‘natural’ **SUSY** models if they are to solve the fine tuning  
2376 problem [99], the limits imposed through interpretations in the T1bbbb and T1tttt **SMS**  
2377 models within the  $\alpha_T$  search, put pressure on such theories, by squeezing the parameter  
2378 space in which ‘natural’ **SUSY** can reside.

# Appendix A.

## <sup>2380</sup> **Miscellaneous**

### <sup>2381</sup> **A.1. Jet Identification Criteria**

<sup>2382</sup> For Calo jets the following criteria were applied:

Loose CaloJet Id	
Variable	Definition
$f_{HPD} < 0.98$	Fraction of jet energy contributed from “hottest” <b>HPD</b> , which rejects <b>HCAL</b> noise.
$f_{EM} > 0.01$	Noise from the <b>HCAL</b> is further suppressed by requiring a minimal electromagnetic component to the jet $f_{EM}$ .
$N_{hits}^{90} \geq 2$	Jets that have $> 90\%$ of its energy from a single channel are rejected, to serve as a safety net that catches jets arising from undiagnosed noisy channels.

**Table A.1.:** Criteria for a reconstructed jet to pass the loose calorimeter jet id.

<sup>2383</sup> For PF jets the following criteria were applied:

---

Loose PF jet Id	
Variable	Definition
<code>nfhJet &lt; 0.99</code>	Fraction of jet composed of neutral hadrons. <b>HCAL</b> noise tends to populate high values of neutral hadron fraction.
<code>nemfJet &lt; 0.99</code>	Fraction of jet composed of neutral electromagnetic energy. <b>ECAL</b> noise tends to populate high values of neutral EM fraction.
<code>nmultiJet &gt; 1</code>	Number of constituents that jet is composed from.
<code>chfJet &gt; 0</code>	Fraction of jet composed of charged hadrons.
<code>cmultiJet &gt; 0</code>	Number of charged particles that compose jet.
<code>cemfJet &lt; 0.99</code>	Fraction of jet composed of charged electromagnetic energy.

---

**Table A.2.:** Criteria for a reconstructed jet to pass the loose PF jet id.

2384 **A.2. Primary Vertices**

2385 The pileup per event is defined by the number of 'good' reconstructed primary vertices  
2386 in the event, with each vertex satisfying the following requirements

---

Good primary vertex requirement	
Variable	Definition
$N_{dof} > 4$	The number of degree of freedom, from the vertex fit to compute the best estimate of the vertex parameters.
$ \Delta z_{vtx}  < 24\text{cm}$	The distance, $ \Delta z_{vtx} $ , to the position of the closest <b>HLT</b> primary vertex.
$\rho < 2\text{cm}$	The perpendicular distance of track position to the beam spot.

---

**Table A.3.:** Criteria for a vertex in an event to be classified as a 'good' reconstructed primary vertex.

# Appendix B.

## <sup>2387</sup> L1 Jets

### <sup>2388</sup> B.1. Jet matching efficiencies

<sup>2389</sup> The single jet turn-on curves are derived from events independent of whether the leading  
<sup>2390</sup> jet in an event is matched to a Level 1 jet using  $\Delta R$  matching detailed in Section (3.4.3)  
<sup>2391</sup> or not. These turn-ons are produced from events which are not triggered on jet quantities  
<sup>2392</sup> and therefore it is not guaranteed that the lead jet of an event will be seeded by a Level  
<sup>2393</sup> 1 jet. Figure B.1 shows the particular matching efficiency of a lead jet to a L1 jet.

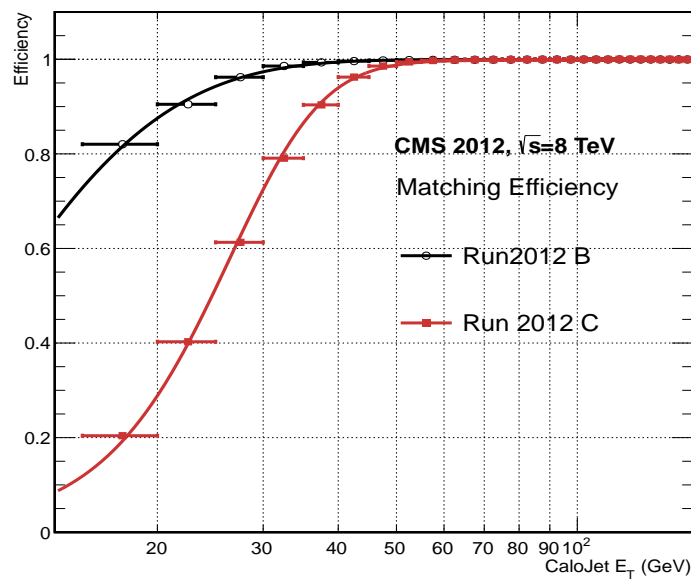


**Figure B.1.:** Leading jet matching efficiency as a function of the offline CaloJet  $E_T$ , measured in an isolated muon triggered dataset in the 2012B and 2012C run periods.

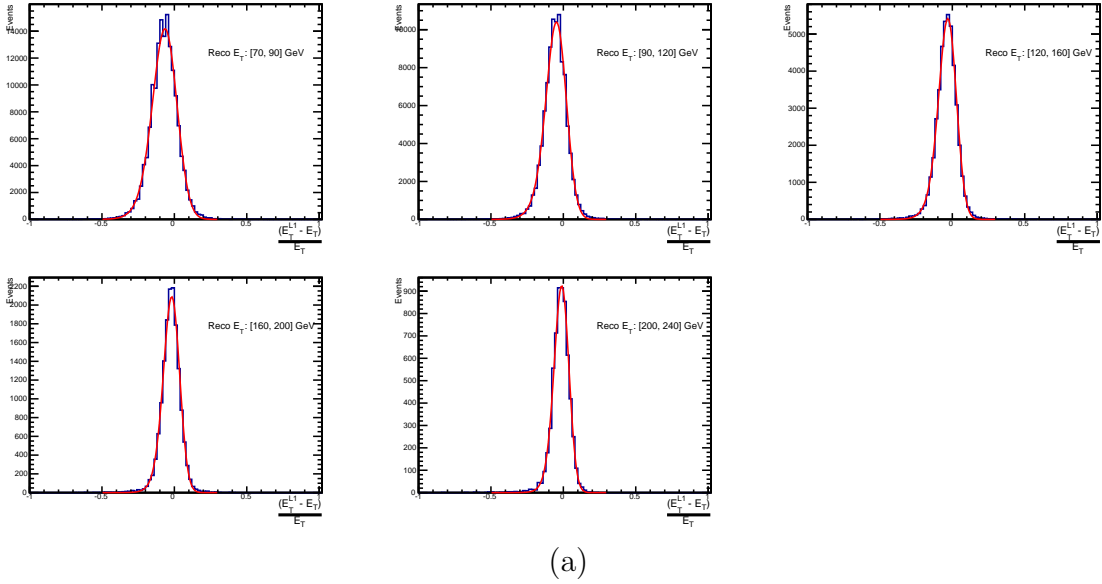
Run Period	$\mu$	$\sigma$
2012B	$6.62 \pm 0.01$	$0.79 \pm 0.03$
2012C	$19.51 \pm 0.03$	$7.14 \pm 0.02$

**Table B.1.:** Results of a cumulative EMG function fit to the turn-on curves for the matching efficiency of the leading jet in an event to a Level-1 jet in run 2012C and 2012B data, measured in an isolated muon triggered sample. The turn-on point,  $\mu$ , and resolution,  $\sigma$ , are measured with respect to offline Calo Jet  $E_T$ .

2394 It can be seen that the turn on is sharper during the 2012B run period. The seed  
 2395 threshold requirement of a 5 GeV jet seed in run 2012C results in more events in which  
 2396 even the lead offline jet does not have an associated L1 jet. For larger jet  $E_T$  thresholds,  
 2397 typical of thresholds used in physics analyses, 100% efficiency is observed, and therefore  
 2398 this effect has no impact to overall physics performance.

2399 The matching efficiencies have a  $\mu$  values of 6.62 GeV and 19.51 GeV for Run 2012B  
 2400 and 2012C respectively and is shown in Table B.1.

## 2401 B.2. Leading Jet Energy Resolution



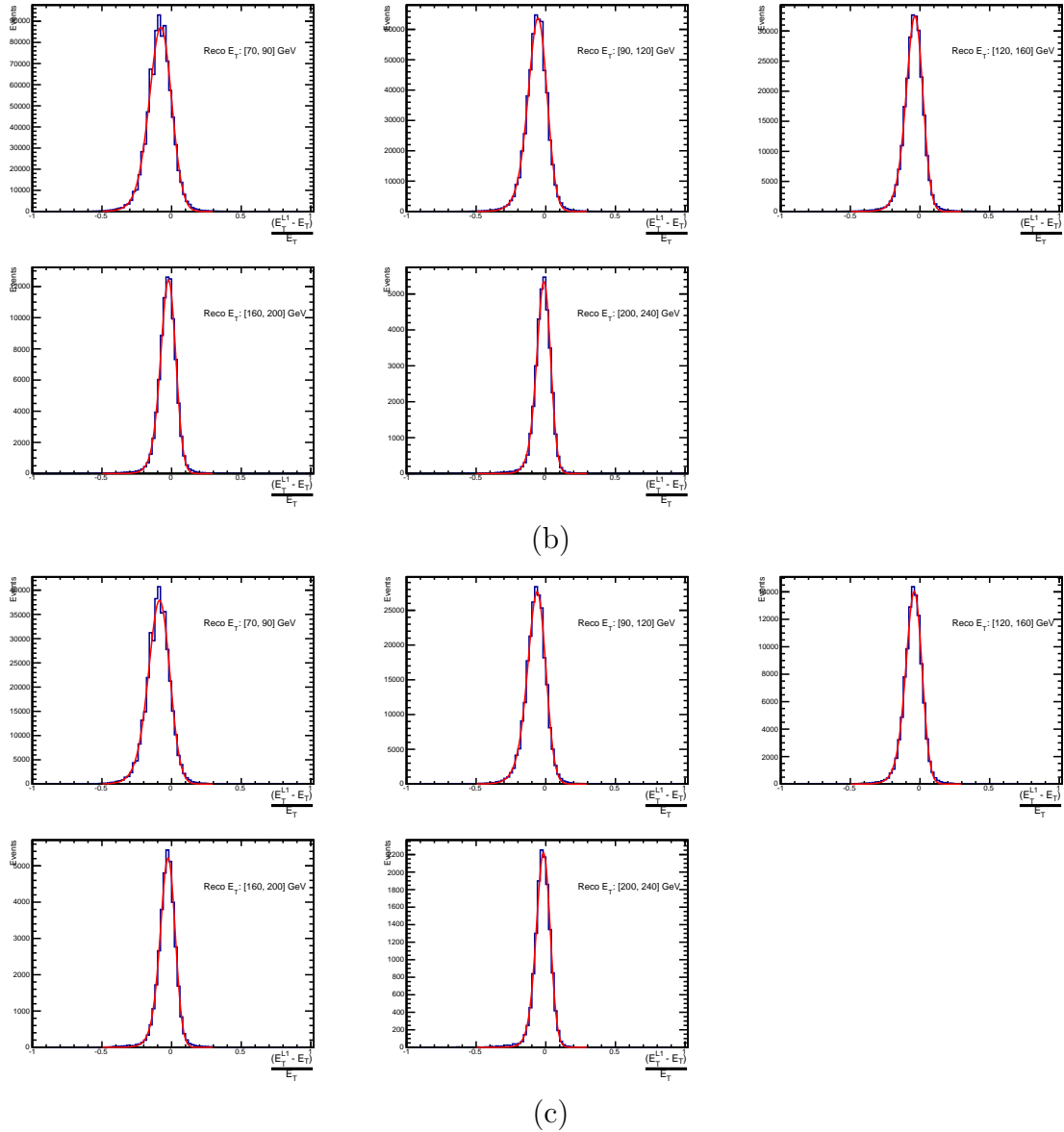
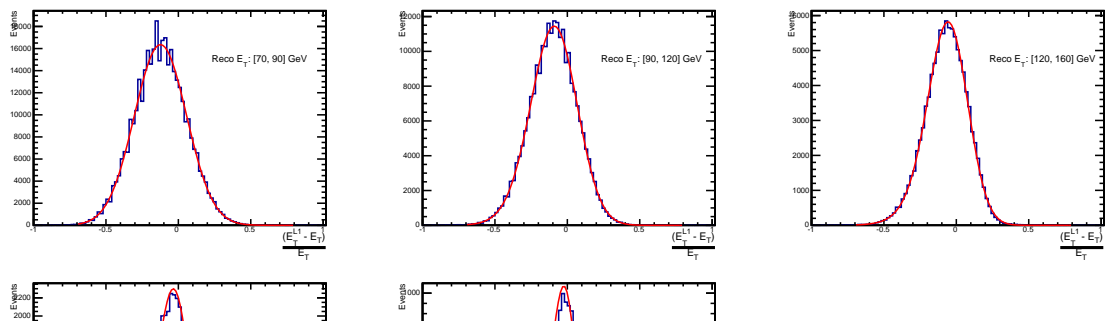
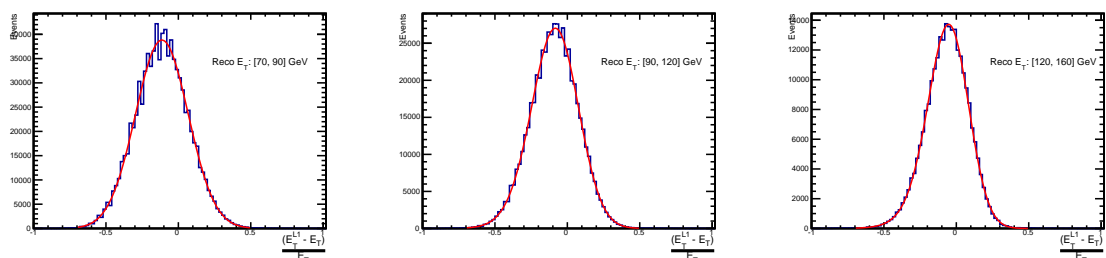


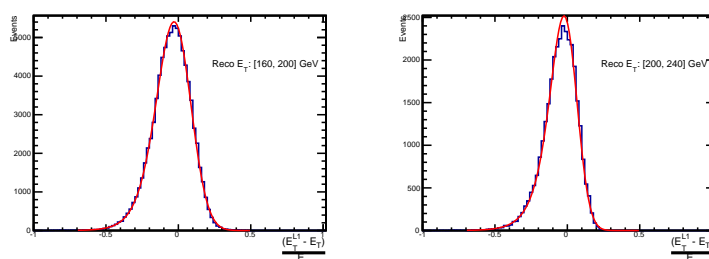
**Figure B.2.:** Resolution plots of the leading offline jet Calo  $E_T$  measured as a function of  $\frac{(L1 E_T - \text{Offline } E_T)}{\text{Offline } E_T}$  for low (a), medium (b) and high (c) pile-up conditions as defined in Section (3.4.4).

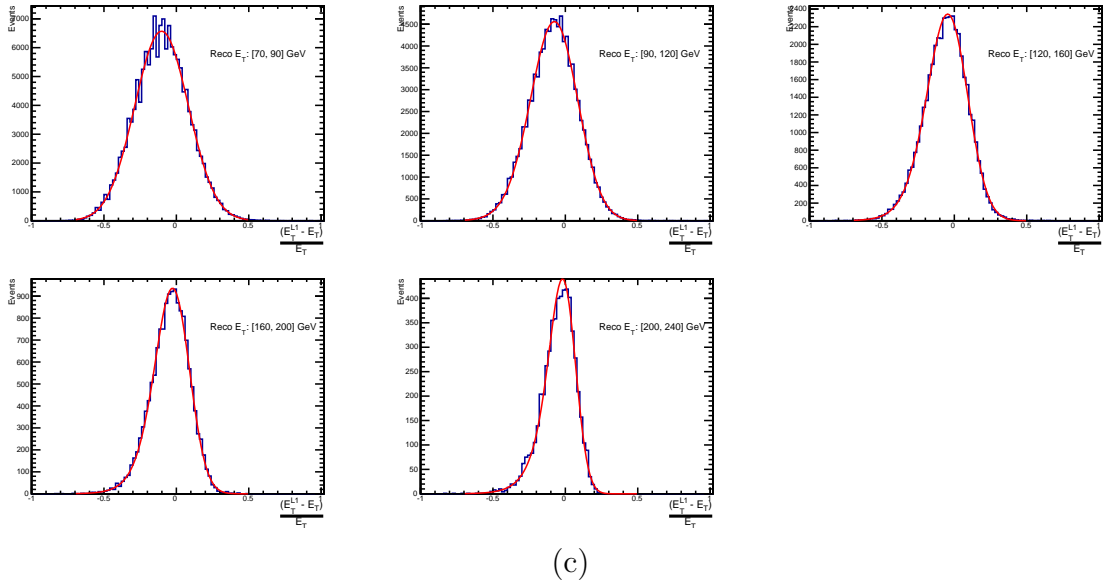


(a)



(b)





(c)

**Figure B.3.:** Resolution plots of the leading offline jet PF  $E_T$  measured as a function of  $\frac{(L1 E_T - \text{Offline } E_T)}{\text{Offline } E_T}$  for low (a), medium (b) and high (c) pile-up conditions as defined in Section (3.4.4).

### 2402 B.3. Resolution for Energy Sum Quantities

2403 The following plots show the resolution parameters for energy sum quantities as a function  
 2404 of the quantity ( $q$ ) itself. In this case, The  $\mu$ ,  $\sigma$  and  $\lambda$  fit values to an **EMG** function  
 2405 defined by Equation (3.3) for each of the individual  $\frac{(L1 q - \text{Offline } q)}{\text{Offline } q}$  distributions, in bins of  
 2406 the quantity  $q$  is displayed.

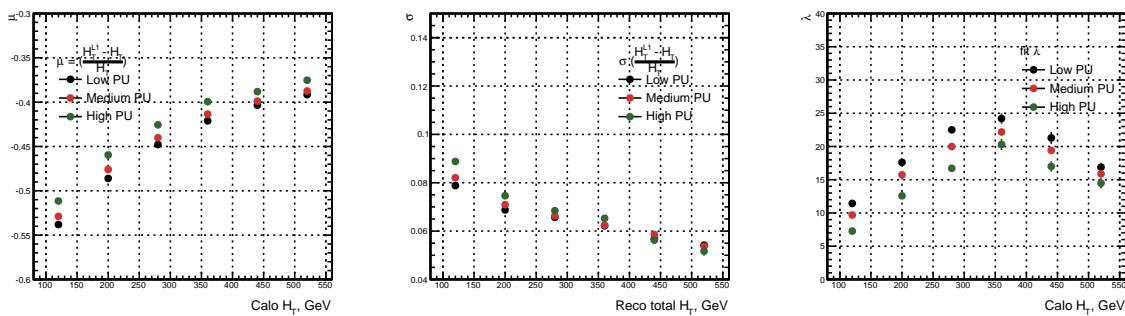


**Figure B.4.:**  $H_T$  resolution parameters in bins of Calo  $H_T$  measured for the defined low, medium and high pile-up conditions. Shown are the mean  $\mu$  (left), resolution  $\sigma$  (middle) and  $\lambda$  (right) fit values to an **EMG** function for the  $\frac{(L1 H_T - H_T)}{H_T}$  distributions.

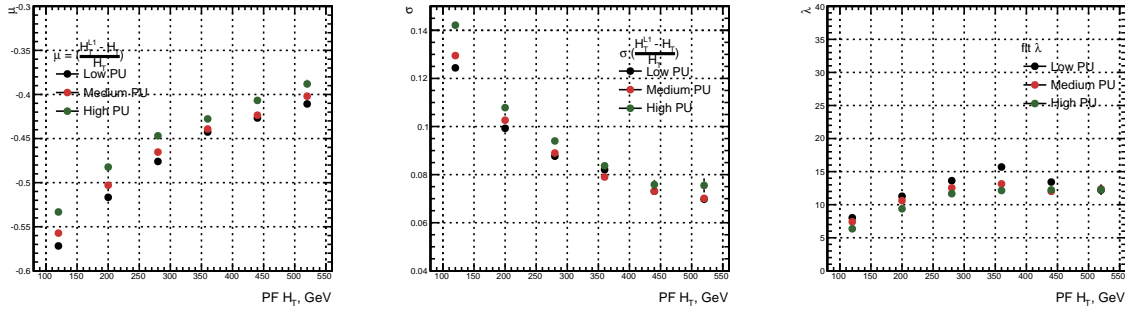


**Figure B.5.:**  $H_T$  resolution parameters in bins of  $\text{PF } H_T$  measured for the defined low, medium and high pile-up conditions. Shown are the mean  $\mu$  (left), resolution  $\sigma$  (middle) and  $\lambda$  (right) fit values to an EMG function for the  $\frac{(L1H_T - H_T)}{H_T}$  distributions.

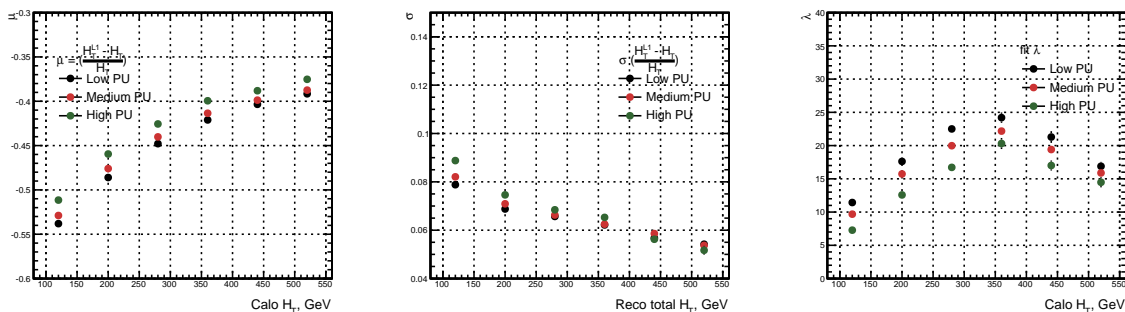


**Figure B.6.:**  $H_T$  resolution parameters in bins of  $H_T$  measured for the defined low, medium and high pile-up conditions. Shown are the mean  $\mu$  (left), resolution  $\sigma$  (middle) and  $\lambda$  (right) fit values to an EMG function for the  $\frac{(L1H_T - H_T)}{H_T}$  distributions.

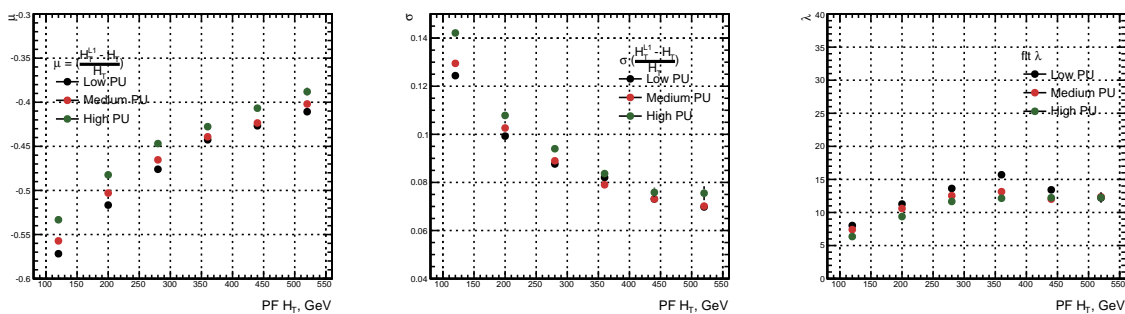


**Figure B.7.:**  $H_T$  resolution parameters in bins of  $\text{PF } H_T$  measured for the defined low, medium and high pile-up conditions. Shown are the mean  $\mu$  (left), resolution  $\sigma$  (middle) and  $\lambda$  (right) fit values to an EMG function for the  $\frac{(L1H_T - H_T)}{H_T}$  distributions.

# Appendix C.

## 2407 Additional material on background 2408 estimation methods

### 2409 C.1. Determination of $k_{QCD}$

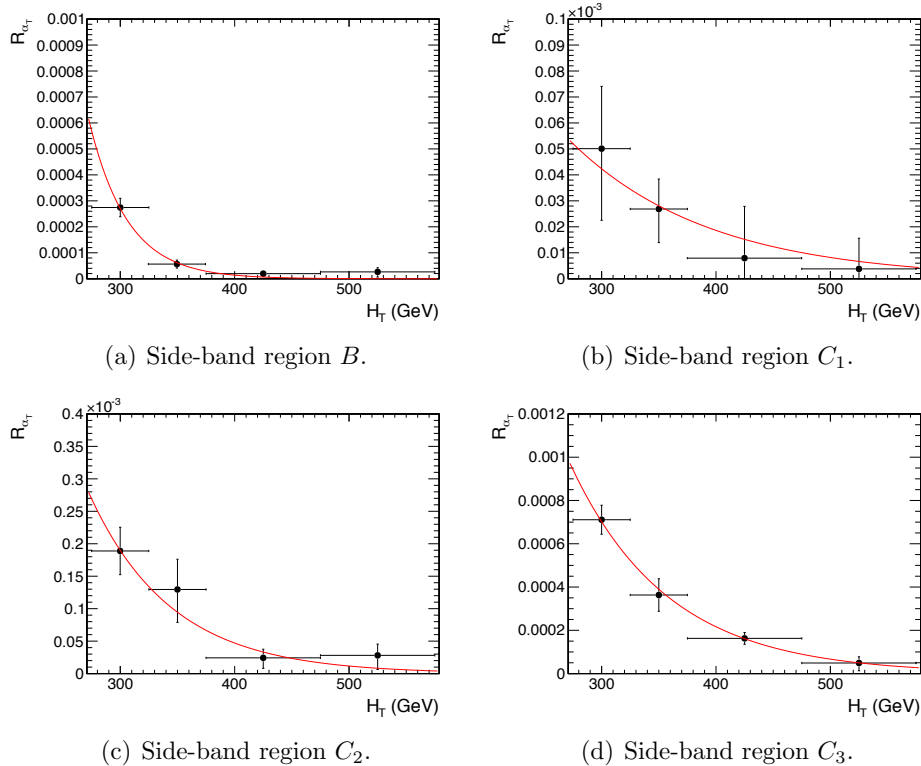


**Figure C.1.:**  $R_{\alpha_T}(H_T)$  and exponential fits for each of the data sideband regions. Fit is conducted between the  $H_T$  region  $275 < H_T < 575$ .

<sup>2411</sup> **C.2. Effect of varying background cross sections on**  
<sup>2412</sup> **closure tests**

<sup>2413</sup> Closure tests with cross section variations of +20% and -20% applied to  $W + \text{jets}$  and  $t\bar{t}$   
<sup>2414</sup> processes respectively.

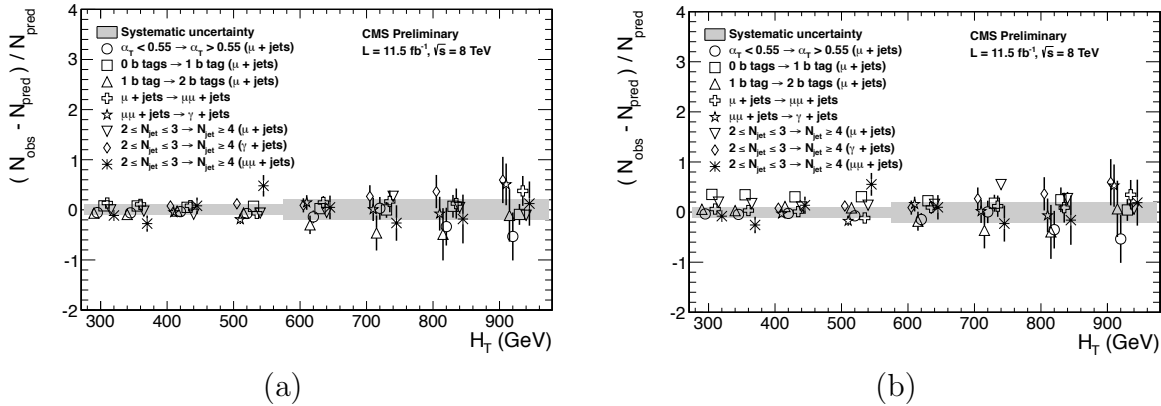


**Figure C.2.:** Sets of closure tests (open symbols) overlaid on top of the systematic uncertainty used for each of the five  $H_T$  regions (shaded bands) and for the two different jet multiplicity bins: (a)  $2 \leq n_{jet} \leq 3$  and (b)  $n_{jet} \geq 4$ .

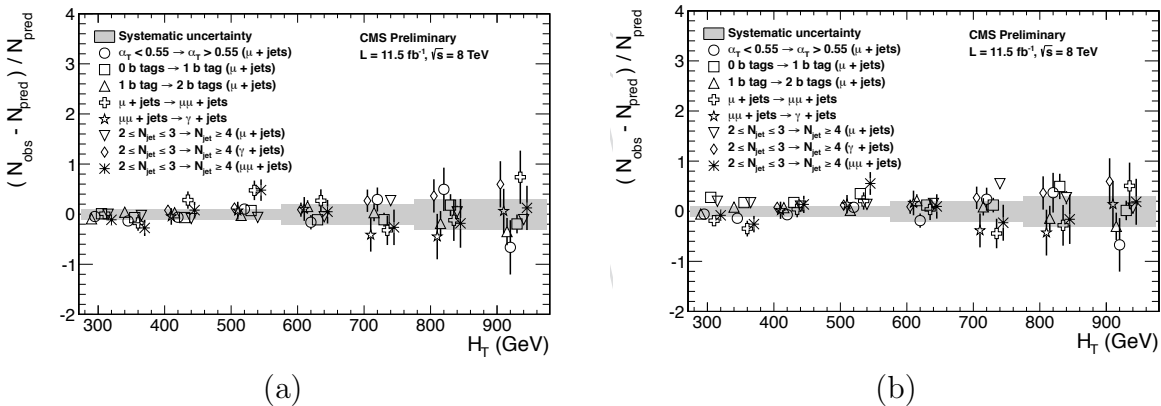


**Figure C.3.:** Sets of closure tests (open symbols) overlaid on top of the systematic uncertainty used for each of the five  $H_T$  regions (shaded bands) and for the two different jet multiplicity bins: (a)  $2 \leq n_{jet} \leq 3$  and (b)  $n_{jet} \geq 4$ .

		$H_T$ (GeV)			
$n_b^{reco}$	Cross Section	275–325	325–375	375–475	475–575
0	Nominal	$0.303 \pm 0.010$	$0.258 \pm 0.007$	$0.192 \pm 0.003$	$0.148 \pm 0.004$
	Varied	$0.300 \pm 0.010$	$0.256 \pm 0.007$	$0.191 \pm 0.003$	$0.147 \pm 0.004$
1	Nominal	$0.294 \pm 0.005$	$0.246 \pm 0.004$	$0.189 \pm 0.003$	$0.139 \pm 0.003$
	Varied	$0.295 \pm 0.006$	$0.248 \pm 0.004$	$0.191 \pm 0.003$	$0.140 \pm 0.003$
2	Nominal	$0.208 \pm 0.003$	$0.183 \pm 0.004$	$0.145 \pm 0.003$	$0.123 \pm 0.004$
	Varied	$0.211 \pm 0.004$	$0.185 \pm 0.004$	$0.147 \pm 0.003$	$0.124 \pm 0.004$
3	Nominal	$0.214 \pm 0.005$	$0.202 \pm 0.007$	$0.159 \pm 0.006$	$0.140 \pm 0.007$
	Varied	$0.215 \pm 0.005$	$0.203 \pm 0.007$	$0.159 \pm 0.006$	$0.140 \pm 0.007$
$\geq 4$	Nominal	$0.220 \pm 0.015$	$0.245 \pm 0.035$	$0.119 \pm 0.009$	-
	Varied	$0.220 \pm 0.015$	$0.245 \pm 0.035$	$0.119 \pm 0.009$	-
$n_b^{reco}$	Cross Section	575–675	675–775	775–875	875– $\infty$
0	Nominal	$0.119 \pm 0.004$	$0.098 \pm 0.005$	$0.077 \pm 0.006$	$0.049 \pm 0.005$
	Varied	$0.120 \pm 0.005$	$0.098 \pm 0.006$	$0.077 \pm 0.007$	$0.049 \pm 0.005$
1	Nominal	$0.115 \pm 0.004$	$0.093 \pm 0.005$	$0.075 \pm 0.007$	$0.063 \pm 0.006$
	Varied	$0.116 \pm 0.004$	$0.098 \pm 0.005$	$0.081 \pm 0.007$	$0.065 \pm 0.006$
2	Nominal	$0.096 \pm 0.005$	$0.070 \pm 0.006$	$0.051 \pm 0.007$	$0.063 \pm 0.008$
	Varied	$0.098 \pm 0.005$	$0.073 \pm 0.006$	$0.053 \pm 0.007$	$0.064 \pm 0.008$
3	Nominal	$0.114 \pm 0.009$	$0.065 \pm 0.007$	$0.070 \pm 0.017$	$0.092 \pm 0.020$
	Varied	$0.114 \pm 0.009$	$0.066 \pm 0.007$	$0.070 \pm 0.016$	$0.093 \pm 0.020$

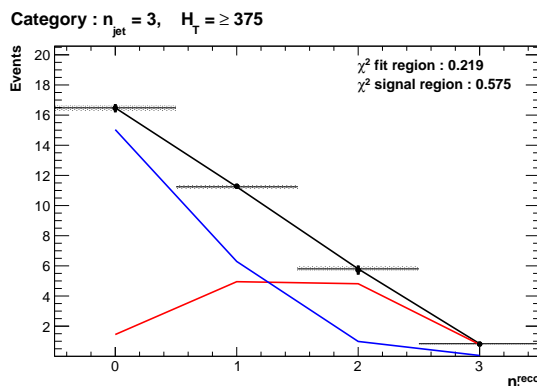
**Table C.1.:** Translation factors constructed from the  $\mu +$  jets control sample and signal selection MC, to predict yields for the  $W +$  jets and  $t\bar{t}$  back-grounds in the signal region with (a) NNLO cross sections corrected by k-factors determined from a data sideband see Section (4.4), marked as Nominal, and (b) the same cross sections but with those for  $W +$  jets and  $t\bar{t}$  varied up and down by 20%, respectively, marked as Varied. No requirement is placed on the jet multiplicity of events within this table.

## Appendix D.

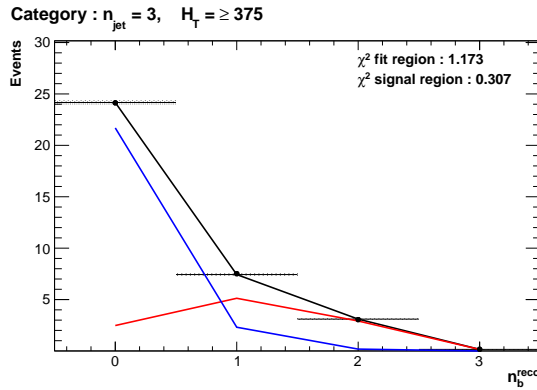
### <sup>2415</sup> Additional Material For B-tag <sup>2416</sup> Template Method

#### <sup>2417</sup> D.1. Templates Fits in Simulation

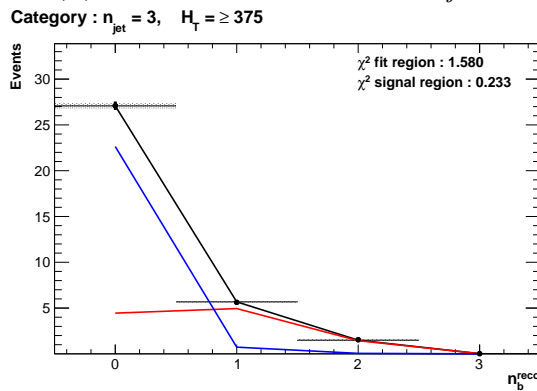
<sup>2418</sup> Template fits for the three **CSV** working points in the  $n_{jet} = 3, H_T > 375$  category :



(a) Loose working point  $n_{jet} = 3$



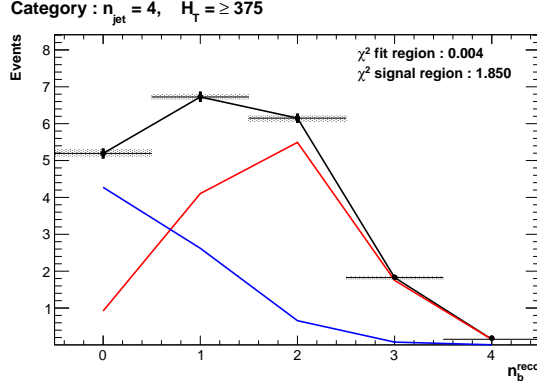
(b) Medium working point  $n_{jet} = 3$



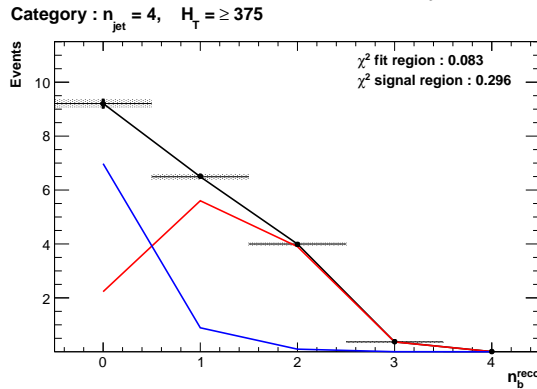
(c) Tight working point  $n_{jet} = 3$

**Figure D.1.:** The results of fitting the  $Z = 0$  and  $Z = 2$  templates to the  $n_b^{reco} = 0, 1, 2$  bins taken directly from simulation in the region  $H_T > 375$  GeV, for the  $n_{jet} = 3$  category. The blue template represents  $Z = 0$ , while the red template represents  $Z = 2$ . Grey bands represent the statistical uncertainty of the fit. The  $\chi^2$  parameter displayed represents the goodness of fit to the low  $n_b^{reco}$  (0-2) control region.

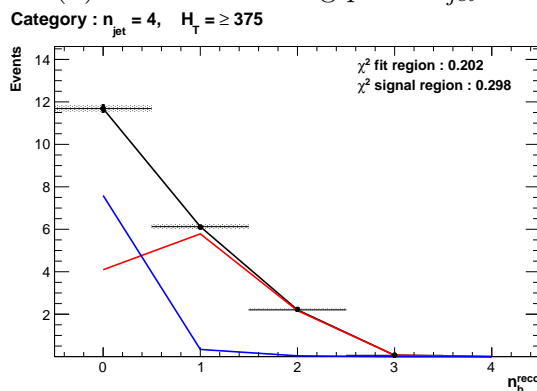
2419 Template fits for the three **CSV** working points in the  $n_{jet} = 4$ ,  $H_T > 375$  category :



(a) Loose working point  $n_{jet} = 4$



(b) Medium working point  $n_{jet} = 4$

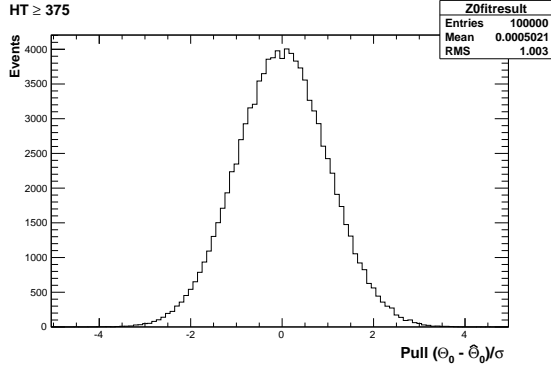


(c) Tight working point  $n_{jet} = 4$

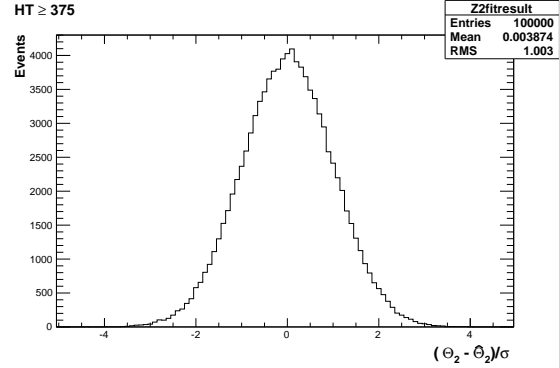
**Figure D.2.:** The results of fitting the  $Z = 0$  and  $Z = 2$  templates to the  $n_b^{reco} = 0, 1, 2$  bins taken directly from simulation in the region  $H_T > 375$  GeV, for the  $n_{jet} = 4$  category. The blue template represents  $Z = 0$ , while the red template represents  $Z = 2$ . Grey bands represent the statistical uncertainty of the fit. The  $\chi^2$  parameter displayed represents the goodness of fit to the low  $n_b^{reco}$  (0-2) control region.

2420

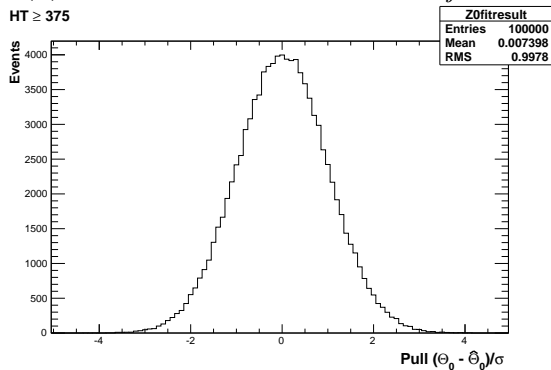
## D.2. Pull Distributions for Template Fits



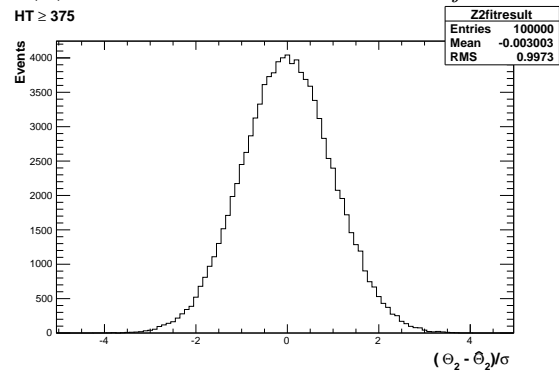
(a) Z0 Template,  $H_T > 375$ ,  $n_{jet} = 3$



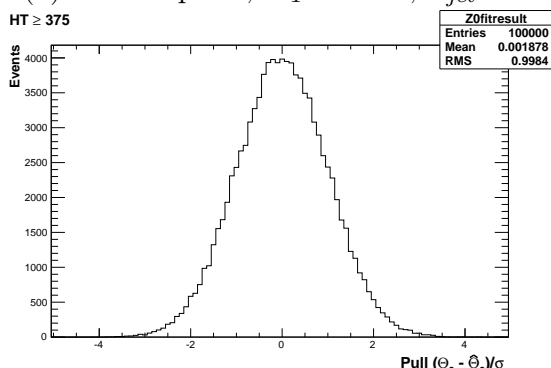
(b) Z2 Template,  $H_T > 375$ ,  $n_{jet} = 3$



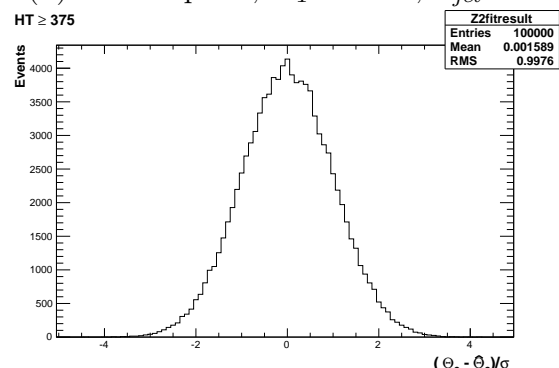
(a) Z0 Template,  $H_T > 375$ ,  $n_{jet} = 4$



(b) Z2 Template,  $H_T > 375$ ,  $n_{jet} = 4$



(a) Z0 Template,  $H_T > 375$ ,  $n_{jet} \geq 5$



(b) Z2 Template,  $H_T > 375$ ,  $n_{jet} \geq 5$

**Figure D.3.:** Pull distributions of  $\frac{(\theta - \hat{\theta})}{\sigma}$  for  $10^4$  pseudo-experiments generated from a gaussian distribution centred on the  $n_b^{reco}$  template values from simulation with width  $\sigma$ . Distributions are shown for both Z0 and Z2 templates for the medium CSV working point.

<sup>2421</sup> **D.3. Templates Fits in Data Control Sample**

<sup>2422</sup> Template fits for the three  $H_T$  bins, in the  $n_{jet} = 3$ , medium **CSV** working point:

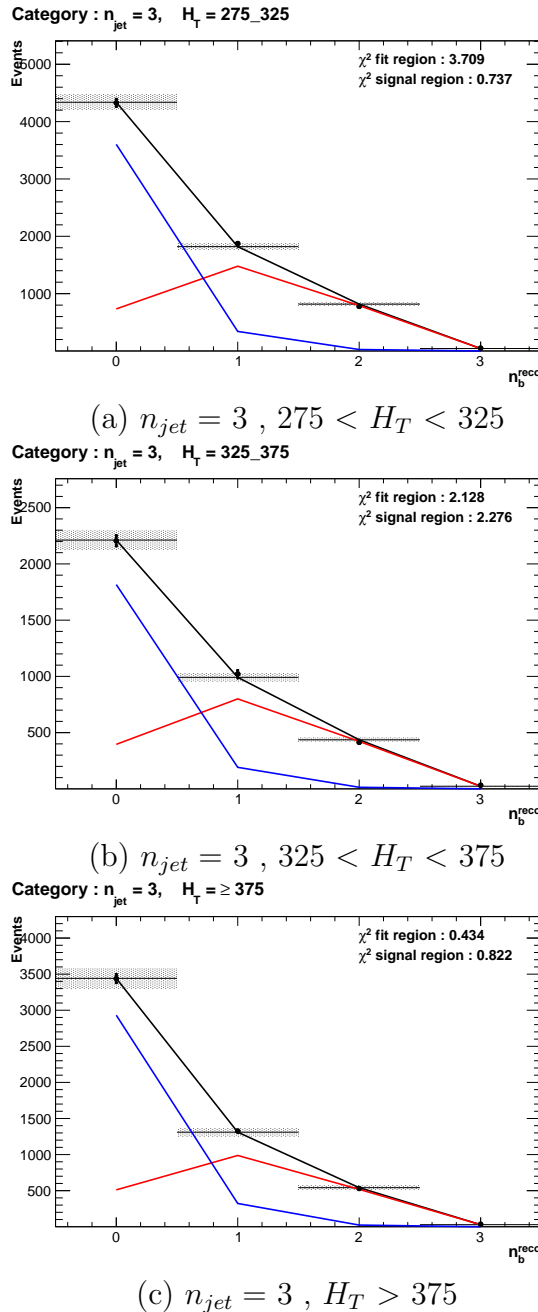


**Figure D.4.:** The results of fitting the  $Z = 0$  and  $Z = 2$  templates to the  $n_b^{reco} = 0, 1, 2$  bins taken from data, for the  $n_{jet} = 3$  category and medium **CSV** working point. The blue template represents  $Z = 0$ , while the red template represents  $Z = 2$ . The  $\chi^2$  parameter displayed represents the goodness of fit to the low  $n_b^{reco}$  (0-2) control region.

2423 Template fits for the three  $H_T$  bins, in the  $n_{jet} = 4$ , medium CSV working point:

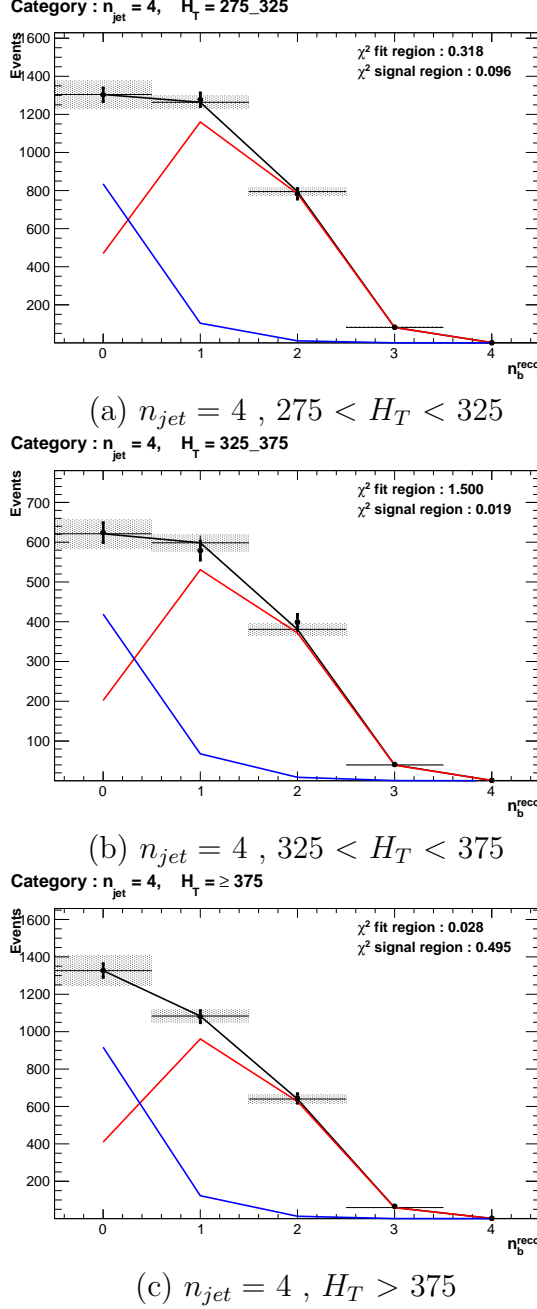
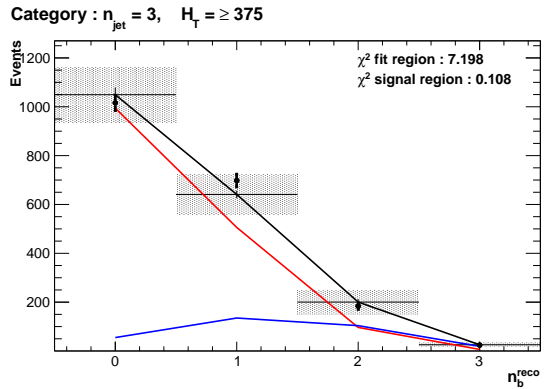


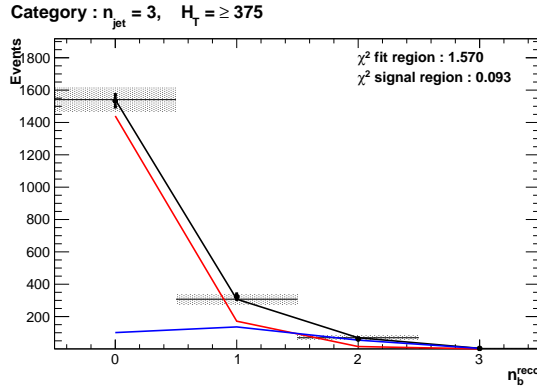
**Figure D.5.:** The results of fitting the  $Z = 0$  and  $Z = 2$  templates to the  $n_b^{reco} = 0, 1, 2$  bins taken from data, for the  $n_{jet} = 4$  category and medium CSV working point. The blue template represents  $Z = 0$ , while the red template represents  $Z = 2$ . The  $\chi^2$  parameter displayed represents the goodness of fit to the low  $n_b^{reco}$  (0-2) control region.

<sup>2424</sup> **D.4. Templates Fits in Data Signal Region**

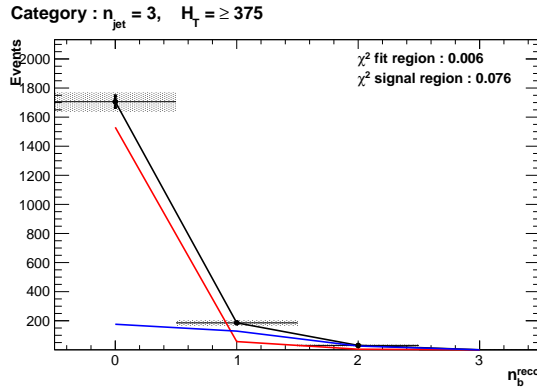
<sup>2425</sup> Template fits for the three **CSV** working points, in the  $n_{jet} = 3, H_T > 375$  category :



(a) Loose working point :  $n_{jet} = 3, H_T > 375$



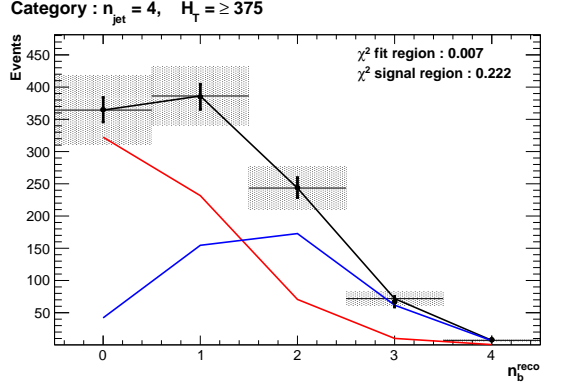
(b) Medium working point :  $n_{jet} = 3, H_T > 375$



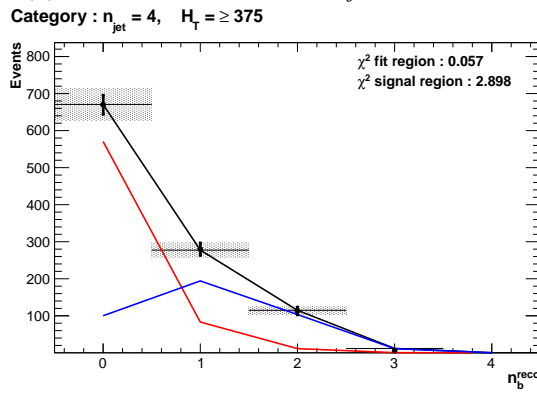
(c) Tight working point :  $n_{jet} = 3, H_T > 375$

**Figure D.6.:** The results of fitting the  $Z = 0$  and  $Z = 2$  templates to the  $n_b^{reco} = 0, 1, 2$  bins taken from data, in the  $n_{jet} = 3$  and  $H_T > 375$  category for all **CSV** working points. The blue template represents  $Z = 0$ , while the red template represents  $Z = 2$ . The  $\chi^2$  parameter displayed represents the goodness of fit to the low  $n_b^{reco}$  (0-2) control region.

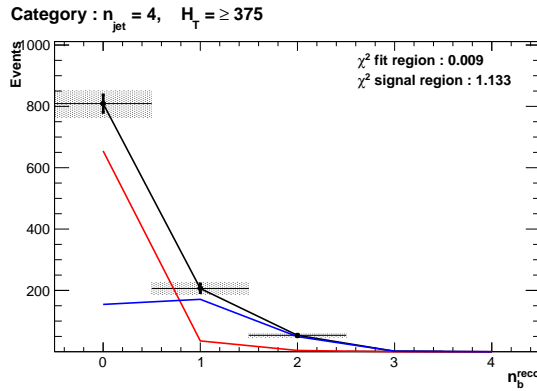
2426 Template fits for the three **CSV** working points, in the  $n_{jet} = 4, H_T > 375$  category :



(a) Loose working point :  $n_{jet} = 4, H_T > 375$



(b) Medium working point :  $n_{jet} = 4, H_T > 375$



(c) Tight working point :  $n_{jet} = 4, H_T > 375$

**Figure D.7.:** The results of fitting the  $Z = 0$  and  $Z = 2$  templates to the  $n_b^{reco} = 0, 1, 2$  bins taken from data, in the  $n_{jet} = 4$  and  $H_T > 375$  category for all **CSV** working points. The blue template represents  $Z = 0$ , while the red template represents  $Z = 2$ . The  $\chi^2$  parameter displayed represents the goodness of fit to the low  $n_b^{reco}$  (0-2) control region.



# <sup>2428</sup> Bibliography

- [1] Particle Data Group Collaboration, “Review of Particle Physics (RPP)”, *Phys.Rev. D* **86** (2012) 010001, [doi:10.1103/PhysRevD.86.010001](https://doi.org/10.1103/PhysRevD.86.010001).
- [2] G. H. et al., “Nine-year Wilkinson Microwave Anisotropy Probe (WMAP) Observations: Cosmological Parameter Results”, *The Astrophysical Journal Supplement Series* **208** (2013), no. 2,,
- [3] ATLAS Collaboration Collaboration, “Observation of a new particle in the search for the Standard Model Higgs boson with the ATLAS detector at the LHC”, *Phys.Lett. B* **716** (2012) 1–29, [doi:10.1016/j.physletb.2012.08.020](https://doi.org/10.1016/j.physletb.2012.08.020), [arXiv:1207.7214](https://arxiv.org/abs/1207.7214).
- [4] CMS Collaboration, “Observation of a new boson at a mass of 125 GeV with the CMS experiment at the LHC”, *Phys.Lett. B* **716** (2012) 30–61, [doi:10.1016/j.physletb.2012.08.021](https://doi.org/10.1016/j.physletb.2012.08.021), [arXiv:1207.7235](https://arxiv.org/abs/1207.7235).
- [5] CMS Collaboration, “Search for supersymmetry in hadronic final states with missing transverse energy using the variables AlphaT and b-quark multiplicity in pp collisions at 8 TeV”, *Eur.Phys.J. C* **73** (2013) 2568, [doi:10.1140/epjc/s10052-013-2568-6](https://doi.org/10.1140/epjc/s10052-013-2568-6), [arXiv:1303.2985](https://arxiv.org/abs/1303.2985).
- [6] S. Weinberg, “A Model of Leptons”, *Phys. Rev. Lett.* **19** (Nov, 1967) [doi:10.1103/PhysRevLett.19.1264](https://doi.org/10.1103/PhysRevLett.19.1264).
- [7] S. Glashow, “Partial Symmetries of Weak Interactions”, *Nucl.Phys.* **22** (1961) [doi:10.1016/0029-5582\(61\)90469-2](https://doi.org/10.1016/0029-5582(61)90469-2).
- [8] A. Salam, “Weak and Electromagnetic Interactions”, *Conf.Proc. C* **680519** (1968).
- [9] G. Hooft, “Renormalizable Lagrangians for massive Yang-Mills fields”, *Nuclear Physics B* **35** (1971) [doi:\[http://dx.doi.org/10.1016/0550-3213\\(71\\)90139-8\]\(http://dx.doi.org/10.1016/0550-3213\(71\)90139-8\)](http://dx.doi.org/10.1016/0550-3213(71)90139-8).
- [10] Gargamelle Neutrino Collaboration Collaboration, “Observation of Neutrino Like

- 2453      Interactions Without Muon Or Electron in the Gargamelle Neutrino Experiment”,  
2454      *Phys.Lett.* **B46** (1973) 138–140, [doi:10.1016/0370-2693\(73\)90499-1](https://doi.org/10.1016/0370-2693(73)90499-1).
- 2455 [11] UA1 Collaboration Collaboration, “Experimental Observation of Lepton Pairs of  
2456      Invariant Mass Around 95-GeV at the CERN SPS Collider”, *Phys.Lett.* **B126**  
2457      (1983) 398–410, [doi:10.1016/0370-2693\(83\)90188-0](https://doi.org/10.1016/0370-2693(83)90188-0).
- 2458 [12] UA2 Collaboration Collaboration, “Observation of Single Isolated Electrons of High  
2459      Transverse Momentum in Events with Missing Transverse Energy at the CERN  $\bar{p}p$   
2460      Collider”, *Phys.Lett.* **B122** (1983) [doi:10.1016/0370-2693\(83\)91605-2](https://doi.org/10.1016/0370-2693(83)91605-2).
- 2461 [13] E. Noether, “Invariante Variationsprobleme”, *Nachrichten von der Gesellschaft der*  
2462      *Wissenschaften zu Göttingen, Mathematisch-Physikalische Klasse* **1918** (1918).
- 2463 [14] F. Halzen and A. D. Martin, “Quarks and Leptons”. 1985.
- 2464 [15] “Introduction to Elementary Particles”. Wiley-VCH, 2nd edition, October, 2008.
- 2465 [16] C. S. Wu et al., “Experimental Test of Parity Conservation in Beta Decay”,  
2466      *Physical Review* **105** (February, 1957) [doi:10.1103/PhysRev.105.1413](https://doi.org/10.1103/PhysRev.105.1413).
- 2467 [17] P. Higgs, “Broken symmetries, massless particles and gauge fields”, *Physics Letters*  
2468      **12** (1964), no. 2, [doi:\[http://dx.doi.org/10.1016/0031-9163\\(64\\)91136-9\]\(http://dx.doi.org/10.1016/0031-9163\(64\)91136-9\)](http://dx.doi.org/10.1016/0031-9163(64)91136-9).
- 2469 [18] F. Englert and R. Brout, “Broken Symmetry and the Mass of Gauge Vector  
2470      Mesons”, *Phys. Rev. Lett.* **13** (Aug, 1964) [doi:10.1103/PhysRevLett.13.321](https://doi.org/10.1103/PhysRevLett.13.321).
- 2471 [19] P. W. Higgs, “Broken Symmetries and the Masses of Gauge Bosons”, *Phys. Rev.*  
2472      *Lett.* **13** (Oct, 1964) [doi:10.1103/PhysRevLett.13.508](https://doi.org/10.1103/PhysRevLett.13.508).
- 2473 [20] G. S. Guralnik, “Global Conservation Laws and Massless Particles”, *Phys. Rev.*  
2474      *Lett.* **13** (Nov, 1964) [doi:10.1103/PhysRevLett.13.585](https://doi.org/10.1103/PhysRevLett.13.585).
- 2475 [21] S. Weinberg, “A Model of Leptons”, *Phys. Rev. Lett.* **19** (Nov, 1967) 1264–1266,  
2476      [doi:10.1103/PhysRevLett.19.1264](https://doi.org/10.1103/PhysRevLett.19.1264).
- 2477 [22] H. Yukawa, “On the Interaction of Elementary Particles. I”, *Progress of*  
2478      *Theoretical Physics Supplement* **1** (1955) [doi:10.1143/PTPS.1.1](https://doi.org/10.1143/PTPS.1.1).
- 2479 [23] (Super-Kamiokande Collaboration) Collaboration, “Evidence for Oscillation of  
2480      Atmospheric Neutrinos”, *Phys. Rev. Lett.* **81** (Aug, 1998)  
2481      [doi:10.1103/PhysRevLett.81.1562](https://doi.org/10.1103/PhysRevLett.81.1562).

- [24] R. Becker-Szendy et al., “A Search for muon-neutrino oscillations with the IMB detector”, *Phys.Rev.Lett.* **69** (1992) doi:10.1103/PhysRevLett.69.1010.
- [25] S. P. Martin, “A Supersymmetry primer”, arXiv:hep-ph/9709356.
- [26] H. Nilles, “Supersymmetry, Supergravity and Particle Physics”. Physics reports. North-Holland Physics Publ., 1984.
- [27] H. E. Haber and G. L. Kane, “The Search for Supersymmetry: Probing Physics Beyond the Standard Model”, *Phys.Rept.* **117** (1985) doi:10.1016/0370-1573(85)90051-1.
- [28] E. Witten, “Dynamical Breaking of Supersymmetry”, *Nucl.Phys.* **B188** (1981) doi:10.1016/0550-3213(81)90006-7.
- [29] J. Wess and B. Zumino, “Supergauge transformations in four dimensions”, *Nuclear Physics B* **70** (1974), no. 1, doi:[http://dx.doi.org/10.1016/0550-3213\(74\)90355-1](http://dx.doi.org/10.1016/0550-3213(74)90355-1).
- [30] H. Muller-Kirsten and A. Wiedemann, “Introduction to Supersymmetry”. World Scientific lecture notes in physics. World Scientific, 2010.
- [31] I. Aitchison, “Supersymmetry in Particle Physics: An Elementary Introduction”. Cambridge University Press, 2007.
- [32] K. A. Intriligator and N. Seiberg, “Lectures on Supersymmetry Breaking”, *Class.Quant.Grav.* **24** (2007) arXiv:hep-ph/0702069.
- [33] Y. Shadmi, “Supersymmetry breaking”, arXiv:hep-th/0601076.
- [34] C. Burgess et al., “Warped Supersymmetry Breaking”, *JHEP* **0804** (2008) doi:10.1088/1126-6708/2008/04/053, arXiv:hep-th/0610255.
- [35] H. Murayama, “Supersymmetry breaking made easy, viable, and generic”, arXiv:0709.3041.
- [36] H. Baer and X. Tata, “Weak Scale Supersymmetry: From Superfields to Scattering Events”. Cambridge University Press, 2006.
- [37] S. P. Martin, “Implications of supersymmetric models with natural R-parity conservation”, doi:10.1103/PhysRevD.54.2340, arXiv:hep-ph/9602349.
- [38] G. L. Kane, C. F. Kolda, L. Roszkowski, and J. D. Wells, “Study of constrained

- 2511        minimal supersymmetry”, *Phys.Rev.* **D49** (1994)  
2512        [doi:10.1103/PhysRevD.49.6173](https://doi.org/10.1103/PhysRevD.49.6173), [arXiv:hep-ph/9312272](https://arxiv.org/abs/hep-ph/9312272).
- 2513 [39] C. Stuge et al., “Updated global fits of the cMSSM including the latest LHC SUSY  
2514        and Higgs searches and XENON100 data”, *JCAP* **1203** (2012)  
2515        [doi:10.1088/1475-7516/2012/03/030](https://doi.org/10.1088/1475-7516/2012/03/030), [arXiv:1112.4192](https://arxiv.org/abs/1112.4192).
- 2516 [40] M. Citron et al., “The End of the CMSSM Coannihilation Strip is Nigh”,  
2517        *Phys.Rev.* **D87** (2013) [doi:10.1103/PhysRevD.87.036012](https://doi.org/10.1103/PhysRevD.87.036012), [arXiv:1212.2886](https://arxiv.org/abs/1212.2886).
- 2518 [41] D. Ghosh, M. Guchait, S. Raychaudhuri, and D. Sengupta, “How Constrained is  
2519        the cMSSM?”, *Phys.Rev.* **D86** (2012) [doi:10.1103/PhysRevD.86.055007](https://doi.org/10.1103/PhysRevD.86.055007),  
2520        [arXiv:1205.2283](https://arxiv.org/abs/1205.2283).
- 2521 [42] LHC New Physics Working Group Collaboration, “Simplified Models for LHC New  
2522        Physics Searches”, *J.Phys.* **G39** (2012) 105005,  
2523        [doi:10.1088/0954-3899/39/10/105005](https://doi.org/10.1088/0954-3899/39/10/105005), [arXiv:1105.2838](https://arxiv.org/abs/1105.2838).
- 2524 [43] J. Alwall, P. Schuster, and N. Toro, “Simplified Models for a First Characterization  
2525        of New Physics at the LHC”, *Phys.Rev.* **D79** (2009) 075020,  
2526        [doi:10.1103/PhysRevD.79.075020](https://doi.org/10.1103/PhysRevD.79.075020), [arXiv:0810.3921](https://arxiv.org/abs/0810.3921).
- 2527 [44] CMS Collaboration, “Interpretation of Searches for Supersymmetry with simplified  
2528        Models”, *Phys.Rev.* **D88** (2013) 052017, [doi:10.1103/PhysRevD.88.052017](https://doi.org/10.1103/PhysRevD.88.052017),  
2529        [arXiv:1301.2175](https://arxiv.org/abs/1301.2175).
- 2530 [45] J. Hisano, K. Kurosawa, and Y. Nomura, “Natural effective supersymmetry”,  
2531        *Nucl.Phys.* **B584** (2000) 3–45, [doi:10.1016/S0550-3213\(00\)00343-6](https://doi.org/10.1016/S0550-3213(00)00343-6),  
2532        [arXiv:hep-ph/0002286](https://arxiv.org/abs/hep-ph/0002286).
- 2533 [46] M. Papucci, J. T. Ruderman, and A. Weiler, “Natural SUSY Endures”, *JHEP*  
2534        **1209** (2012) 035, [doi:10.1007/JHEP09\(2012\)035](https://doi.org/10.1007/JHEP09(2012)035), [arXiv:1110.6926](https://arxiv.org/abs/1110.6926).
- 2535 [47] B. Allanach and B. Gripaios, “Hide and Seek With Natural Supersymmetry at the  
2536        LHC”, *JHEP* **1205** (2012) 062, [doi:10.1007/JHEP05\(2012\)062](https://doi.org/10.1007/JHEP05(2012)062),  
2537        [arXiv:1202.6616](https://arxiv.org/abs/1202.6616).
- 2538 [48] ALICE Collaboration, “The ALICE experiment at the CERN LHC”, *JINST* **3**  
2539        (2008) S08002, [doi:10.1088/1748-0221/3/08/S08002](https://doi.org/10.1088/1748-0221/3/08/S08002).
- 2540 [49] ATLAS Collaboration, “The ATLAS Experiment at the CERN Large Hadron  
2541        Collider”, *JINST* **3** (2008) [doi:10.1088/1748-0221/3/08/S08003](https://doi.org/10.1088/1748-0221/3/08/S08003).

- 2542 [50] CMS Collaboration, “The CMS experiment at the CERN LHC”, *JINST* **0803**  
2543 (2008) S08004,  
2544 [doi:10.1088/1748-0221/3/08/S08004](https://doi.org/10.1088/1748-0221/3/08/S08004).
- 2545 [51] LHCb Collaboration, “The LHCb Detector at the LHC”, *JINST* **3** (2008) S08005,  
2546 [doi:10.1088/1748-0221/3/08/S08005](https://doi.org/10.1088/1748-0221/3/08/S08005).
- 2547 [52] J.-L. Caron, “LHC Layout. Schema general du LHC.”, (Sep, 1997).
- 2548 [53] CMS Collaboration, “CMS Luminosity - Public Results”, , (2011).  
2549 <http://twiki.cern.ch/twiki/bin/view/CMSPublic/LumiPublicResults>.
- 2550 [54] CERN, “CMS Compact Muon Solenoid.”, (Feb, 2010).  
2551 <http://public.web.cern.ch/public/Objects/LHC/CMSnc.jpg>.
- 2552 [55] “The CMS Electromagnetic Calorimeter Project: Technical Design Report”.  
2553 Technical Design Report CMS. CERN, Geneva, 1997.
- 2554 [56] “The CMS Muon Project: Technical Design Report”. Technical Design Report  
2555 CMS. CERN, Geneva, 1997.
- 2556 [57] CMS Collaboration, “The CMS Physics Technical Design Report, Volume 1”,  
2557 *CERN/LHCC 2006-001* (2006).
- 2558 [58] M. Cacciari, G. P. Salam, and G. Soyez, “The anti- $k_t$  jet clustering algorithm”,  
2559 *Journal of High Energy Physics* **2008** (2008), no. 04, 063.
- 2560 [59] “Jet Performance in pp Collisions at 7 TeV”, CMS-PAS-JME-10-003, CERN,  
2561 Geneva, (2010).
- 2562 [60] X. Janssen, “Underlying event and jet reconstruction in CMS”, CMS-CR-2011-012,  
2563 CERN, Geneva, (Jan, 2011).
- 2564 [61] CMS Collaboration, “Determination of jet energy calibration and transverse  
2565 momentum resolution in CMS”, *Journal of Instrumentation* **6** (2011), no. 11.,
- 2566 [62] R. Eusebi, “Jet energy corrections and uncertainties in CMS: reducing their impact  
2567 on physics measurements”, *Journal of Physics: Conference Series* **404** (2012).
- 2568 [63] CMS Collaboration, “Algorithms for b Jet identification in CMS”,  
2569 CMS-PAS-BTV-09-001, CERN, 2009. Geneva, (Jul, 2009).
- 2570 [64] CMS Collaboration, “Performance of b-tagging at  $\sqrt{s} = 8$  TeV in multijet,  $t\bar{t}$  and

- 2571 boosted topology events”, CMS-PAS-BTV-13-001, CERN, Geneva, (2013).
- 2572 [65] CMS Collaboration, “Identification of b-quark jets with the CMS experiment”,  
2573 *Journal of Instrumentation* **8** (2013), no. 04.,
- 2574 [66] CMS Collaboration, “CMS. The TriDAS Project. Technical design report, Vol. 1:  
2575 The trigger systems”,.
- 2576 [67] CMS Collaboration, “CMS: The TriDAS Project. Technical design report, Vol. 2:  
2577 Data acquisition and high-level trigger”,.
- 2578 [68] CMS Collaboration, “Calibration and Performance of the Jets and Energy Sums in  
2579 the Level-1 Trigger”, CMS IN 2013/006 (2013), CERN, Geneva, (2013).
- 2580 [69] CMS Collaboration, “Study of Level-1 Trigger Jet Performance in High Pile-up  
2581 Running Conditions”,.
- 2582 [70] J. J. Brooke, “Performance of the CMS Level-1 Trigger”, CMS-CR-2012-322,  
2583 CERN, Geneva, (Nov, 2012).
- 2584 [71] CMS Collaboration, “Search for supersymmetry in final states with missing  
2585 transverse energy and 0, 1, 2, or at least 3 b-quark jets in 7 TeV pp collisions using  
2586 the variable alphaT”, *JHEP* **1301** (2013) 077, [doi:10.1007/JHEP01\(2013\)077](https://doi.org/10.1007/JHEP01(2013)077),  
2587 [arXiv:1210.8115](https://arxiv.org/abs/1210.8115).
- 2588 [72] CMS Collaboration, “SUSY searches with dijet events”, CMS-PAS-SUS-08-005,  
2589 (2008).
- 2590 [73] L. Randall and D. Tucker-Smith, “Dijet Searches for Supersymmetry at the Large  
2591 Hadron Collider”, *Phys. Rev. Lett.* **101** (Nov, 2008) 221803,  
2592 [doi:10.1103/PhysRevLett.101.221803](https://doi.org/10.1103/PhysRevLett.101.221803).
- 2593 [74] CMS Collaboration, “Search strategy for exclusive multi-jet events from  
2594 supersymmetry at CMS”, CMS-PAS-SUS-09-001, CERN, 2009. Geneva, (Jul, 2009).
- 2595 [75] CMS Collaboration, “Calorimeter Jet Quality Criteria for the First CMS Collision  
2596 Data”, CMS-PAS-JME-09-008, CERN, 2010. Geneva, (Apr, 2010).
- 2597 [76] The CMS Collaboration, “Performance of CMS muon reconstruction in pp collision  
2598 events at 7 TeV”, *Journal of Instrumentation* **7** (October, 2012) 2P,  
2599 [doi:10.1088/1748-0221/7/10/P10002](https://doi.org/10.1088/1748-0221/7/10/P10002), [arXiv:1206.4071](https://arxiv.org/abs/1206.4071).
- 2600 [77] CMS Collaboration, “Search for supersymmetry in events with photons and missing

- 2601 energy”, CMS-PAS-SUS-12-018, CERN, Geneva, (2012).
- 2602 [78] M. Cacciari and G. P. Salam, “Pileup subtraction using jet areas”, *Phys.Lett.*  
2603 **B659** (2008) [doi:10.1016/j.physletb.2007.09.077](https://doi.org/10.1016/j.physletb.2007.09.077), [arXiv:0707.1378](https://arxiv.org/abs/0707.1378).
- 2604 [79] Z. Bern et al., “Driving missing data at next-to-leading order”, *Phys. Rev. D* **84**  
2605 (Dec, 2011) 114002, [doi:10.1103/PhysRevD.84.114002](https://doi.org/10.1103/PhysRevD.84.114002).
- 2606 [80] Z. Bern et al., “Driving Missing Data at Next-to-Leading Order”, *Phys.Rev.* **D84**  
2607 (2011) 114002, [doi:10.1103/PhysRevD.84.114002](https://doi.org/10.1103/PhysRevD.84.114002), [arXiv:1106.1423](https://arxiv.org/abs/1106.1423).
- 2608 [81] CMS Collaboration Collaboration, “Data-Driven Estimation of the Invisible Z  
2609 Background to the SUSY MET Plus Jets Search”, CMS-PAS-SUS-08-002, CERN,  
2610 2009. Geneva, (Jan, 2009).
- 2611 [82] T. Sjostrand, S. Mrenna, and P. Z. Skands, “PYTHIA 6.4 Physics and Manual”,  
2612 *JHEP* **0605** (2006) 026, [doi:10.1088/1126-6708/2006/05/026](https://doi.org/10.1088/1126-6708/2006/05/026),  
2613 [arXiv:hep-ph/0603175](https://arxiv.org/abs/hep-ph/0603175).
- 2614 [83] W. Beenakker, R. Hopker, M. Spira, and P. Zerwas, “Squark and gluino production  
2615 at hadron colliders”, *Nucl.Phys.* **B492** (1997) 51–103,  
2616 [doi:10.1016/S0550-3213\(97\)80027-2](https://doi.org/10.1016/S0550-3213(97)80027-2), [arXiv:hep-ph/9610490](https://arxiv.org/abs/hep-ph/9610490).
- 2617 [84] S. Abdullin et al., “The Fast Simulation of the CMS Detector at LHC”, *Journal of*  
2618 *Physics: Conference Series* **331** (2011), no. 3,.
- 2619 [85] S. Banerjee, M. D. Hildreth, and the CMS Collaboration, “Validation and Tuning  
2620 of the CMS Full Simulation”, *Journal of Physics: Conference Series* **331** (2011).
- 2621 [86] CMS Collaboration, “CMS Btag POG : CMS b-tagging performance database”, ,  
2622 (2013). <https://twiki.cern.ch/twiki/bin/viewauth/CMS/BtagPOG>.
- 2623 [87] CMS Collaboration, “CMS Luminosity Based on Pixel Cluster Counting - Summer  
2624 2012 Update”, CMS-PAS-LUM-12-001, CERN, Geneva, (2012).
- 2625 [88] M. Botje et al., “The PDF4LHC Working Group Interim Recommendations”,  
2626 [arXiv:1101.0538](https://arxiv.org/abs/1101.0538).
- 2627 [89] E. M. Laird, “A Search for Squarks and Gluinos with the CMS Detector”,.
- 2628 [90] R. Cousins, “Probability Density Functions for Positive Nuisance Parameters”.  
2629 2012. <http://www.physics.ucla.edu/cousins/stats/cousinslognormalprior.pdf>.

- 2630 [91] L. Moneta, K. Cranmer, G. Schott, and W. Verkerke, “The RooStats project”,  
2631 2010. [arXiv:1009.1003](https://arxiv.org/abs/1009.1003).
- 2632 [92] F. James and M. Roos, “Minuit: A System for Function Minimization and Analysis  
2633 of the Parameter Errors and Correlations”, *Comput.Phys.Commun.* **10** (1975)  
2634 343–367, [doi:10.1016/0010-4655\(75\)90039-9](https://doi.org/10.1016/0010-4655(75)90039-9).
- 2635 [93] A. L. Read, “Presentation of search results: the CL s technique”, *Journal of  
2636 Physics G: Nuclear and Particle Physics* **28** (2002).
- 2637 [94] T. Junk, “Confidence level computation for combining searches with small  
2638 statistics”, *Nuclear Instruments and Methods in Physics Research Section A* **434**  
2639 (1999), no. 23, [doi:\[http://dx.doi.org/10.1016/S0168-9002\\(99\\)00498-2\]\(http://dx.doi.org/10.1016/S0168-9002\(99\)00498-2\)](https://doi.org/10.1016/S0168-9002(99)00498-2).
- 2640 [95] A. L. Read, “Modified frequentist analysis of search results (the  $CL_s$  method)”,  
2641 CERN-OPEN-2000-205, (2000).
- 2642 [96] G. Cowan, K. Cranmer, E. Gross, and O. Vitells, “Asymptotic formulae for  
2643 likelihood-based tests of new physics”, *The European Physical Journal C* **71**  
2644 (2011) [doi:10.1140/epjc/s10052-011-1554-0](https://doi.org/10.1140/epjc/s10052-011-1554-0).
- 2645 [97] G. Cowan, K. Cranmer, E. Gross, and O. Vitells, “Asymptotic formulae for  
2646 likelihood-based tests of new physics”, *European Physical Journal C* **71** (February,  
2647 2011) [doi:10.1140/epjc/s10052-011-1554-0](https://doi.org/10.1140/epjc/s10052-011-1554-0), [arXiv:1007.1727](https://arxiv.org/abs/1007.1727).
- 2648 [98] CMS Collaboration Collaboration, “Search for supersymmetry in final states with  
2649 missing transverse energy and 0, 1, 2, or at least 3 b-quark jets in 7 TeV pp  
2650 collisions using the variable alphaT”, *JHEP* **1301** (2013) 077,  
2651 [doi:10.1007/JHEP01\(2013\)077](https://doi.org/10.1007/JHEP01(2013)077), [arXiv:1210.8115](https://arxiv.org/abs/1210.8115).
- 2652 [99] E. Hardy, “Is Natural SUSY Natural?”, *JHEP* **1310** (2013) 133,  
2653 [doi:10.1007/JHEP10\(2013\)133](https://doi.org/10.1007/JHEP10(2013)133), [arXiv:1306.1534](https://arxiv.org/abs/1306.1534).

2654 **Acronyms**

- 2655 **ALICE** A Large Ion Collider Experiment
- 2656 **ATLAS** A Toroidal LHC ApparatuS
- 2657 **APD** Avalanche Photo-Diodes

2658	<b>BSM</b>	Beyond Standard Model
2659	<b>CERN</b>	European Organization for Nuclear Research
2660	<b>CMS</b>	Compact Muon Solenoid
2661	<b>CMSSM</b>	Compressed Minimal SuperSymmetric Model
2662	<b>CSC</b>	Cathode Stripe Chamber
2663	<b>CSV</b>	Combined Secondary Vertex
2664	<b>CSVM</b>	Combined Secondary Vertex Medium Working Point
2665	<b>DT</b>	Drift Tube
2666	<b>ECAL</b>	Electromagnetic CALorimeter
2667	<b>EB</b>	Electromagnetic CALorimeter Barrel
2668	<b>EE</b>	Electromagnetic CALorimeter Endcap
2669	<b>ES</b>	Electromagnetic CALorimeter pre-Shower
2670	<b>EMG</b>	Exponentially Modified Gaussian
2671	<b>EPJC</b>	European Physical Journal C
2672	<b>EWK</b>	Electroweak Sector
2673	<b>GCT</b>	Global Calorimeter Trigger
2674	<b>GMT</b>	Global MuonTrigger
2675	<b>GT</b>	Global Trigger
2676	<b>HB</b>	Hadron Barrel
2677	<b>HCAL</b>	Hadronic CALorimeter
2678	<b>HE</b>	Hadron Endcaps
2679	<b>HF</b>	Hadron Forward
2680	<b>HLT</b>	Higher Level Trigger
2681	<b>HO</b>	Hadron Outer
2682	<b>HPD</b>	Hybrid Photo Diode

2683	<b>ISR</b>	Initial State Radiation
2684	<b>LUT</b>	Look Up Table
2685	<b>L1</b>	Level 1 Trigger
2686	<b>LEP</b>	Large Electron-Positron Collidor
2687	<b>LHC</b>	Large Hadron Collider
2688	<b>LHCb</b>	Large Hadron Collider Beauty
2689	<b>LO</b>	Leading Order
2690	<b>LSP</b>	Lightest Supersymmetric Partner
2691	<b>NLL</b>	Next to Leading Logorithmic Order
2692	<b>NLO</b>	Next to Leading Order
2693	<b>NNLO</b>	Next to Next Leading Order
2694	<b>POGs</b>	Physics Object Groups
2695	<b>PS</b>	Proton Synchrotron
2696	<b>QED</b>	Quantum Electro-Dynamics
2697	<b>QCD</b>	Quantum Chromo-Dynamics
2698	<b>QFT</b>	Quantum Field Theory
2699	<b>RBXs</b>	Readout Boxes
2700	<b>RPC</b>	Resistive Plate Chamber
2701	<b>RCT</b>	Regional Calorimeter Trigger
2702	<b>RMT</b>	Regional Muon Trigger
2703	<b>SUSY</b>	SUPerSYmmetry
2704	<b>SM</b>	Standard Model
2705	<b>SMS</b>	Simplified Model Spectra
2706	<b>SPS</b>	Super Proton Synchrotron
2707	<b>TF</b>	Transfer Factor

2708	<b>TP</b>	Trigger Primitive
2709	<b>VEV</b>	Vacuum Expectation Value
2710	<b>VPT</b>	Vacuum Photo-Triodes
2711	<b>WIMP</b>	Weakly Interacting Massive Particle